DOCTOR OF PHILOSOPHY

Development of bioprocessor chip technology

Hayden, Christopher John

Award date:
2002

Awarding institution:
Bangor University

Development of Bioprocessor Chip Technology

by

Christopher John Hayden

Thesis submitted for the degree of Doctor of Philosophy

University of Wales, Bangor
2002

Acknowledgements

I would like to thank my supervisors, Prof. Ron Pethig and Dr. Julian Burt for their help and encouragement in this field, as well as Dr. Mark Talary for showing me the basics of laser machining. Dr. Xiao-Feng Zhou's many cups of tea and encouragement was greatly appreciated, Mr. John Tame for his help with all clean room and darkroom related matters, then still managing to smile after yet another question. Dr. Andrew Goater and Dr. Sally Cotterill for their help with cell culture and bead related work. Dr. Richard Lee, Mr. Colin Dalton and Mr. James Drysdale for their friendship, help at the conference drinking sessions, as well as some academic related matters. I would also like to thank Dr. Jan Eijkel (Imperial College, London) for his cooperation and assistance with the cACEOP devices.

Finally I would like to thank my parents and family for their support and encouragement throughout the last three and a half years.

Summary

Micro ElectroMechanical Systems (MEMS) is a term that describes a wide range of miniaturised systems, including Biofactory-on-a-chip devices that are currently under development at Bangor. Traditionally, silicon fabrication processes have been used to allow micro-structuring of components needed to create such MEMS, although polymer based fabrication technologies are gaining popularity. Polymer based MEMS are well suited to rapid development and mass manufacture, so allowing low-cost, disposable devices. However, alternative methods have to be developed to allow high-resolution patterning of such materials. One such method is excimer laser ablation. This process is ideally suited to fabricating small, micron sized features in a wide variety of materials.

This work investigates utilising an excimer laser micromachining system to fabricate micron-resolution structures. Conventional laser ablation was used to create planar structures in thin films between 1μm and 200μm thick. This allowed the fabrication of miniaturised polymer-based on-chip optical sensors, both optical fibre and planar waveguide based, compatible with existing Biofactory fabrication processes. Laser patterning of thin films combined with optical reduction-projection was used to produce high-resolution contact masks. This enabled the in-house fabrication of a circular AC electroosmotic chromatography device, with electrode sizes as small as 4.2μm. The unwanted side-effect of excimer laser machining, where laser ablation generated debris is re-cast onto the sample, was also investigated and it was found that the debris could be prevented using an electrostatic collection system. Laser machining was also used to create greyscale masks, suitable for use in a contact exposure photolithographic process, allowing the fabrication of a fluidic manifold system. Greyscale masks were then applied to laser machining. Implementing such masks allowed arbitrary surface profiles to be machined in a wide variety of materials. The complex structures that were defined were machined to depths in excess of 100μm, without mask degradation. This is not known to have been previously reported.

The excimer laser system was also used as a stereolithography exposure source, in a preliminary investigation. The results obtained suggest that sub-micron patterning is possible using such an approach.

Contents

		Page
Chapter 1	**Introduction**	
1.1	Introduction	1
1.2	References	5
Chapter 2	**Laser micromachining and associated processes**	
2.1	Introduction	10
2.2	The process of ablation	12
2.3	Beam delivery optics	17
2.4	Common machining techniques	17
2.4.1	Serial machining	18
2.4.2	Patterned masks	20
2.5	Optical system resolution limits	21
2.5.1	Diffraction	22
2.5.2	Limit of resolution	23
2.5.3	Wall angle of machined structures	27
2.5.4	Effect of depth of field	28
2.6	Laser micromachining applications at the start of the project	29
2.7	Summary	29
2.8	References	30
Chapter 3	**Experimental methods**	
3.1	Introduction	33
3.2	Excimer laser micromachining system	33
3.3	Cleanroom fabrication processes	46
3.3.1	Evaporation of metal films	46
3.3.2	Laminate coatings	47
3.3.3	Spin coatings	47
3.3.4	Contact exposure mode photolithography	49
3.3.5	Wet etching	50
3.4	Mask substrate characterisation	51
3.5	Aperture production	52
3.5.1	Chemically etched copper beryllium	52
3.5.2	Laser machined apertures	53
3.6	Mask production	56
3.6.1	Photographic mask plates	56
3.6.2	Photolithographically produced masks	57
3.6.3	Laser machined masks	57
3.6.3.1	Exposed photographic mask plates	58
3.6.3.2	Spin coated S1818 layers	58
3.6.3.3	Evaporated chrome-on-glass	58
3.6.3.4	Dry-film-laminate layers	59
3.7	Problems of laser machining	59

3.7.1	Problems of laser machining masks with quartz substrates	59
3.7.2	Laser ablation generated debris	61
3.8	Examining the machined structures	64
3.9	References	65

Chapter 4 Fabricating a circulas AC electroosmotic pump

4.1	Introduction	67
4.2	Design of cACEOP pump	69
4.3	Fabricating the x10 laser mask	71
4.4	Fabrication of 1:1 contact masks	76
4.4.1	Photographic mask plates	77
4.4.2	S1818 on glass	83
4.4.3	Chrome on glass	87
4.4.4	Measurement of mask feature size	88
4.5	Fabrication of microelectrodes for use as cACEOP pump	89
4.5.1	Photographic mask plates	90
4.5.2	S1818 on glass	91
4.5.3	Chrome on glass	94
4.6	Direct machining of resist coatings	94
4.7	Direct machining of devices	96
4.8	Device encapsulation	97
4.9	Discussion	99
4.9.1	Problems encountered fabricating devices	102
4.10	Conclusions	102
4.11	References	104

Chapter 5 On-chip optical detection

5.1	Introduction	105
5.2	Theory of absorption measurement	106
5.3	Optical fibre-based sensors	108
5.3.1	Limitations of optical absorption detectors	109
5.3.2	Optical fibre based device fabrication	109
5.3.3	Experimental setup	114
5.3.4	Particle detection results	116
5.3.5	Measuring the absorption of dyes	117
5.3.6	Inherent limitations of fibre-based optical sensors	122
5.4	On-chip planar waveguide optical sensor design	122
5.4.1	Planar waveguide fabrication	124
5.4.2	Detection and measurement of cell suspensions	130
5.4.3	Improving planar device detection sensitivity	135
5.4.4	Problems encountered developing planar on-chip sensors	139
5.5	Conclusions	140
5.6	References	141

Chapter 6 Development of greyscale mask micro-fabrication technology

6.1	Introduction	144
6.2	Greyscale masks	145
6.2.1	The concept of greyscale masks	145
6.2.2	Mask patterning options	147
6.2.2.1	Line / space ratio	148
6.2.2.2	Variable rectangular apertures	148
6.2.2.3	Binary dithering algorithms	149
6.2.2.4	Clustered-dot-ordered-dither	150
6.2.2.5	Periodic grids	152
6.3	Implementing greyscale masks into photolithography	155
6.3.1	Mask requirements	156
6.3.2	Creating three-dimensional test structures in a single exposure	160
6.3.3	Fabricating a fluidic manifold	168
6.4	Excimer laser machining using greyscale masks	174
6.4.1	Laser mask requirements	174
6.4.2	Excimer laser greyscale mask creation	175
6.4.3	Implementing test masks	177
6.4.4	Results of using ill-matched mask dimensions	182
6.4.5	Machining glass using greyscale masks	183
6.4.6	Creating complex three-dimensional structures	184
6.5	Conclusions	190
6.6	References	193

Chapter 7 Stereolithography using excimer laser exposure

7.1	Introduction	197
7.2	Principle of stereolithography	198
7.3	Experimental setup	201
7.3.1	Initial characterisation investigation	201
7.4	Results of suitability trials	205
7.5	Investigation to create three-dimensional structures	209
7.6	Results	212
7.7	Conclusions	217
7.8	References	219

Chapter 8 Conclusions and suggestions for future work

8.1	Conclusions	222
8.2	Suggestions for future work	224
8.2.1	Mask fabrication process	225
8.2.2	On-chip optical detector	225
8.2.3	Machining with greyscale masks	226
8.2.4	Development of a stereolithography micro-fabrication system	226

Appendices

Appendix I	Spin Speed Curves	228
Appendix II	Listing of laser code used to implement mask scanning	229
Appendix III	Optical detection circuit diagram	233
Appendix IV	Re-useable device mount	234
Appendix V	Published work	242

Chapter 1

Introduction

1.1 Introduction

Micro electromechanical systems (MEMS) is a general term used to describe various microdevices and microsystems. Such systems include the wide range of miniaturised devices, such as accelerometers [1, 2], micro-actuators [3, 4], pressure sensors [5-7], chemical sensors [8] and biosensors [8-12], which are used in various applications, including automotive, pharmaceutical, healthcare, and aerospace [1-15]. These miniaturised devices have considerable advantages over conventional, large-scale devices. For example, accelerometers are smaller so can be operated over a larger measurement range without device deterioration while miniaturised sensors and chemical reactors require smaller analyte volumes. This can be particularly beneficial where a chemical reactor is used to contain a strongly exothermic reaction between two materials. In such circumstances macro-scale mixing may be hazardous. The smaller volumes used in a micro-mixer allows any heat generated to be dissipated rapidly. Another advantage of smaller fluidic channels is that the temperature throughout the channel can be accurately controlled, which can be beneficial for the processing task in-hand [12]. The smaller volumes used allow a reduction in the processing time, as the diffusion times and hence reaction times within the devices are reduced. For example, biological molecules can be processed and the result detected in seconds [8]. The smaller analyte volumes required and the rapid detection of results that are possible using such systems have led to the development of micro-devices that can simultaneously perform hundreds of tests on a sample [16]. For example, Affymetrix, Caliper and Nanogen, to name but a few, have developed such systems.

Micro-devices are typically fabricated using processing techniques originally developed to produce silicon integrated circuits. However, more recently MEMS specific processes have been developed. Such techniques include photolithography, etching, LIGA and focused ion beam processes that are outlined here.

Photolithography is a common process used to selectively pattern a radiation sensitive material, described in detail in Chapter 3.3.4. Etching, usually used in conjunction with a selectively patterned resist layer to allow the etching of selected regions only, is a common method used to remove material from a workpiece. Wet etching is a term that describes using aqueous chemical solutions to etch the workpiece. These solutions are caustic to the workpiece, but do not damage any resist present, so allowing selective patterning. An alternative to wet etching is dry etching, implemented by bombarding the surface of the workpiece with ions. A typical process is Reactive Ion Etching (RIE), where a gas is ionised to produce a plasma. The ions present are accelerated towards the workpiece, allowing anisotropic etching of the workpiece, which can be formed from a variety of materials [17-19]. RIE can be used to machine arbitrary shapes with vertical walls up to hundreds of microns deep and is not limited by the crystal planes found in silicon.

The term 'LIGA' (from the German LIthographie, Galvanoformung, Abformung) describes the process of producing microstructures by defining a pattern using photolithography and electroplating the structured substrate before the remaining photoresist is removed [20]. The metal structure produced can be used as a precision mould. The original process used an X-ray synchrotron source, but this is expensive and alternative processes, using Ultra-Violet (UV) sources and lasers have been developed [21, 22].

Focused ion beams can be used to selectively remove and deposit material [23-25] without the use of a mask. The material removal process is sputtering, where ions are electrically accelerated and focused to a point on the workpiece [26]. By adding a suitable gas, material can also be deposited onto the workpiece.

As such these are well established and well-characterised processes that use existing, readily available, manufacturing equipment [1-8, 13-15] for fabricating small structures, e.g. micro-actuators, micro-fluidic channels and micro-sensors. Another advantage of utilising these fabrication techniques is that devices are readily suited to mass production, as this is an inherent property of the techniques used.

At the University of Wales, Bangor, a specific type of micro-device is being developed to allow the manipulation, characterisation and detection of bio-particles. These devices are termed 'Biofactory-on-a-chip' devices and commonly consist of an integrated system of micro-fluidic channels and microelectrodes. A common requirement is the visual inspection of the channel contents, generally by using an optical microscope. This requirement does not lend itself to silicon-based fabrication processes, as optically transparent upper and lower substrates are required.

Typical materials used in Biofactory construction are glass and polymer-based and because these materials must also be patterned with small structures, complimentary fabrication processes are required to those used in photolithography.

Several methods can be used to create micro-patterned structures in polymers [27, 28]. Hot embossing allows materials to be shaped by pressing a pre-formed patterned mould into a heated polymer, so replicating the shape of the mould [2, 29, 30]. Injection moulding can also be used to create microstructures by injecting molten plastic into a suitable mould [28, 31]. However, both of these processes require the mould to be fabricated in the first place. This has been accomplished previously by electroplating processed silicon with metal [27]. Furthermore, the mould resolution is critical, as its features will be accurately reproduced.

Micro-milling can be used to machine a variety of materials, including metals and polymers and consists of a miniaturised milling machine, typically with computer controlled motion stages. This allows direct machining of micro-components and metal moulds, suitable for use in the hot embossing and injection moulding processes. The resolution attainable with such machines, however, is generally limited to approximately 5μm, although specialist sub-micron equipment is available. Other problems with processes based on the mechanical removal of material, such as micro-milling and micro-turning, include deflection and cutter positioning. Workpiece deflection generated during machining by the cutter contacting the workpiece has been reported to limit the final accuracy of the process [32], as has the ability to reliably and accurately position the cutter used [33].

Photolithography, as used in semiconductor processes, can be used to pattern a photosensitive material to very high resolution using a mask to selectively expose the material to a suitable illumination source [34, 35]. Chemical development can then be used to remove selectively regions of the material, depending which areas have been exposed. The patterned layer can either form the final structure or, alternatively, be used as a selective masking layer in subsequent processes, such as etching or electroplating [36].

Laser machining, on the other hand, allows direct, high-resolution patterning of materials [37-47], for example by using laser ablation to selectively remove material from thin films or machine simple fluidic channels [28]. Such a process is well suited to micromachining, since the areas surrounding the laser machined regions are minimally affected, if at all, by the machining processes used, and sub-micron resolution can easily be attained [39, 43, 47, 48].

The structures produced using either photolithography or laser machining, when applied to suitable materials, can be used as masters in hot embossing systems [48, 49], although the longevity of the master is limited. However, both laser machined and photolithographically produced structures can be used to form moulds, for example to shape curable resins [50], or in electroplating processes. Here, 'hard' metal masters with resolutions similar to those fabricated are formed by coating the structure with metal, suitable for use in both hot embossing and injection moulding procedures [49, 51].

The ability of laser machining to accurately structure polymers and other materials to sub-micron resolutions is of interest for the production of Biofactory devices and components, as the materials used require patterning to a high-resolution [52]. Such components can either be directly laser machined [28], for example in a research and development environment, or used to structure high-resolution 'masters' for use in other processes, allowing mass-production of components and the widespread use of such inexpensive, polymer based devices.

The work reported in this thesis is concerned with developing flexible, polymer-based laser micromachining fabrication processes, capable of high-resolution structures and

components. The methods used are well suited to rapid fabrication using existing equipment and facilities, as well as being compatible with low-cost, mass-production processes.

1.2 References

[1] 'Silicon micro-accelerometer with mg resolution, high linearity and large frequency bandwidth fabricated with two mask bulk processes', Z. Xiao, M. Chen, G. Wu, C. Zhao, D. Zhang, Y. Hao, G. Zhang, Z. Li, *Sensors and Actuators* **77** (1999) 113-119.

[2] 'Fabrication of LIGA-acceleration sensors by aligned moulding', A. Both W. Bacher, M. Heckele, K.-D. Muller, R. Ruprecht and M. Strohrmann, *Microsystem Technologies* **2** (1996) 104-108.

[3] 'A bidirectional silicon micropump', R. Zengerle, J. Ulrich, S. Kluge and A. Richter, *Sensors and Actuators A* **50** (1995) 81-86.

[4] 'A large-force fluidic device micromachined in silicon', C. Cho, J. Kin and D. D. Cho, *J. Micromech. Microeng.* **8** (1998) 195-199.

[5] 'A micromachined pressure sensor for biomedical applications', G. Bistue, J. G. Elizalde, I. Garcia-Alonso, S. Olaizola, E. Castano, F. J. Gracia and A. Garcia-Alonso, *J. Micromech. Microeng.* **7** (1997) 244-246

[6] 'A capacitive absolute-pressure sensor with external pick-off electrodes', J-S. Park and Y. B. Gianchandai, *J. Micromech. Microeng.* **10** (2000) 528-533

[7] 'Optimised technology for the fabrication of piezoresistive pressure sensors', A. Merlos, J. Santander, M. D. Alvarez and F. Campabadal, *J. Micromech. Microeng.* **10** (2000) 204-208

[8] 'Micromachining chemical and biochemical analysis and reaction systems on glass substrates', D. J. Harrison, K. Fluri, N. Chiem, T. Tang and Z. Fan, *Sensors and Actuators B* **33** (1996) 105-109.

[9] 'Degenerate Oilgonucleotide Primed-Polymerase Chain Reactions and Capillary Electrophoretic Analysis of Human DNA on Microchip-Based Devices', J. Cheng, L. C. Walters, P. Fortina, G. Hvichia, S. C. Jacobsen, J. M. Ramsey, L. J. Kricka and P. Wilding, *Analytical Biochemistry* **257** (1998) 101-106

[10] 'Isolation of Cultured Cervical Carcinoma Cells Mixed with Peripheral Blood Cells on a Bioelectronic Chip', J. Cheng, E. Sheldon, L. Wu, M. J. Heller and J. P. O'Connell, *Anal. Chem.* **70** (1998) 2321-2326

[11] 'Preparation and hybridisation analysis of DNA/RNA from *E. coli* on microfabricated bioelectronic chips', J. Cheng, E. L. Sheldon, L. Wu, A. Uribe, L. O. Gerrue, J. Carrino, M. J. Heller and J. P. O'Connel, *Nature Biotechnology* **16** (1996) 541-546

[12] 'Integrated Cell Isolation and Polymerase Chain Reaction Analysis Using Silicon Microfilter Chambers', P. Wilding, L. J. Kricka, J. Cheng, G. Hvichia, M. A. Shoffner and P. Fortina, *Analytical Biochemistry* **257** (1998) 95-100

[13] 'A silicon resonant sensor structure for coriolis mass-flow measurements', P. Enoksson, G. Stemme and E. Stemme, *J. Microelectromech. Sys.* **6, 2** (1997) 119-125.

[14] 'Two simple micromixers based in silicon', M. Koch, D. Chatelain, A. G. R. Evans and A. Brunnschweiler, *J. Micromech. Microeng.* **8** (1998) 123-126.

[15] 'A three-dimensionally silicon-micromachined fluidic amplifier device', T. H. Kim, C. H. Cho and D.-I. D. Cho, *J. Micromech. Microeng.* **8** (1998) 7-14.

[16] 'Revolution on a square centimetre', L. J. Kricka, *Nature Biotechnology* **16** (1998) 513-514

[17] 'Deep reactive ion etching of Pyrex glass using SF6 plasma', X. Li, T. Abe, M. Esashi, *Sensors and Actuators A* **87** (2001),139-145

[18] 'Release of metal structures in MEMS devices by dry-etching technique', N. C. Das, *Solid State Electronics* **46** (2002) 501-504

[19] 'Electron beam lithography and reactive ion etching of nanometer size features in niobium films', T. T. Piotrowski, A. Piotrowska, E. Kaminska, Z. Szopniewski, S. Kolesnik, J. Wrobel, P. Gierlowski and S. Lewandowski, *Materials Science and Engineering C* **15** (2001) 171-173

[20] 'Ultra-deep LIGA process and its applications', Y. Cheng, B.-Y. Shew, M. K. Chyu and P. H. Chen, *Nuclear Instruments and Methods in Physics Research A* **467-468** (2001) 1192-1197

[21] 'Low cost fabrication of micromechanical systems', Z. Cui and R. A. Lawes, *Microelectronic Engineering* **35** (1997) 389-392

[22] 'UV-LIGA process for high aspect ratio structure using stress barries and C-shaped etch hole', H-K. Chang, Y-K. Kim, *Sensors and Actuators* **84** (2000) 342-350

[23] 'Future trends in diagnosis using laboratory-on-a-chip technologies', M. S. Talary, J. P. H. Burt and R. Pethig, *Parasitology* **117** (1998), S191-S203

[24] 'The growth and modification of materials via ion–surface processing', L. Hanley and S. B. Sinnott, *Surface Science* **500** (2002) 500 –522

[25] 'Self-aligned formation of a vertical-type micro field emitter with a volcano-shaped gate electrode protruding towards the cathode by focused ion-beam sputter etching and deposition', Y. Gotoh, N. Fujita, H. Tsuji, J. Ishikawa, S. Nagamachi and M. Ueda, *J. Micromech. Microeng.* **9** (1999) 364–368

[26] 'Focused ion beams for microfabrication', J. H. Daniel, D. F. Moore and J. F. Walker, *Engineering Science and Education Journal*, **7,2** (1998) 53-56

[27] 'Polymeric MST – high precision at low cost', H. Elderstig, O. Larsson, *J. Micromech. Microeng.* **7** (1997) 89-92

[28] 'A poly-methylmethacrylate electrophoresis microchip with sample preconcentrator', Yu-C. Lin, H-C. Ho, C-K. Tseng and S-Q. Hou, *J. Micromech. Microeng.* **11** (2001), 189-194

[29] 'Hot embossing – the moulding technique for plastic microstructures', M. Heckele, W. Bacher and K. D. Muller, *Microsystem Technologies* **4,3** (1998) 122-124.

[30] 'Modular moulding equipment for quasi monolitic integration of micromechanical and microelectronic components', M. Heckele and W. Bacher, *Proceedings of the 3rd France-Japan Congress & 1st Europe-Asia Congress on Mechatronics* (1996)

[31] 'Micro moulding – a powerful tool for the large-scale production of precise microstructures', L. Weber, W. Ehrfeld, H. Freimuth, M. Lacher, H. Lehr and B. Pech, *Proc. SPIE* **2879** (1996) 156-167

[32] 'The Miniaturisation Technologies: Past, Present and Future', A. B. Frazier, R. O. Warrington and C. Friedrich, *IEEE Trans. Indust. Elec.* **42** (1995) 423-430

[33] 'Micromechanical engineering: a basis for the low-cost manufacture of mechanical microdevices using microequipment', E. M. Kussl, D. A. Rachkovskij, T. N. Baidyk and S. A. Talayev, *J. Micromech. Microeng.* **8** (1996) 410-425

[34] "*Fundamentals of Microfabrication*", M. J. Madou, *CRC press*, 1997, Boca Raton, Florida

[35] 'Ultra line-narrowed F_2 laser for microlithography', H. Komori, T. Ariga, H. Watanabe, T. Kumazaki, N. Kitatochi, K. Sasano, Y. Ueno, T. Nishisaka, R. Nohdomi, K. Hotta, H. Mizoguchi and K. Nakao, *RIKEN Review* **43** (2002) 76-79

[36] 'Micro heat flux sensor using copper electroplating in SU8 microstructures', S. H. Oh, K-C. Lee, J. Chunn, M. Kim and S. S. Lee, *J. Micromech. Microeng.* **11** (2001) 221-225.

[37] 'GaN ablation etching using short wavelength pulsed laser', T. Akane, K. Sugioka, K. Midorikawa, K. Obata, N. Aoki and K. Toyoda, *RIKEN Review* **43** (2002) 45-48

[38] 'Supplemental multilevel interconnects by laser direct writing: Application to GaAs digital integrated circuits', J. G. Black, S. P. Doran, M. Rothschild and D. E. Ehrlich, *Appl. Phys. Lett.* **50** (1987) 1016-1018

[39] 'Multishot ablation of polymer and metal films at 248nm', E. Hunger, H. Pietsch, S. Petzoldt and E. Matthias, *Applied Surface Science* **54** (1992) 227-231

[40] 'Metal film removal and patterning using a XeCl laser', J. E. Andrew, P. E. Dyer, R. D. Greenough and P. H. Key, *Appl. Phys. Lett.* **43** (1983) 1076-1078

[41] 'Direct etching of polymeric materials using a XeCl laser', J. E. Andrew, P. E. Dyer, D. Foster and P. H. Key, *Appl. Phys. Lett.* **43** (1983) 717-719

[42] 'Excimer laser etching of polyimide', J. H. Brannon, J. R. Lankard, A. I. Baise, F. Burns and J. Kaufman, *J. Appl. Phys.* **58** (1985) 2036-2043

[43] 'Laser ablation as a processing technique for metallic and polymer layered structures', E. E. Guzzo and J. S. Preston, *IEEE Transactions on semiconductor manufacturing* **7** (1994) 73-78

[44] 'UV laser machined polymer substrates for the development of microdiagnostic systems', M. A. Roberts, J. S. Rossier, P. Bercier and H. Girault, *Anal. Chem.* **69** (1997) 2035-2042

[45] 'Ultraviolet laser ablation of polyimide films', R. Srinivasan, B. Braren and R. W. Drefus, *J. Appl. Phys.* **61** (1987) 372-376

[46] 'Ultraviolet laser ablation of organic polymers', R. Srinivasan and B. Braren, *Chem. Rev.* **89** (1989) 1303-1316

[47] 'Excimer laser projection photoetching', M. Latta, R. Moore, S. Rice and K. Jain, *J. Appl. Phys.* **56** (1984) 586-588

[48] "*Laser processing in manufacturing*", R. C. Crafer and P. J. Oakley, *Chapman & Hall*, 1993, London

[49] 'Patterning, electroplating and removal of SU8 moulds by excimer laser micromachining', M. K. Ghantasala, J. P. Hayes, E. C. Harvey and D. K. Sood, *J. Micromech. Microeng.* **11** (2001) 133-139.

[50] 'Excimer laser micromachining and replication of 3D optical surfaces', A. Braun, K. Zimmer, B. Hosselbarth, J. Meinhardt, F. Bigl and R. Mehnert, *Applied Surface Science* **127-129** (1998) 911-914.

[51] 'Laser-assisted chemical micromachining of metals and alloys', A. Stephen, T. Lillenkamp, S. Metev and G. Sepold, *RIKEN Review* **43** (2002) 56-62

[52] 'Direct manufacture of miniature bioparticle electro-manipulators by excimer laser mask projection', N. H. Rizvi P. T. Rumsby, J. P. H. Burt, M. S. Talary, J. A. Tame and R. Pethig, *ICPE* **2** (1997) 971-974

Chapter 2

Laser micromachining and associated processes

2.1 Introduction

Lasers have various uses in micro-fabrication including exposure sources for photolithography and laser-LIGA processes [1], deposition systems [2, 3] and machining systems [4-8]. UV lasers are used as the illuminating source for deep-UV lithography systems [9, 10], allowing increased resolution, due to such lasers having a shorter wavelength and narrow linewidth, compared to a high-pressure mercury-arc lamp. For example, a KrF laser shows a sharp emission peak at a wavelength (λ) of 248 nm with a linewidth of 0.4 nm [11], whereas a mercury lamp typically emits between λ=350 nm and λ=450 nm with various emission peaks. Pulsed laser-plasma deposition (PLPD) is a technique that allows various materials to be deposited onto substrates by irradiating a target located in close proximity to the workpiece. By placing the target and workpiece in a vacuum chamber, the material ablated from the target coats the workpiece, allowing polycomponent thin film layers to be deposited [12]. Laser machining is used to fabricate structured components in a variety of materials directly, with no subsequent processing steps, e.g. a development stage is not required [6].

The process of laser machining relies on bombarding the surface of a material with high-intensity laser generated radiation. The incident radiation reacts with the surface of the material causing it to be removed. Excimer laser systems, used extensively in this work, generally implement optical systems that guide, profile and focus the laser beam onto the workpiece. Masks can also be included in the optical path to allow selective transmission of the laser beam, thus patterning the workpiece [13-16]. By fixing the beam path and moving the mask and workpiece accurately in a controlled manner, complex structuring can also be achieved. A list of materials, their ablation thresholds and the results of machining them at different wavelengths is shown in Table 2.1. The principal mechanisms of laser machining and the relevant implementation methods are important if micro-machining using excimer lasers is to be

used to fabricate structures. Hence the relevant details are given in the following sections.

Material	**Wavelength (nm)**	**Threshold energy density (J/cm^2)**	**Machined surface quality**	**Optimum laser type [wavelength]**
Polyacetylene	193	0.06	Smooth etch	ArF [193nm]
Polyamide (PA) [*Nylon 6 & 66*]	193 248	0.35 0.75	Smooth at both wavelengths	KrF [248 nm]
Polycarbonate (PC) [*Lexan*®]	193 248	0.05 0.12	Some rippling on surface	KrF [248nm]
Polyethylene (PE)	193	0.25	Smooth etch	ArF [193nm]
Polyethylene terephthalate (PET) [*Mylar*®]	193 248 308	0.03 0.10 0.20	Small surface structures	XeCl [308nm]
Polyimide (PI) [*Kapton*®]	193 248 308	0.05 0.06 0.05	Similar at all λs. Coned structures at threshold, smooth above	XeCl [308nm]
Poly(methylmethacrylate) (PMMA)	193 248	0.05 0.30	Smooth above $0.6J/cm^2$ Melting at 248nm	ArF [193nm]
Borosilicate glass	193 248 308	4 8 10	Smooth above $7J/cm^2$ Rough at 248nm and 308nm	ArF [193nm]
Alumina (Al_2O_3)	193 248 308	1.0 2.0 3.0	Highly structured at threshold, porous above	XeCl [308nm]

Table 2.1 *List of materials and the associated machining characteristics when machined using excimer lasers. Data from Reference [11].*

2.2 The process of ablation

Laser ablation describes the removal of a solid material by bombarding it with a pulse of laser radiation of sufficient energy and intensity [17, 18]. Excimer lasers are commonly used to implement photoablation due to the properties of the laser light generated, namely a short, high-intensity pulse of UV radiation [13-17, 19-22]. The generated laser beam is spectrally relatively narrow, so produces well-defined output wavelengths that allow specific chemical bonds exposed to the laser beam to be broken, but leave other materials with a different chemical composition intact. This is well suited to ablation, as such wavelengths can react simultaneously with all exposed molecular bonds, of a suitable strength, present in the workpiece, allowing efficient material removal. Laser light is inherently spatially coherent and this property allows it to be focused to a spot, whose dimensions can be as smaller than a micron, or used to convey a pattern to a material over long distances without significant deterioration of the beam intensity. Hence ablation is highly suited to the machining of polymer-based materials, as these materials absorb strongly in the UV spectrum, which is a prerequisite of an efficient ablation process. An example of this process is the removal of regions of a polyimide film using an excimer laser [17, 21].

Although other lasers, such as a longer wavelength Infrared (IR) CO_2 laser, can be used to machine polymers, many photons have to be absorbed to heat the material sufficiently to cause bond scission [23, 24]. This is so because the photon energies are lower, typically about 0.12eV when $\lambda = 10.6\mu m$ (CO_2) and 1.2eV when $\lambda = 1.06\mu m$ (Nd:YAG) [11]. This is not an ideal situation, since the heating effects are not localised at the exposed region and deformation of surrounding areas may result and damage, such as charring, melting and combustion may occur. Excimer lasers, described in Chapter 3.1, on the other hand, are ideally suited to machining man-made materials, such as the polymers used in Biofactory devices. This is because the photon energies lie between 3.5eV [XeCl] and 7.9eV [F_2], depending on the gases used in the lasing medium and are sufficient, therefore, to break a 3.5eV C—H bond commonly found in organic materials [11].

The process of laser ablation is a complex light-solid interaction process with two major destructive processes: photochemical and photothermal, although the precise removal mechanism is controversial [14]. The photochemical process describes the bond-scission caused by the incident radiation, whereas the photothermal effects relate to the localised temperature increase in the irradiated zone. The dominating destructive effect is dependent on the material absorption at the applied wavelength and the energy density used. It has been reported [25] that at low fluences, the thermal effects are negligible and photochemical effects dominate. As the fluence is increased, photothermal effects become more significant.

Let us consider the ablation process resulting from bombarding a polymer material, such as polyimide, with a high-intensity UV radiation pulse, typically 10ns to 30ns in duration [11]. This will cause the area exposed to the laser beam to be removed in a precisely defined manner. The incident radiation will affect a shallow region below the surface, generally less than 10 μm, the actual depth depending on the energy density used. The ablation process, which lasts for short periods of time (approximately 40ns to 80ns), also generates a marked increase in the temperature of the irradiated material. Temperatures in excess of 1000 °C have been reported [17]. As the incident radiation energy density is above that required for bond-scission, the incident photons break the weak polymer bonds of the long chain molecules that form the material. As the individual polymer bonds are broken by the UV photons, the polymer chains fragment, so reducing the structural integrity of the material. However, the volume of the ablated region does not change, even though the local particle density increases significantly. This causes a rapid increase in pressure and the particles present in the ablation region are ejected at supersonic speeds [17], resulting in the generation of shockwaves [17, 19] that magnify the destructive process by removing weakly attached material. Figure 2.1 shows a diagrammatic representation of the process. Analysis of the particles ejected when polyimide was ablated revealed that the main constituent (other than particles of intact polymer) was elemental carbon [17, 21].

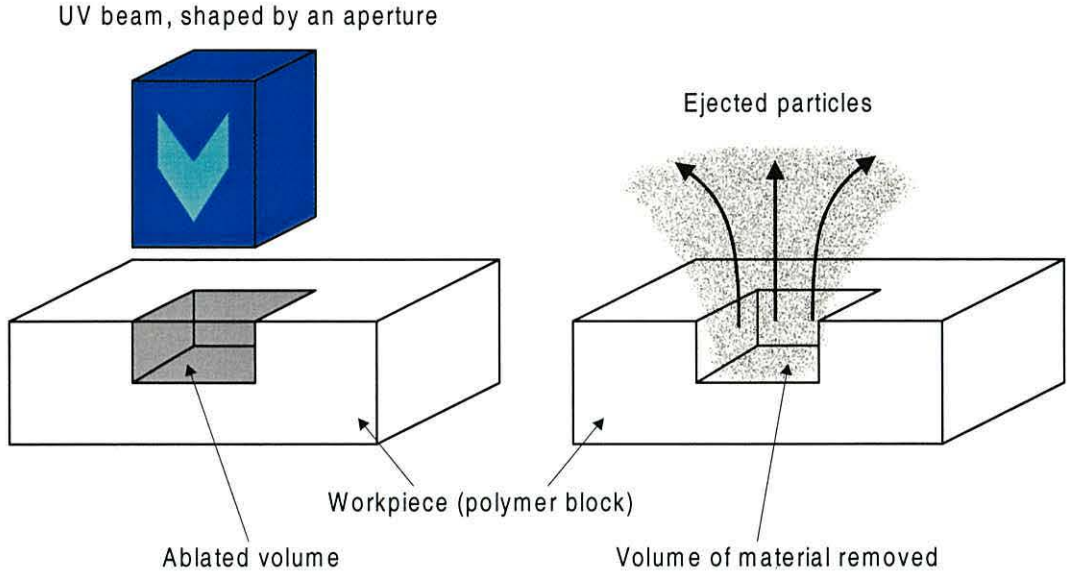

Figure 2.1 *Laser ablation of a polymer block using an UV laser beam. The high-energy pulse of radiation is absorbed by the material and breaks inter-atomic bonds within a shallow region defined by the beam. This causes the material to degrade and the particle density to increase rapidly in the exposed region, so ejecting the particles at supersonic speeds.*

When a material is ablated, an acoustic 'crack' can be heard, due to the pressure increase and the associated shockwave. The small flame, or ablation plume, that is seen, Figure 2.2, was found to be very repeatable if the ablation parameters used are similar [26] and is due to the ejection of and fluorescence from fragments ejected from the ablated region.

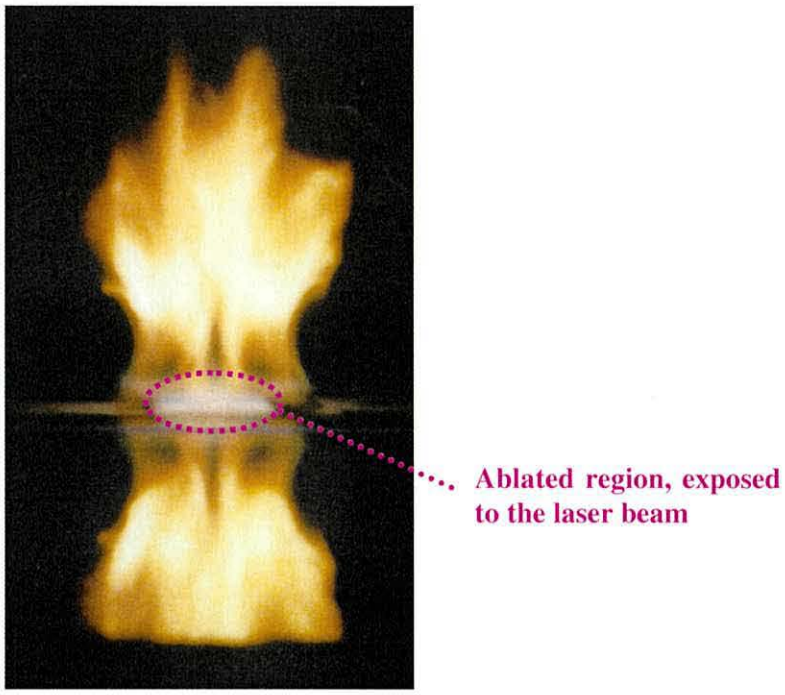

Figure 2.2 *Image of an ablation plume produced by excimer laser ablation machining of a polyimide film. The image was recorded photographically onto 35mm film. The plume generated is the upper flame-like shape. The mirror image is caused by reflection from the surface of the workpiece. The radiated region is indicated and can be seen as the pale region beneath the plume.*

The amount of heat transferred to surrounding areas is small when a suitable energy density is used to avoid photothermal effects from dominating. This enables very fine patterning of materials to take place with negligible damage to surrounding areas. The depth of the ablation zone is controlled by the energy density of the incident beam, so allowing the volume removed to be accurately controlled. Although well suited to polymer-based machining, laser ablation can also be used to pattern various other materials, including metals, glass, paper, ceramics and biological tissue [11].

It can also be deduced that if the incident radiation is below the material-dependent threshold energy density†, ablation will not occur owing to a lack of photons of sufficient energy being present. Hence insufficient chemical bonds will be broken within the irradiated material to cause a large enough pressure increase to overcome the mechanical integrity of the material.

Hence, for typical laser ablation processes, the energy density of the beam should be

† Energy density is defined as the energy per unit area, typically mJ/cm^2

within two limits for optimal machining quality of the workpiece: the ablation threshold and the point at which photothermal processes dominate. If the energy density is below the material's ablation threshold level then machining will not occur. If the energy density present at the workpiece is too high, photothermal effects dominate the ablation process and distortion of the surrounding material begins to occur. Photothermal processes will dominate if a material is machined with too high an energy density, or laser repetition rate. There is, therefore, an upper limit on the rate at which a material can be machined which is defined in terms of the maximum laser firing frequency and energy density used. By operating below these limits, materials can be excimer laser machined to a high-resolution using ablation, precise amounts of material being removed with very little, or no thermal damage to surrounding regions.

Although polymers can be efficiently ablated, however, the same is not true of metals. In this case, thermal processes dominate [27, 28] when thin films are machined. This is reported to be a two stage process [27] consisting of vaporisation of the surface of the exposed metal film, followed by expulsion due to the plasma re-coil pressure. The vapour produced by the beam is confined by the surrounding atmosphere, but continues to absorb incident radiation, causing further heating of the vapour and so generating a plasma. This causes pressure to be exerted on the molten material remaining on the substrate surface, which expels molten material over unexposed regions. If the incident energy density is increased, the surface of the substrate also melts, allowing molten fragments of the metal film to become embedded in the surface, preventing complete material removal.

Although good patterning was reported at a wavelength of 248nm, it was only possible over a narrow range of energies, making reliable metal film removal problematical. There was also a tendency for the films to crack, peel and contaminate surrounding areas with re-solidified molten material [22, 27, 28]. These findings have been confirmed during this work, with unpredictable results being obtained.

2.3 Beam delivery optics

The output from excimer lasers is generally not of a suitably high quality, as the uniformity, divergence, energy density and beam size can vary significantly from those required at the workpiece to allow machining to occur [11]. However, placing an optical system between the laser output and the workpiece is one method commonly employed to provide the required beam characteristics at the workpiece. Such a system can be used to shape the beam, for example into a square, as well as average the energy over the beam area, so allowing uniform machining rates across the beam. Mask stages can also be included in the optical system by allowing the beam to reach a focal plane at the mask. If the beam then passes through the mask and into a demagnification projection lens before reaching the workpiece, a more flexible system can be created. The beam can be selectively patterned, allowing complex structures to be machined quickly. Mask degradation is limited, as the energy density at the mask plane is less than that at the workpiece – the demagnification projection lens effectively increases the beam energy density by focusing it onto a smaller area at the sample. Because the mask pattern is optically reduced, the resolution of the mask can be low, but still produce a high-resolution laser machined structure. The range of laser fluences is determined by a combination of the energy density present at the laser, the losses throughout the optical system and the projection lens used. The optical losses will generally be fixed as the optical system will not change during use and the laser energy can normally be varied over a set range. This allows a variety of materials to be machined by altering the demagnification ratio of the projection lens to create the required energy density.

2.4 Common machining techniques

If an optical system similar to the one described above is implemented, i.e. one where the beam path is fixed and the workpiece and mask positions can be controlled, several methods of machining can be used to create structures.

2.4.1 Serial machining

If the laser beam is shaped using an aperture mask, the result will be a beam with known dimensions, focused onto the workpiece. As the laser beam is fixed, the region of the workpiece corresponding to the beam size at the workpiece will be removed by ablation. If the surface of the workpiece is kept in focus and the workpiece is then moved, patterning of the workpiece will result, depending on the motion of the workpiece. This system defines structures in a similar manner to a pen-plotter. However, the depth of machining is not uniform, but depends on various factors: the ablation properties of the material, the laser energy density at the workpiece and the total energy delivered. The ablation properties of the material are inherent to that particular material, so controlled machining is achieved by using the appropriate laser fluence. The total amount of energy delivered to any irradiated point of the workpiece is determined by the laser fluence used, and the number of pulses that point receives which in turn depends on the laser firing rate and the speed at which the workpiece moves.

Using a square aperture to define a square beam profile and moving it in the manner shown in Figure 2.3a allows constant erosion over the beam axis perpendicular to the direction of motion. This is ideally suited to fabricating square-section structures, such as channels. However, if the workpiece is moved in the manner shown in Figure 2.3b, where the motion is not perpendicular to the beam axis, but along the diagonal of the square shaped beam, the resulting machined area will appear as a 'V-groove'. This is because a point at the edge of the 'V-groove' receives less total energy than a point in the middle, as it is exposed for less time due to the beam effectively being narrower at the edges. If a circular beam is used, as shown in Figure 2.3c, an elliptical channel results. Here, the effective total energy is higher at the centre of the channel than at the edges. If the total amount of energy applied at the centre of the beam removes a depth of material equivalent to the beam radius, then a semi-circular channel will be produced. Using a circular aperture presents advantages in that the direction of motion of the workpiece relative to the beam does not affect the channel width or depth, unlike a square aperture, which must be moved perpendicularly to the beam axes to achieve the same effect.

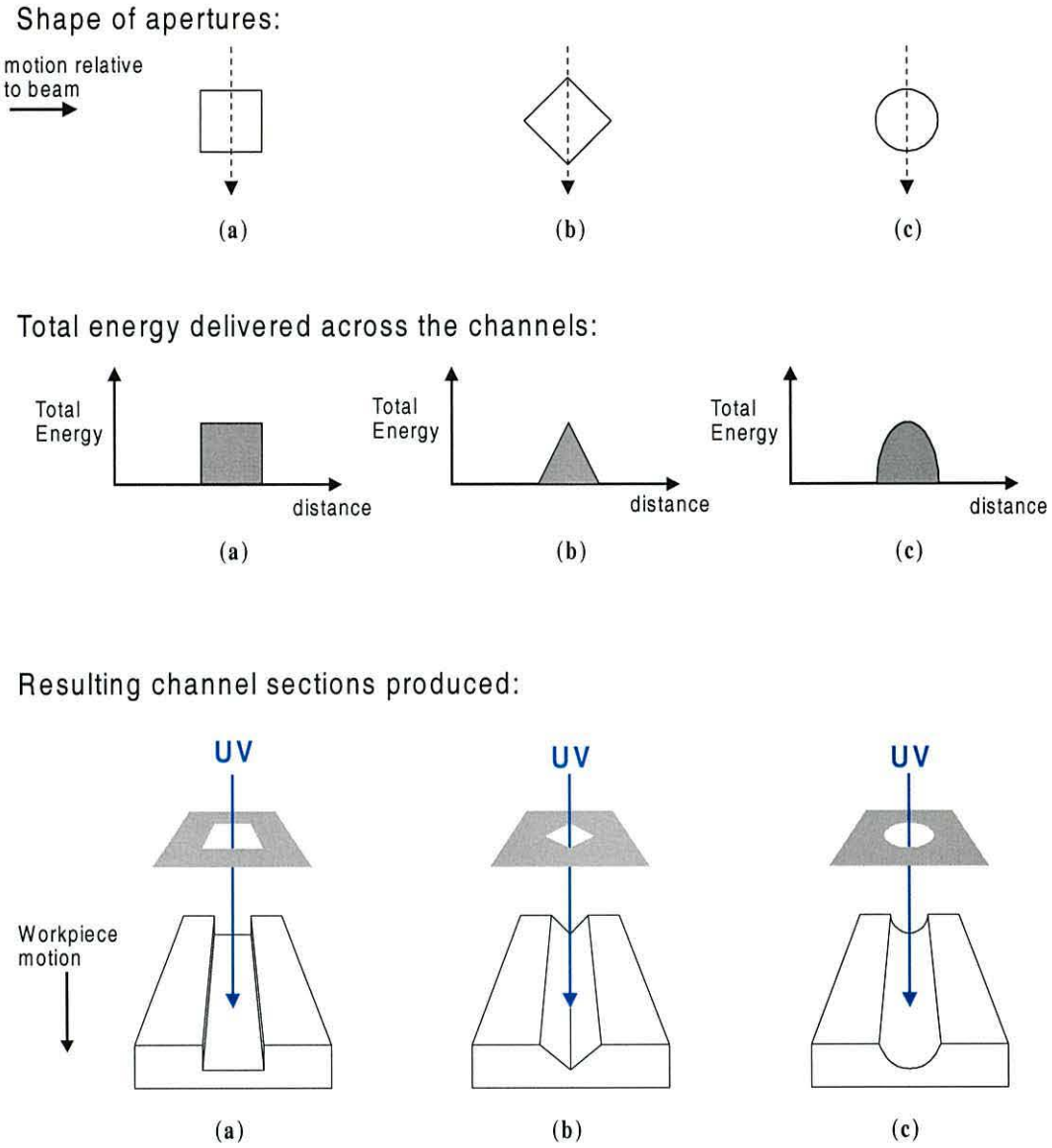

Figure 2.3 *Structures resulting from moving the workpiece at different angles to an apertured beam. The effect of moving the workpiece perpendicularly to the axis of the beam creates a square section channel (a). If the workpiece is not moved along a beam axis, non-uniform etching rates result (b). Circular apertures allow motion in any direction and still produce a semi-circular profile (c).*

It should be noted that the ratio of the channel width to the channel depth can be controlled by altering the total energy density delivered. For similar reasons, the channel shown in Figure 2.3a will also be contoured at the start and end of the machined regions, as a point at the very end of the channel will receive less total energy than a point more than a beam width away from the end.

Similar effects can also be achieved by moving the mask through the laser beam while keeping the workpiece stationary [22, 29]. This has a comparable effect to moving the

workpiece, in that the total energy, hence the depth machined, can be varied across the (stationary) laser beam, so producing various machining depths.

These effects allow the profile of machined structures to be controlled to a higher degree than if stationary machining is used. Furthermore, if a suitable mask is used that effectively controls the total energy density of each exposed point, complex topographies can be created [6, 29, 30].

2.4.2 Patterned masks

Binary masks, which consist of areas that either fully transmit or completely block incident radiation, allow more detailed control of the shape of the laser beam reaching the workpiece than can be achieved with a simple aperture. By patterning the laser beam, selected regions of the workpiece can be removed simultaneously and to a uniform depth, which can decrease machining times provided that the beam is large enough to cover the entire mask pattern. This is useful when patterning a substrate with repeatable units, such as a step and repeat process.

If the mask pattern extends over an area larger than the size of the beam at the mask plane, mask-scanning [31] can be implemented to allow the total energy density reaching the workpiece through the entire mask to be uniform. This term describes the process of moving the mask and workpiece synchronously, as illustrated in Figure 2.4. Because a demagnification projection lens focuses the laser beam passing through the mask onto the workpiece to allow machining, the direction of motion of the mask and workpiece must be in opposite directions, as well as being scaled to ensure correct patterning. For example, if a x10 demagnification projection lens is being used, the mask must move synchronously with the workpiece, but 10 times faster and in the opposite direction. The actuators used to implement motion of the mask and workpiece define the accuracy and repeatability of the process, as well as the maximum processing speed possible. This process allows low-resolution masks to produce high-resolution structures, especially if a large demagnification factor projection lens is used.

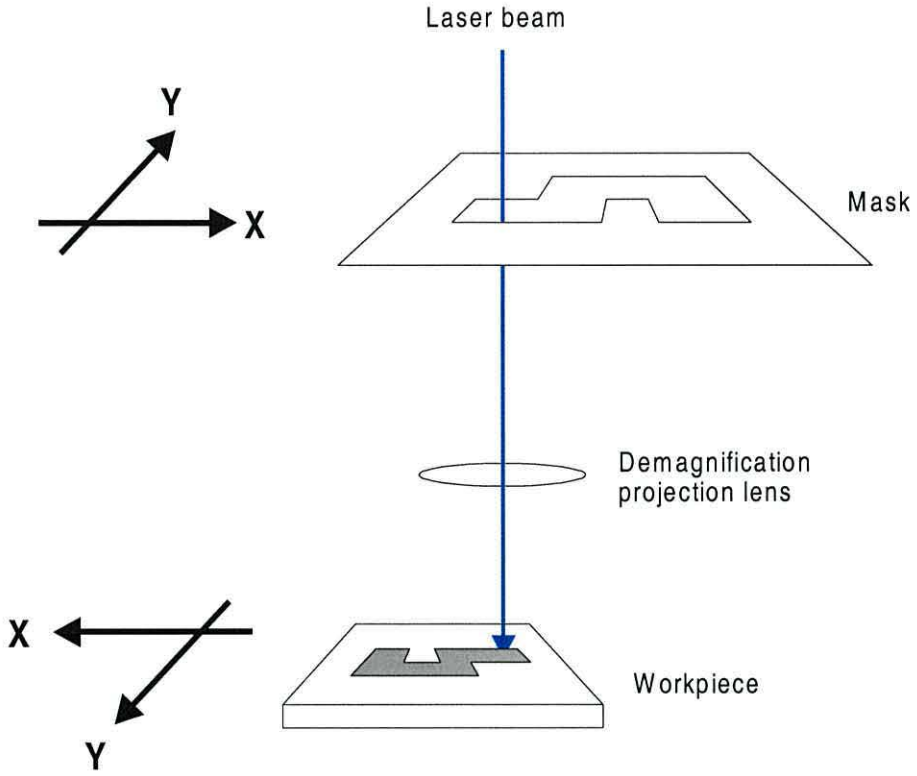

Figure 2.4 *Illustration of a mask-scanning process, where the pattern of a mask is larger than the size of the beam present at the workpiece. By moving the mask and workpiece synchronously, a uniform total energy density can be created over the entire mask area. This reproduces the mask pattern at the workpiece, allowing uniform machining depths over the entire structure.*

The main disadvantage of mask-scanning, namely that precision motion stages are required to accurately position and move both mask and workpiece, means that the quality of this process is limited by the motion stages used. Although machining with an apertured beam does not allow as much flexibility in terms of speed of patterning and uniformity of machining depth, fewer hardware components are required, as only the mask or workpiece need to be moved.

2.5 Optical system resolution limits

One of the primary functions of the optical system is to average the energy density of the laser beam over its cross-sectional area. This determines the machining rate at all points exposed and if not constant will result in non-uniform machining depths. The homogenisation stages used typically allow a high degree of uniformity over the beam

area, e.g. ±5% RMS in 86% of the beam at the mask plane in the system used, so allowing good machining characteristics of the open beam.

The optical systems used in most excimer laser-based machining systems utilise optical elements to alter the properties of the laser beam. Although relevant at the design stage of the optical transport system, diffraction limits of such elements are not relevant when reproducing mask features at the workpiece. This is because the entire beam is being transported to the mask and is not apertured or shaped, so has no pattern to preserve. The divergence of the beam, which will affect the smallest feature size that can be resolved, is usually fixed at a minimum by a beam-telescope to reduce the laser beam divergence from 2mrad to 10mrad at the laser aperture to ~200 μrad at output of the beam-telescope [11]. The laser beam, now more spatially coherent, is then transported, via beam shaping optics, to the mask plane where it can be patterned by a mask.

A projection lens, however, is used to project the patterned laser beam onto the surface of the workpiece and the characteristics of the lens used determine the minimum feature size that can be resolved. The main limit to the minimum feature size attainable is the diffraction limit of the lens used and the depth of field.

2.5.1 Diffraction

Diffraction describes the divergence of light from its normal straight path when incident at an edge or a narrow slit [32]. The observed image is not a precise line, as would be expected, but a series of stripes that correspond to positions of maxima and minima in the light intensity that extend into the regions that would not be expected to be illuminated, as shown in Figure 2.5.

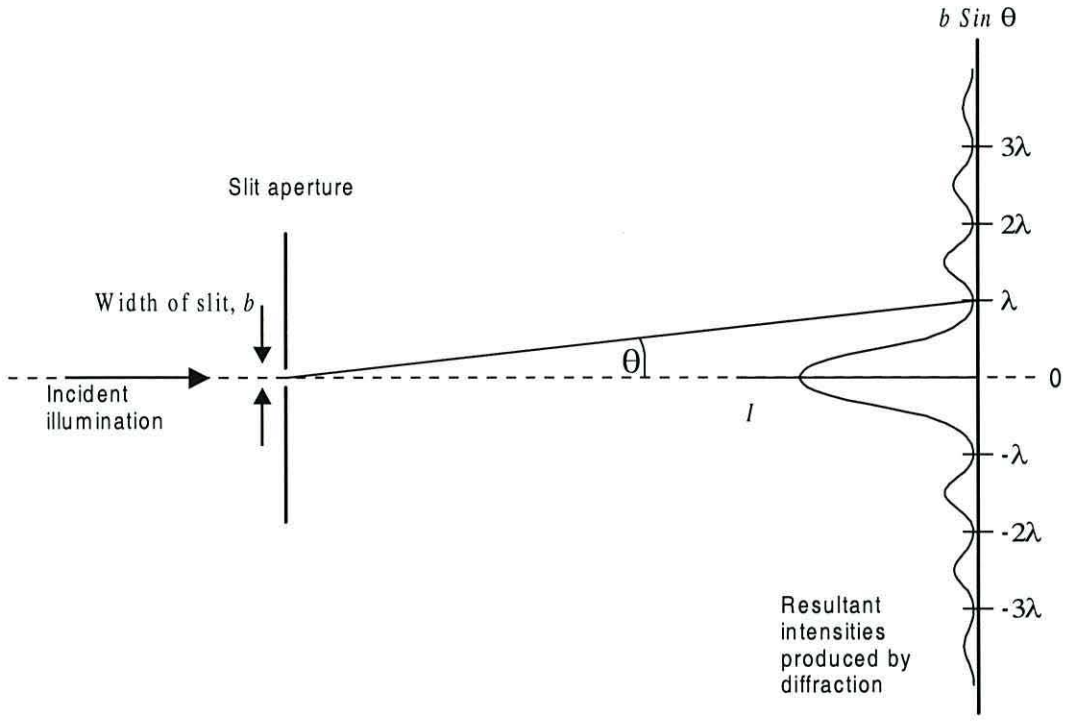

Figure 2.5 *Diagrammatic representation of the intensities of waves projected through a slit*

At angle $\theta = 0$ the deviation from the original light path is unchanged and the waves from various parts of the slit are in phase, causing a region of high-intensity. However, as the angle from the slit centre increases, superposition occurs, causing the intensity of the projected pattern to vary. In general, regions of *minimum* illumination will occur when:

$$b \sin \theta = n\lambda \qquad \text{for n} = 1, 2, 3, \ldots. \qquad (2.1)$$

2.5.2 Limit of resolution

Diffraction effects causes light to bend around obstacles and spread into regions that would not normally be illuminated. This, in turn, limits the resolution of any optical element. Consider the arrangement shown in Figure 2.6, where the emission from two distant light sources is being focused onto a plane.

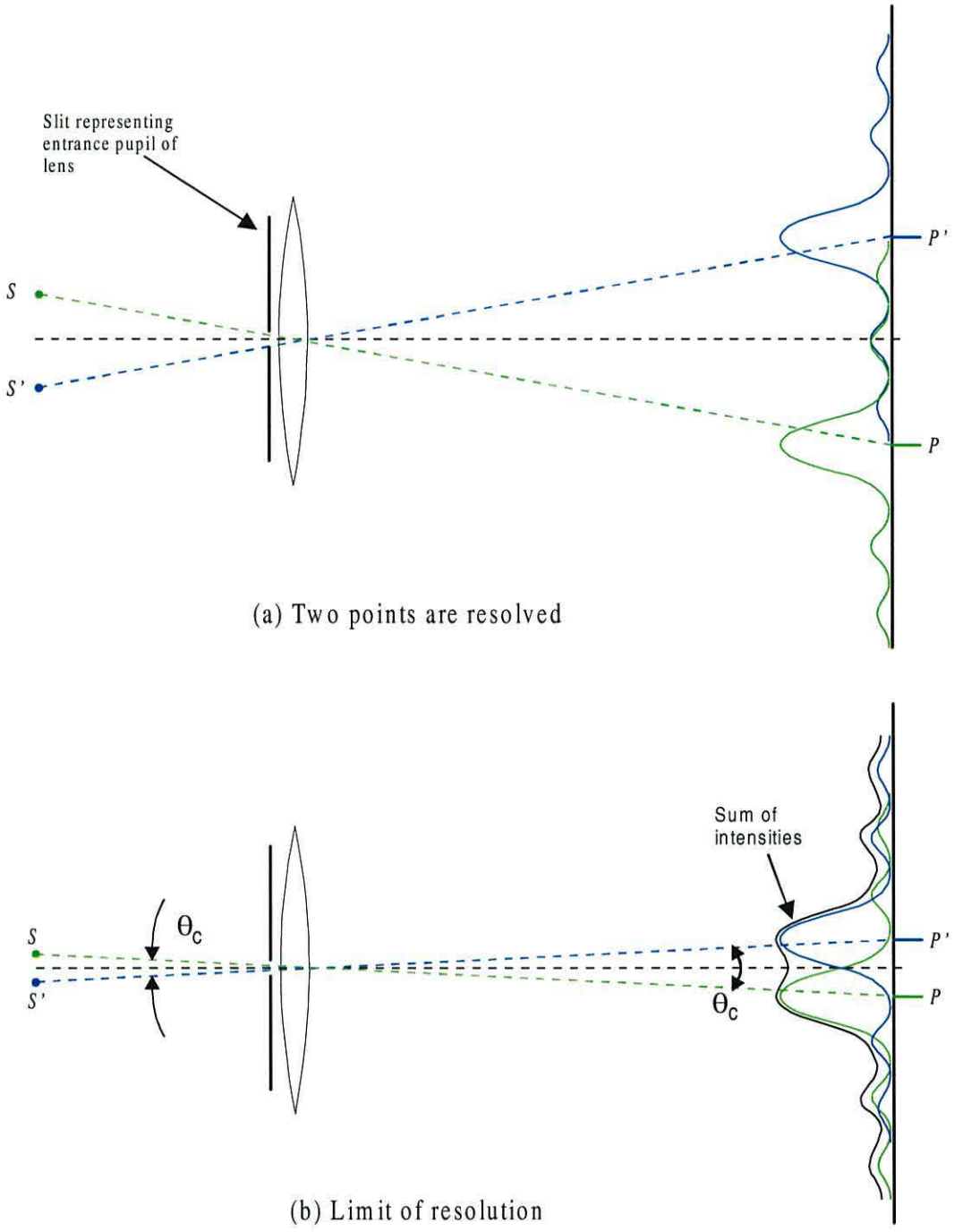

Figure 2.6 *Effects of focusing two point sources through a lens. The slit is a representation of the physical properties of the lens, in that the light passage through the lens is restricted. If the separation of the two points is large enough, they can be identified on the projected image (a). However, if the separation is too small, the points cannot be distinguished.*

The slit shown represents the physical properties of the lens as the amount of light through the lens is limited by the size of the lens' entrance pupil, normally termed the numerical aperture of the lens (*NA*). This is defined as the sine of the angular

restriction, α, of the imaging rays from a lens by the entrance pupil of the lens [9] as shown in Figure 2.7, or:

$$\sin \alpha = NA \tag{2.2}$$

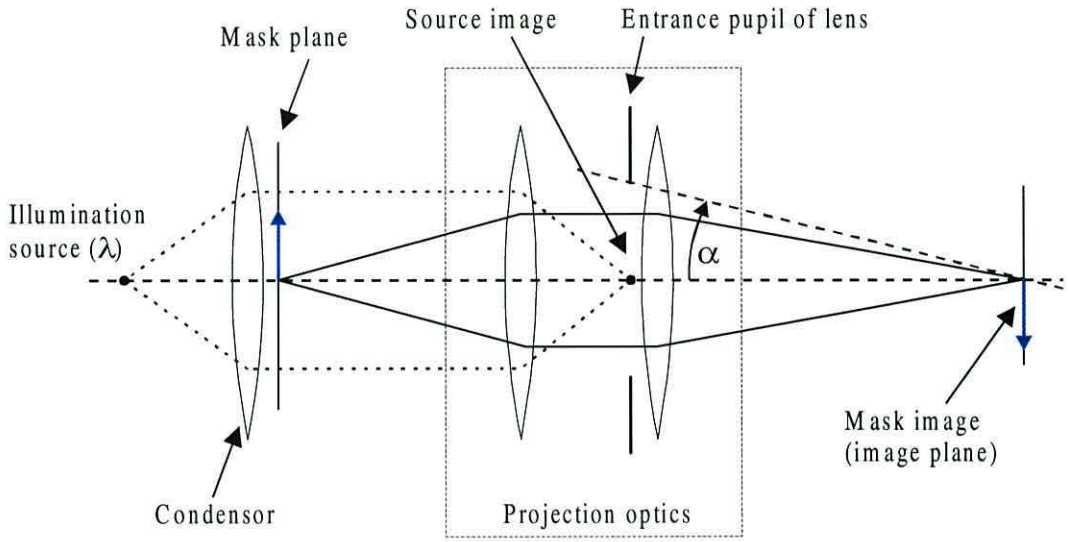

Figure 2.7 *Diagram showing α for an typical optical mask projection system*

If diffraction effects did not occur, the two points would be distinguishable as two separate points. However, the diffraction present due to the slit causes the two images of the point sources to be distributed, as shown in Figure 2.5. The separation of the two points in Figure 2.6a is such that the images of the points do not overlap significantly and can be resolved, unlike the situation in Figure 2.6b. Here, the maximum of one image appears at the minimum of the second image. This is the *Rayleigh criterion* for resolution, as the two images are barely identifiable [32]. In such a condition, the angular separation between the two sources is the same as the angular separation between the central maximum and the first minimum and is called the *limiting angle of resolution*, θ_c [32]. For a slit

$$\theta_c = \frac{\lambda}{b} \tag{2.3a}$$

where λ is the wavelength and b is the size of the slit.

For a circular aperture,

$$\theta_c = 1.220 \times \frac{\lambda}{D} \tag{2.3b}$$

where D is the diameter of the circular aperture, or the size of a lens' entrance pupil.

The minimum resolution, θ_c, can be improved by using a shorter wavelength or a larger entrance pupil. The limit of resolution of a given lens is dependent on the physical properties of the lens, namely the numerical aperture and laser wavelength used, and is given by [9]:

$$\text{Resolution limit} = k \times \frac{\lambda}{NA} \tag{2.4}$$

where k is a constant dependant on the exact nature of the process being considered.

Typically, k ~0.8 for conventional mask projection techniques due to the effects of diffraction and the type of mask used [11]. The resolution limit, hence the smallest resolvable feature, can be improved by decreasing the wavelength, λ, or increasing the *NA* of the lens used. However, both are limited by the equipment used. When considering the capabilities of the excimer laser system used in this work, the shortest operational wavelength possible is 193nm, with the maximum projection lens *NA* being 0.3 when a x4 demagnification projection lens is used.

Although it is not possible to generate sharp transitions in intensity at the workpiece due to diffraction, the quality of the machined region is not affected as the machined region is typically much larger. This, coupled with the energy threshold that must be exceeded to cause machining of the workpiece, makes the requirement of sharp intensity transitions less important for most machining applications. Section 2.5.4 shows the calculated parameters for the laser system projection lenses used in this work.

2.5.3 Wall angle of machined structures

When excimer lasers are used to machine structures, an associated wall angle is generated, which describes the angle at which the side-walls of machined regions deviate from the vertical. For example, if a circular aperture is used to define a circular beam and this used to machine a deep hole in the workpiece, a conical structure will result. If the material is thick enough, machining will stop, unless the fluence used is increased. Two effects are reported to limit the steepness of the wall angle. Diffraction, in addition to limiting the machining resolution, can reduce the energy fluences around the edge of the machined region, thus reducing machining rates [11]. Therefore as the machining depth increases, so the width (diameter) of the machined region decreases.

An alternative explanation is that, because the beam is focused onto the surface of the workpiece to achieve the required energy density to cause ablation, the beam will diverge either side of the focal plane. This will induce an associated drop in energy density of the beam, depending on the distance from the focal plane, along the beam path. Hence the profile of the ablated region is dependent on the focusing conditions and the energy density used [33]. This is shown in Figure 2.8, where a cross-section through the middle of an ablated region is shown. In each case, the number of shots fired remains constant, but the energy density used is increased.

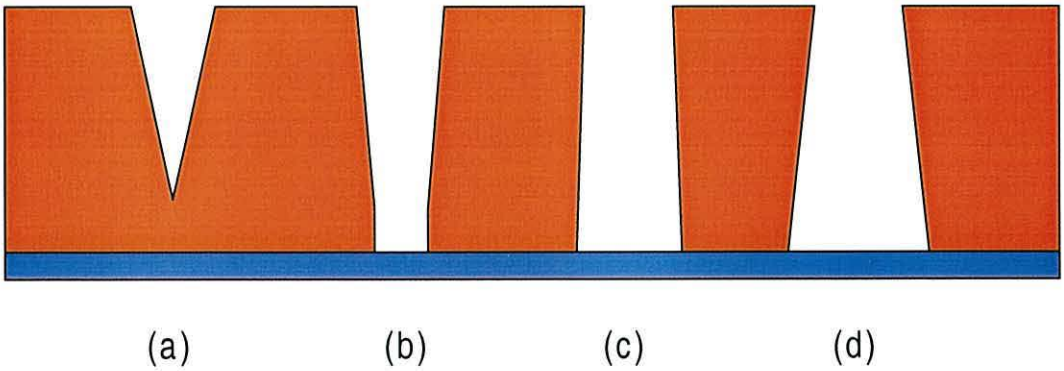

Figure 2.8 *Variation in wall angle of a machined structure caused by different energy densities: (a) at low energies, a limited region either side of the focal point is etched. As the energy is increased, (b) to (d), the wall angle changes from positive to negative.*

It is believed that the most likely cause of this effect is a combination of both processes as well as the optical beam delivery setup used. It was found, for a standard optical

setup, that the wall angles became more vertical if the energy density used during machining was increased. The optical system used to convey the beam from the laser to the projection lens also affects the wall angle of machined regions, allowing over-cut, vertical or under-cut walls to be machined [34].

2.5.4 Effect of depth of field

The demagnification projection lens used also determines the distance over which the projected image is in focus, also known as the depth of field (DOF). The DOF of a lens, Z, can be calculated as [11]:

$$Z \approx 0.8 \frac{\lambda}{NA^2}. \tag{2.5}$$

This determines the accuracy to which the workpiece must be positioned relative to the focal point of the lens in order to produce well defined structures. It also determines the depth of machining that is possible before considerable deterioration occurs. For practical purposes, this can be equated to the amount of deviation either side of the focal plane where the out-of-focus blur equals that of diffraction in the image plane [9], i.e.

$$\text{DOF} = \frac{\lambda}{2(NA^2)}. \tag{2.6}$$

Table 2.2 shows the resolution limit, using Equation 2.4 and the depth of field calculated using Equations 2.5 and 2.6, for each projection lens used in this work.

Projection lens description [λ, demagnification factor]	Numerical aperture (NA) of lens	Calculated resolution limit [μm]	Calculated depth of Field (DOF) [μm]	
			(2.5)	(2.6)
193nm, x4	0.1	1.54	15.44	38.60
193nm, x10	0.15	1.03	6.86	17.15
248nm, x4	0.2	0.99	4.96	12.40
248nm, x10	0.3	0.66	2.20	5.51

Table 2.2 *Calculated optical properties of the projection lenses used during this work*

2.6 Laser micromachining applications at the start of the project

At the onset of the work described in this thesis, excimer laser machining was a known process, although not commonly implemented in producing polymer-based micro-components for micro-devices. It was known that excimer laser machining was capable of fabricating polymer structures to micron resolutions at 248nm and sub-micron resolutions at 193nm [15]. As polymers are used extensively in 'Biofactory-on-a-chip' devices and the components require micron-resolution structuring, this process is of great interest as it was believed to be capable of solving several manufacturing problems, for example fabricating micro-components directly as well as the possibility of mould manufacture.

2.7 Summary

The effectiveness of laser machining has been shown to be determined by the wavelength of the laser source used, the optical delivery system of which the characteristics of the projection lens are most important, the energy density at the workpiece and the inherent properties of the material being machined. The ability of a material to absorb at the UV wavelengths used when machining is a good indication of the ease with which it can be machined [14, 17, 20]. A material that absorbs strongly at the laser wavelength used is likely to machine well, as photochemical ablation processes will dominate.

Excimer laser micromachining of fluidic systems on polymer based chips had been reported [13, 29], although these were limited to simple channel structures and shapes, patterned using fixed apertures. Alternative methods, not only for fabricating more elaborate devices, but also for patterning moulding masters were ideally required to allow mass-fabrication of cheap and disposable polymer devices. Some of the problems associated with laser machining have also been addressed, namely laser ablation generated debris collection.

Methods of using laser machining to create sub-micron resolution masks for use in various processes have been investigated, which is not known to have been reported before, allowing low cost, rapid fabrication. This allowed more flexible laser machining processes, using greyscale masks, to be implemented to allow three-dimensional profiling of a workpiece. An alternative method, using an excimer laser as a stereolithography exposure source has also been investigated.

Laser micromachining is ideally suited to solving some of the fabrication problems associated with devices consisting of various polymer materials, for example machining a micro-fluidic channel though an embedded waveguide structure, which has also been investigated.

2.8 References

[1] 'Laser processes for MEMS manufacture', A. S. Holmes, *RIKEN Review* **43** (2002) 63-69

[2] 'Carbon nitride materials synthesised by ion-assisted pulsed laser depisition', Z-M. Ren, Y-F. Lu and Z-F. He, *RIKEN Review* **43** (2002) 41-44

[3] 'Supplemental multilevel interconnects by laser direct writing: Application to GaAs digital integrated circuits', J. G. Black, S. P. Doran, M. Rothschild, D. E. Ehrlich, *Appl. Phys. Lett.* **50** (1987) 1016-1018

[4] 'High-accuracy laser mask repair technology using ps UV solid state laser', Y. Morishige, *RIKEN Review* **43** (2002) 70-75

[5] 'Laser fabrication and assembly processes for MEMS', A. S. Holmes, *Proc. SPIE* **4274** (2001) 297-306

[6] 'Excimer laser micromachining and replication of 3D optical surfaces', A. Braun, K. Zimmer, B. Hosselbarth, J. Meinhardt, F. Bigl and R. Mehnert, *Applied Surface Science* **127-129** (1998) 911-914

[7] 'Laser-assisted chemical micromachining of metals and alloys', A. Stephen, T. Lillenkamp, S. Metev and G. Sepold, *RIKEN Review* **43** (2002) 56-62

[8] 'GaN ablation etching using short wavelength pulsed laser', T. Akane, K. Sugioka, K. Midorikawa, K. Obata, N. Aoki and K. Toyoda, *RIKEN Review* **43** (2002) 45-48

[9] "*Resolution enhancement techniques in optical lithography*", A. K-K. Wong, *SPIE press*, 2001, Bellingham, Washington

[10] 'Ultra line-narrowed F_2 laser for microlithography', H. Komori, T. Ariga, H. Watanabe, T. Kumazaki, N. Kitatochi, K. Sasano, Y. Ueno, T. Nishisaka, R. Nohdomi, K. Hotta, H. Mizoguchi and K. Nakao, *RIKEN Review* **43** (2002) 76-79

[11] "*Laser processing in manufacturing*", R. C. Crafer and P. J. Oakley, *Chapman & Hall*, 1993, London

[12] '$Pr_{0.67}Ca_{0.33}MnO_3/YBa_2Cu_3O_7$ thin film bilayers grown by pulsed laser ablation deposition', S. K. Singh, S. B. Palmer, D. McK Paul and M. R. Lees, *J. Phys. D: Appl. Phys.* **29** (1996) 2522-2524

[13] 'UV laser machined polymer substrates for the development of microdiagnostic systems', M. A. Roberts, J. S. Rossier, P. Bercier and H. Girault, *Anal. Chem.* **69** (1997) 2035-2042

[14] 'Ultraviolet laser ablation of organic polymers', R. Srinivasan and B. Braren, *Chem. Rev.* **89** (1989) 1303-1316

[15] 'Excimer laser projection photoetching', M. Latta, R. Moore, S. Rice and K. Jain, *J. Appl. Phys.* **56** (1984) 586-588

[16] 'Metal film removal and patterning using a XeCl laser', J. E. Andrew, P. E. Dyer, R. D. Greenough and P. H. Key, *Appl. Phys. Lett.* **43** (1983) 1076-1078

[17] 'Ultraviolet laser ablation of polyimide films', R. Srinivasan, B. Braren and R. W. Dreyfus, *J. Appl. Phys.* **61** (1987) 372 - 376

[18] 'Polymer laser photochemistry, ablation, reconstruction and polymerisation', H. Sato and S. Nishio *Journal of photochemistry and photobiology C* **2** (2001) 139-152

[19] 'Multishot ablation of polymer and metal films at 248nm', E. Hunger, H. Pietsch, S. Petzoldt and E. Matthias, *Applied Surface Science* **54** (1992) 227-331

[20] 'Direct etching of polymetric materials using a XeCl laesr', J. E. Andrew, P. E. Dyer, D. Foster and P. H. Key, *Appl. Phys. Lett.* **43** (1983) 717-719

[21] 'Excimer laser etching of polyimide', J.H.Brannon, J.R.Lankard, A.I.Balse, F.Burns and J.Kaufman, *J. Appl. Phys.* **58** (1985) 2036 – 2043

[22] 'Laser ablation as a processing technique for metallic and polymer layered structures', E. E. Guzzo and J. S. Preston, *IEEE Transactions on semiconductor manufacturing* **7** (1994) 73-78

[23] 'TEA CO_2 laser ablation of Upilex Polyimide', P. E. Dyer, G. A. Oldershaw and G. C. Roberts, *J. Phys. D: Appl. Phys.* **29** (1996) 2554-2563

[24] 'Fine-hole drilling us Upilex polyimide and glass by TEA CO_2 laser ablation', P. E. Dyer, I. Waldeck and G. C. Roberts, *J. Phys. D: Appl. Phys.* **30** (1997) L19-L21

[25] 'Excimer laser etching of polymers', R. Srinivasan, M. A. Smrtic, S. V. Babu *J. Appl Phys.* **59** (1986) 3861-3867

[26] "*An Investigation Into Micro-machining Using Laser Ablation*" C. J. Hayden, *MEng Honours dissertation*, UWB, 1998

[27] 'KrF excimer laser ablation of thin Cr film on glass substrate', S. K. Lee and S. J. Na, *Appl. Phys. A* **68** (1999) 417-423

[28] 'Excimer laser ablation of thin gold films on a quartz crystal microbalance at various agron background pressures', X. Zhang, S. S. Chu, J. R. Ho, C. P. Grigoropoulos, *Appl. Phys. A* **64** (1997) 545-552

[29] 'A poly-methylmethacrylate electrophoresis microchip with sample preconcentrator', Yu-C. Lin, H-C. Ho, C-K. Tseng and S-Q. Hou, *J. Micromech. Microeng.* **11** (2001), 189-194

[30] 'Combination of contour and half-tone masks used in laser ablation', A. Braun, K. Zimmer, F. Bigl, *Applied Surface Science* **168** (2000) 178-181

[31] 'Direct manufacture of miniature bioparticle electro-manipulators by excimer laser mask projection', N. H. Rizvi P. T. Rumsby, J. P. H. Burt, M. S. Talary, J. A. Tame and R. Pethig, *ICPE* **2** (1997) 971-974

[32] "*Introduction to physics for scientists and engineers*", F. J. Beuche, *McGraw-Hill Book Company*, 1980, New York

[33] 'Excimer laser ablation of microstructures: A numerical model', C. Paterson, A. S. Holmes and R. W. Smith, *Journal of Applied Physics* **86** (1999) 6538-6546

[34] 'Future trends in diagnosis using laboratory-on-a-chip technologies', M. S. Talary, J. P. H. Burt and R. Pethig, *Parasitology* **117** (1998), S191-S203

Chapter 3

Experimental methods

3.1 Introduction

The common fabrication processes used to create the structures presented in this work are detailed in this chapter. Materials have been structured using photolithographical-based processes and excimer laser machining. Use was made of different inspection instruments to quantify the structures fabricated, including a Scanning Electron Microscope (SEM) and an optical microscope.

3.2 Excimer laser micromachining system

The excimer laser machining system used throughout this work consists of an Exitech Series 8000 microfabrication workstation with a Lambda Compex 110 excimer laser. The laser used, shown in Figure 3.1, produces short, high energy output pulses of a fixed, Ultra Violet (UV) wavelength at either 193nm or 248nm, depending on the lasing medium used. Two mixtures of lasing gases were used in the eximer laser for this work to produce two output wavelengths: 248nm was produced using krypton and fluorine, whereas 193nm radiation was generated by an argon / fluorine mixture.

The UV light is generated using high voltage pulses to excite a diatomic gas, such as fluorine (F_2) contained within a quartz tube. Since the gases used in the lasing medium are diatomic molecules, the laser is termed an 'excimer laser' which is an abbreviation of the term 'excited dimers', that are generated when each high voltage pulse is applied. The rare gas halide molecules, formed by applying a high voltage pulse to the laser tube, in this case containing either argon fluoride (ArF) or krypton flouride (KrF), form the active lasing media, each with a characteristic output wavelength. The rare gases, which are inert under normal atmospheric conditions (all electron orbits filled), can be excited by an electronic charge. The charge changes the orbital motion of the electrons and can remove one completely, so the gas atoms become highly reactive. This change in orbital motion causes the atoms to appear chemically similar to their periodic table

neighbours, i.e. argon behaves as potassium would. When the atoms are in such an excited state, pairs of positive and negative rare gas and halogen ions bind together to form metastable rare gas halide molecules. However, such molecules are unstable and have a limited lifetime of approximately 5ns to 15ns. After this, the rare gas halide molecules break down to re-form the original inert atoms at their ground X-state. The energy released by this recombination causes an UV-photon to be emitted whose wavelength is characteristic of the gases used. Such gases are useful in constructing UV lasers because they provide good laser gain owing to the high degree of population inversion that is possible.

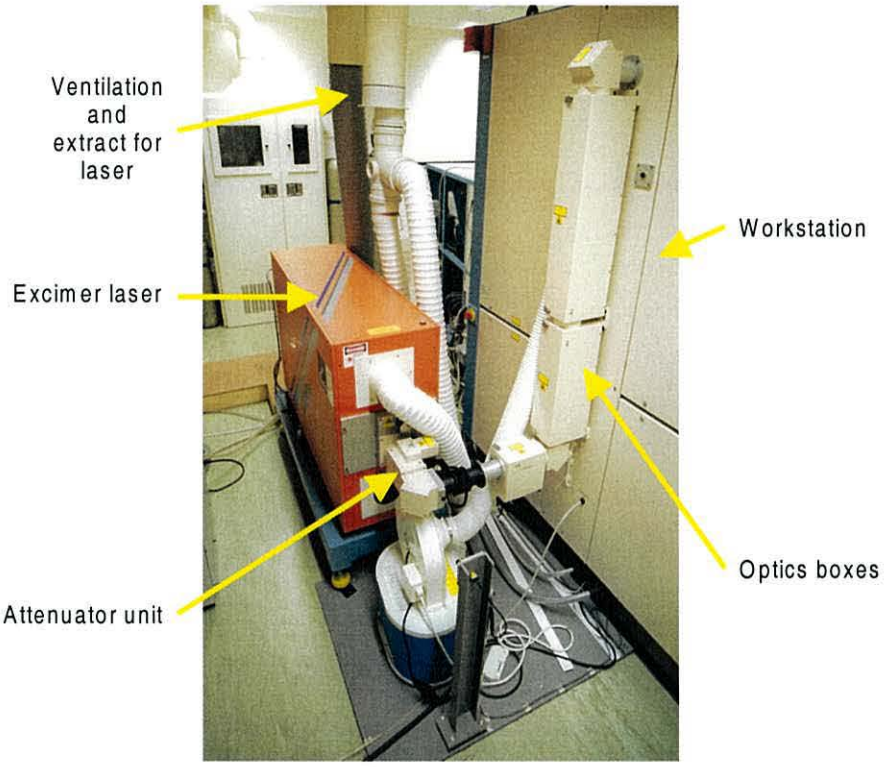

Figure 3.1 *Photograph of the excimer laser (orange box) and the associated ventilation pipework. The laser beam generated is fed into the optic system which is made up of the series of boxes that can be seen at the right of the picture.*

The stimulation voltage used to excite the lasing medium is provided by two parallel electrodes that run down the length of the laser tube, which have a high voltage, typically 35kV to 50kV DC, applied for approximately 50ns to 100ns [1]. This causes a self sustained electrical discharge with peak current densities of 1kA per cm^2 within the lasing medium, which is housed in a resonant cavity. The cavity consists of two mirrors, one with a 100% reflective coating and the other with a partially reflective coating through which the laser light is emitted. The excimer laser used in this work is capable

of producing pulsed UV output at a maximum frequency of 100 Hertz, up to a maximum energy density of 300mJ/cm^2 at the laser output.

The laser can be operated in one of two modes: internal or external, depending on the task in-hand. If the laser is set to internal control, the laser operating conditions can be user controlled via a remote handset. This allows various functions, such as the firing repetition rate to be set independently of the workstation control system. When the laser is set to external control mode, it is controlled from the workstation control computer, allowing synchronisation of laser firing and workpiece movement. This allows integrated, automated operation of the entire system using laser control programs. Hence complex machining procedures can be achieved and repeated easily. The laser control system operates a standard CNC language that uses 'G codes' (ISO 6983, EIA RS274) to control the position and motion of the stages, with some extra commands to determine the laser pulse duration. This is a useful function when a set number of shots per mm of motion is required. The system allows simple programs to be manually written and run, although a dedicated CAM package (AlphaCAM, Licom systems Ltd.) can be used to convert CAD designs, such as DXF files, into laser control programs allowing rapid production of complex components.

The workstation used in conjunction with the excimer laser, shown in Figure 3.2, consists of an Exitech Series 8000 microfabrication workstation. This allows a workpiece to be accurately positioned and moved relative to the laser beam, which has been profiled and shaped by projecting it through a mask, before it is focused onto the workpiece to allow machining.

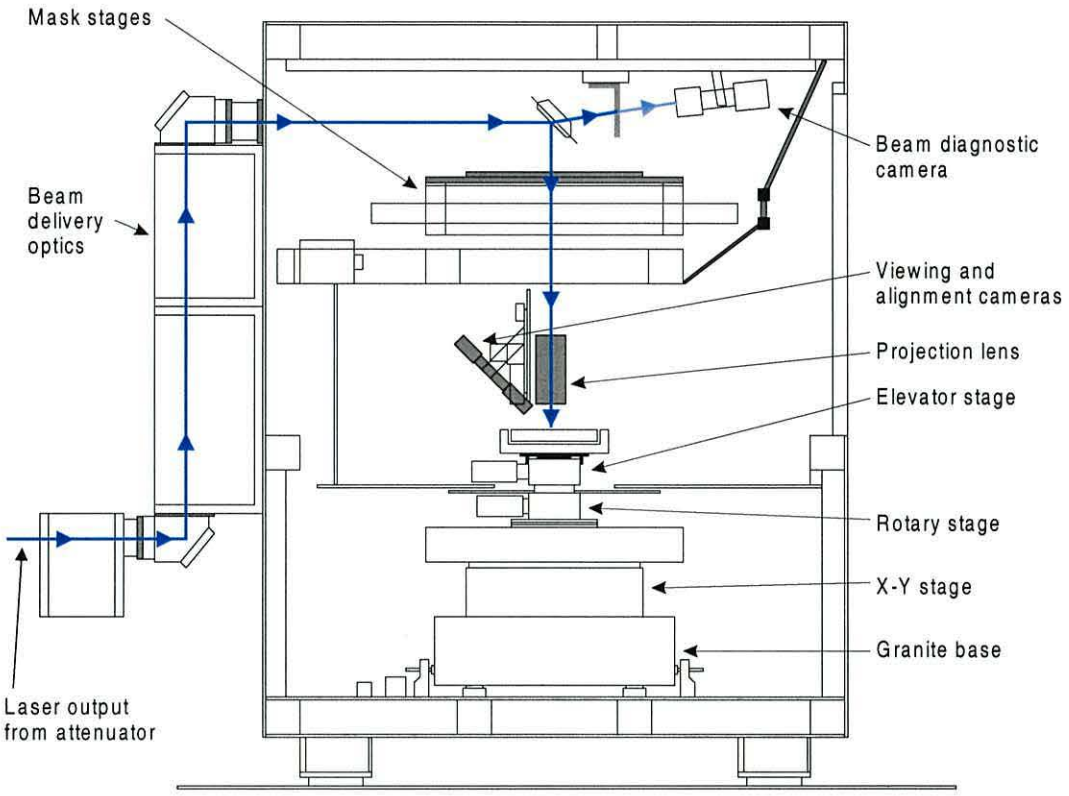

Figure 3.2 *Diagram showing the major components of the workstation. Access to the workpiece is from the right of the diagram, via two doors. The mask stage is accessed through a hinged side access panel. The workstation and associated components weighs 2500kg.*

The output from the laser consists of a rectangular beam, approximately 6mm x 30mm, whose energy density profile over the beam area is not particularly uniform. The beam passes through a mechanical shutter that is capable of blocking the laser output from entering the subsequent optical system thus ensuring that no laser light enters the workstation, for example when changing the workpiece or mask. Figure 3.3 shows a plan view of the beam path through the shutter and attenuator.

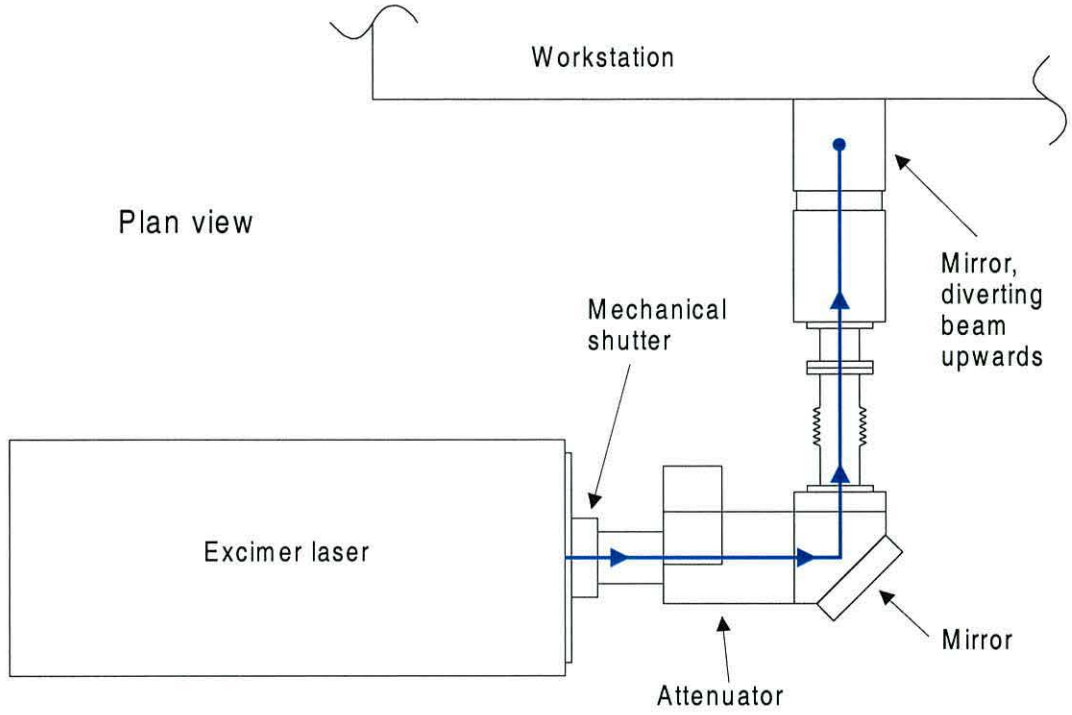

Figure 3.3 *Plan view of the beam path when it exits the excimer laser, showing the positions of the mechanical shutter assembly and the attenuator.*

With the shutter open, the beam passes into an attenuator unit, shown diagramatically in Figure 3.4, that allows the energy density of the laser beam reaching the workpiece to be accurately controlled. The attenuator consists of two servo-operated dielectric coated plates that are geared to rotate synchronously in opposite directions. The transmission through the plates is dependent on the angle of the plates relative to the incident laser beam. Any light not transmitted through the attenuating plates is reflected and dumped onto a specifically ribbed surface connected to a heatsink that dissipates the attenuated laser energy as heat. Two plates are used to cancel any deviation of the beam that would otherwise result from a change in orientation of a single plate. Thus a constant output beam position is maintained regardless of attenuator setting.

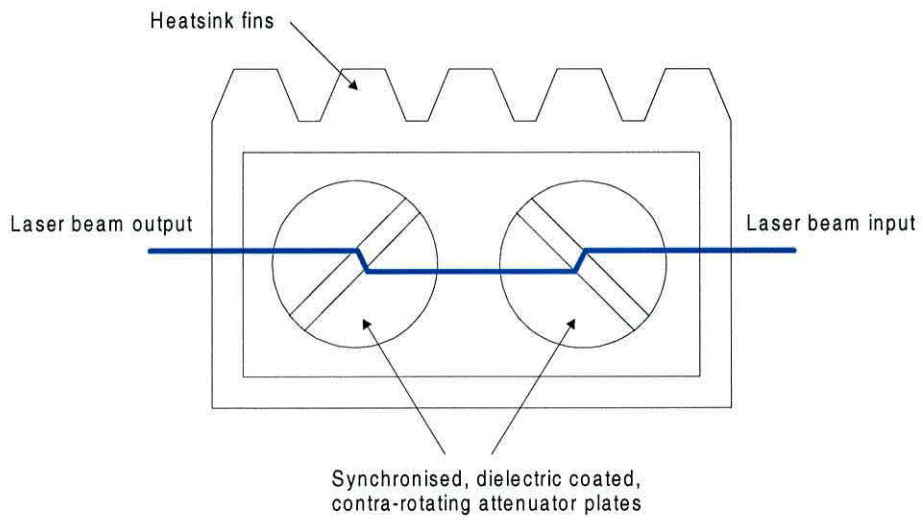

Figure 3.4 *Diagram of the attenuator used to control the energy density of the laser beam present at the workpiece. The counter-rotating dielectrically coated plates are indicated, along with the path of the laser beam.*

However, the attenuator transfer characteristic is not linear. Instead, it is a function of the plate angle to the beam and so requires characterising. This is achieved by measuring the energy density at the workpiece for a given attenuator setting using a Joule meter. The energy meter consisted of a pyroelectric Joulemeter (J25LP) attached to a portable energy meter (EM400, molectron), that converts incident photons into heat, so allowing the energy present in the beam to be accurately measured. As the beam size is known, the energy density of the laser beam at the workpiece can be calculated. Figure 3.5 shows an example of the recorded energy densities of the laser, shown in mJ/cm^2, over the full range of the attenuator (0.0000 to 1.0000). The plot shows the average measured energy density at the workpiece as the data points, with the error bars representing the maximum and minimum devitations. This data is automatically generated by the EM400 unit, which calculates the relevant energy density values by measuring the energy density of 200 shots at each attenuator setting. Recording this profile prior to any machining or exposure operation allows the desired energy density to be provided by setting the attenuator accordingly.

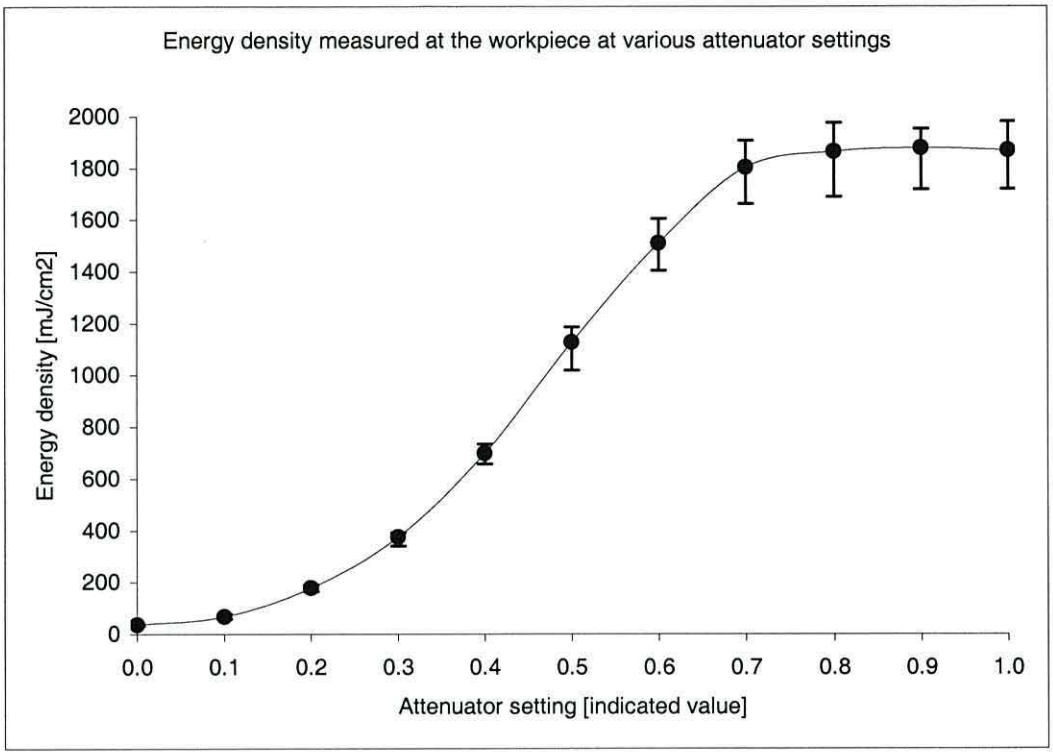

Figure 3.5 *A typical plot of measured energy density at the workpiece as the attenuator setting is varied over its full range (0.0000 to 1.0000)*

The attenuated laser beam passes though a beam telescope to reduce its divergence, so as to reduce the smallest feature size that can be machined. At this stage, the beam is still rectangular with a poor energy density profile over its area, a common feature of excimer lasers. Such qualities are not ideal for machining – non-uniform energy densities result in unequal machining rates over the beam area. In the current system, these problems are addressed by passing the beam through two single-axis curved optical elements, which compress the long axis of the beam and expand the short axis to form a square beam. The square beam then enters a homogenisation stage, where the energy of the laser beam is averged over its area. The homogenisation stage consists of two elements that split the beam into 36 beamlets and then optically recombines them, averaging the energy density over the beam. This has the effect of greatly improving the uniformity of the energy density profile. The optical elements used to profile the laser beam prior to entering the workstation are shown in-situ in the relevant optics boxes in Figure 3.6. Each element can be adjusted relative to the X and Y axis of the beam and moved along the beam on a sliding rail system, so allowing the optimum performance to be obtained. A maximum energy density variation of less than

±5% RMS in 86% of the total beam area is possible by adjustment of the various optical elements.

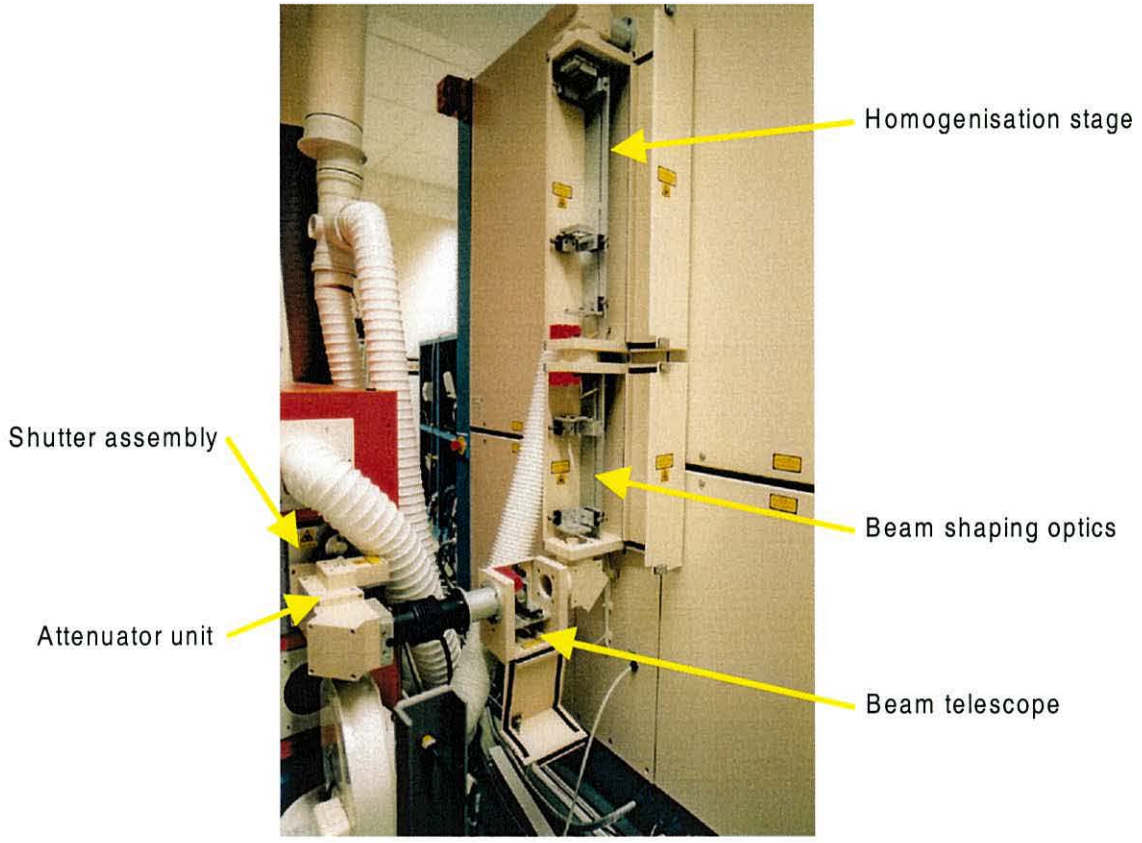

Figure 3.6 *Photograph showing the optical elements used to profile the laser beam. The position of elements relative to the laser beam can be adjusted so allowing the optimum beam characteristics to be defined. It should be noted that the optics box doors are normally closed during operation and are safety interlocked to prevent the laser from operating with them open.*

The laser beam, now square and more uniform, is brought to a focus at the mask stage by a mirror above the mask plane, as can be seen in Figure 3.7. This allows a small amount, ~0.5%, of the incident laser energy to pass through, where it strikes a fluourescent coated plate, located at the focal point of the beam. The fluorescence intensity of the plate is proportional to the energy present in the beam. A CCD camera is used to measure and monitor the energy uniformity of the beam by recording the intensity of the image produced by the CCD camera. Passing the beam through a mask allows the 12mm square laser beam produced at the mask plane to be selectively patterned using a suitable mask or aperture. The mask stage, also shown in Figure 3.7, can hold a maximum of four standard 4 inch mask plates simultaneously, although smaller masks can also be mounted. As the laser beam path remains fixed throughout

the optical system, mask alignment and motion is provided in both X and Y directions by ATS3400 brushless linear servo drives (Aerotech, Inc.). The open frame mask stages allow movement over a range of 300mm to a resolution of 0.1 microns under computer control.

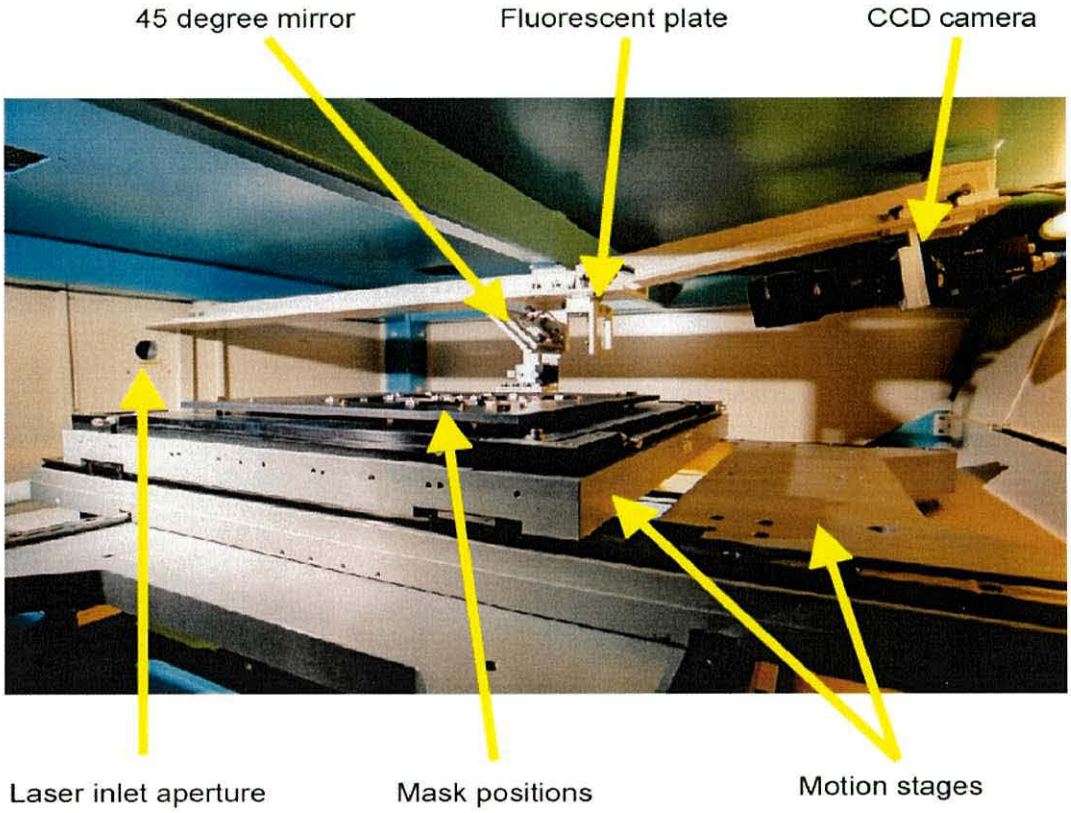

Figure 3.7 *Photograph of the mask stage showing the four maskplate mounting positions. The mirror that directs the beam onto the mask, the fluorescent plate and the CCD camera used for beam profile measurements are also visible.*

The patterned laser beam passes through a de-magnification projection lens before reaching the surface of the workpiece. The projection lens has the effect of increasing the energy density at the workpiece to a level suitable for laser ablation machining, while maintaining a lower energy density at the mask plane, in order to reduce the damage to the masks used. Various projection lenses can be used, including x4, x10 and x30 with trade-offs between the maximum energy density achieveable at the workpiece and the size of mask required to produce a given feature size. The maximum fluences attainable at the workpiece ranged between approximately 1.5 J/cm^2 and 10 J/cm^2, depending on the de-magnification of the projection lens used.

The workpiece is mounted on a vacuum chuck to maintain positional accuracy during machining. The surface of the workpiece that is to be machined requires positioning at the focal point of the beam if accurate machining is to occur. As the focal point of the laser beam is fixed, the workpiece is moved relative to the beam, to the appropriate height. This is accomplished using an elevation stage that can move the workpiece through a height of 5mm to an accuracy of 0.1μm. The elevation stage is mounted on a rotation stage that allows rotation of the workpiece through ±45°, facilitating workpiece alignment. The workpiece can be positioned and moved horizontally using an X-Y air bearing stage. Again, brushless linear servo motors (ATS80020, Aerotech, Inc.) are used as actuators. These allow positioning of the workpiece to an accuracy of 0.1μm over a range of 200mm along each axis. All of the motion stages in the workstation are CNC controlled using PC-based motion controllers (Unidex 500, Aerotech, Inc.), with one PC containing a laser firing control card to allow control of the excimer laser. The workpiece stage and associated motion stages are mounted on a large block of granite to reduce vibration of the workpiece as well as provide structural rigidity. Figure 3.8 shows the arrangement of the projection lens, workpiece stage and chuck.

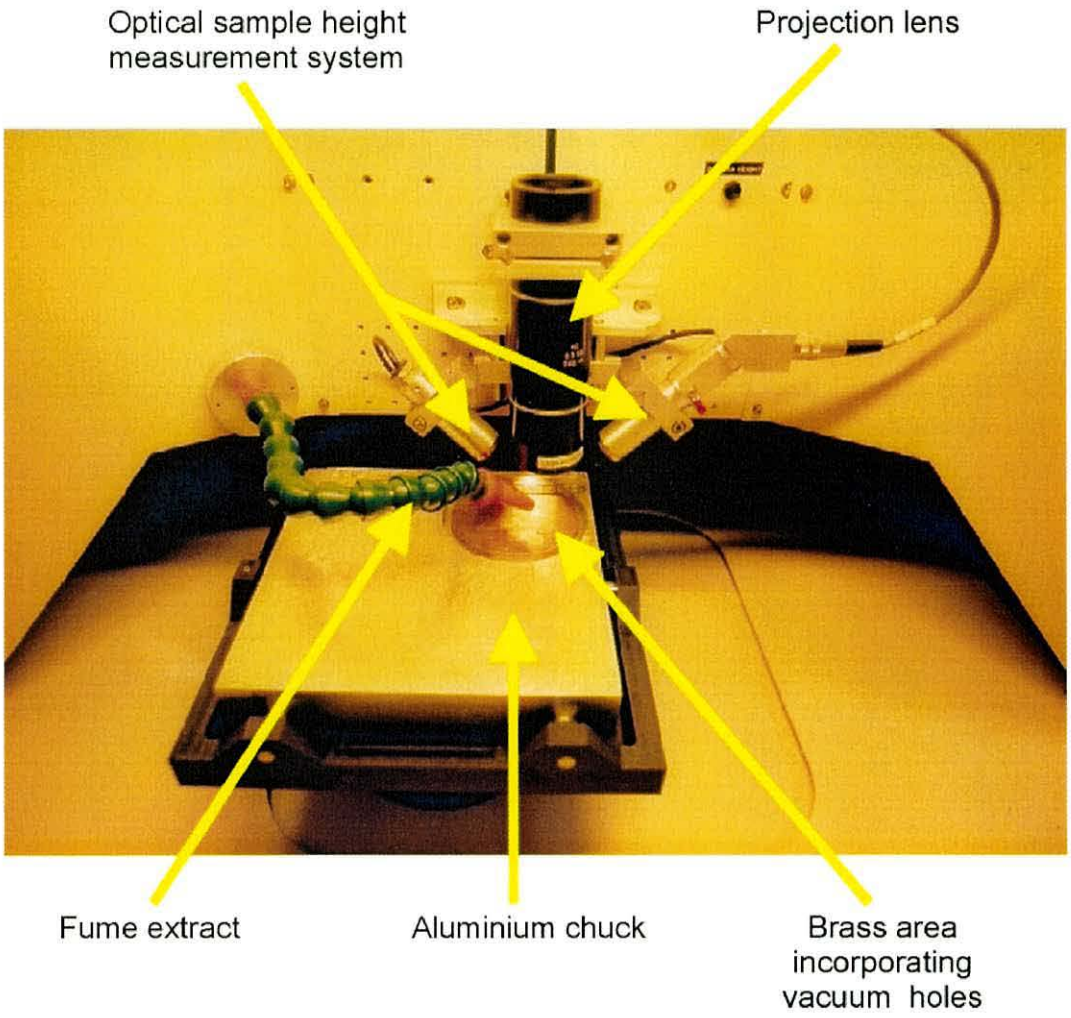

Figure 3.8 *Picture showing the arrangement of the workpiece stage, projection lens and height measurement system. The black cylindrical object is a x10, 248nm projection lens. The aluminium block is the workpiece chuck and the brass area is drilled with vacuum holes to retain samples on the chuck during processing. The two aluminium cylinders, oriented at 45 degrees, are the height sensing system and the flexible pipework at the left is connected to an extract system to remove any fumes generated during the ablation process. The yellow colour cast in the photograph is because the workstation lighting is covered with UV blocking filters to allow UV sensitive materials to be exposed by the laser.*

The height of the surface of the workpiece is measured using an optical position sensing system that consists of a laser diode source, operating at 633nm. The output from the diode is reflected from the surface of the sample to a quadrant photodetector, allowing accurate measurement of sample height to a resolution of 0.5μm. Although the elevation stage is capable of higher resolution movement, this system allows the surface of the workpiece to remain within the projection lens' depth of field (Table 2.2). The output from the sensor is displayed on a readout on the control console, as well as being connected to the control computer, to allow continuous monitoring and correction of the sample height when machining.

Three CCD cameras were also included in the laser system, for monitoring the beam uniformity, sample alignment and the sample itself during machining. Apart from the profile camera which does not require a light source, the other CCD cameras were connected to individually variable light sources. This allowed the monitored object to be illuminated appropriately; reflective samples required a lower illumination intensity during machining. The workpiece can safely be viewed on a monitor on the control console, allowing real-time monitoring of the sample. However, this camera could not be positioned vertically over the machining area because of the position of the de-magnification projection lens. Instead it was positioned at 45° behind the projection lens and therefore producing an elongated image, which although acceptable for monitoring machining progress and coarse alignment, was not suitable for aligning samples accurately. An additional camera with a high magnification optical system was mounted vertically above the sample at a known offset from the point where the beam reached the workpiece. This allowed the sample to be moved to the alignment camera, then aligned accurately to the orientation of any apertures or masks in the system. The alignment camera was connected to a computer which could display any of the outputs from the three CCD cameras. The image produced by the alignment camera could be used by the computer to allow automatic alignment of the workpiece. This can be useful when processing multilayer devices [2] and the workpiece is removed from the laser system for other fabrication processes.

The components of the workstation are all fastened to a heavy steel frame to enhance the structural integrity and hold the various components ridgidly relative to each other. The framework is also mounted on anti-vibration mountings that are situated under the corners of the workstation. Such rigidity is important when machining micron resolutions as even slight variations in the relative position of the optical components will cause noticeable distortion in any machined structure. Machining errors due to thermal expansion are reduced by operating the laser system in a temperature controlled environment (±1°C).

Figure 3.9 *Photograph of the excimer laser micromachining workstation. The control console can be seen on the right of the image and the unit at the left of the image is the workstation that houses the motion stages and optics. The three monitors on the control console are used for alignment (left), workpiece viewing (centre) and motion control (right). The gases used are housed in the extract cabinet at the right of the picture.*

The excimer laser can be operated at two wavelengths, determined by the lasing gases used. An argon and fluorine mix will generate a 193nm output and a krypton and fluorine mix will produce 248nm output. However, the optical elements used to direct and profile the laser beam are coated with a dielectric film for optimum performance at a specific wavelength, i.e. 193nm or 248nm. This necessitated changing, re-aligning and re-calibrating the optical system components whenever the lasing medium gases were changed to alter the operating wavelength. Failure to do this resulted in damage to the dielectric coatings and a departure from the optimum operation of the optical system.

The excimer laser micromachining system, shown in Figure 3.9, can be used to machine a variety of materials. The laser operating wavelength used determines which materials are best machined, as the machining process is dependent on inherent material properties. For example, machining polyimide at 248nm produces superior results than

machining at 193nm. On the other hand, ceramics, silicon and glass are best machined at 193nm (Table 2.1).

3.3 Cleanroom fabrication processes

A number of fabrication tasks were conducted in the School's in-house class 10,000 cleanroom to reduce problems associated with particulate contamination when fabricating micro-structures. The tasks undertaken included thermal evaporation of thin metal films, spin coating, UV exposure of photoresists and wet etching.

3.3.1 Evaporation of metal films

Thin metal coatings have several applications, including forming electrodes and providing thin conductive coatings on samples so they can be examined using a SEM. However, the thicknesses of the coating differ depending on the task. Electrodes required for the present work were fabricated by first depositing 5nm of chrome onto a glass substrate, followed by 70nm of gold. The chrome improves adhesion of the gold, which provides inert electrode structures. SEM coatings are thinner, typically 35nm, as this thickness of material will provide a suitably conducting coating to stop charge buildup while minimally changing the dimensions of the structures to be imaged.

The coatings used in this work were applied using a thermal evaporator (Edwards Auto 306 Turbo) with a rotating substrate holder. The evaporator can hold two different evaporation sources simultaneously, so removing possible atmospheric contamination had it been necessary to release the vacuum to allow evaporation source changes. The thickness of the deposited film was monitored during evaporation using a quartz crystal microbalance, which allowed control of coating thickness to better than 1nm.

3.3.2 Laminate coatings

Dry-film laminate layers are available in a variety of thicknesses from tens of microns to hundreds of microns. These coatings laser machine well and allow deeper structures to be fabricated without requiring complex substrate fabrication procedures. The coatings were applied using a standard printed circuit board (PCB) laminator before they were cut from the laminating sheet using a scalpel. One problem of these coatings is that the layers produced were relatively uneven, the variation in height typically 2μm to 3μm for a 90μm thick coating. Although this is not ideal, it does allow rapid fabrication of coated substrates with no other steps being required. The laminate used is photosensitive allowing patterning by selective exposure, followed by development that reveals the exposed structure.

3.3.3 Spin coatings

Spin coating allows uniform layers of a liquid-based material, such as a photoresist, to be applied to a substrate - the thickness of the layer being determined by the spin speed used. The spinner used in this work, a EMS spin-coater (model 4000-1), can accommodate substrates up to 100mm square and was capable of computer controlled spin-speeds up to 10,000 RPM with a resolution of 10 RPM.

This process was used to produce uniform layers of polymers, such as S1818 photoresist (Microposit, Shipley) coatings on glass and quartz substrates. Prior to spin-coating, the substrates were cleaned in a class 10,000 cleanroom using DECON 90® solution, before being rinsed in Ultra-Pure-Water (UPW) and hot-air dried. This removed the particulate and grease contamination from the surface of the substrates to provide a suitable surface onto which materials could be applied.

The procedure was to place the substrate on the spinner chuck, which was held in place using vacuum retention and dispense a small amount of the liquid resist onto the surface of the substrate. The substrate rotation speed was then ramped up to the required value, before being ramped down again, using computer control. The spin speeds and ramp

rates used were optimised for the relevant material and stored in programs in the memory of the control computer for future use. Figure 3.10 is a schematic diagram of the spin-coating system used.

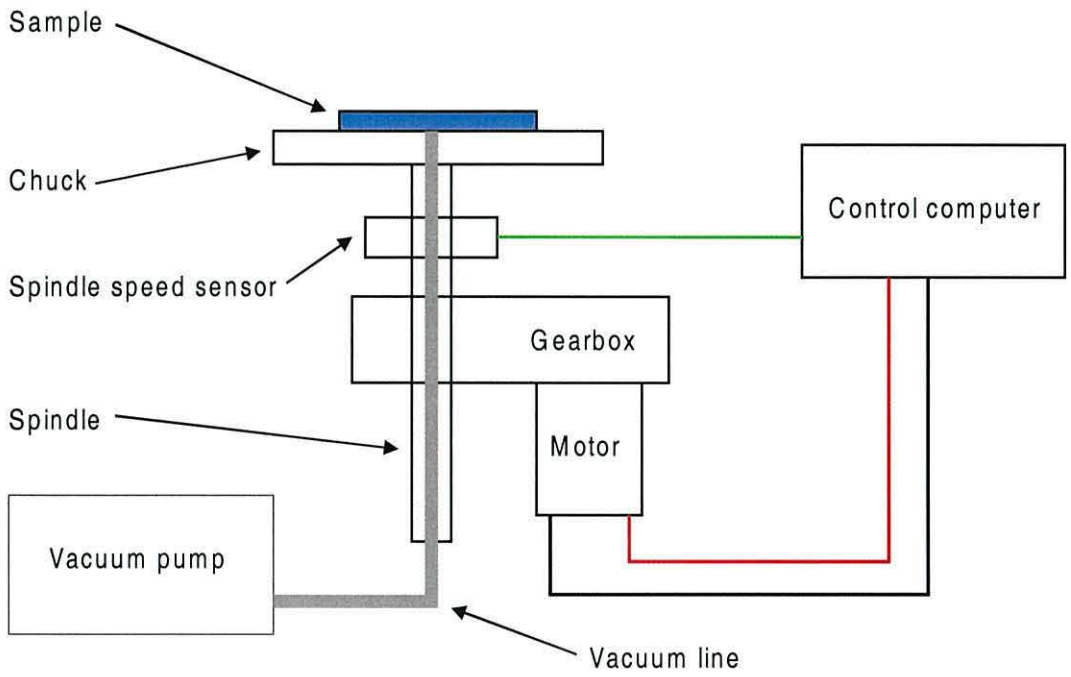

Figure 3.10 *Diagram of the spin-coating system*

Thin films of S1818 used in this work were prepared by placing the required substrate onto the spinner chuck. The surface of the sample was then covered with S1818 photoresist, before a control program was activated to accurately rotate the sample at 4000RPM. This caused the photoresist to form a thin layer, approximately 1.5μm thick. After spinning the sample for 1 minute, the rotation was stopped and the sample post-baked. The post-bake consisted of placing the sample on a hot plate heated to 116°C for a minute, which hardened the photoresist. The sample was then left to cool unaided, before subsequent processing could commence. Both exposed and unexposed S1818 layers were removed from the substrate using an acetone rinse, if the S1818 layer was no longer required.

SU8 was also coated onto substrates using spin-coating, following a documented protocol [3], to produce a uniform film. The thickness of the SU8 layer was controlled by the spin-coating speed used. The relationship between spin-speed and layer

thickness is shown in Appendix I. Typically 25μm and 100μm thick coatings were applied, although other thicknesses were used.

3.3.4 Contact exposure mode photolithography

Photolithography is a well known process [4], commonly used in micro-fabrication, where a radiation sensitive coating, such as a photoresist, is patterned by selective exposure to a suitable illumination source. The coating is then developed to remove either exposed or unexposed material, depending on the polarity of the material used. The remaining patterned material can either form the structure required, or be used in subsequent processes, such as etching, to protect underlying regions, where the resist remaining acts as a barrier to the etchant, allowing the resist pattern to be reproduced in underlying materials. Figure 3.11 shows an overview of a typical contact-exposure mode photolithography process.

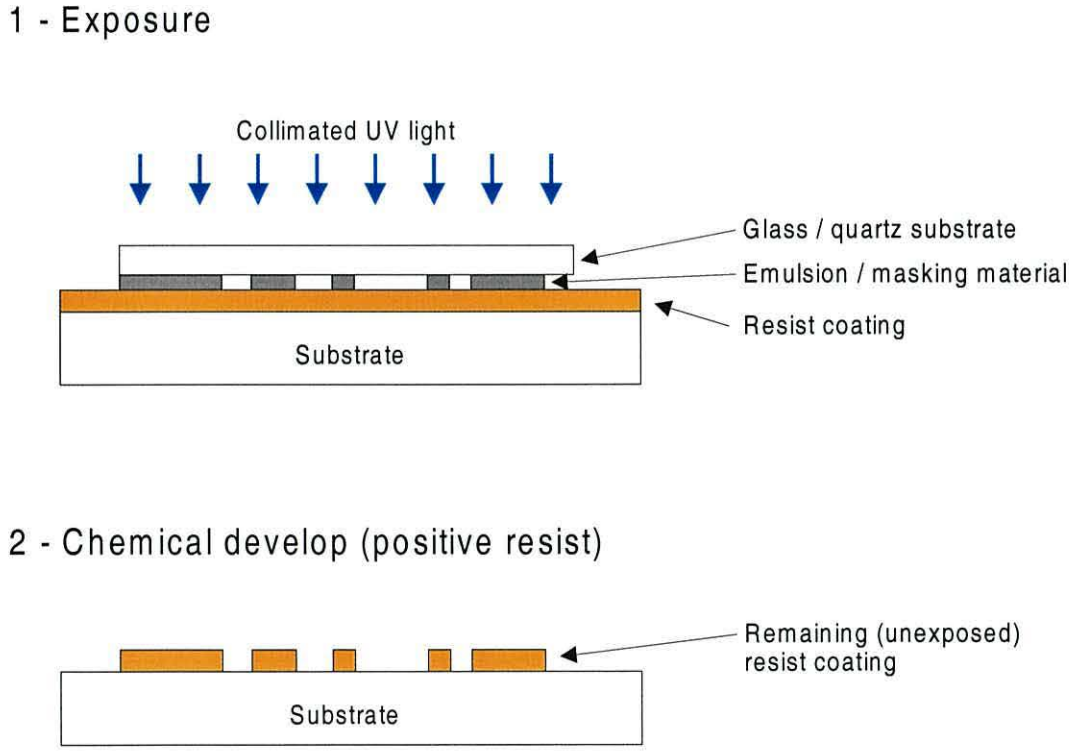

Figure 3.11 *Overview of a contact exposure mode photolithography process to reproduce a mask pattern in a photopositive resist layer.*

After spin-coating and cooling to room temperature, the photoresist coated substrate was placed on the stage of a Tamarack MAS12 mask aligner. The photoresist was exposed through a 1:1 contact mask using collimated UV light from a high-pressure mercury arc discharge lamp. The main emission lines were: g – 436nm, h – 405nm and i – 365nm [5]. The contact mask was made from either chrome-on-glass or a photographic plate. This procedure was also used to pattern dry-film laminate coatings, which are photosensitive.

3.3.5 Wet etching

Wet etch processes were used to selectively remove evaporated metal coatings, so allowing microelectrodes to be created. Having coated a substrate with thin metal layers using evaporation, a 1.5μm S1818 coating was spin-coated and exposed using contact mode photolithography. The selectively exposed photoresist was then chemically developed for 40 seconds (Microposit developer MF319, Shipley) to reproduce the mask pattern. This formed a structure with selected regions of the evaporated metal films exposed, whereas others were covered with S1818 photoresist. This facilitated selective chemical etching of the metal films by immersing the structure into chemical baths.

A two stage etch process was used: aqua-regia was used to remove the exposed gold regions, followed by a chrome etch that removed the underlying chrome seed layer. Table 3.1 shows the chemical constituents used in each of the etchants. The remaining regions of photoresist were then removed using acetone to leaving a patterned gold on chrome structure.

	Aqua-regia	**Chrome etch**
Chemical formulae	3 : 1 HCl and HNO_3	150g $(NH_4)_2Ce(NO_3)_6$ - cerric ammonium nitrate 35ml CH_3COOH – Acetic Acid 1000ml H_2O

Table 3.1 *Chemicals used in the metal film etch solutions*

3.4 Mask substrate characterisation

Suitable masks can provide selective patterning of the illumination sources for both the laser machining and photolithographic process. However, the materials that are used to construct masks have to be compatible with the process in which they are to be used. This is particularly important when choosing an appropriate substrate for the mask. For example Figure 3.12 shows the UV-visible spectrum for quartz and glass measured using a Hitachi U-2000 spectrophotometer. Clearly, glass substrates show cut-off at a much longer wavelength than quartz. This is important to note, since glass substrates are used for the photographic mask plates used in the in-house mask fabrication system. While glass is a suitable mask substrate over a wide range of incident illumination wavelengths, from approximately 1100nm to 400nm. Below 400nm, significant attenuation occurs. At 248nm and 193nm, the wavelengths generated by the laser, almost all incident radiation is blocked: transmission at 193nm is 0.1% and at 248nm it is 0.0%. Quartz on the other hand does not attenuate incident radiation significantly over the range of wavelengths measured with the transmission at 193nm and 248nm being 79.9% and 90.6% respectively.

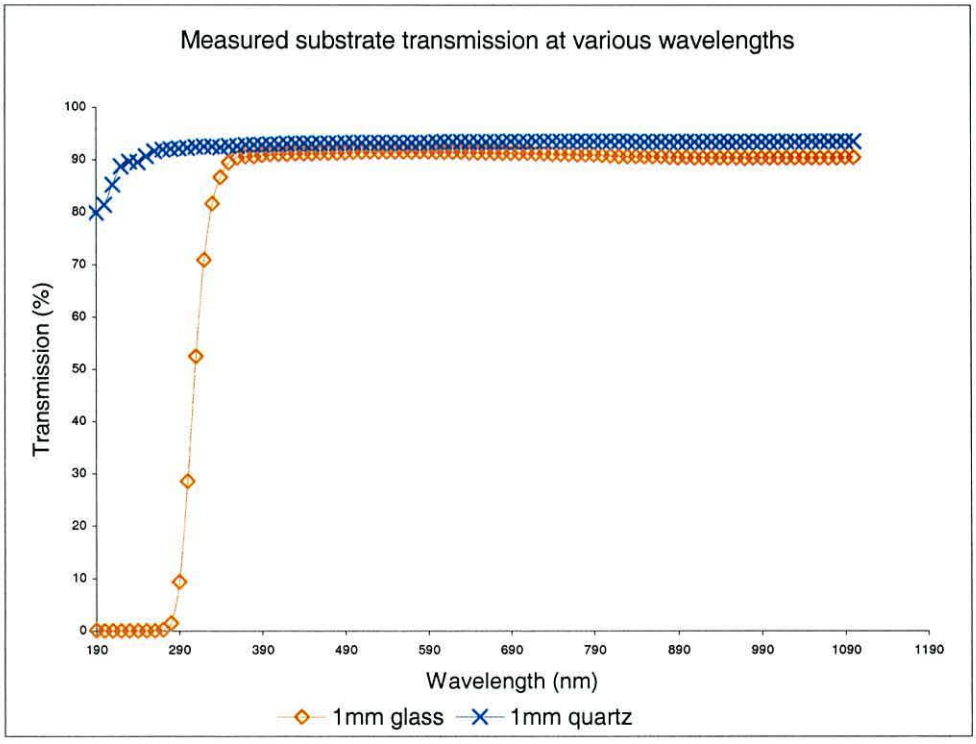

Figure 3.12 *Plot of percentage transmission measured at various wavelengths for glass and quartz.*

From this it can be deduced that glass is suitable for use in the mask aligner, as it attenuates light only minimally at wavelengths above 300nm, but not in the laser system. Instead, quartz must be used, since it attenuates minimally at the laser frequencies used.

3.5 Aperture production

Placing an aperture in the laser beam allows a predefined area of material to be removed from the workpiece. An example of this is drilling a hole where a circular aperture is used to create a circular beam at the workpiece allowing material to be removed from within the exposed regions, but leave surrounding material undamaged. Apertures can be created in a variety of ways, for example mechanically in a metal sheet, or by laser machining a hole in a material that does not transmit the laser wavelengths. Mechanically drilling, punching or etching metal sheets allows very durable masks to be produced, as the maximum energy density present at the mask plane is less than the ablation threshold for such materials, although the dimensional resolution is limited.

3.5.1 Chemically etched copper beryllium

Metal sheet based apertures can withstand the maximum fluences generated by the excimer laser with minimal distortion. A range of different sizes and shapes of aperture (circular, elliptical, square and rectangular) were fabricated externally in a 100μm thick copper beryllium sheet by a chemical etching process. The accuracy obtained was not as high as laser machined masks, with features below approximately 150μm not being resolved. The edges of the smaller apertures were also rough, which was not ideal. However, the larger mask apertures were used to shape the laser beam to a reasonable degree and provided a number of useful beam profiles. Figure 3.13 shows a micrograph of the 1mm circular and square apertures, produced by chemically etching through a copper beryllium sheet. Although such apertures could be used to machine patterns in a workpiece, they were typically used to machine aperture masks for use in the laser to define patterns, as a higher resolution could then be obtained. The edges of the

apertures appear 'roughened', most likely due to the etching process. The rounded corners of the square aperture can also be explained by the etching process.

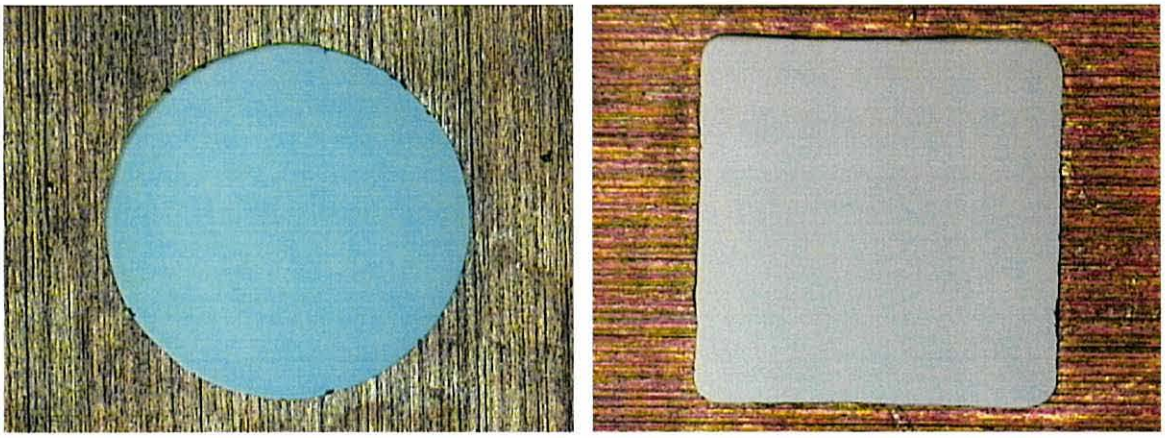

Figure 3.13 *Optical micrograph of circular and square 1mm aperture, chemically etched in a copper beryllium sheet 100μm thick. The edges of the apertures can be seen to be 'rough' with some distortion present, for example the edges of the square are not perfectly straight.*

3.5.2 Laser machined apertures

Laser machined apertures allow a high degree of accuracy and repeatability in the dimensions of the aperture. However, unlike apertures fabricated by drilling a metal sheet, laser machined apertures can be damaged when high energy densities are present at the mask plane, as the damage threshold of the masking material can be exceeded. Nevertheless, using laser machined masks is preferable because of their high dimensional accuracy.

Figure 3.14 shows the transmission of two materials that can easily be coated on a wide range of substrates: S1818 photoresist (Microposit, Shipley) and dry-film laminate (Laminar 5038, Ozatec). This shows that both materials absorb strongly over the range of 190nm and 300nm. Hence both materials are suitable for selectively patterning the beam generated by the excimer laser.

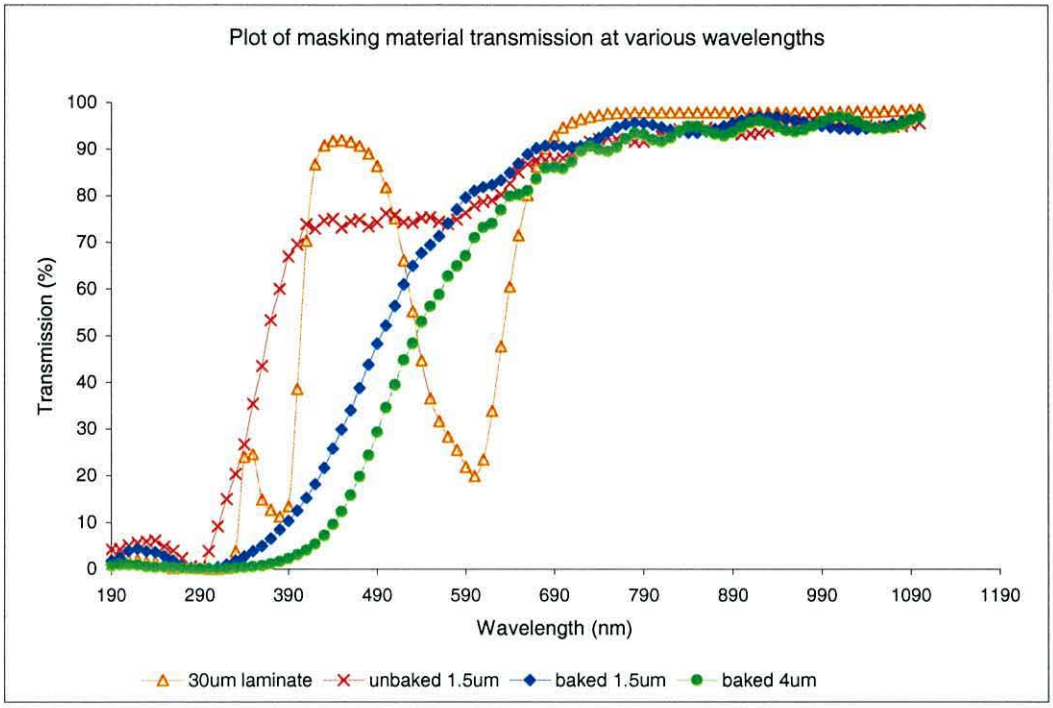

Figure 3.14 *Plot of material transmission at various wavelengths for two coatings: S1818 photoresist and dry-film laminate. Both materials almost block wavelengths below 300nm so are suitable for laser masks. The laminate also attenuates strongly around 600nm, which is probably because it appears blue to the eye.*

The S1818 coating normally applied is 1.5μm thick, whereas the dry-film laminate material is available in a range of thicknesses. Generally a laminate 30μm thick is used, as this can still be machined quickly with reasonable wall angles (Chapter 2.5.3).

The rate of mask erosion is related to the optical absorption characteristics of the material. If the threshold energy density for the onset of mask erosion can be found, the workpiece can be machined at lower energies in order to minimise mask damage. However, if running at higher energies is necessary, the rate of mask erosion at these energies must be determined since this will control the time a mask can be used before a replacement is required. Therefore, determining mask erosion characteristics is important.

Figure 3.15 shows the results of measuring mask erosion rates at various laser energy densities for a 30μm thick dry-film laminate. S1818 coatings were found to degrade much faster than the thicker laminate coating, with pinholes developing almost as soon as the ablation threshold was exceeded. The ablation threshold for S1818 was found to be approximately 105mJ/cm^2, whereas the threshold for dry-film laminate was

measured at approximately 350 mJ/cm^2. However, if fine structures, such as a thin strip of material, are used, thermal degradation of the mask may occur below the measured ablation threshold. This is primarily due to a thin strip of material being less able to dissipate heat compared to a larger area of the same material. This was found to vary depending upon the precise mask geometries used.

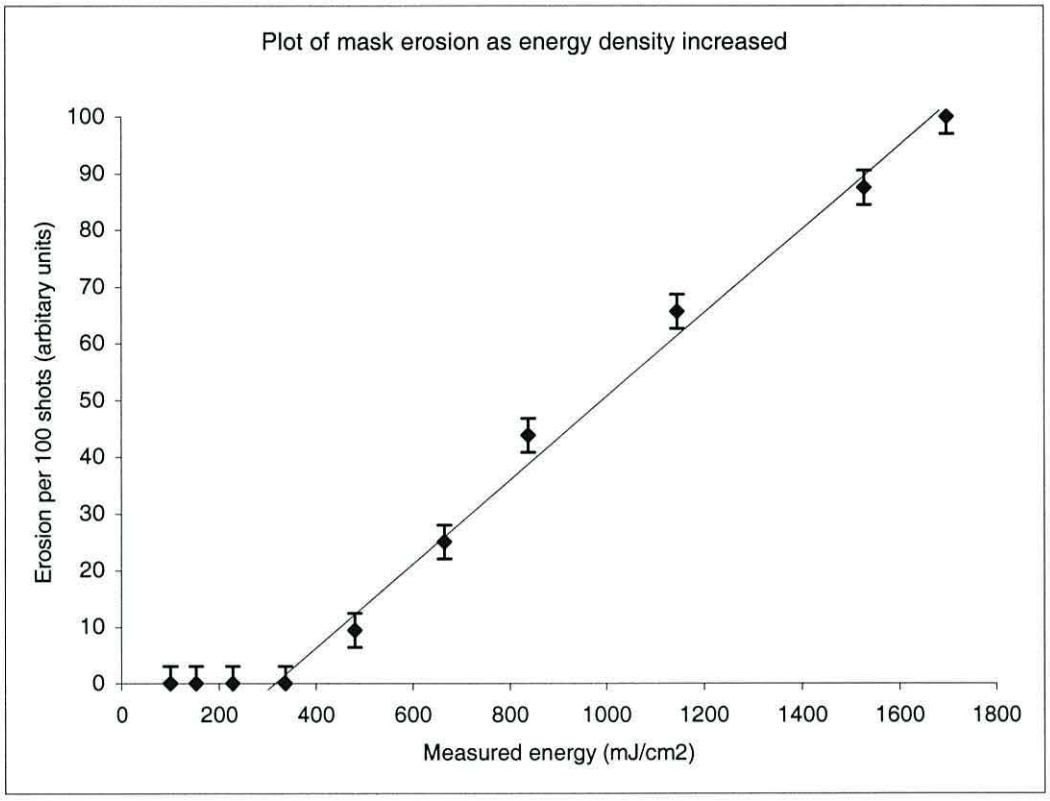

Figure 3.15 *Plot showing the measured erosion of a 30μm dry-film laminate layer at various laser energy densities. The line shows a linear regression of the measured points and indicates that the relationship is linear, as R^2 = 0.9927.*

These data allowed possible mask degradation problems to be avoided, by operating the laser below the damage threshold. If this was not possible and dry-film laminate masks were being used, the useful machining time of the mask was known and machining could be stopped before the mask developed pin-holes.

3.6 Mask production

Masks allow more complex patterning of an incident light source than can be achieved using a simple aperture. Various forms of mask were used in this work, depending upon the application and resolution requirements of the task in-hand.

3.6.1 Photographic mask plates

The photographic mask plates (GVPSR, AGFA millimask) consisted of a glass substrate coated with a thin layer of light sensitive photographic emulsion, capable of resolving at least 2μm features. The mask pattern was defined conventionally using in-house photo-reduction cameras, shown diagrammatically in Figure 3.16, to project a pattern formed by a scaled 'master' onto the photographic emulsion. Various forms of 'masters' can be used, depending upon the application. These include designs printed on paper using a conventional printer and PC with a suitable graphics package, although the resolution is limited to approximately 30μm. However, designs plotted commercially on acetate were generally used due to the higher resolution possible, approximately 6μm (4000 lines per inch).

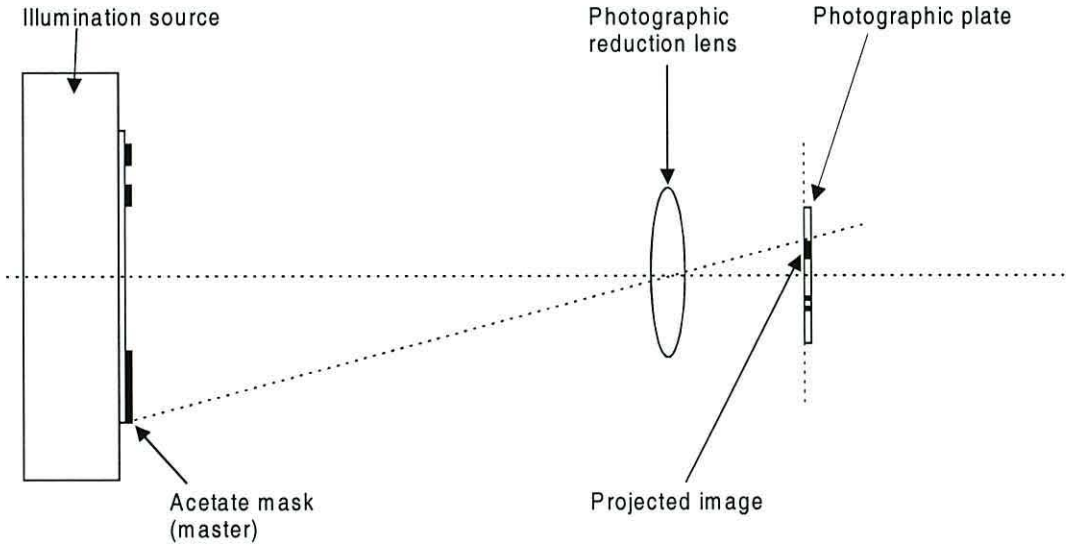

Figure 3.16 *Diagrammatic representation of the in-house photographic-reduction camera system used to pattern photographic mask plates.*

After exposure, the emulsion was chemically developed (G282c millimask developer, AGFA) for four minutes, fixed for two minutes (G333c millimask fixer, AGFA), followed by an UPW rinse and hot air drying. This reveals the transmissive and non-transmissive regions that form the mask - exposed regions turned black when the plate was chemically developed, whereas unexposed regions were left clear. These masks were suitable for use in the in-house lithography process. Although the smallest feature size that could be accurately and reliably produced was approximately 6μm, such masks were ideally suited to a research environment, as they are cheap and fast to produce.

3.6.2 Photolithographically produced masks

It is known that photographic mask plates can be rapidly patterned using a photograhpic reduction process, but such masks are not compatible with the laser. The glass substrates used will attenuate almost all of the incident radiation from the laser beam, so preventing high enough energy densities from reaching the workpiece to cause ablation. However, photographic masks can be used to produce other masks that can be used in the laser. This was achieved by using the photographic masks in conjunction with a photolithographic step to pattern a spin-coated S1818 layer on quartz. S1818 has been shown to absorb strongly at the laser operating wavelengths, whereas quartz will not. This allows complex laser masks to be fabricated quickly in a single exposure. Other photosensitive materials, such as dry-film laminate, can be patterned in a similar manner.

3.6.3 Laser machined masks

Direct laser machining allows high dimensional accuracy apertures to be fabricated in a range of materials, including polymer films such as S1818. It is also possible to machine more complicated patterns in such layers using a suitable aperture in the laser to shape the beam. This has the advantage of high positional and dimensional accuracy over a large area, although the fabrication time may be significant.

3.6.3.1 Exposed photographic mask plates

Trial excimer laser machining at 248nm of an exposed photographic mask plate revealed that the photographic emulsion could easily be machined to a high resolution without cracking or deformation of the emulsion. Hence, laser machining the required pattern into the emulsion produced contact-exposure mode masks, suitable for use with the photolithography process.

The method of producing the plates was to expose them for 1 minute, using the photoreduction camera system without a mask present, then development as normal. This produced photographic mask plates that were completely exposed, i.e. the developed emulsion was non-transmissive. Selective excimer laser machining of the emulsion to create cleared areas allowed mask patterns to be fabricated with higher resolution features than was possible using the optical photographic reduction system. The photographic emulsion that covered the plates appeared as a uniform film, approximately 6μm thick. This allowed easier machining since constant laser settings could be used to completely remove the emulsion.

3.6.3.2 Spin coated S1818 layers

Spin coated layers of S1818, typically 1.5μm thick, can be produced on a variety of substrates. It has already been shown (Figure 3.14) that such films attenuate the UV produced by the excimer laser. S1818 also machines well using laser ablation and micron resolution is easily possible, thus allowing complex, high-resolution masks to be fabricated directly using the laser system.

3.6.3.3 Evaporated chrome-on-glass

Patterned evaporated metal layers are commonly used to create masks, because the metal layer will completely block incident radiation. Such masks can be used in the laser system, if a quartz substrate is used, as well as in photolithographic processes using either quartz or glass substrates. Laser machining can selectively remove regions

of evaporated thin metal films, although the process is not perfectly reproducible. The process of material removal is not dominated by ablation, instead thermal degradation and shockwaves dominate [Chapter 2.2]. This leads to unpredictable and unrepeatable machining, where some samples will machine much better than others.

3.6.3.4 Dry-film-laminate layers

Dry-film laminate is also well suited to laser machining and can be patterned easily. Unlike S1818 though, it is not capable of fine patterning, owing to its greater thickness (~30μm). However, it does attenuate strongly the UV produced by the excimer laser, and coating onto a quartz substrate allows more durable laser masks to be created. Although the patterning resolution attainable is not as good as S1818, it is ideal for forming apertures to produce a shaped laser beam at the workpiece, as well as larger, low-resolution binary masks. The dry-film laminate layers used in this work were applied to substrates using a standard PCB laminator, after they had been cleaned using DECON 90® to remove any particulate contamination and grease.

3.7 Problems of laser machining

Several problems were encountered when using laser ablation to pattern materials. In particular, laser machining of masks on quartz plates proved problematical, as did the production of debris over the workpiece when materials were ablated.

3.7.1 Problems of laser machining masks with quartz substrates

Machining masks on quartz substrates, for example the x10 laser mask used in Chapter 4, was not straightforward. The laser beam used to machine the mask material passed through the 1.5mm thick quartz substrate with minimal attenuation. Although the beam was focused at the top surface of the plate, the energy density at the lower surface was still relatively high and was sufficient to cause machining of the brass

vacuum chuck used to hold the workpiece. This resulted in ablated material being deposited on and embedded in the lower surface of the mask. This reduced the transparency of cleared regions of the mask, as well as reducing the resolution by reducing the substrate surface quality. Higher machining energies used to reduce the total machining time exacerbated the problem. Attempts to remove the material present on the lower surface of the substrate were not successful. The damage caused to the surface during machining left a permanent damage pattern on the quartz plate, as shown in Figure 3.17. Because of this, although the resist layer had been removed, the quartz plate was rendered unusable.

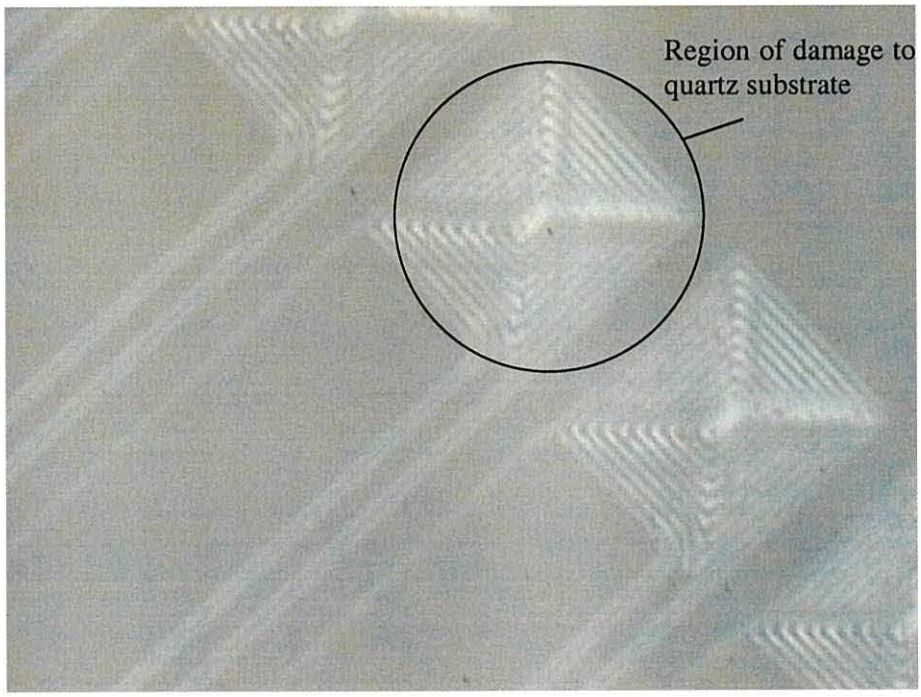

Figure 3.17 *Optical micrograph showing the damage to the rear surface of a machined quartz substrate. The damaged areas can be seen as the lighter coloured regions, where the beam path used to clear the S1818 masking layer can be seen. As the plate is quartz, it will not attenuate the machining laser beam significantly, so allowing enough energy to reach the surface of the chuck and cause machining. The damaged areas are not well defined as the laser beam is no longer focused.*

The problem was addressed by placing an additional quartz plate under the workpiece to act as a buffer. The workpiece was held in place by drilling holes in the additional quartz plate to allow vacuum retention of both plates. The holes were positioned so as not to be under any machined areas, as shown schematically in Figure 3.18.

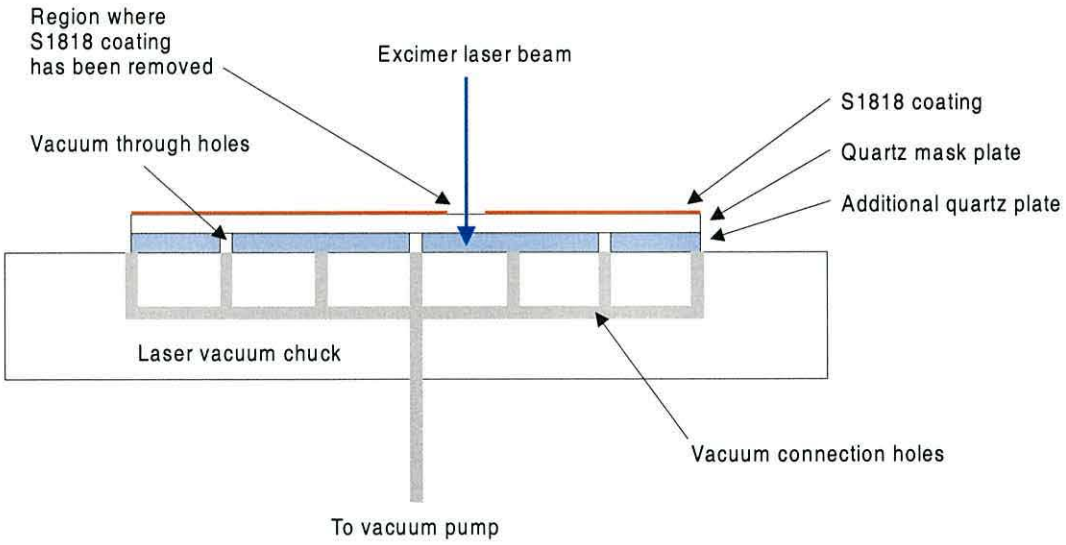

Figure 3.18 *Overview of the arrangement used to machine the laser mask plate. The lower quartz plate was drilled to allow vacuum retention of the upper quartz plate during machining. The holes were drilled away from the machined areas and over the vacuum region of the laser system chuck. This allowed the coating on the upper plate to be machined without damage to the back surface of the mask.*

3.7.2 Laser ablation generated debris

The debris generated during laser ablation of polymers is an unwanted side effect of the process [6]. Some of the debris generated is deposited onto the surface of the workpiece, covering the areas immediately surrounding the ablation area, as well as the ablated area itself. This reduces the quality of the structures produced. The material in the ablated areas can be removed by re-scanning the exposed area. However, this slows down the machining rate. Attempts were made to direct the debris away from the ablated zone using electrostatic forces. The approach, which required high electric fields to be applied in the vicinity of the workpiece was moderately successful as described in reference [7] (the full publication is given in Appendix V).

In [7] the electric field was established between two parallel plate electrodes. In later work, one of the plates was replaced by a 200μm diameter wire suspended 500μm above the surface of the workpiece. This had the effect of creating a non-uniform electric field above the surface of the sample. A diagram of the experimental setup used is shown in Figure 3.19.

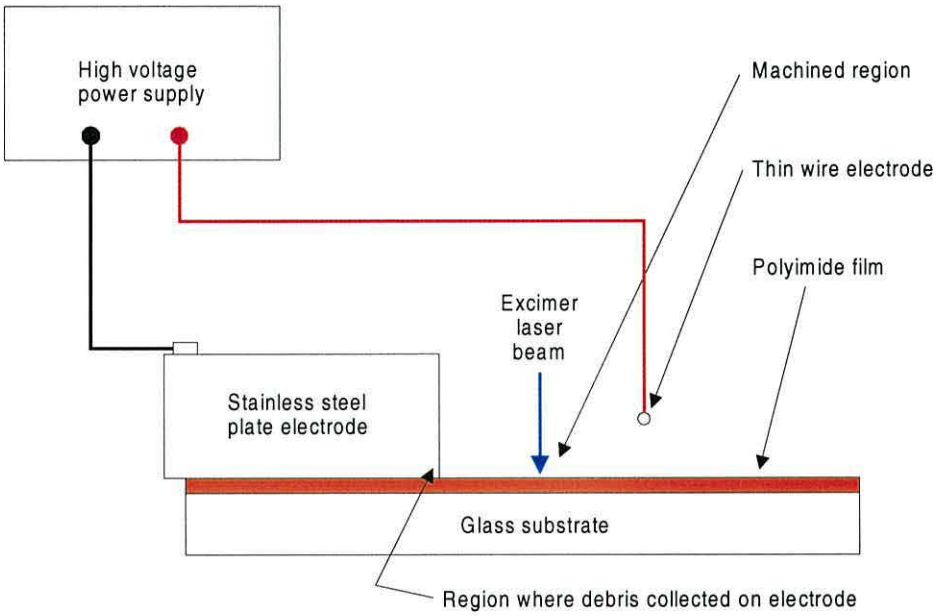

Figure 3.19 *Setup used to apply the electric fields while laser machining test patterns.*

The two SEM micrographs in Figure 3.20 show the results of machining a polyimide film with and without an electric field applied. In both cases, a 50μm square aperture was used to pattern the machined areas, with the laser energy density used kept constant at 103mJ/cm^2 at the workpiece.

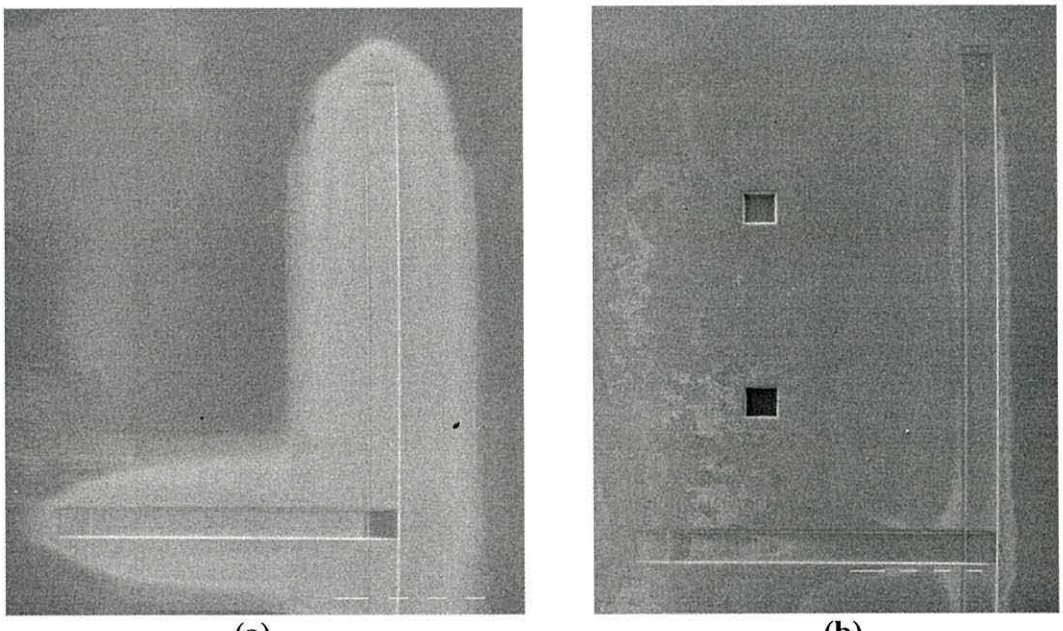

(a) **(b)**

Figure 3.20 *Scanning electron micrographs of regions machined using laser ablation. (a) shows the effect of laser ablation of a polyimide film between the non-uniform electrodes. The debris generated can be seen as the powder-like substance surrounding and covering the ablated regions. (b) shows the effect of applying a non-uniform field while laser machining a similar pattern in a polyimide film. The debris present in (a) can be seen to be almost completely removed.*

These images show that with no field applied, debris covers the areas surrounding the ablation zone, including previously machined regions. However, when a suitable electric field is applied, generated in this case by a voltage of 3kV, the debris present on the sample is almost completely removed.

Optical inspection of the electrodes used showed that some material was present on the plate electrode surface. Figure 3.21 shows an optical micrograph of the edge of the plate electrode, the darkened region is most likely to be debris collected from the ablation process.

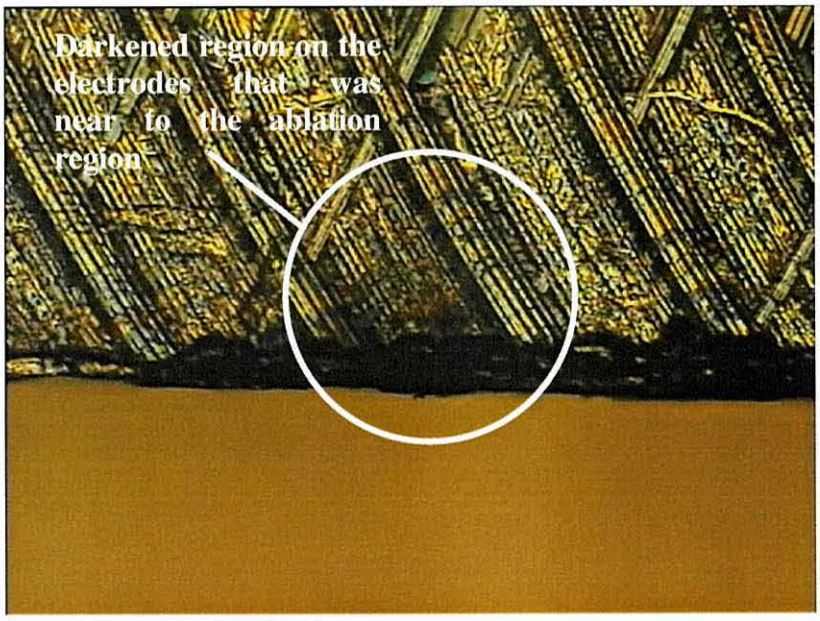

Figure 3.21 *Optical micrograph of the edge of the plate electrode. The darkened region is most likely due to ablation generated debris, collecting on the electrode surface.*

Although it has been demonstrated that non-uniform electric fields can be used to almost completely remove ablation generated debris, the interaction between the ablation plume and the electric field is not fully understood due to there being many processes occurring simultaneously. The system has not been implemented due to (a) the need to use high-voltages to generate the fields required [7-9], (b) the problems associated with permanently mounting the electrodes and (c) integrating such a system into the workstation.

3.8 Examining the machined structures

The machined structures produced by the techniques already described were examined and measured using an ISI-40 Scanning Electron Microscope (SEM) that allowed accurate measurement of feature sizes as well as inspection at up to 200,000 times magnification. The SEM was connected to an I-SCAN 100 III data capture unit and associated PC, which allowed the SEM images to be recorded. The SEM was calibrated using a calibration standard, traceable to NPL, that was placed next to the sample under investigation. Using the identical SEM settings, the dimensions of the calibration grid were measured. Figure 3.22 shows a SEM capture of the features on the calibration standard, which consist of two sets of parallel rulings. These are scribed at a frequency of 19.7 lines per mm (50.76 μm apart). This allowed known design dimensions to be overlayed on captured SEM micrographs for comparison. The scale bar generated by the SEM was found to be in very good accordance with the scribed lines.

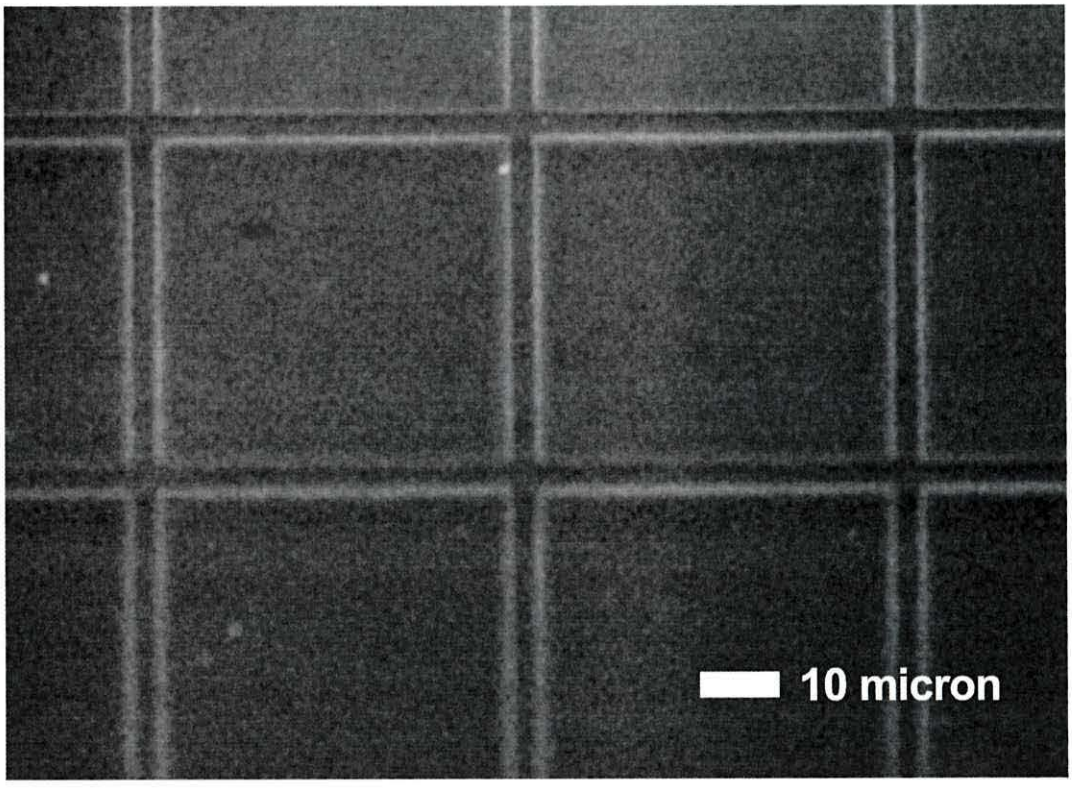

Figure 3.22 *SEM capture of the calibration grid, showing the square regions created by the two sets of scribed lines, 50.76 μm apart.*

An Olympus BX60 optical microscope, with an attached CCD camera was also used to record images. This allowed direct image capture onto a PC with a video capture card, as well as recording events onto a S-VHS video. The Olympus microscope is capable of Diffraction Interference Contrast (DIC) illumination that causes different sample heights to appear as different colours. This is useful when examining machined structures as any irregularities in the height of a surface can easily be identified. An additional microscope (Labophot, Nikon), with a similar image recording system, was used for observing and recording the motion of latex spheres presented in Chapter 7. Optical transmission and absorption measurements of materials were recorded using a Hitachi U-2000 spectrophotometer, allowing measurement over a large range of wavelengths from 190nm (UV) to 1100nm (IR).

3.9 References

[1] "*Laser processing in manufacturing*", R. C. Crafer and P. J. Oakley, *Chapman & Hall*, 1993, London

[2] 'Direct manufacture of miniature bioparticle electro-manipulators by excimer laser mask projection', N. H. Rizvi, P. T. Rumsby, J. P. H. Burt, M. S. Talary, J. A. Tame and R. Pethig, *ICPE* **2** (1997) 971-974

[3] 'Polymerisation optimisation of SU-8 photoresist and its applications in microfluidic systems and MEMS', J. Zhang, K. L. Tan, L. J. Yang and H. Q. Gong, *J. Micromech. Microeng.* **11** (2001) 20-26

[4] "*Fundamentals of Microfabrication*", M. J. Madou, *CRC press*, 1997, Boca Raton, Florida

[5] "*Resolution enhancement techniques in optical lithography*", A. K.-K. Wong, *SPIE press*, 2001, Bellingham, Washington

[6] 'The effects of debris formation on the morphology of excimer laser ablated polymers', R.S.Taylor and K.E.Leopold, *J. Appl. Phys.* **64** (1988) 2815 – 2818

[7] 'Electric Field Interaction with Debris Generated by Laser Ablation of Polyimide Films', C. J. Hayden, R. Pethig and J. P. H. Burt, *Electrostatics 1999, Inst. Phys. Conf. Ser.* **163** (1999) 261-264

[8] 'Electrostatic collection of debris resulting from 193nm laser etching of polyimide', R. J. von Gutfield and R. Srinivasan, *Appl. Phys. Lett.* **51** (1987) 15-17

[9] "*Industrial electrostatics – fundamentals and measurements*" D. M. Taylor and P. E. Secker, *Research Studies Press*, 1994, Taunton

Chapter 4

Fabricating a circular AC electroosmotic pump

4.1 Introduction

Chromatography is commonly used to separate different analytes from an analyte mixture. Typically, a slug of the analyte mixture is injected into a particle filled column. The particles in the column are coated with a material to which the different analytes have different affinities ('stationary phase'). Separation of the analytes is achieved by flushing the analyte through the column, causing one of the analytes to be ejected from the column prior to the other, as it spends less time on the stationary phase.

However, the finite length of the column limits the process as this determines the efficiency of the separation process, denoted by the 'plate number', N, where the higher the value of N, the better the quality of separation. The plate number can be determined from the relationship

$$N = 16 \left(t_r / t_w \right)^2 \qquad (4.1)$$

where t_r is the retention time (the time between sample entering column and exiting) and t_w is the baseline width of the detector output pulse when the analyte exits the column [1].

The particles present in conventional chromatography columns can be replaced with stationary phase coatings applied to the channel walls (open tubular chromatography). In this case the channel height should be made small so that the diffusion time across the channel is reduced and equilibration between analyte and stationary phase is accelerated, enhancing the analysis process by increasing the plate number of the device.

By replacing the conventionally used straight column with a circular channel, the effective length of the column can be increased to infinity as the analyte can now be pumped continuously [2]. As the plate number is directly proportional to the length of the column, circular devices allow high values. As circular devices allow the effective column length to be varied, rapid separations can also be conducted in less time.

Implementing AC electroosmotic pumping (ACEOP) to move the liquid using a suitable electrode array provides a self-contained analysis system with an in-built pumping system [3, 4]. Laser micromachining is particularly suited to the fabrication of such a system and indeed the structure was used to demonstrate the capability of the machining process. The ACEOP system was produced by patterning a thin gold layer to provide the microelectrodes required to generate the electric fields. As the micro-channel was circular, the system developed was termed a circular-AC electroosmotic pump, or a cACEOP pump.

The required electrodes were fabricated by patterning a gold film thermally deposited onto a glass substrate (Chapter 3.2.1). Using a glass substrate allowed optical inspection and measurement of the contents of the fluidic channel during testing while gold electrodes are inert and do not oxidise or react with the contents of the channel. A binary photomask was used to pattern a resist layer which selectively protected areas of the gold from a subsequent chemical etch process, so allowing patterned electrodes to be fabricated. The device then had a circular fluidic channel bonded onto it, with fluidic connection ports and access to electrical connection pads so that the electrodes could be energised. In order to pattern the photoresist with the required design using in-house processes, a photomask with 1:1 scale electrode pattern was required.

However, the smallest electrode geometry required to implement ACEOP pumping is 4.2 μm, which is below the 10 μm limit of the in-house photographic mask making system. An alternative method of fabricating masks was to use excimer laser ablation to machine the mask directly by clearing the required areas in an optically non-transparent material. It is already known that excimer laser ablation allows high resolution machining in a variety of materials, for example polymers [5-8]. The advantages of using this system are that contact masks can be rapidly fabricated and sub-micron resolution is possible over a large (200mm^2) area. Another advantage of this system is

that the resolution of the mask is constant from one edge to the other, unlike conventional projection systems that use lenses. This makes the excimer laser machining system an ideal tool for producing high-resolution masks, for use in both the laser system and conventional photolithography.

In light of this, excimer laser machined masks were developed to produce contact masks that could be used in the in-house 1:1 photolithographic system to produce the microelectrodes required to fabricate the cACEOP pump.

4.2 Design of cACEOP pump

The initial specifications for the electrode geometries were supplied by Jan Eijkel of Imperial College. These were translated into the electrode design shown in Figure 4.1, a section of which is shown enlarged in Figure 4.2. The electrodes are the white regions, the black regions being removed from the gold film during fabrication. The electrodes are either 4.2 μm or 25.7 μm wide and 150 μm long. The inter-electrode gaps are 4.5 μm and 15.6 μm wide. The fluidic channel used is 100 μm wide, the radius of the channel centre being 4.488 mm, as shown in Figure 4.1. Because the electrodes are arranged radially, it is not possible to maintain a constant electrode width throughout its profile. Instead, the electrode dimensions are fixed at the centre of the channel and the edges are defined by lines converging at the centre of the pattern, maintaining a constant ratio of electrode to inter-electrode gap.

As laser projection was used to transfer a pattern onto the contact masks using the mask-scanning mode (Chapter 2.4.2), the maximum size of the electrode array was determined by the size of mask plate (100mm x 100mm) that could be used in the laser system. The final device was 9mm x 9mm in size and was generated from a 90mm x 90mm laser mask.

The design was drawn using Autosketch [Autodesk, Inc.], a commercially available CAD package. The design was then imported into the laser systems' dedicated CAM package, AlphaCAM [Licom Systems, Ltd.] to allow laser machining.

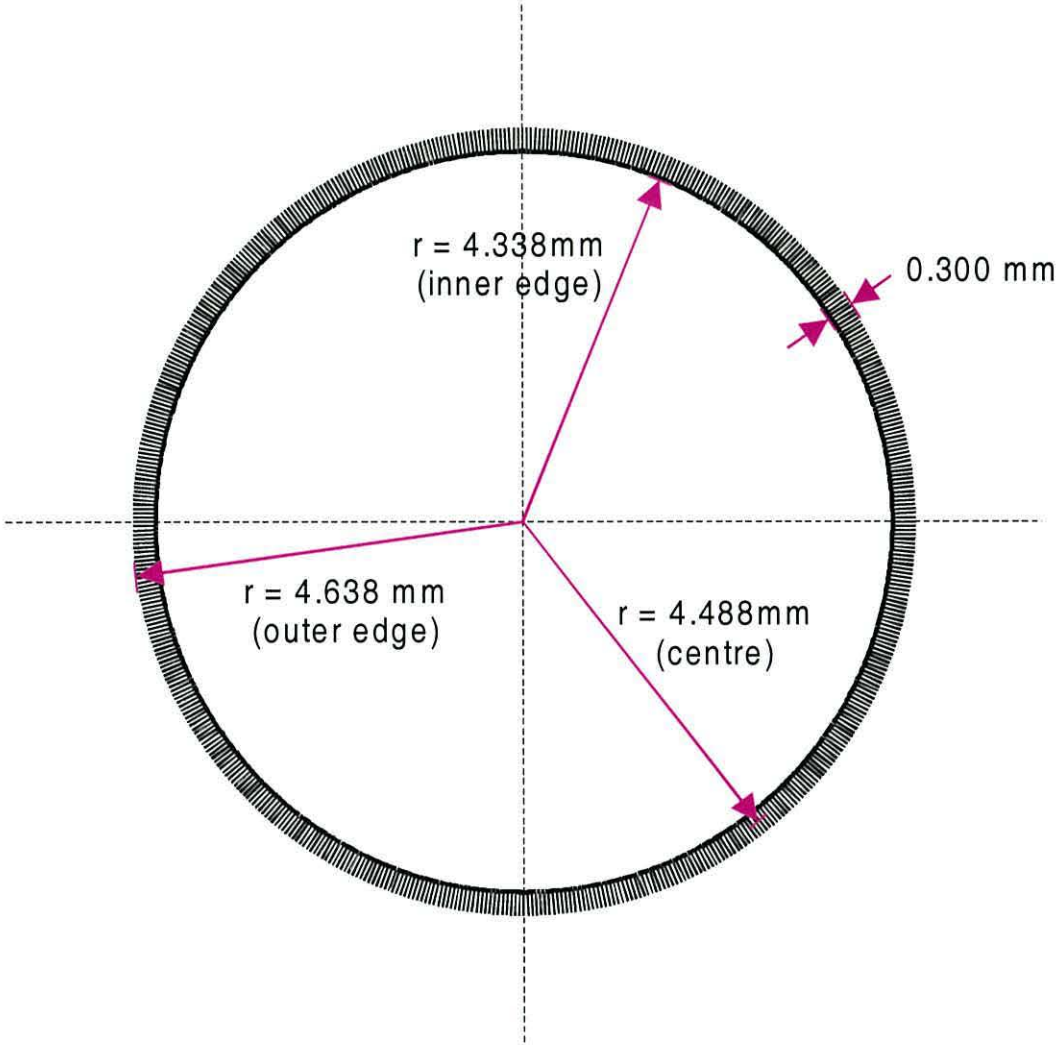

Figure 4.1 *View of the complete circular-ACEOP pump electrode track design. Here, the areas to be machined are black and the white areas will eventually consist of a gold layer, forming the electrodes and associated electrical connections. The dimensions shown indicate the size of the final device.*

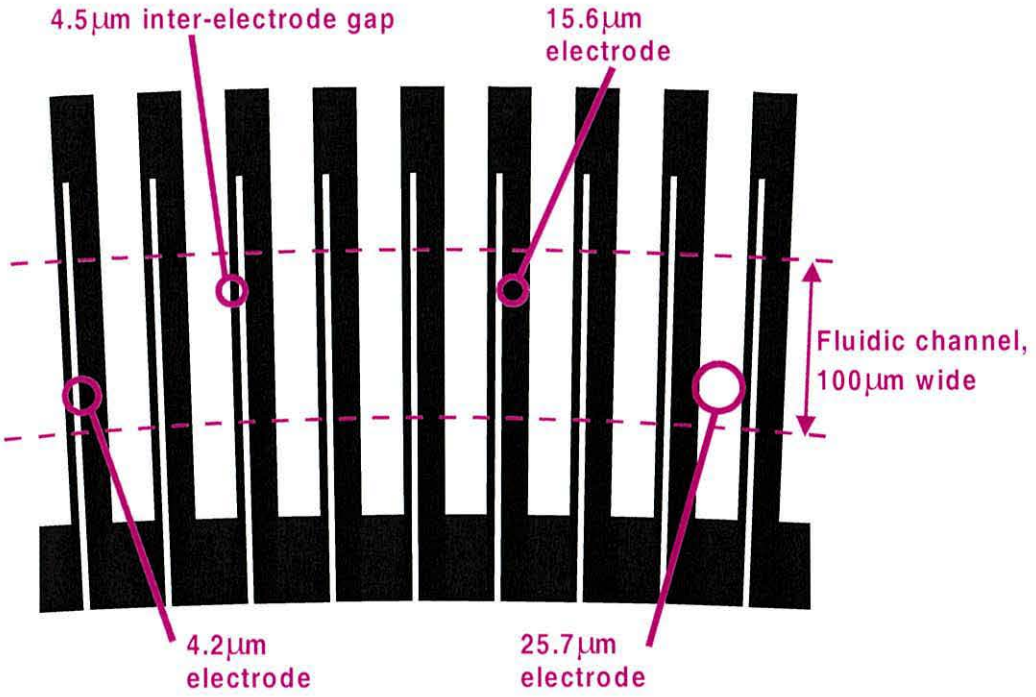

Figure 4.2 *Enlarged section of circular-ACEOP electrode track design. This shows the arrangement of the two sizes of electrodes and the two sizes of interelectrode gaps. The white areas shown will not be machined and will form the electrodes and associated electrical connections.*

4.3 Fabricating the x10 laser mask

The contact masks were fabricated in two stages: firstly, a 100mm x 100mm quartz plate was spin-coated with S1818 (Chapter 3.2.3). This was then machined with the electrode pattern, detailed in the previous section, ten times larger than required. This was then used as a laser mask to fabricate the required contact mask using a x10 demagnification projection lens in the laser system. This replicated the correctly sized mask pattern at a higher energy density that was suitable for machining. The laser mask could have been fabricated using several more rapid processes, but laser machining was chosen for its high dimensional accuracy and repeatability. Photographic reduction of a larger pattern could have been used, but the resolution limits of the camera used for this size of mask would limit the x10 laser mask resolution. A commercially produced, 4000lpi mask could have been contact exposed to produce the mask, but as the cACEOP design was circular, the quantisation levels (approximately 7μm) would have produced unwanted distortion in the final device.

The laser micromachining system is optimised to produce high-resolution structures (Chapter 3.1), therefore a mask produced using such a technique will be high quality and have sub-micron accuracy. Although the machining time required to produce the initial laser mask is significant, typically 10 hours, this approach had the advantage of being able to pattern suitable photolithography mask materials quickly, without having to serially machine each one. This then allowed the rapid production of photolithography masks as well as the possibility for fabricating electrodes directly by machining into a gold layer, while maintaining the accuracy and repeatability.

As the electrodes are arranged radially around a point, it was not possible to use a single electrode-shaped aperture to machine the mask. Instead, the electrodes were drawn using a single aperture whose diameter was determined by the minimum feature size of the electrodes. Because the laser beam was being used to generate straight lines at various angles, a circular aperture was used. This is because the distance machined from the centre of the beam is constant, regardless of the direction of motion. If a square aperture had been used, then the electrode sizes and inter-electrode separation would have varied depending upon the electrode orientation: for example, vertical and horizontal electrodes would have been narrower than electrodes oriented at 45 degrees.

The aperture used to machine the x10 laser mask was a 380 μm diameter circular aperture, fabricated using the laser to machine dry film laminate coated onto quartz plates. By using the laser to fabricate the aperture, a dimensional accuracy of 0.1 μm was obtained. This aperture was used subsequently to create a 38 μm diameter circular beam at the workpiece, which was slightly below the minimum feature size of the laser mask design, so allowing serial machining of the patterned laser mask. As the laser optical system is designed for sub-micron resolution machining and the motion stages resolution is 0.1 μm, serially machining the x10 laser mask produced a mask with better than micron resolution. The x10 laser mask used consisted of a 100mm x 100mm quartz plate, which was coated with a 1.5 μm layer of S1818 photoresist, as detailed in Chapter 3.2.3.

Before the mask was machined, the optimum machining settings were determined, namely the laser energy and workpiece motion speeds. Initially, the ablation threshold of the S1818 coating was found by machining a sample at various energy densities and observing the point at which material removal was detected. The number of shots required to completely remove the coating at this energy density was also measured.

The required pattern was then produced by operating with a slightly higher energy density to guarantee that material was cleared from the machined regions. However, using these settings to produce the mask did not necessarily result in the fastest possible machining of such a complex mask. The total machining time was decreased by increasing the laser firing rate, which in turn allowed faster workpiece motion speeds. However, this approach was limited by the maximum laser firing rate of 100Hz. Further decreases to the processing time were made possible by increasing the energy density delivered per shot. This had the effect of removing more material with each shot, but was also limited by the rate of mask aperture erosion. This is not a problem if metal apertures are being used, but can become so when laser machined coatings are being used as apertures.

Another problem associated with using higher energy densities is that the S1818 coating tended to crack, chip or lift as the shockwaves generated by the ablation of a larger volume of material become strong enough to damage surrounding areas not exposed to the beam. Heating effects also became more significant and could be detected when high laser energies were used. Increased debris was also apparent as the machining energy increased. This reduced the machining rate since it became necessary to remove material from machined areas more than once. Hence the lower limit of the useful laser energy density was found to be just above the ablation threshold of the material. The upper limit was the energy at which machining quality starts to degrade, as detailed in Chapter 3.4.2.

In a series of controlled experiments, the optimum machining rate was achieved using a workpiece motion speed of 30mm/min at an energy density of 1017mJ/cm^2. This ensured complete removal of the S1818 coating within the beam area and also any debris settling in the machined areas. The use of a circular beam meant that a higher energy density was needed to clear material up to the edges of the beam. This is

because the total energy per unit area when a circular mask is moved over the workpiece surface varies perpendicularly to the axis of motion and an elliptical profile would result from the effects of mask dragging, as described in Chapter 2.4.1.

The optimum settings, used to machine the laser mask, resulted in a total machining time of 10 hours and 12 minutes. During this time the workpiece moved a total of 18 metres with an accuracy of ±0.1 μm, the laser fired approximately 3.6 million times and the thickness of the laminate layer that formed the mask aperture eroded 13 μm.

Figure 4.3 shows a section of the x10 laser mask produced by serially machining the electrode features using the 38 μm diameter beam. It can be seen that the definition is very good and that the separate areas of the electrodes align correctly. The machined areas, which allow UV light to pass with minimal attenuation, create the inter-electrode gaps and are lighter coloured than the unmachined areas which will block the UV radiation from the laser.

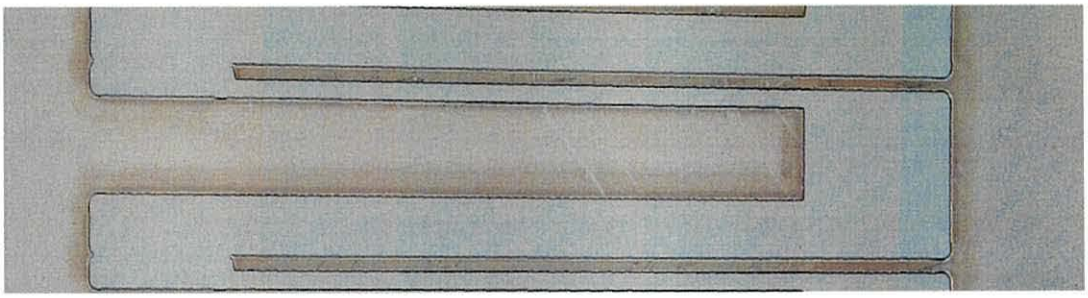

Figure 4.3 *Optical micrograph showing a section of the cACEOP electrode. The image is constructed from a collage of images of smaller sections of the x10 laser mask. This was machined serially using a 38 μm diameter beam at the workpiece. The lighter coloured areas are the machined regions, where the 1.5 μm S1818 layer has been removed. The surrounding areas are undamaged S1818, on top of which the debris generated by the laser ablation can be seen as the darker regions.*

An image of the x10 laser mask captured from the workpiece camera of the laser system is shown in Figure 4.4. The red dot visible on the left of the image is generated by the optical system for measuring the height of the workpiece surface (Chapter 3.1).

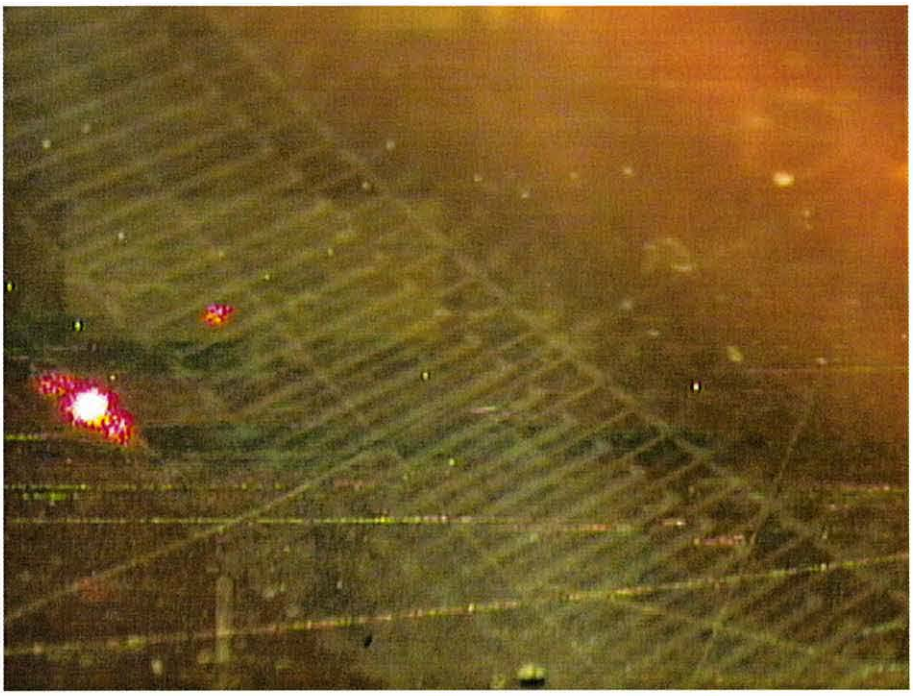

Figure 4.4 *Image capture from the workpiece camera of the laser system showing the areas that have been cleared of S1818 to form the desired mask pattern. The brass block on which the assembly is sitting is the workstation chuck and the hole that can be seen at the bottom of the picture is a vacuum retention hole, in this case securing the lower quartz plate. The red dot is an additional laser used to determine if the sample is in focus for machining.*

When machining of the x10 laser mask was complete, it was possible to project the correctly scaled design onto the workpiece. Mask scanning was implemented in which the mask and workpiece moved synchronously as described in Chapter 2.4.2. This allowed the entire mask pattern to be machined into the workpiece, despite the dimensions of the laser beam being smaller than the laser mask. Figure 4.5 shows the completed x10 laser mask, the machined electrode pattern can be seen as the faint circular structure on the plate.

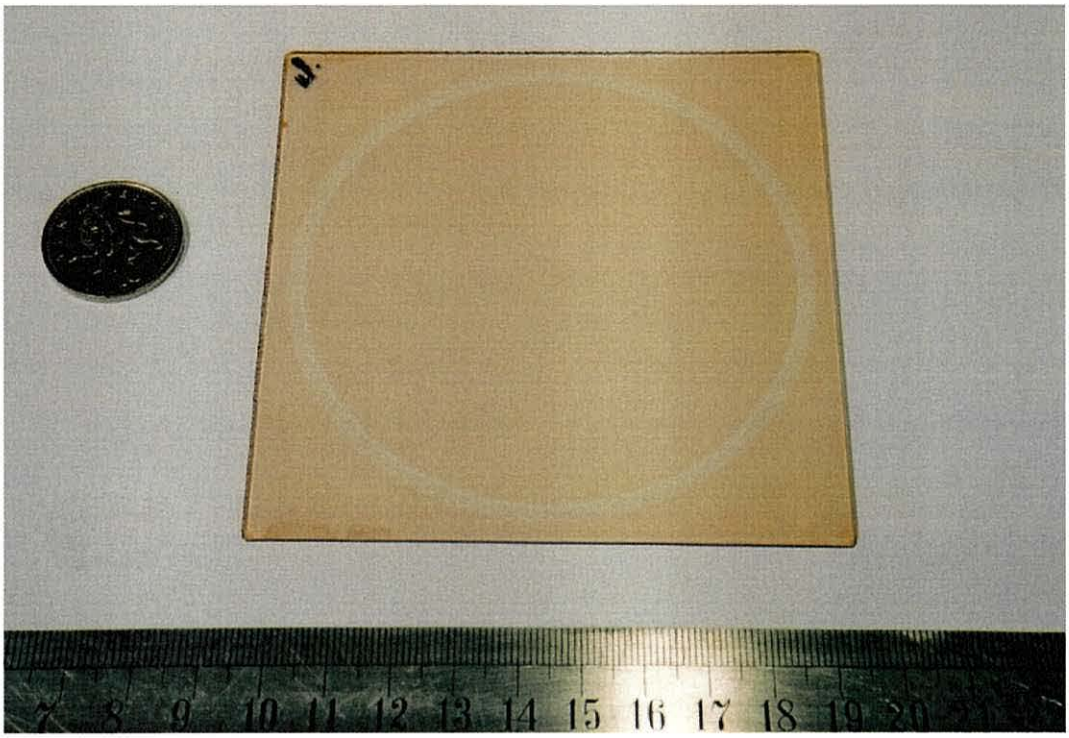

Figure 4.5 *Photograph of the complete x10 laser mask, serially machined into a spin-coated, 1.5μm thick S1818 layer on a quartz substrate. The ruler scale shown is in centimetres and the machined region can be seen as the fainter coloured circular ring.*

4.4 Fabrication of 1:1 contact masks

The final contact mask was produced by projecting the laser beam through the laser mask and a x10 demagnification lens onto the surface of the workpiece. By moving the mask stage and the workpiece stage synchronously under computer control, mask scanning was implemented to allow the entire laser mask, which is still considerably larger than the beam size, to be projected onto the workpiece. The laser program code used is listed in Appendix II.

In a series of exploratory experiments, two types of contact mask were found to give good results, one machined into the emulsion of an exposed photographic mask plate and the other in spin-coated S1818 layers. Examples of each type were coated with 50nm of gold and examined using a SEM. This allowed accurate measurement of the features machined in the mask as well as high magnification examination of the profiles and effects of machining each material to be observed. In order to determine the

machining resolution over the entire mask area, five measurements were taken per mask for each size of 'gap' and 'electrode'. From this, the accuracy and deviation of the machined mask features were obtained. These were compared with similar measurements on the laser machined masks using an optical microscope.

Evaporated metal films were also patterned to ascertain their suitability as either masks or devices. Using such films it should be possible to create higher resolution masks as the wall angles generated in thicker films, which will form overhangs when the mask is in use, will not be present. At approximately 70nm the films are sufficiently thin to avoid diffraction of the incident radiation. Hence, the mask pattern should be reproduced more accurately than would be possible with other materials.

4.4.1 Photographic mask plates

All of the photographic mask plates were prepared as described in Chapter 3.5.3.1 and machined at an energy density of 596mJ/cm^2 at the surface of the workpiece, corresponding to an energy density of ~7mJ/cm^2 at the mask plane. This allowed many photographic masks to be machined with minimal degradation of the x10 laser mask.

Figure 4.6 and Figure 4.7 both show micrographs of sections of a typical machined photographic mask plate. Figure 4.6 shows an angled view of the electrode track machined in the emulsion layer and Figure 4.7 shows an overhead view of a section of the machined areas, showing a comparison between the machined features and a similarly scaled design overlaid on the image. The measured mask feature sizes are presented in Table 4.1. In both images, the areas cleared of the coating correspond to areas of maximum mask transmission.

Mask pattern feature [machined photoplate]	Required feature size [μm]	Average measured size [μm]	Measured average error [μm]
Small electrode	4.5	4.405	0.095
Large electrode	15.6	15.594	0.006
Small interelectrode gap	4.2	4.284	0.084
Large interelectrode gap	25.7	25.612	0.087

Table 4.1 *Measured feature sizes of a machined exposed photographic plate*

The maximum average dimensional error was found to be 0.095 μm, or 2.2% of the minimum feature size confirming the high accuracy to which the features have been machined. The slight discrepancy between the measured feature sizes and the intended design dimensions can be attributed to several factors, including the actual projection lens demagnification factor and the laser energy used. The actual demagnification factor of the projection lens, which varies slightly whenever the lens is changed due to the minute positional errors incurred, was found experimentally to be x10.029 (±0.001).

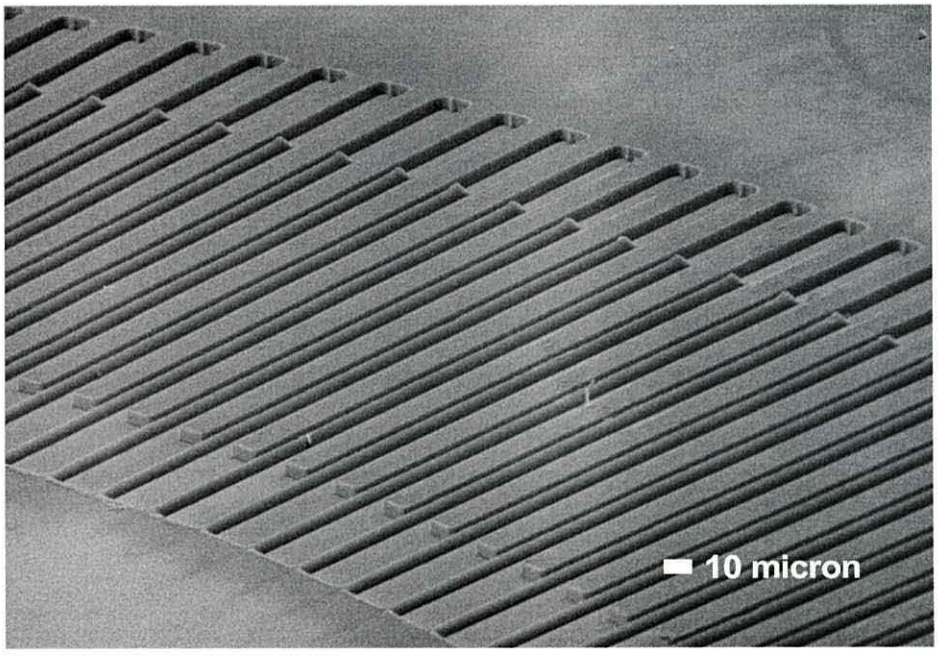

Figure 4.6 *Scanning electron micrograph of an angled view of a section of the photoplate*

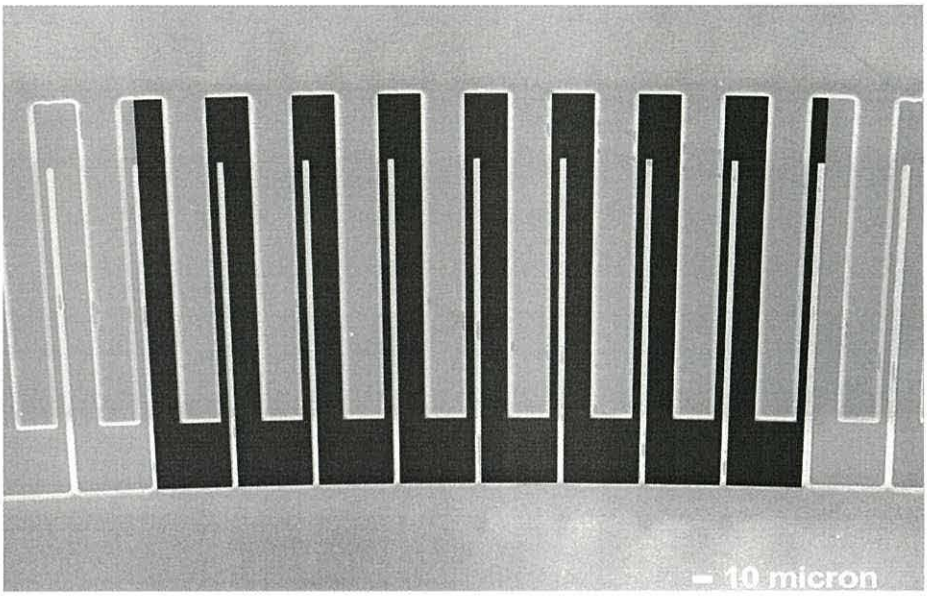

Figure 4.7 *Scanning electron micrograph showing a detail from the machined regions, which allows accurate measurement of the machined features on the mask. From this it can be seen that there is a very good replication of the required mask feature sizes, as a section of the design pattern, scaled similarly (dark grey shaded region), matches the machined areas well.*

Figure 4.8 shows a view of the end of a 4.5 μm electrode feature defined in the mask. Clearly visible are (a) the wall angle effect arising from the focusing of the beam (Chapter 2.5.3), (b) surface irregularities from non-uniformities in machining and (c) the ablation debris (Chapter 3.6.2) visible on the unmachined emulsion surface to the right of the image. Obviously all such features could be problematical in contact printing. In particular the presence of the wall angle means that the width of the masking region in contact with the photosensitive later will be smaller than designed (upper surface is in contact with the photosensitive layer). The overhang resulting from the wall angle can potentially lead to diffraction effects.

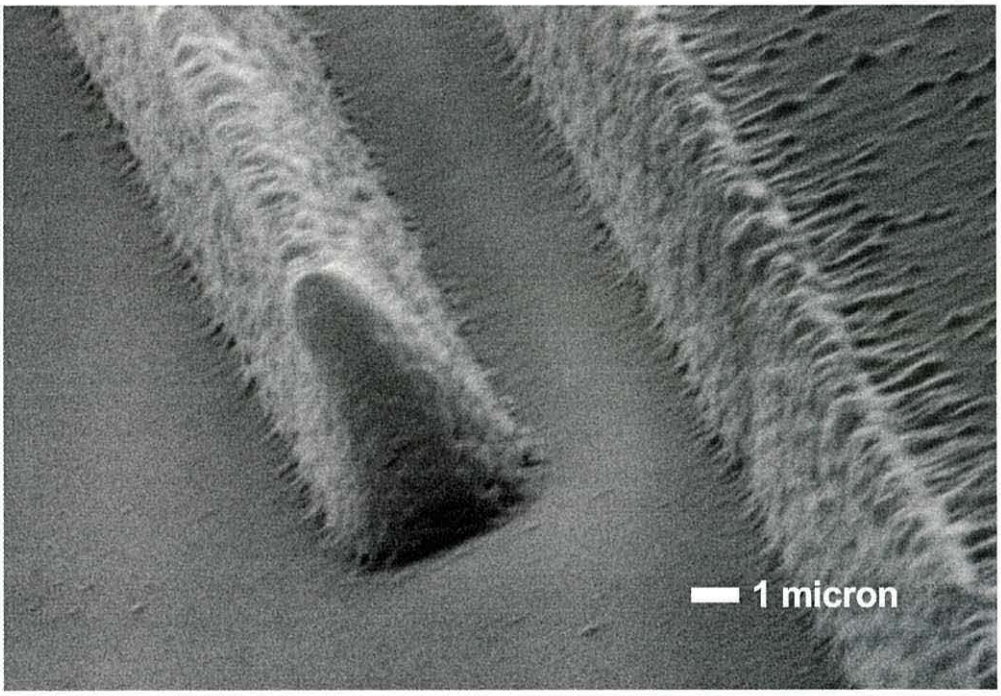

Figure 4.8 *Scanning electron micrograph view of the end of the unmachined emulsion layer that defines the smaller electrode region. The sloping walls, due to the focused beam profile, can be seen, as well as the machining properties present. The steepness of the wall angle could be improved by using a higher energy to machine the mask, but this would cause mask degradation and eventually lead to unfavourable machining conditions. This also demonstrates that smaller features would lead to a lower height of the emulsion layer.*

Optical micrographs of the machined photographic mask plates are shown in Figure 4.9 and Figure 4.10. In both cases the mask is backlit and shows that the design pattern has been produced in the photographic emulsion using the laser workstation. A picture of an entire laser machined photographic plate is shown in Figure 4.11.

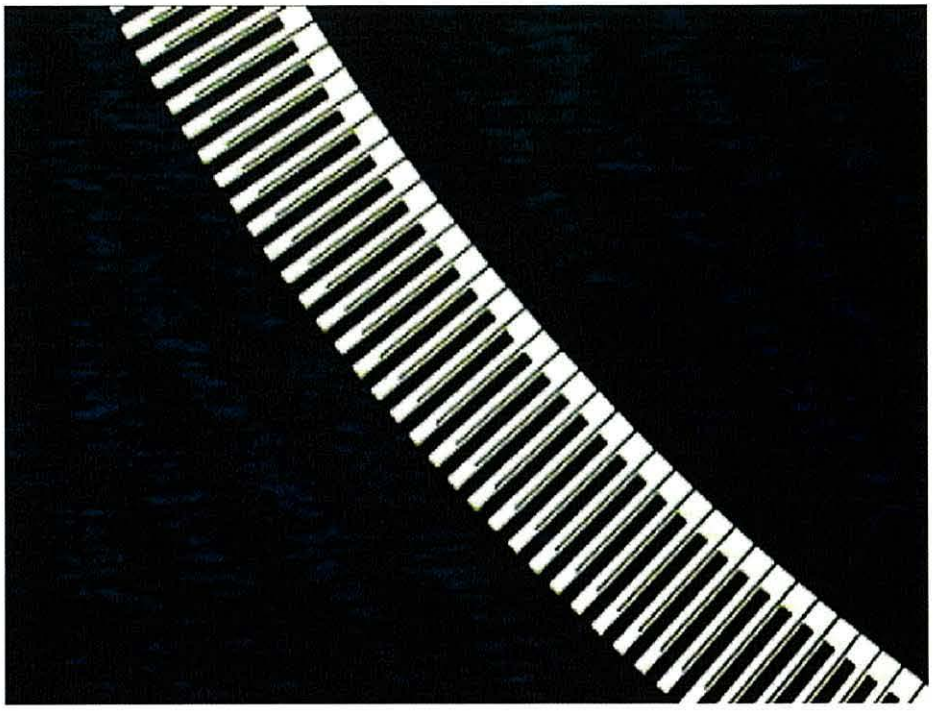

Figure 4.9 *Low magnification optical micrograph view of an exposed photographical plate that has been laser machined. The photographic plate is backlit, so the cleared regions of the mask appear lighter coloured compared to the remaining emulsion.*

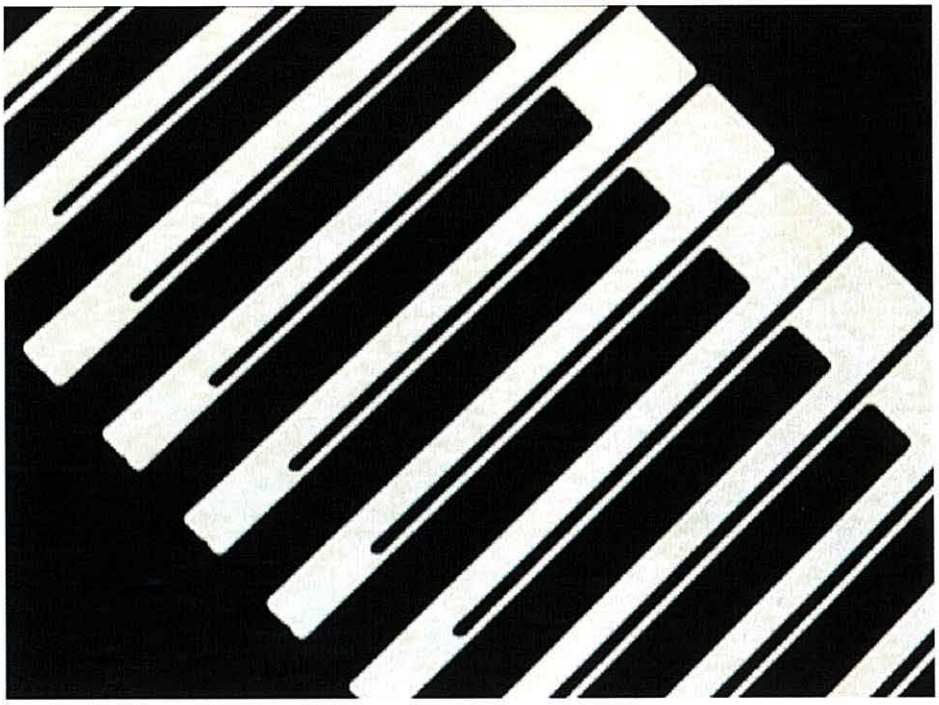

Figure 4.10 *Higher magnification view of a section of an exposed photographic plate that has been excimer laser machined. The mask is backlit, so the areas that have been cleared by the laser machining appear as light coloured regions. The dark regions correspond to areas where the photographic emulsion is intact, hence blocking the illuminating source. This indicates that the machined photographic plate could be used as a binary photomask.*

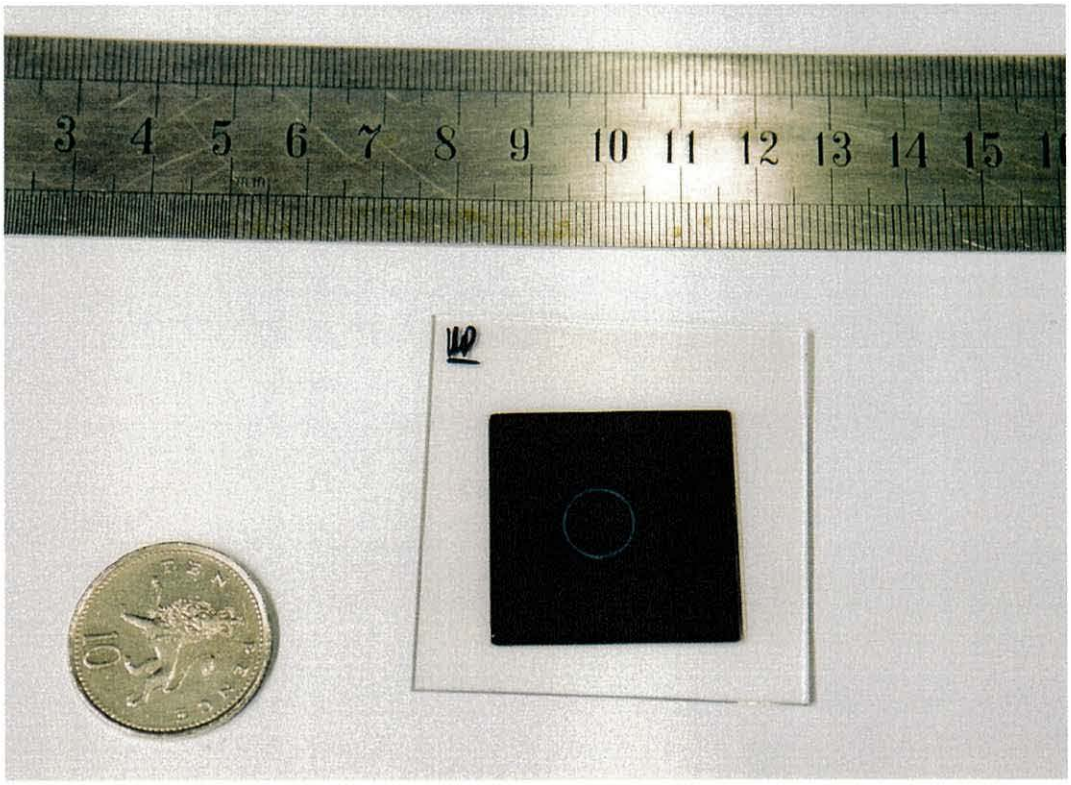

Figure 4.11 *Photograph of a laser machined 1:1 contact mask produced using a photographic plate. The cACEOP pump electrodes compose the ring shaped region in the middle of the mask plate. The region exposed by the photoreduction camera can be seen as the black region of the mask. The ruler scale is centimetres.*

Figure 4.12 shows a DIC (Diffraction Interference Contrast) optical micrograph of a section of the machined mask plate, in which the debris generated by the ablation process can be seen as the dark powder like substance covering the unmachined areas. However, there is very little present in the cleared regions so debris has no effect on the resolution of the final mask. In any event, it was found that most of the debris was removed by placing the machined photographic mask plate in an ultrasonic bath for 5 minutes.

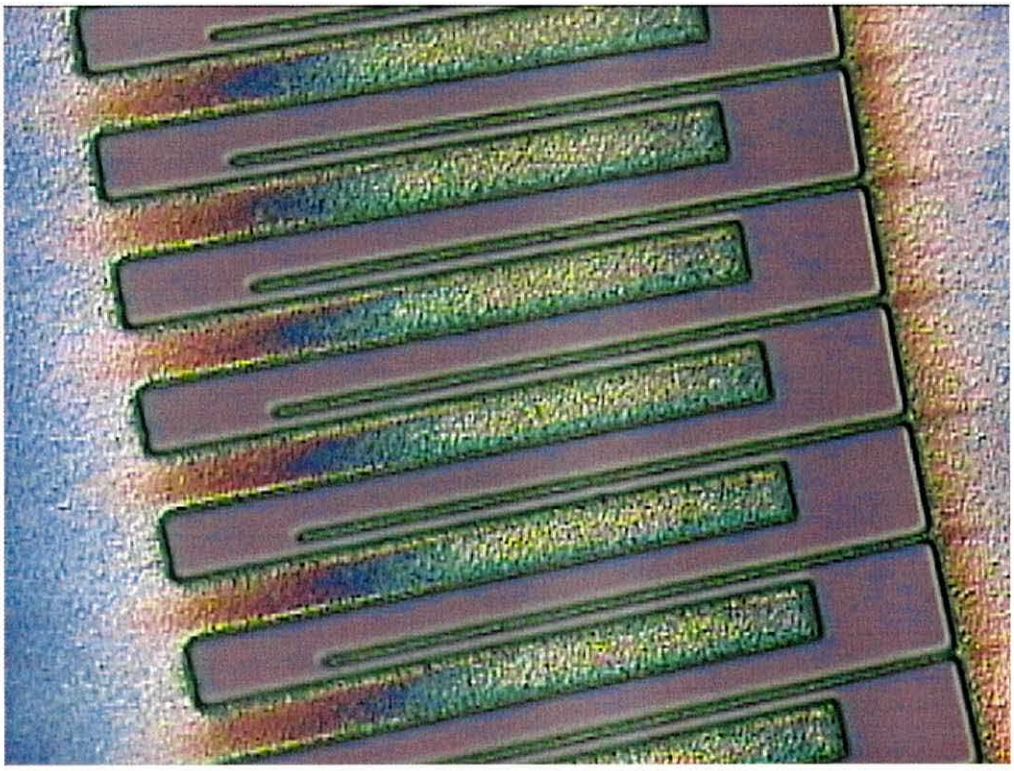

Figure 4.12 *DIC optical micrograph of a machined region on an exposed photographic mask plate. The debris recast by the ablation process can be seen as the powder like substance that covers the unmachined areas. This sample has not been ultrasonically cleaned, although in this case it is not really necessary, as the debris is not impairing the accuracy of the cleared regions of the mask.*

4.4.2 S1818 on glass

An alternative to machining exposed photographic mask plates was to use a thin polymer film, as it is known that these can easily be machined to a high resolution, such as the mask serially machined for use in the laser. Thin films of S1818 were applied to glass substrates, using a similar method as that used to coat the 100 mm x 100 mm plate used as the laser mask. These films were then machined in the laser system to produce the required mask. A section of a machined, unbaked, S1818 layer is shown in Figure 4.13.

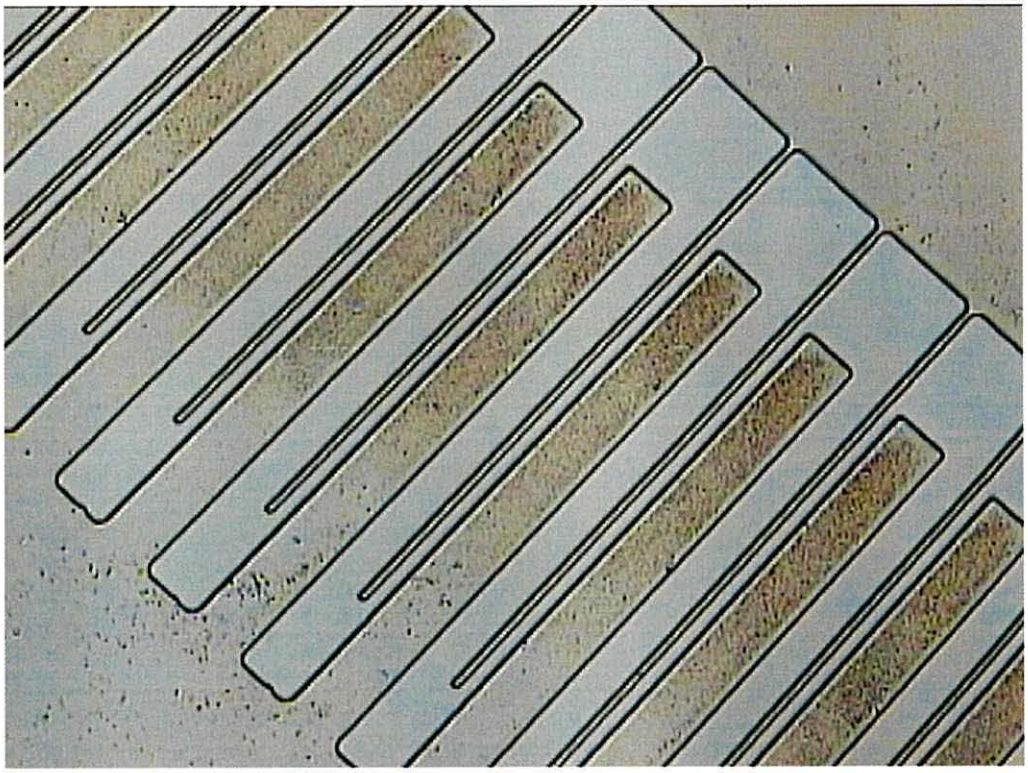

Figure 4.13 *A DIC optical micrograph of a glass substrate with a spin coated, unbaked, 1.5μm S1818 layer that has been laser machined. Debris from the laser machining process can be seen to be present on the unmachined regions, but there is no effect on the resolution of the mask structure.*

However, it was not possible to use unbaked masks to successfully pattern photoresists. The subsequent exposure caused the machined resist layer to become more transparent, hence losing its masking properties, at the wavelengths emitted by the mask aligner.

All of the S1818 coatings were machined using an energy density of 504mJ/cm^2 at the surface of the workpiece, which corresponded to an energy density of ~6mJ/cm^2 at the mask plane. This was below the damage threshold of the laser mask, so theoretically the mask could be used indefinitely at such energies. The number of shots per cm^2 was altered for the various masks, as there was a difference in polymer thickness. The number of shots per cm^2 used for the 1.5 μm coatings was 7, whereas 19 shots per cm^2 area were used for the 4 μm thick layers. Machining the polymer photoresist films was found to be much less time consuming than the photographic plates, as the material ablated more efficiently, so required less total energy.

If the S1818 photoresist is baked at an elevated temperature it becomes visibly darker, producing a dark brown film. Two sets of coatings were prepared, one spin-coated at 4000 RPM as before and the other spin-coated at 1000 RPM, producing a 1.5 μm and 4 μm thick films respectively. These were then baked at 200 °C for 25 minutes. Subsequently, the samples were left to cool, before being laser machined as before. The photograph in Figure 4.14 shows a machined 4 μm thick, baked S1818 layer, which forms a contact mask and Figure 4.15 shows a micrograph of a section of the same mask.

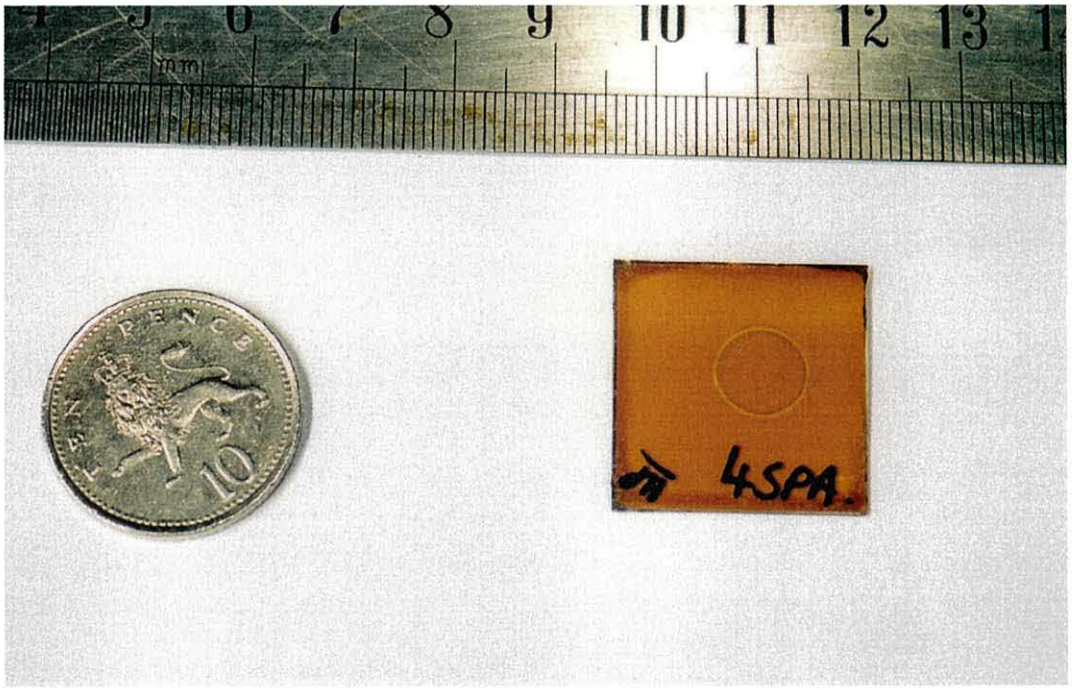

Figure 4.14 *Photograph of a laser machined 4 μm thick, baked S1818 layer on glass. The cACEOP pump electrodes are the ring shaped region in the middle of the structure.*

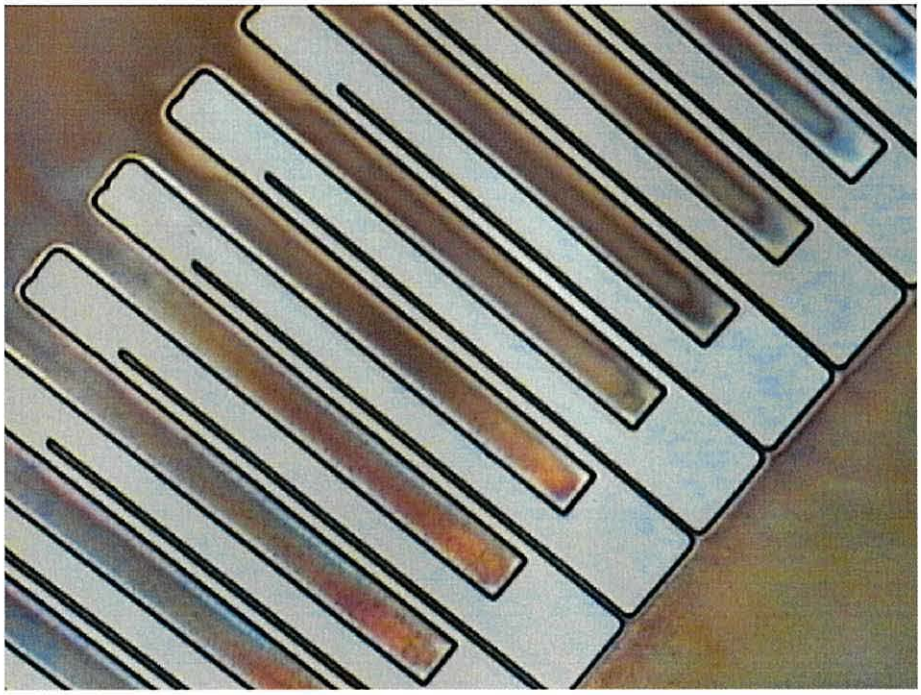

Figure 4.15 *Optical micrograph showing the results of laser machining a 4 μm thick S1818 layer, baked at 200 °C for 20 minutes. The resist is visibly darker than the unbaked resist and machining quality appears to be unaffected.*

The SEM micrograph in Figure 4.16 shows the result of machining a 4 μm thick S1818 film that has been baked. Table 4.2 and Table 4.3 show the recorded mask feature sizes of a 1.5 μm and 4 μm thick S1818 coating that has been laser machined to form a mask. These results indicate that machining thinner films allow higher resolution masks to be fabricated. This is most likely because the dimensions of the mask material in contact with the photoresist being exposed are nearer to the intended dimension, as there is less variation in feature size throughout the masking layer caused by wall angle effects.

Mask pattern feature [machined 1.5 μm S1818 layer]	**Required feature size [μm]**	**Average measured size [μm]**	**Measured average error [μm]**
Small electrode	4.5	4.546	0.046
Large electrode	15.6	15.594	0.006
Small interelectrode gap	4.2	4.244	0.044
Large interelectrode gap	25.7	25.693	0.008

Table 4.2 *Measured feature sizes of a machined 1.5 μm thick S1818 layer*

Mask pattern feature [machined 4 μm S1818 layer]	Required feature size [μm]	Average measured size [μm]	Measured average error [μm]
Small electrode	4.5	4.528	0.028
Large electrode	15.6	15.645	0.045
Small interelectrode gap	4.2	4.184	0.016
Large interelectrode gap	25.7	25.622	0.078

Table 4.3 *Measured feature sizes of a machined 4 μm thick S1818 layer*

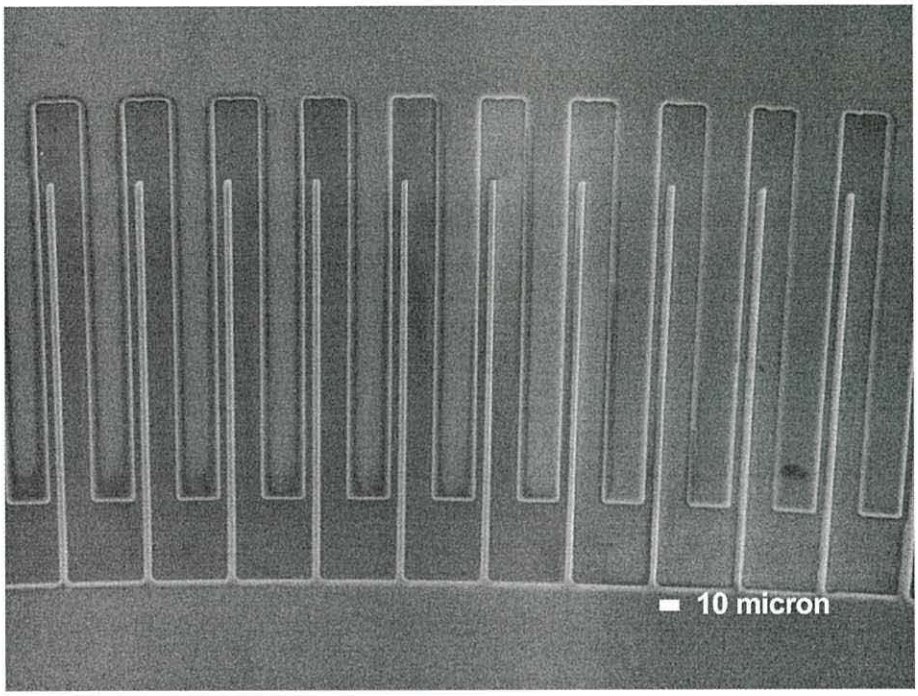

Figure 4.16 *Scanning electron micrograph showing detail typical of an excimer laser machined S1818 layer, 1 μm in thickness.*

4.4.3 Chrome on glass

Laser machining of thin evaporated metal films was also investigated, but was found to be inconsistent. Although one high quality mask was produced by machining evaporated chrome layers on glass, this success proved elusive to repeat. This is most likely because removal of such films is due mainly to thermal and shockwave effects (Chapter 2.2), which are not conducive to high-resolution machining [9, 10].

Figure 4.17 shows a section of the chrome coated glass contact mask produced by mask-scanning the x10 laser mask. The mask is shown illuminated from the back,

hence the chrome free areas appear light and areas covered with chrome appear dark. Although the mask pattern is visible, the large number of opaque areas between the electrode features render the mask unusable. It is possible that using a higher machining energy, i.e. one that exceeds the current laser mask erosion rate, may produce better results, but this would destroy the laser mask in a short time. The chrome coating shown was machined using an energy density of 870mJ/cm^2 at the surface of the workpiece.

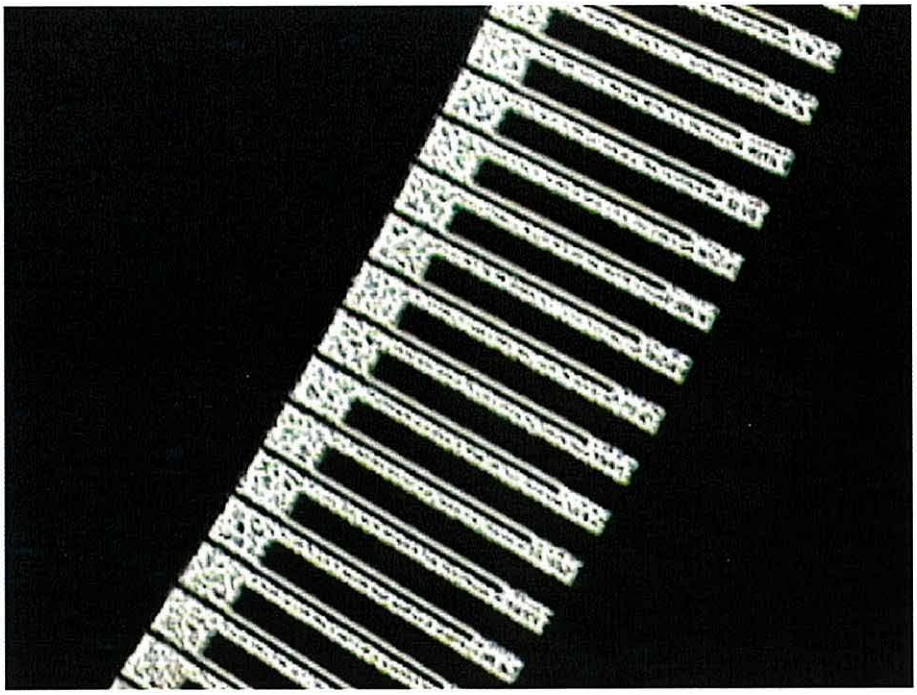

Figure 4.17 *Backlit optical micrograph of a machined chrome layer on a glass substrate. The machining quality of this film is not suitable to be used as a contact mask to create the required electrode design.*

4.4.4 Measurement of mask feature size

The measured mask dimensions and the error present when exposed photographic plates are machined were given in Table 4.1. Table 4.2 gave the results of machining a spin coated, 1.5 μm thick baked S1818 layer on glass, while Table 4.3 gave the corresponding results for a 4 μm thick baked S1818 layer on glass. These data present, for each mask type, the averages of measurements on fifteen regions on each mask using a SEM. The error quoted is the difference between the average distances and the design dimensions.

The results obtained show that when machining an exposed photographic mask plate, there is less than 95 nm error between the measured mask feature sizes and the design feature sizes, despite machining though a 6 μm thick photographic emulsion. The average measured mask dimension of a machined 4 μm thick, baked S1818 layer is even better giving an error less than 78 nm. The machined 1.5 μm thick layer shows the least average error at 46 nm. This is not unexpected owing to the thinner films suffering less from wall angle effects.

The sub-micron accuracy of the mask machining process is significantly higher than that possible with the current photographic based system (Chapter 3.5.1). The most time-intensive part of the process is producing the x10 laser mask, which if laser machined takes several hours to complete. This could be fabricated using photolithography (Chapter 3.5.2) if a lower resolution were required. However, producing high-resolution, 1:1 contact masks is very rapid, typically taking 15 minutes. This method of mask production is useful (contact masks degrade during use) and is not known to have been reported previously.

4.5 Fabrication of microelectrodes for use as cACEOP pump

In the previous section, the various methods of producing the contact masks required for fabricating gold-on-glass electrode structures have been described. Based on the results obtained a demonstrator device was fabricated using machined photographic mask plates.

Apart from the contact mask used, the fabrication of the microelectrodes followed the same procedures, i.e. the contact mask was used to pattern a 1.5μm spin-coated S1818 layer spin-coated on top of an evaporated gold / chrome layer on a glass substrate. The resist layer was then developed and the underlying metal layers chemically etched (Chapter 3.3).

4.5.1 Photographic mask plates

Figure 4.18 is an optical micrograph of the final electrode pattern illuminated using top-lighting. The etched (gold free) areas appear dark whereas the gold film is yellow-orange in colour. Figure 4.19, illuminated using a combination of lighting from above and below the sample, shows regions with gold present as yellow and the cleared areas, which transmit the illuminating source, as light grey. This electrode pattern was fabricated using a second laser machined photographic plate to test the repeatability of the process.

Both images show that the mask features have been faithfully reproduced in the gold film, demonstrating the feasibility of using the machined photographic plate contact masks for this application. This was confirmed by comparing the etched electrode structures and the mask feature dimensions: no discernible differences in the measured feature dimensions were found.

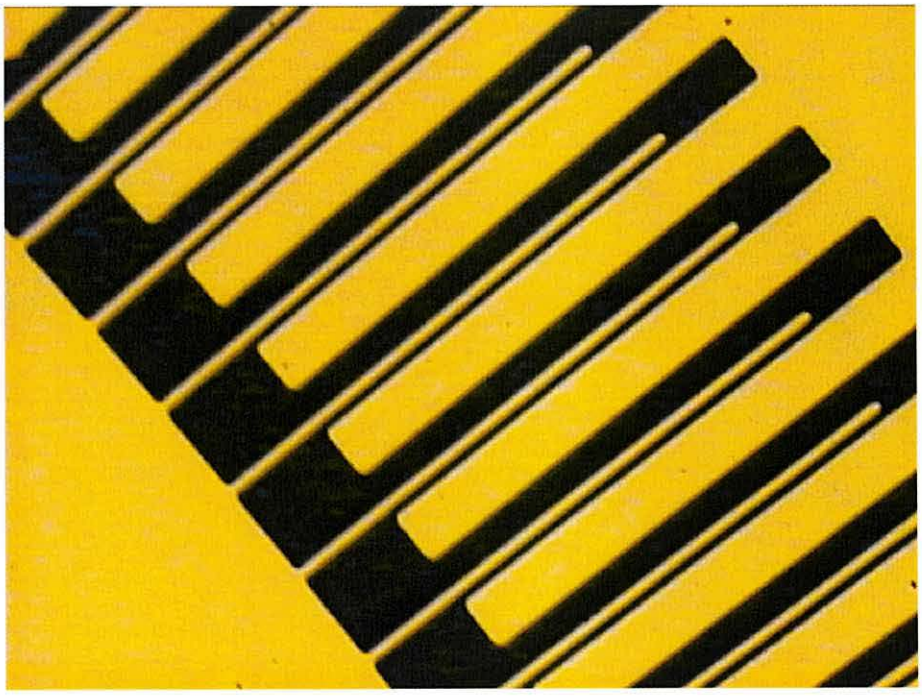

Figure 4.18 *Optical micrograph of a section of the final device. This was fabricated by using a laser machined photographic mask plate to pattern a S1818 layer in a photolithographic process. This allowed selective etching of the underlying metal film. After the etch process, the remaining S1818 layer was removed with an acetone rinse.*

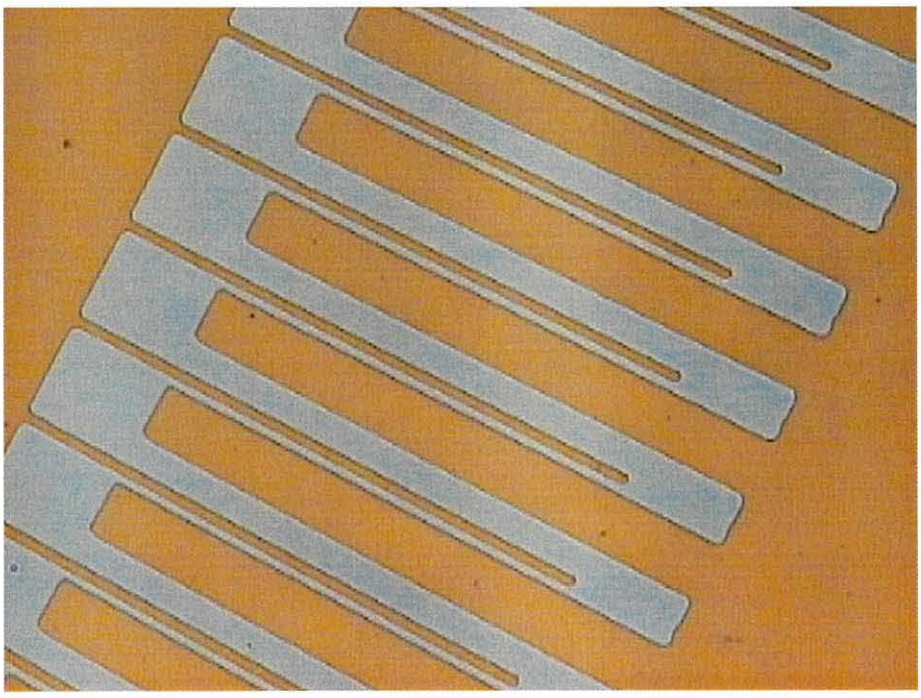

Figure 4.19 *Optical micrograph of a section of the final device, produced using a different machined mask. The cleared regions of the gold layer show as light grey, as the backlighting can pass through the sample and the gold regions appear as yellow areas.*

4.5.2 S1818 on glass

The initial investigations to photolithographically pattern an unexposed S1818 layer, using laser machined S1818 contact masks, did not produce viable results. It was observed that during the exposure stage, the laser machined S1818 masking layer changed from a light yellow colour to transparent. This indicated that subsequent exposure of the machined layer to the UV aligner source caused the absorption of the S1818 layer to fall, making differential exposure impossible. Figure 4.20 shows the results of etching thin metal films coated in S1818, after the S1818 layer has been exposed (using a laser machined S1818 on glass contact mask) and developed.

Although the intended pattern is visible, the metal electrodes are too thin to be usable. Further etching was found to completely remove the remaining metal regions.

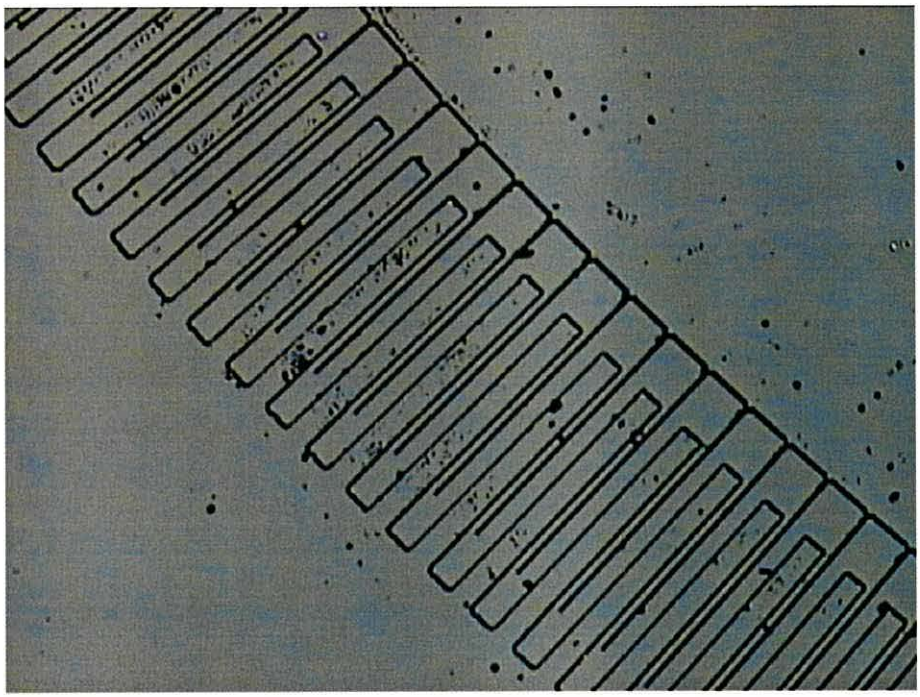

Figure 4.20 *Optical micrograph showing the result of using a laser machined S1818 coating that has not been baked at an elevated temperature. It can be seen that the result is considerably inferior to the that obtained using machined photographic plates. The metal layer remaining on the glass substrate was barely noticeable, so too thin for use as an electrode structure for use in a micro-device.*

The pattern that can be seen is most likely due to the to laser ablation generated debris deposited around the machined areas of the S1818 contact mask attenuating the exposure source sufficiently and causing some patterning of the exposed resist on the metal films. These results indicate that the longevity of non-baked S1818 layers, when used as contact masks, is insufficient as the S1818 layer becomes bleached by subsequent UV exposure in the mask aligner. The film is then unable to attenuate the incident UV source significantly. It is interesting to note that bleaching does not occur when S1818 is exposed to shorter wavelengths, such as those used in the laser.

When the spin-coated substrates were baked for 200°C for 20 minutes, they became much darker in colour and were no longer as sensitive to incident radiation or chemicals.

The results of using the baked 1.5 μm and 4 μm thick films as photolithographic masks are shown in Figure 4.21 and Figure 4.22. These results show that such masks can be used successfully to selectively pattern a photosensitive layer, thereby allowing the

subsequent patterning of a metal layer to fabricate electrodes. No observable deterioration of the resist coating was noticed after exposure.

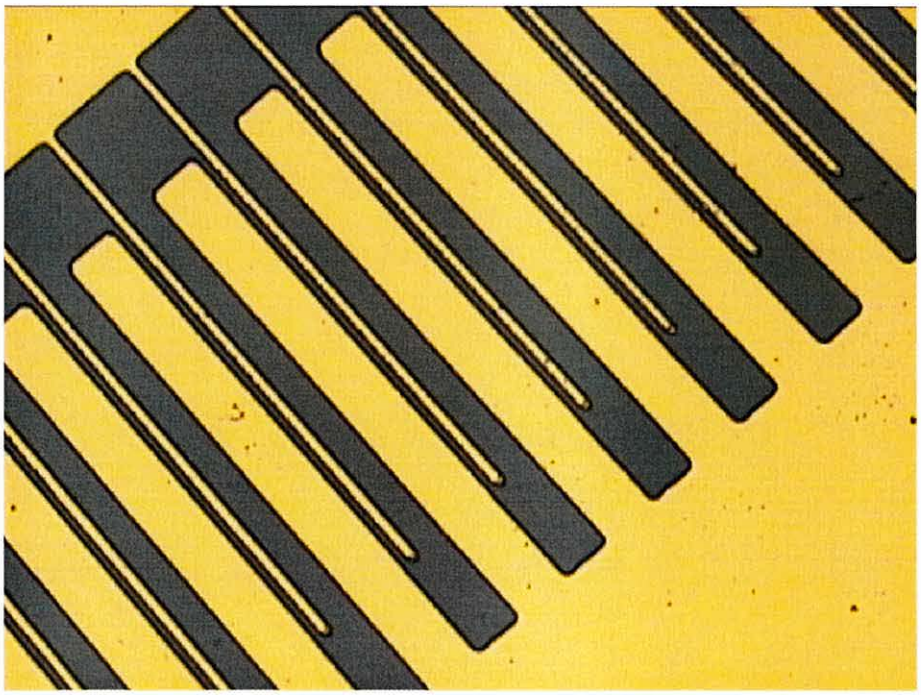

Figure 4.21 *Final electrode structure produced when a baked, 1.5 μm S1818 resist coating was used as a contact-mode exposure mask.*

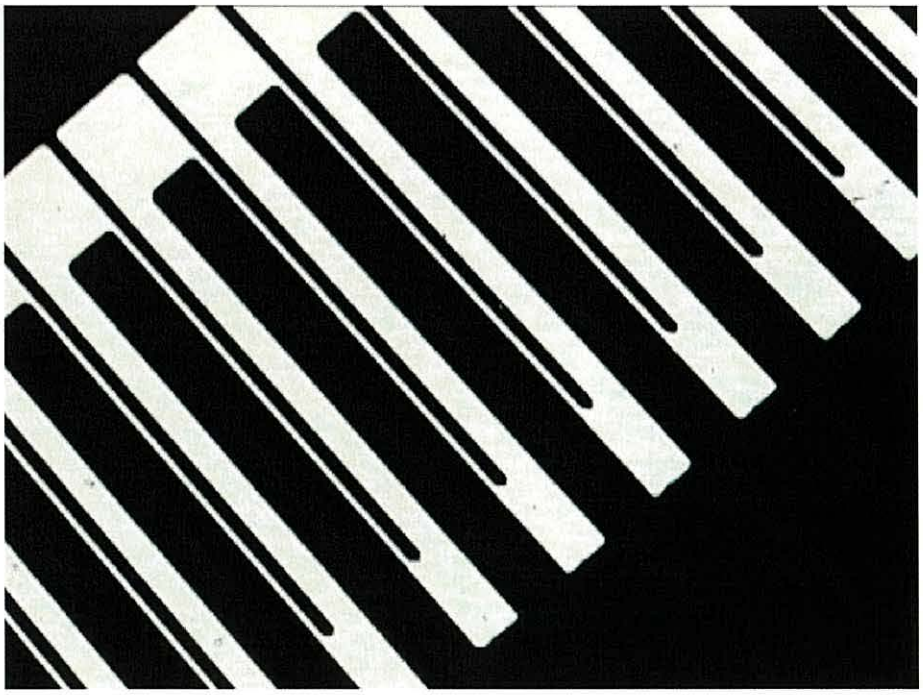

Figure 4.22 *Final electrode structure produced when a baked, 4 μm S1818 resist coating was used as a contact-mode exposure mask.*

4.5.3 Chrome on glass

The one machined metal mask of reasonable quality was also tested. Despite the flaws in the mask, the resulting electrode patterns (Figure 4.23) were reasonable. This suggests that if metal masks can be produced repeatably and with fewer flaws, high-resolution masks can be made without the problems associated with wall angle effects when thicker films are machined.

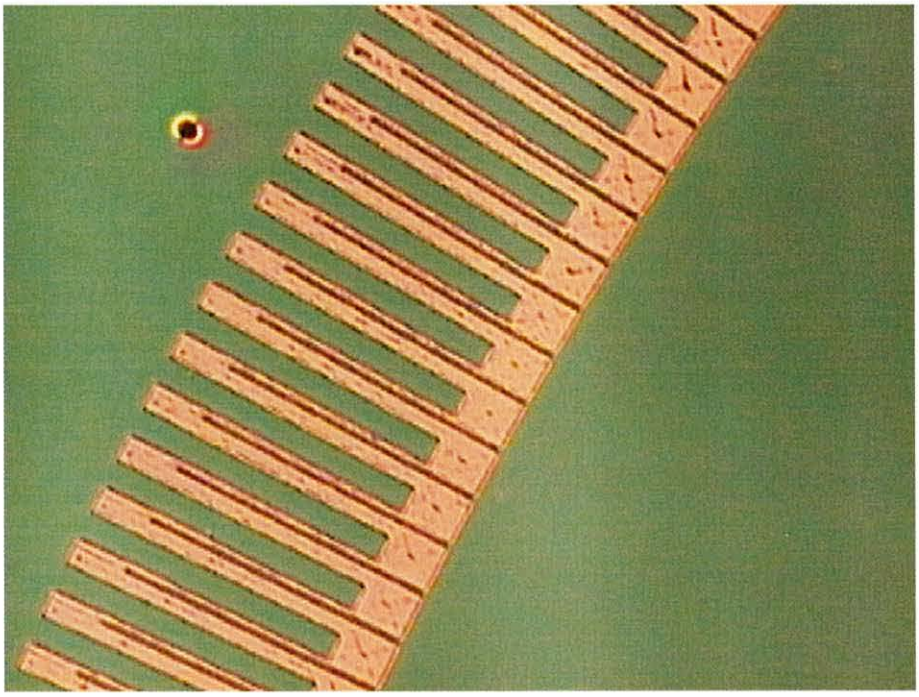

Figure 4.23 *Optical micrograph of a section of the device produced using one of the better quality laser machined chrome layers on a glass substrate. The image was recorded using DIC microscopy. Areas where gold remains have a green hue whereas cleared areas have an orange appearance. There is very good correlation between the mask and the structure produced.*

4.6 Direct machining of resist coatings

An alternative approach to machining 1:1 contact masks for use in subsequent processing, is to coat the metallised substrate with photoresist and then use laser machining to selectively remove the photoresist coating. This removes the need for a lithography stage and relevant development stage, as the resist coating is laser machined directly. The electrode structure can then be formed by chemically etching the exposed

metal regions. It was found that by using suitable machining conditions, a S1818 coating could be removed with minimal damage to the underlying metal film. Figure 4.24 shows an optical micrograph of such a device, where a 1.5 μm S1818 coating has been selectively removed to expose the evaporated gold film underneath. The energy used to achieve this was 504mJ/cm^2 and a total of 7 shots per cm^2.

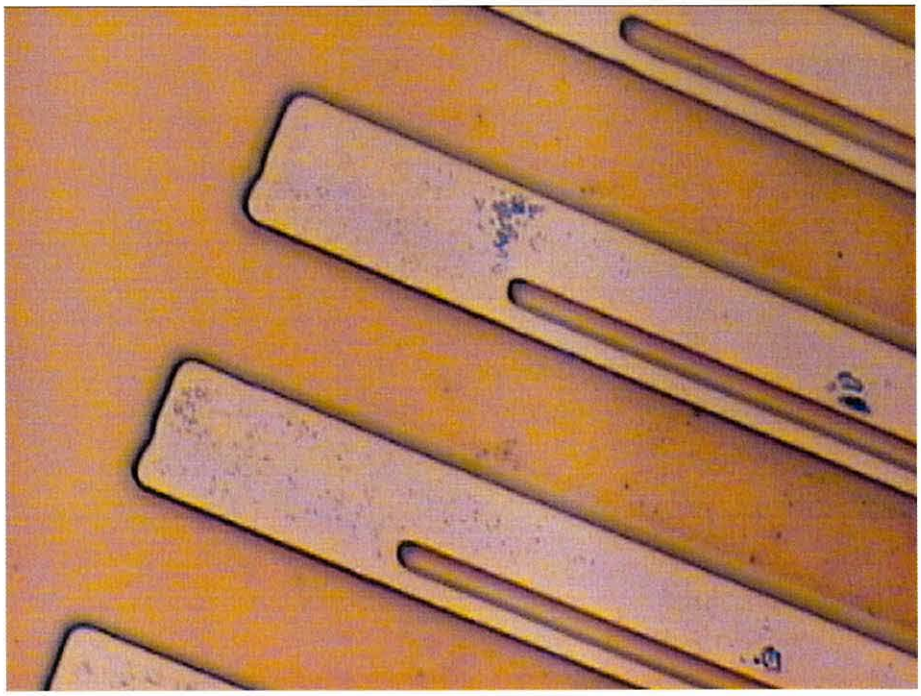

Figure 4.24 *Optical micrograph showing a glass substrate with an evaporated gold film, covered with a 1.5 μm thick S1818 layer. The S1818 has been laser machined to remove selected regions, leaving the underlying metal film intact. The dark speckled areas in the cleared regions are due to slight damage to the underlying gold film, although this did not appear to affect the device geometries during the chemical etch stage.*

A standard wet etching process was then used to produce the electrode structure in Figure 4.25. This shows that the mask features have been reproduced and the areas of gold damaged by laser removal of the resist layer have been successfully cleared in the chemical etching process. However, the process was very dependent on the uniformity of the resist layer, which was found to be inadequate, thus leading to damage of the protected metal areas. This approach can also be used to produce patterned metal masks if a suitable chrome layer were used instead of gold.

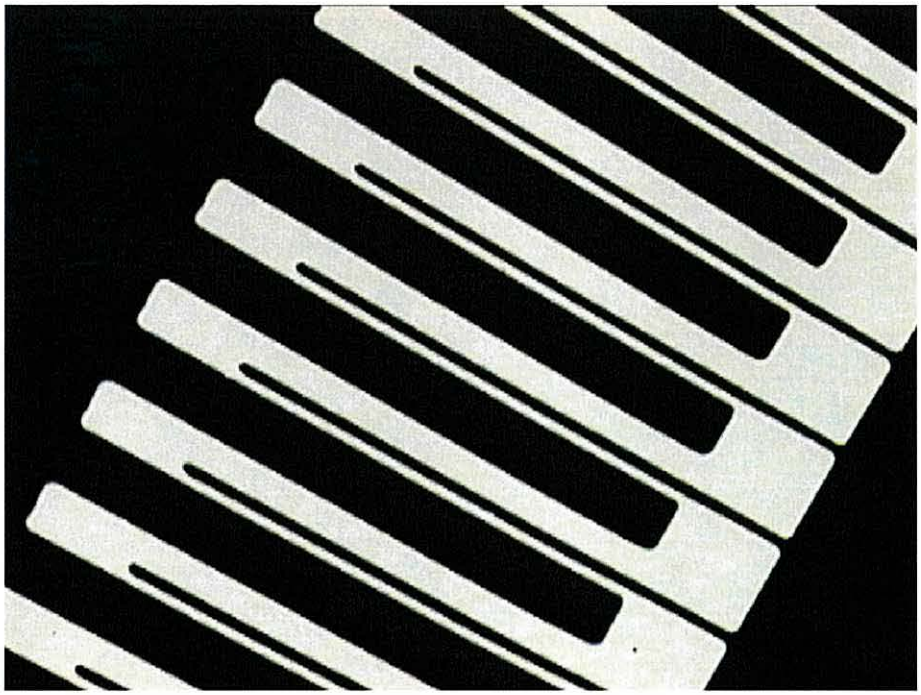

Figure 4.25 *Result of using a machined photoresist layer to allow selective etching of the underlying metal film. The light coloured regions are areas cleared of the metal film.*

4.7 Direct machining of devices

Direct laser machining of a device was also investigated. A glass substrate was coated with a chrome seed layer and then a 70 nm gold layer as before. It was then placed in the laser micromachining system and machined using a mask-scanning technique. The results obtained were also quite variable, similar to machining chrome layers. Figure 4.26 shows a section of a directly machined electrode track.

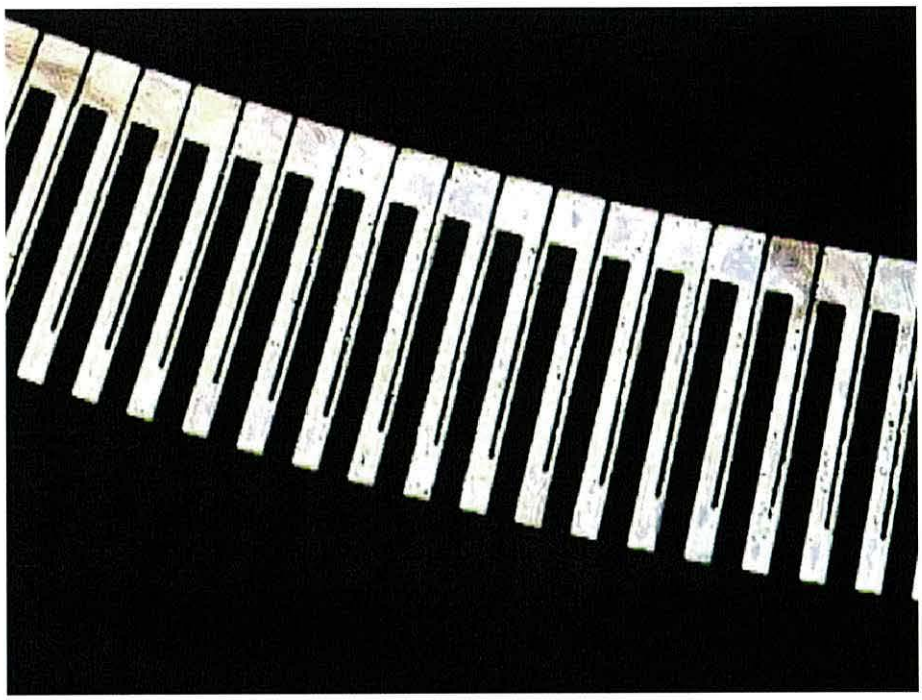

Figure 4.26 *Backlit optical micrograph showing the result of directly machining a gold coating on glass. Although the intended pattern is present, there are still regions of material that have not been completely removed which form electrical connections between the electrodes, making the device unusable.*

A 1.5 μm thick S1818 layer was spin-coated on top of the evaporated metal films to try to improve the quality of machining. The S1818 layer was used due to its good machining characteristics and was intended to improve localised heat dissipation from the metal films, so reducing thermal degradation of areas surrounding machined regions and also reduce the shockwaves generated during ablation from lifting the metal film. Although this did appear to increase the edge quality of the machined areas, the areas exposed to the beam were not completely cleared of material. Subsequent chemical etching of the exposed metal regions proved to be unreliable as the resist covered material was etched as well, due to the resist lifting from the surface of the metal, most probably due to the shockwaves generated during the machining process.

4.8 Device encapsulation

Figure 4.27 shows a photograph of a completed electrode structure, etched into a chrome / gold coating on a glass substrate. This was produced using a conventional

photolithography process with a laser machined 1:1 photographic plate contact mask, followed by a wet etch process to pattern the gold film.

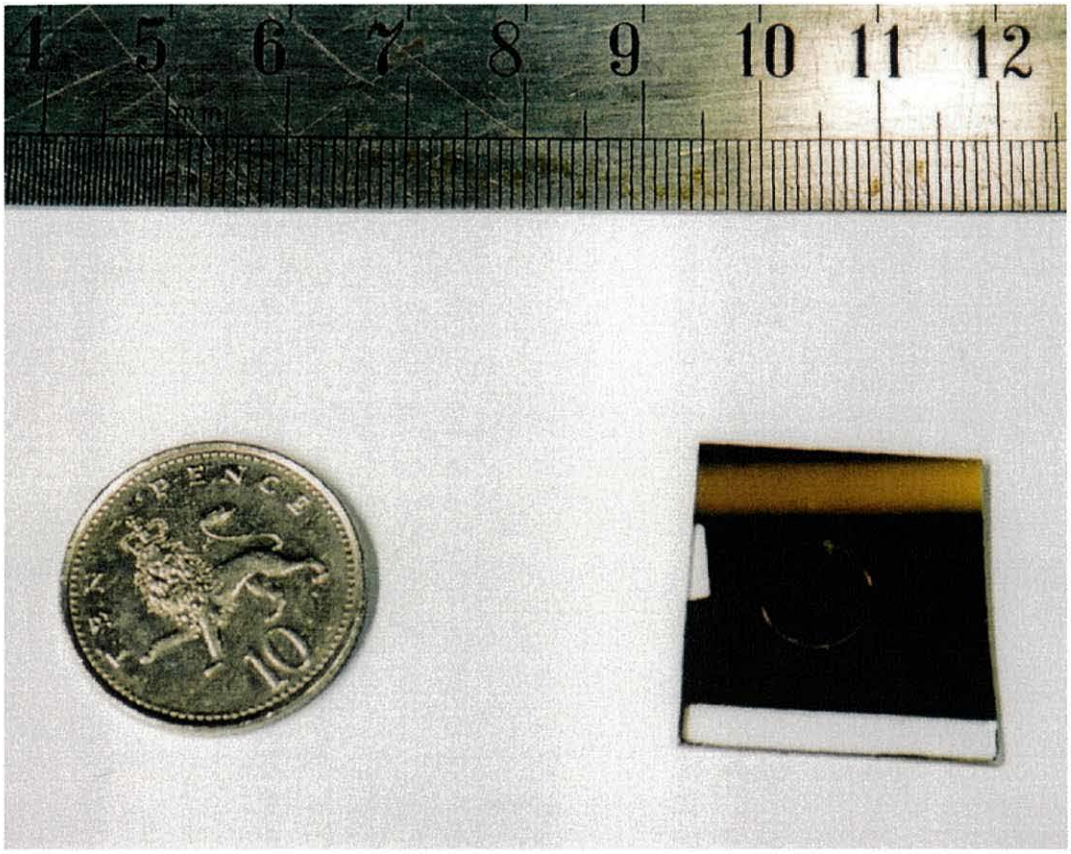

Figure 4.27 *Photograph of a completed electrode structure in a thin gold film, seen as the ring in the middle of the device. The ruler units are cm.*

An example of a completed, encapsulated device to allow testing of the suitability of cACEOP pumping is shown in Figure 4.28. The microfluidic channel was laser machined into a 30 μm thick dry-film laminate layer that was laminated onto a pre-drilled glass substrate. The holes drilled form the two electrical connection points and the fluidic connections to the device. The dry-film laminate was machined using laser ablation to create a well defined, accurately sized channel. After aligning the upper and lower sections of the device, they were bonded together by placing them in a hot-press at a temperature of 130°C at a pressure of 5 bar for thirty minutes. This caused the laminate to adhere to the lower glass substrate, forming a sealed channel. The electrical connections and fluidic inlet and outlet ports will be attached prior to testing.

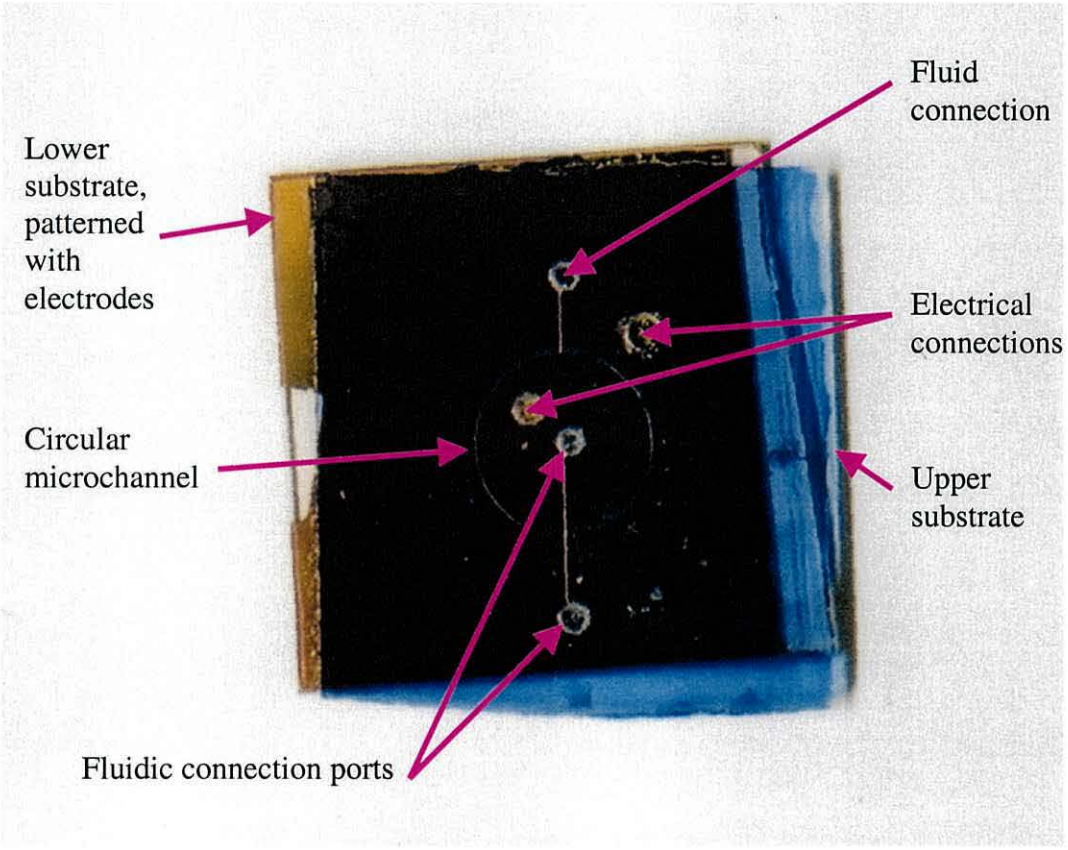

Figure 4.28 *Photograph of the completed, encapsulated device.*

4.9 Discussion

Photographic plates are known to be compatible with the current photolithographic process and so were investigated first. Laser machining of such plates produced acceptable results that allowed the final cACEOP device to be fabricated in a thin metal layer. However, the thickness of the photographic emulsion used, which is approximately 6 μm, may cause problems if higher resolutions were required, as the wall angle inherent in the machining process would produce regions that are significantly lower than the surrounding, unmachined emulsion layer. This could lead to diffraction problems and features not being resolved as parts of the mask are not in contact with the photoresist that is being exposed.

Machining thin polymer films to create usable masks also proved to be successful, provided that the resist layers were baked at an elevated temperature. This caused visual darkening of the resist layers and also prevented them from being bleached during subsequent exposure when used as masks in an aligner.

Measurement of the feature sizes of each type of mask revealed that the dimensional error present was not significant, 95 nm. It was also found that the accuracy improved if thinner mask layers were used. The minimum error in the feature decreased to 45 nm when a 1.5 μm thick spin coated S1818 layer was used.

The time taken to produce the x10 laser mask was approximately 11 hours, which equates to a production cost of ~£605 (see Table 4.4). Assuming an initial design cost of ~£100, this figure rises to ~£705. This process is costly because of the large amount of machine time required to pattern the 100 mm x 100 mm mask area using a 38 μm diameter beam. However, the laser mask produced can then be used repeatedly, with negligible degradation, to produce high-resolution 1:1 contact masks. This allows multiple 1:1 contact masks to be produced cheaply, at ~£20, in 15 minutes. Hence if a particular contact mask pattern is required for a mass production process, this method of mask production is well suited because although the initial laser mask production is expensive, producing 1:1 contact masks from it is cheap and fast.

Process	**Cost**
Purchase of laser system	£400,000
Equipment cost, per hour [1]	£50
Replacement gases and overheads [2]	£1,000
Mask materials [3]	£5
Cost of machining x10 laser mask [4]	£605.63
Cost per contact mask [5]	£20

Notes:
1 Assuming a depreciation over 5 years, 40 operational weeks per year with 8 hour days
2 Per year, based on average consumption rates, including housing overheads and operator time
3 Materials, chemicals and processing required for each mask
4 Assuming an 11 hour machining time
5 Assuming a 15 minute machining time

Table 4.4 *Laser machining costs, based on average consumption rates*

An alternative method of producing nanometer resolution masks is to use e-beam generated masks. Here a chrome coated quartz plate is coated with an electron sensitive resist, which is then selectively exposed using an electron beam. The electron beam serially writes the required pattern, effectively exposing the resist. When complete the resist is developed and is then used to allow selective etching of the chrome layer. The remaining resist is then removed, leaving a patterned chrome on quartz mask plate. Although very high resolutions are possible using this technique, the mask writing time is high (typically several hours) and specialised equipment is required. When masks are fabricated externally, a typical cost is approximately £1000 with an associated turn-around time of three weeks.

Direct machining of chrome masking layers was not particularly successful, as material in the machined areas was not completely removed. This is to be expected, as machining metal films is not ideally suited to excimer laser ablation, as detailed in Chapter 2. It is feasible that using a higher energy density to machine such layers would produce better results, but the laser mask used would be damaged. It is also known that the machining results are very dependent on operating conditions used [5, 6]. However, the structures produced using such masks indicated that there was a very high reproducibility of extremely small features on the mask. This also demonstrates that the machining resolution possible using the laser system is increased if the machined layer is thin, as the laser beam is focused to a point on the surface of the workpiece.

Machining a thin metal film on a glass substrate to produce the required electrode pattern directly was also unsuccessful. Although machining metal films to produce electrodes has been reported [4], the preferred films were sputtered. The results of that work could not be repeated, most probably due to the higher energies that were used, which in this case would cause rapid mask degredation. The features produced were also much larger (~20 μm) than those required in this work.

The high quality alignment and positioning of the mask features demonstrates the precision that the laser workstation is capable of, as well as the ability to accurately machine a CAD file over a relatively large area. It can also be seen that laser ablation is

suitable for producing sub-micron resolution masks for use in both photolithographic processes and in the laser system itself.

It should be noted that directly machined devices and devices produced using the machined mask plates are mirror images, c.f. Figure 4.19 and Figure 4.26 (the contact mask is placed over the final workpiece so that the machined coating is in contact with the photoresist during exposure). In the example fabricated here, the effect is expected to be that the fluid flow will be in opposite directions in the two device types.

4.9.1 Problems encountered fabricating devices

The biggest problem encountered during device fabrication arose from the build up of debris on the contact mask after it had been used about twenty to thirty times. The debris tended to accumulate in the machined grooves of the mask, thus reducing the quality of the mask and giving rise to electrical shorts in the final electrode structure. The debris was difficult to remove without damaging the mask. However, by laser machining the 1:1 contact masks using mask scanning (Chapter 2.4.2) the problem is easily overcome as the time to produce another mask is only about 15 minutes.

Laser machining a S1818 layer to allow subsequent chemical removal of the underlying material was very dependent on the energy settings used and was not as repeatable as other methods, although operational devices were produced without a photolithographic step being required.

4.10 Conclusions

The initial aim of this investigation was to utilise the laser machining system to produce a high-resolution contact mask that could subsequently be used in a photolithographic process. The work has demonstrated that excimer laser ablation is a suitable method for producing large area, high-resolution masks for use in conventional photolithography processes and in laser machining systems. By using a CNC excimer laser

micromachining workstation, it was possible to fabricate precise apertures and complex masks accurately over large areas. These masks have subsequently been used in a contact exposure photolithographic process to produce high quality electrodes. The masks produced have been found to match the original design requirements with a maximum measured error of 95nm over an area of 81mm^2. Other methods have also been investigated to produce both suitable masks and devices directly. The preferred method for this work was to use laser machined photographic plates.

A two-stage process was used, where a larger laser mask was fabricated and then projection reduced onto a workpiece to create the required pattern. Although the fabrication time of the large area high-resolution laser mask may take several hours, depending on the complexity of the mask, the production of the final patterned contact masks is far faster, typically taking 15 minutes. This is ideal if the masks are to be used in a contact exposure process in a mass production environment, as the masks come into contact with the samples during exposure, resulting in eventual mask degradation which was occasionally experienced during this work. Interchangeable demagnification projection lenses also allow a degree of flexibility in the size of the final structure. For example, by using a x4 demagnification projection lens, the maximum machineable area is approximately 25 mm as opposed to the 10 mm possible with the x10 projection lens. The advantage of using higher demagnifications is that a lower energy density is required at the mask plane to produce a set energy at the workpiece, so enhancing mask longevity.

Other advantages of this mask fabrication process include shorter turn-around times from mask design to useable contact mask and the minimum feature size attainable being determined by the resolution of the projection lens in use, which is known to be sub-micron for the x10 lens. If repeating, tessellating elements were present in a design that could be patterned from the same binary laser mask, the machining time could be reduced. This would allow a larger area to be patterned, instead of serially writing using a simple aperture.

The process of defining 1:1 contact masks described here is capable of higher resolutions than the current photographic system, as sub-micron feature dimensions

have been defined. It should also be noted that this method of mask production is not known to have been reported previously.

4.11 References

[1] "*Introduction to Modern Liquid Chromatography*", L. R. Snyder and J. J. Kirkland, *John Wiley and Sons, Inc.*, 1979, New York

[2] 'Development of a micro system for circular chromatography using wavelet transformation detection', J. C. T. Eijkel, C. Dalton, C. J. Hayden, J. A. Drysdale, Y. C. Kwok and A. Manz, *Micro Total Analysis Systems 2001*, 541-542

[3] 'Pumping liquids using asymmetric electrode arrays', A. Ajdari, *Physical Review E* **61, 1** (2000) R45-R48

[4] 'Pumping of water with ac electric fields applied to asymmetric pairs of microelectrodes', A. B. D. Brown, C. G. Smith and A. R. Rennie, *Physical Review E* **63** (2000)

[5] 'Ultraviolet laser ablation of polyimide films', R. Srinivasan, B. Braren and R. W. Dreyfus, *J. Appl. Phys.* **61** (1987) 372 - 376

[6] 'Ultraviolet laser ablation of organic polymers', R. Srinivasan and B. Braren, *Chem. Rev.* **89** (1989) 1303-1316

[7] 'Multishot ablation of polymer and metal films at 248nm', E. Hunger, H. Pietsch, S. Petzoldt and E. Matthias, *Applied Surface Science* **54** (1992) 227-331

[8] 'Polymer laser photochemistry, ablation, reconstruction and polymerisation', Hiroyasu Sato and Satoru Nishio *Journal of photochemistry and photobiology C* **2** (2001) 139-152

[9] 'KrF excimer laser ablation of thin Cr film on glass substrate', S. K. Lee and S. J. Na, *Appl. Phys. A* **68** (1999) 417-423

[10] 'Excimer laser ablation of thin gold films on a quartz crystal microbalance at various agron background pressures', X. Zhang, S. S. Chu, J. R. Ho, C. P. Grigoropoulos, *Appl. Phys. A* **64** (1997) 545-552

Chapter 5

On-chip optical detection

5.1 Introduction

The observation, measurement and analysis of materials held in microdevices are likely to be key requirements for the advancement of Lab-on-a-chip technology [1]. All three can be achieved using optical methods. Typically, the materials will be liquids (normally aqueous fluids) or suspensions of particles in liquids. As such they will be contained at some stage within micro-fluidic channels. It is here that the optical method can be applied by guiding light to and from the channel. Measuring the optical properties of the contents of a micro-channel allows several parameters of the analyte in the micro-device to be found, such as the concentration of particles present or the optical absorption of the medium, as well as detecting specific analytes [2-9].

Optical detection is particularly well suited to micro-devices, which commonly contain sensitive electrical systems, such as micro-sensors. No additional electric fields are used, hence electrical interference within the micro-device is avoided. A simple method of optical particle detection in micro-fluidic channels and used here, is to monitor the degree of absorption and scattering of a light beam passing through a micro-channel. Water, which is commonly used to suspend particle solutions, will not attenuate a light beam significantly, whereas any particles present will increase the absorption or scattering. This will also be true of any other changes in the channel contents.

Several methods of optical inspection can be utilised to analyse such properties. Manual detection of the presence of cells relies on a trained observer monitoring the flow of analyte through the micro-device using, for example, a microscope. Although it should be possible to replace manual observation with a computer based image recognition system, a microscope and associated image capture and processing hardware and software are still needed. An improvement would be the inclusion of self-contained, on-chip optical sensors, integrated into the device using existing fabrication methods. This would allow the automatic operation of such systems and a

reduction in equipment costs since the observation equipment would not be required. Such an approach is well suited to mass-production of low-cost devices that can detect and analyse biological cells and chemical reactions.

This approach has been reported already [4-6, 8], using silicon based devices, so that the inclusion of on-chip photodiode detectors can be accomplished relatively easily. This allowed light scatter measurements to be made, which are not possible in a planar device with transparent glass top and bottom surfaces, commonly used in Biofactory construction [10]. Using a pre-fabricated fibre optic to guide light into and out of the micro-channel has also been reported [2]. Here, individual particle detection was possible, although the fabrication stage involved in creating the devices requires manual insertion and careful alignment of the optical fibres, which is not an ideal situation.

Two methods of integrating optical detection systems into existing device fabrication stages have been investigated. The results of these initial investigations are presented here: a laser cut optical fibre based sensor and a laser machined, planar waveguide based device.

5.2 Theory of absorption measurement

The absorption of light by a solution is usually measured with the typical arrangement shown in Figure 5.1. Here, a beam of monochromatic light of intensity I_o passes a distance d through the analyte, having concentration C. This causes the intensity of the light beam to be attenuated to a lower value, I_t.

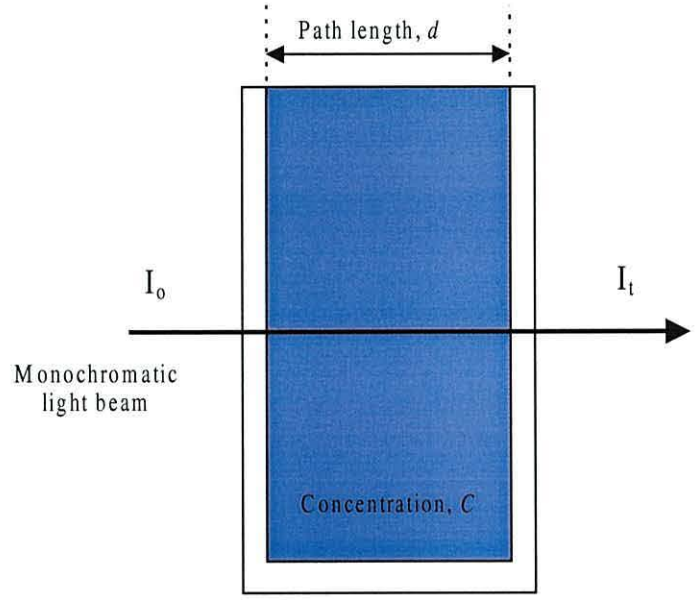

Figure 5.1 *Arrangement used to measure the absorption of a medium using a light beam*

The degree of attenuation is expressed by the Beer-Lambert Law

$$\frac{I_t}{I_o} = t = 10^{-\varepsilon C d} \tag{5.1}$$

where ε is a sample dependent constant known as the absorptivity. The transmittance, t, is often expressed as a percentage transmission across the sample, i.e. T = 100 t. The absorbance of a sample, A, is calculated from Equation 5.2 and is seen to be proportional to the analyte concentration, *C*, since

$$\mathrm{A} = \mathrm{Log}\left(\frac{1}{t}\right) = \varepsilon\ C\ d. \tag{5.2}$$

Measuring the absorption of a sample is useful, as it allows quantitative analysis to be undertaken as well as a comparison of different analytes. In the case of cells, however, light scattering will dominate over absorption to reduce the transmission across the analyte and a similar proportionality between concentration and absorbance can be expected to exist.

5.3 Optical fibre-based sensors

Suitable on-chip optical emitters and detectors have not yet been developed at Bangor. Therefore, a method of guiding light from an external emitter into a device, across a micro-channel within the device and then from the device to a sensor has been developed. Directing a suitably small light beam, required for optical measurements, to a sample in a micro-device can be accomplished using standard optical fibres. These are available in a range of materials and dimensions, allowing the optimum fibre type to be selected for the detection wavelengths and the micro-channel dimensions used. Reports have been published [2, 4, 9] describing the coupling of light into an analyte volume and also guiding the resulting light emissions to a sensor [2, 9]. Typically, the fibres are pre-cut and polished, before being manually positioned in the device at the appropriate point and bonded into position. The advantages of such a system are that the optical characteristics of the fibre are known and the optical losses from the fibre will be low.

Although this approach has allowed successful optical connections to micro-devices, there are several drawbacks. Manual alignment of each fibre in each device is required to small tolerances, because the axial alignment is critical so as to minimise the disturbance to the optical path thus reducing losses. This is a time intensive process, not well suited to mass production or repeatable manufacturing. Typically, the fibres are inserted into alignment trenches whose profile is not similar to that of the fibre [2, 4, 5, 11, 12]. This leads to discontinuities in the fluidic channel that are not ideal as interrupted flow profiles and dead-volumes may arise. The fibre cladding can be relatively thick [~10μm to ~100μm], so reducing the sensitivity of the device, as a significant portion of the channel height is occupied by the fibre cladding.

An alternative fabrication method, investigated in this work, is to embed a continuous length of fibre in resin then machine the resin and fibre in one process. This creates a fluidic channel that a light beam can be directed across and through which analytes can be passed. If the channel machined is small, the ends of the fibre will be well aligned, as the mechanical integrity of the fibre will maintain axial alignment during encapsulation. Excimer laser machining was used to create the channel, as it is an ideal method for rapid and accurate machining of an optical fibre. As the optical fibre used

[ESKA acrylic fibre, Mitsubishi] was made of polymethyl methacrylate (PMMA), the laser was operated at 193nm to allow efficient cutting of the fibre. Laser machining an optical fibre has the added advantage that the ends of the fibre self-polish [13, 14], so increasing optical transmission into the channel region. This allows precisely machined devices to be produced both repeatably and rapidly (~10 mins). As the fibre is completely embedded in resin prior to machining, the join between the fibre and the rest of the machined channel will be smooth. This removes the problems of dead space or discontinuities that arise when using alignment channels to position the fibres. In addition to allowing good fibre alignment the method provides good consistency from one device to another and is well suited to mass production.

5.3.1 Limitations of optical absorption detectors

The light emerging from a flat, polished fibre end will not propagate as a circular beam that is the same diameter as the fibre core. Instead, the emergent rays will expand, forming a cone of light. The maximum divergence of the light from the fibres optical axis is defined by the numerical aperture (NA) of the fibre, similar to that of a lens (Equation 2.2). As the detectors used in this work are effectively two opposing fibres, the detection volume will consist of two cones: light will be emitted into the channel in the form of a cone from one fibre and the detector fibre will receive any light within a similar, reversed cone. This is not ideal, as the device sensitivity will be lowered due to losses as well as scattering from particles and surfaces outside the intended detection volume coupling unwanted light into the detector fibre.

5.3.2 Optical fibre based device fabrication

Most Biofactory-type devices consist of a base layer, typically glass, with microelectrodes fabricated on the upper surface and the necessary fluidic ports drilled through [10]. The micro-fluidic system is then fabricated by removing selected regions from a thick polymer layer that has been bonded to the device lid, for example another glass substrate. Bonding the two halves together completes the device, so forming

enclosed micro-fluidic channels over the microelectrodes. External fluidic connections are made to the device using the pre-drilled fluid ports in the base layer and electrical connections are made to electrical connection pads, which are left exposed. By fabricating the optical sensor in the thick polymer layer, compatibility with the standard fabrication process is maintained.

A glass substrate was cleaned and a centre section of a length of optical fibre (250μm diamter, 230μm core), whose ends had already been polished, was placed over the glass substrate using a simple jig, as shown in Figure 5.2. This pulled the fibre straight and held it in position during subsequent stages. Precise alignment of the fibre was not critical, as the device would be accurately aligned in the laser system prior to the channel being machined. Spacers, consisting of short lengths of the optical fibre, were placed near the edge of the glass substrate (as shown in Figure 5.2) and were used to support a polycarbonate lid parallel to the surface of the glass substrate. UV-curing resin (Loctite 350, RS Components, UK) was then injected into the volume between the glass substrate and the polymer lid, completely surrounding the optical fibre. This formed a uniform thickness resin layer on the glass substrate, in which the optical fibre was embedded.

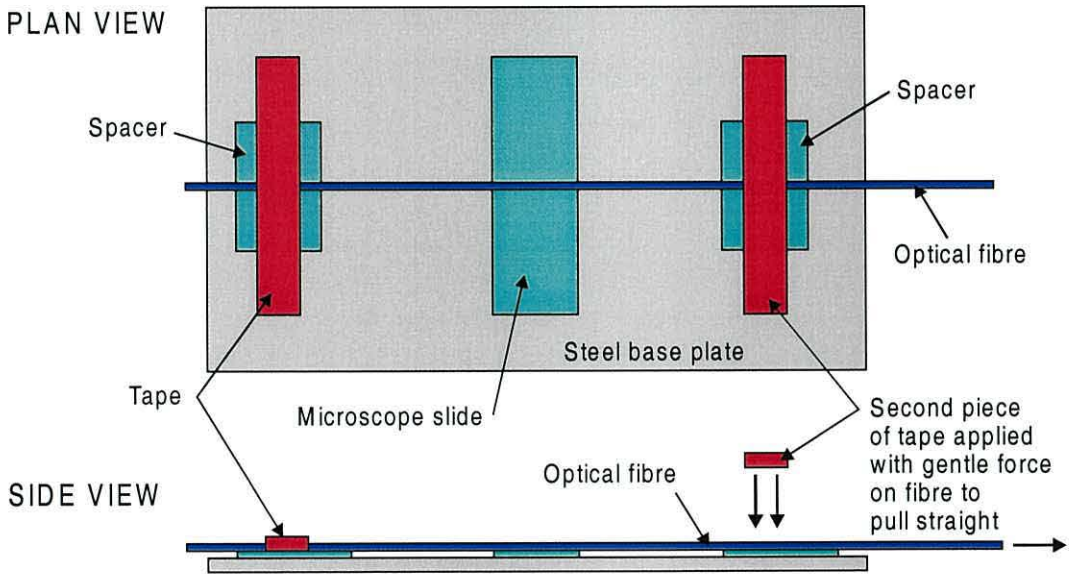

Figure 5.2 *Diagram of the jig used to align and hold the optical fibre during UV exposure*

The entire assembly was then placed in an UV-exposure cabinet for 15 minutes to polymerise the UV-resin. The device was then removed from the jig and placed in the

excimer laser system. After alignment, a simple channel system consisting of an inlet, channel and outlet was machined. Figure 5.3 gives a plan view of the fluidic system and a photograph of the machined device. A laser fluence of $2J/cm^2$ at the workpiece was used to machine the 250μm wide fluidic system through the cured UV-resin and fibre optic cable to the glass substrate.

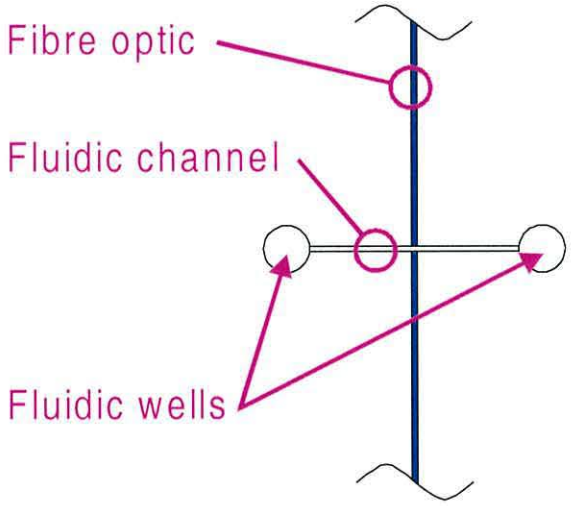

(a)

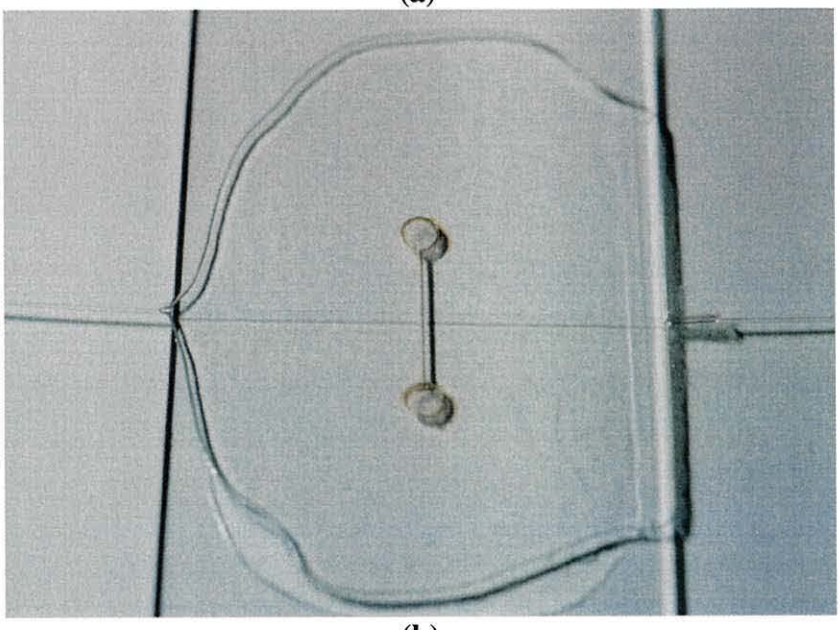

(b)

Figure 5.3 *Design of the fibre-based optical detector (a) and photograph of the machined structure (b).*

Figure 5.4 shows an image recorded from the laser systems workpiece camera where the fluidic channel has been machined in the resin and through the fibre. Here, the straight part of the fluidic system has been machined, prior to the machining of the fluidic inlet

and outlet wells shown in Figure 5.3. The continuity of the fluidic channel walls is shown in the SEM micrograph in Figure 5.5, where a section of a channel that passes through a fibre is shown.

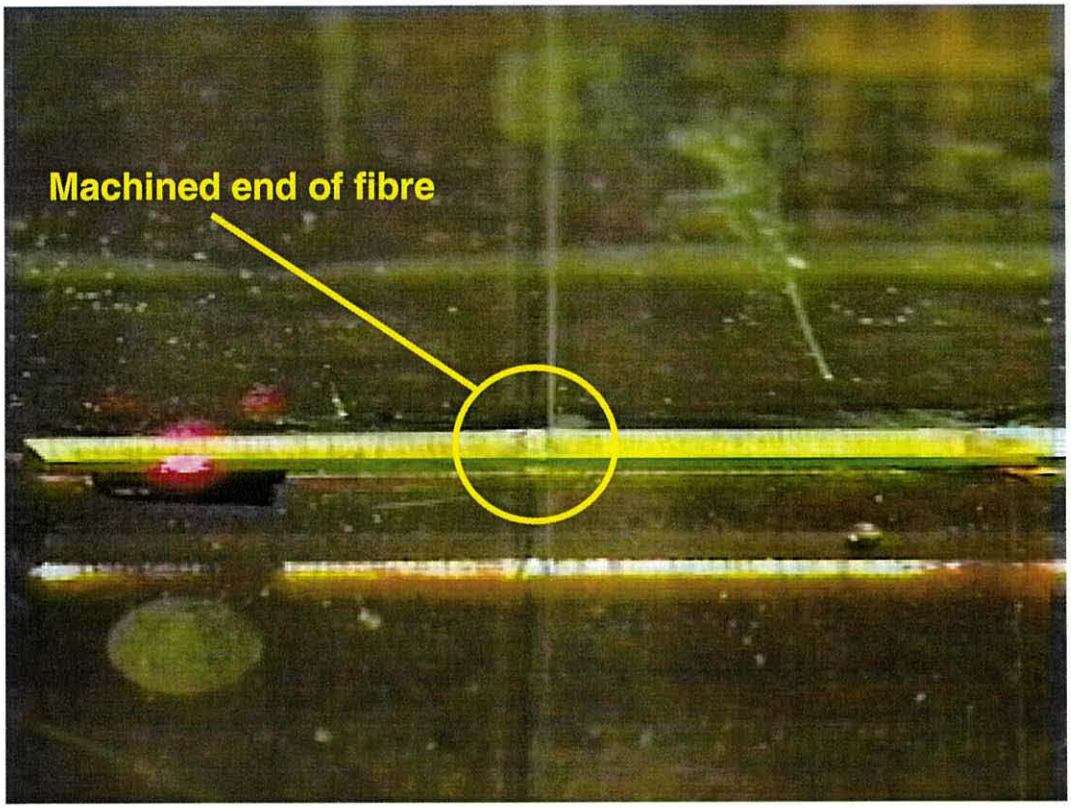

Figure 5.4 *Frame captured from the laser systems workpiece camera during machining showing the fluidic channel that has been machined through the resin and the embedded optical fibre. The end of the fibre can be seen as the round shape in the wall of the channel.*

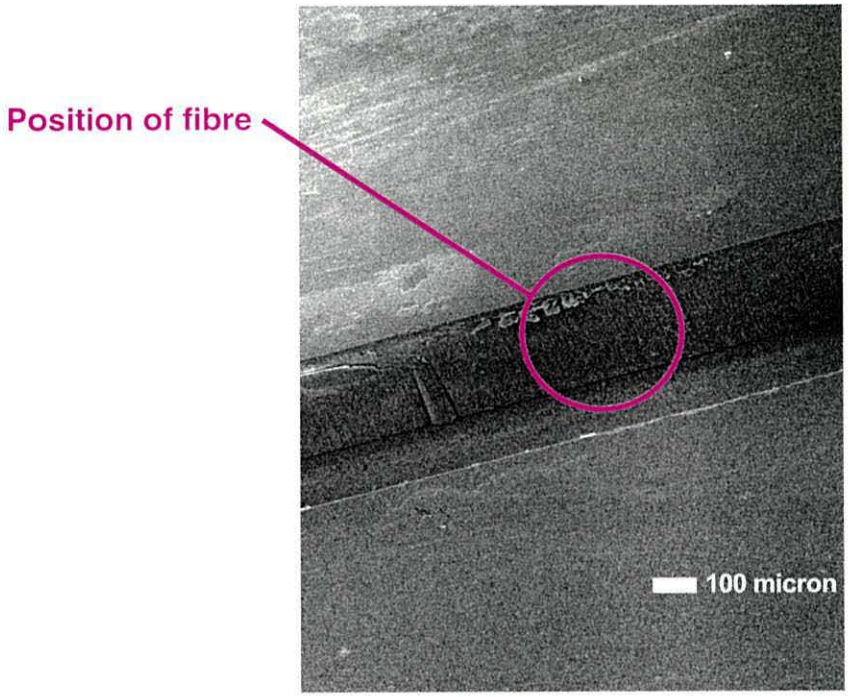

Figure 5.5 *SEM micrograph of a section of the machined channel that passes through the fibre*

A lid, with fluidic connections, was then bonded onto the machined section to form an enclosed fluidic channel with inlet and outlet that passed through the fibre and completed the device, as shown in Figure 5.6.

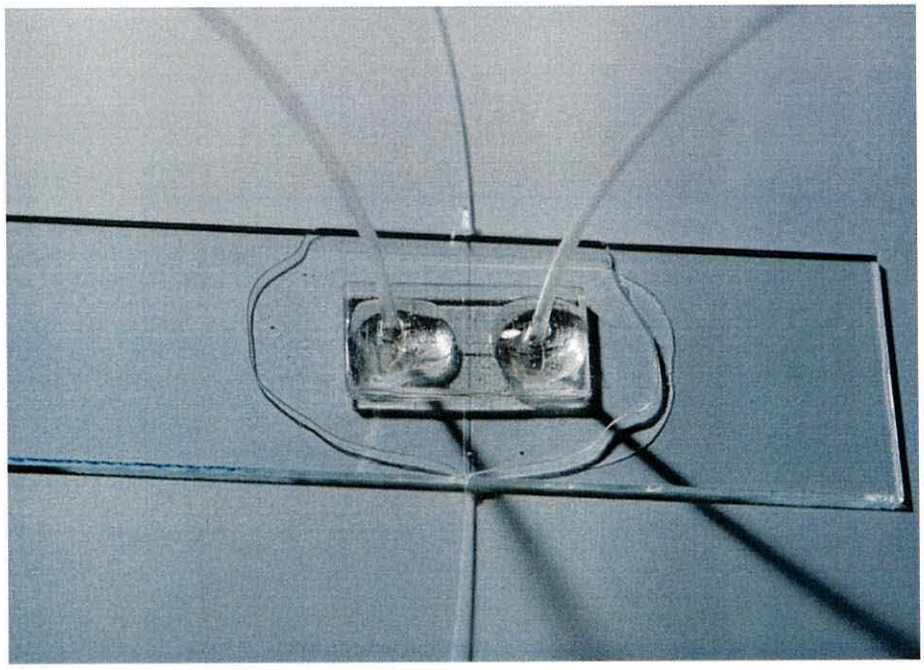

Figure 5.6 *Photograph of the competed device, showing (a) the fluidic connections and (b) the optical fibres*

5.3.3 Experimental setup

To test the optical sensor devices, it was necessary to couple a suitable illumination source of predetermined wavelength to one of the optical fibres and attach an optical detector to the end of the other. Various emitters were used in this work, including LED's and a laser diode. Figure 5.7 shows the experimental setup used to test the devices.

The detector used throughout this work consisted of a photodiode [SFH250V, Siemens] that was sensitive to a wide range of wavelengths (400nm to 1100nm). The detector output was fed into a high-input impedance amplifier. The photodiode produced an output current that was linearly proportional to the intensity of light incident on the detection area. This output current was fed into the fixed gain amplifier, which was used to produce a larger amplitude output signal that could be easily measured. The amplifier circuit used is shown in Appendix III. Both the photodiode and the amplifier circuit were enclosed in a metal box to reduce electrical and optical noise to a minimum.

The output signal from the amplifier was fed via a BNC socket to an oscilloscope (Hameg HM1507-3) for real-time observation or to a PC-based oscilloscope (Picoscope ADC-200, Pico technology) for data logging the sensor output for future analysis. The PC based system could also function as a digital voltmeter, allowing easier inspection of the output level, if required.

All of the devices fabricated in this work (including planar waveguide devices described later in this section) used 250μm diameter fibre, which was connected to the detector photodiode using a larger diameter polymer optical fibre. This was done for two reasons: primarily because the detector was specifically designed to couple to larger diameter fibres (1.2mm) and secondly the detector could remain undisturbed in the screened box, regardless of the device under test. The two different diameter fibres were connected using a custom made alignment clamp that maintained the ends of the two fibres co-axially. Optical coupling gel was used to improve the transmission between the two polished fibre ends.

If the input to the detection fibre was blocked off, the background noise was less than 2 mV. This was suitable for data collection since the full-scale output of the detector was several orders of magnitude greater at 10 V.

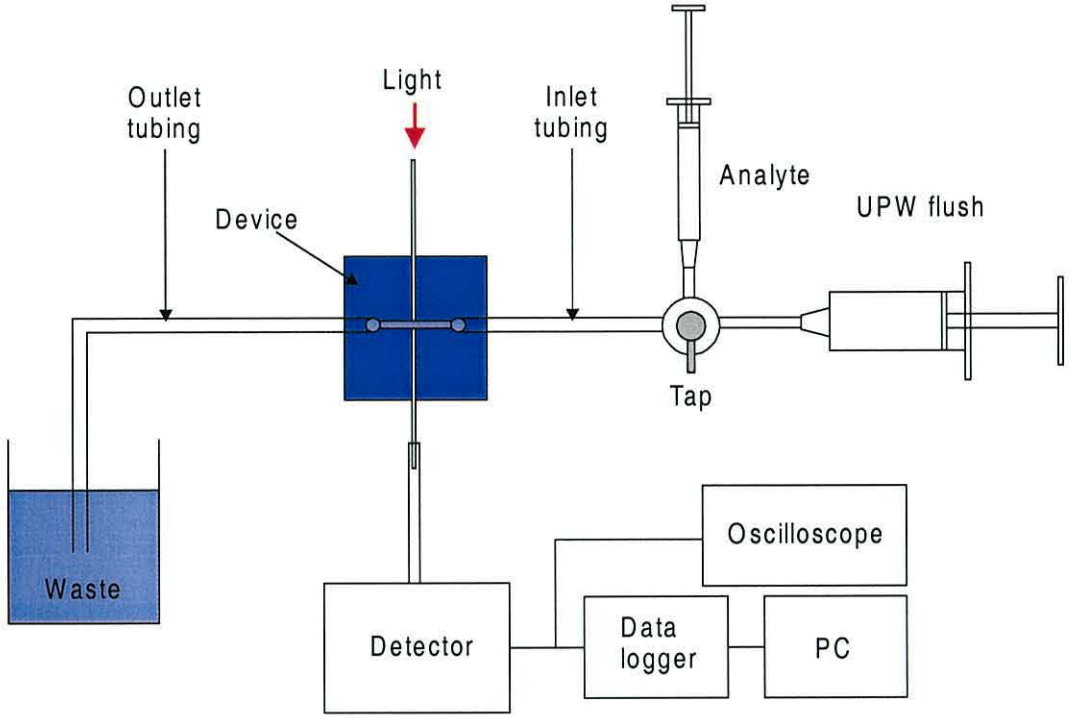

Figure 5.7 *Diagram of the experimental setup used to measure the optical absorption of various analytes.*

The tubing, shown in Figure 5.7, provided fluidic connection to and from the device under test. The inlet to the device was connected to a three-way tap that allowed either analyte or water to be injected into the device. The fluidic outlet was taken from the device to a waste container. A sample of analyte was injected into the device inlet and then flushed through with water, so allowing the device response to a 'slug' of analyte to be recorded. The pipe runs were kept as short as possible (~10 cm) to reduce the amount of fluid present in the system and decrease the diffusion of analyte into the flushing solution.

Although the experimental setup operated successfully under ambient light conditions, the device was shielded from light during measurements to increase its sensitivity by reducing the background noise caused by stray light entering the optical waveguide. Taking this precaution reduced the background noise level from ~215 mV to less than 58 mV.

5.3.4 Particle detection results

Figure 5.8 shows the result of flushing three slugs of 25.7μm latex beads (Sigma Aldrich Co., Ltd., UK) through an optical fibre based device. Each fall in the detector output is due to a slug of beads attenuating or scattering the light beam across the channel. The channel width was 250μm which was equal to the diameter of the fibre used and a red LED emitter was used (λ=660μm). The concentration of the cell solutions used was measured with a haemacytometer grid [improved neubauer, Gelman Hawksley (England), B.S. 748]. By counting the number of beads within the measurement areas, with an optical microscope [Nikon Labophot II], the number of cells in the solution used could be found. This was found to be $1.34x10^4$ beads per ml, which equates to 256 beads in the detection volume. This assumes that the detection volume is defined by the volume where the two cones from each of the fibre ends overlap and any scattering from outside this region is not significant.

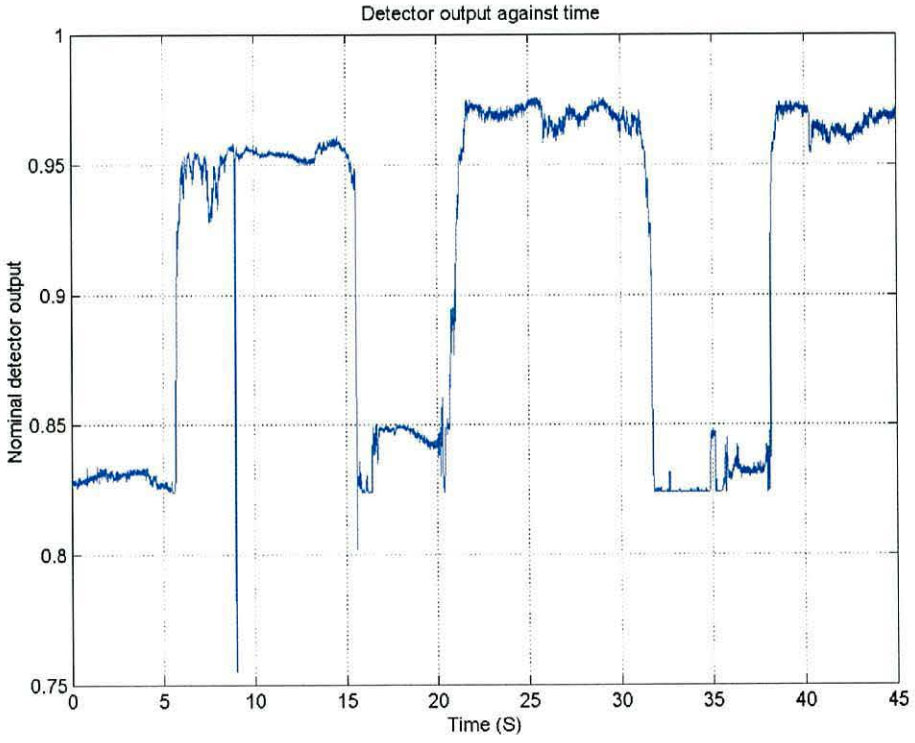

Figure 5.8 *Recorded output of a $1.34x10^4$ beads per ml (256 beads in the detection volume) solution passing through a 250μm channel machined though an embedded 250μm diameter fibre.*

5.3.5 Measuring the absorption of dye solutions

The absorption of dye solutions was also measured, as other possible applications of an embedded absorption sensor include measuring water quality [9, 15], or measuring characteristics of chemical reactions involving a colour change. This was done using different food dyes, which were pumped through a device at various dilutions. The device used had a channel width of 250 μm, as before and the measurement setup was unchanged from previous experiments.

Four coloured food dyes were used, red, green, blue and black. Each colour dye was diluted to five different concentrations: 1:1, 1:9, 1:99, 1:999 and 1:9999. The various dilutions were then pumped through the on-chip detector and the output level recorded. Four different wavelength emitters were used to determine the optimum detection wavelength for a given colour of dye.

Different concentration dye solutions were first analysed in a U-2000 Hitachi spectrophotometer for comparison with the output from the fabricated optical detector. Figure 5.9 shows a plot of the transmission of various concentration black dye solutions, measured in the spectrophotometer, at various measurement wavelengths. The other colour dyes exhibited a similar response.

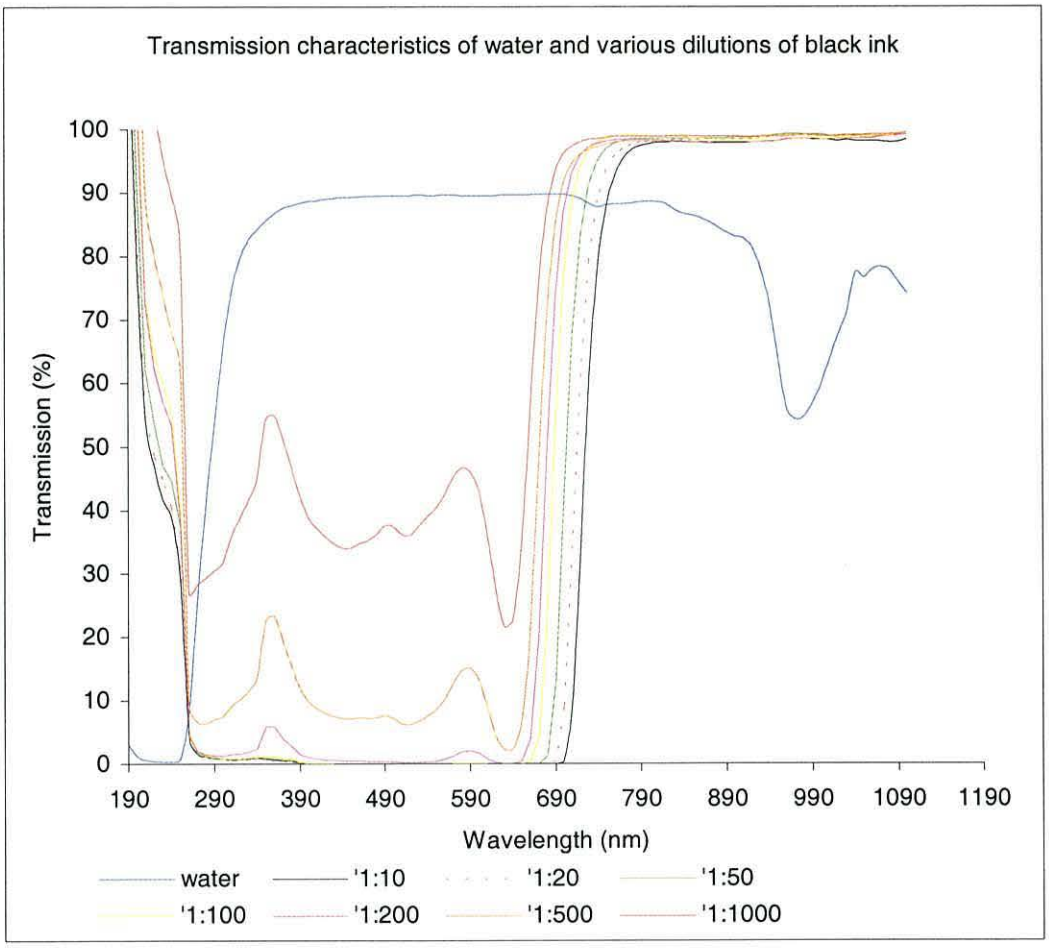

Figure 5.9 *Plot showing the measured absorption of various concentration dye solutions using the U-2000 spectrophotometer.*

Figure 5.9 shows that the responses for the various concentrations of dye are similarly shaped, but of different magnitudes, which is a good indication that diluting the dyes has little effect on the spectral sensitivity.

Table 5.1 shows the dye absorptions calculated for the 1:99 dilution black dye solution using Equation 5.2 at the emitter wavelengths used for both the spectrophotometer and the fabricated optical fibre based sensor.

	Calculated absorption (1:999 black dye)	
Wavelength (nm)	**Spectrophotometer**	**Fibre detector device**
Red LED (λ=660)	0.262	0.067
Green LED (λ=525)	0.442	0.045
Blue LED (λ=430)	0.348	0.041

Table 5.1 *Comparison of dye absorptions measured using the spectrophotometer and the fibre based device using a 1:999 dilution of black dye*

The results obtained from the fibre detector are shown in Figure 5.10 to Figure 5.13, where the nominal detector output for each emitter wavelength is shown for various dye solutions.

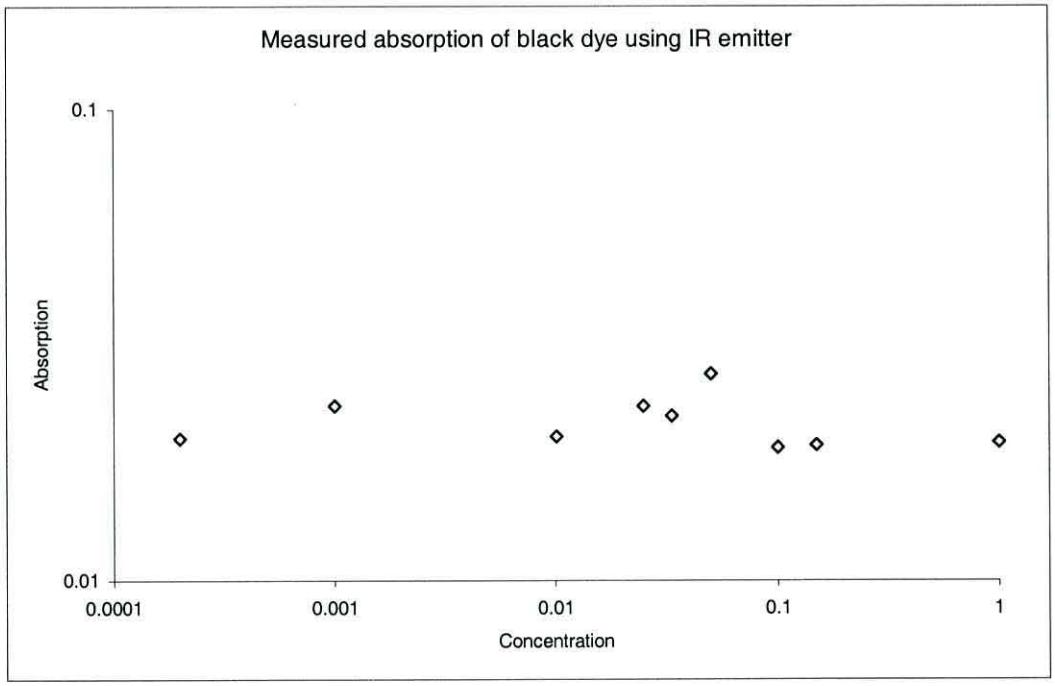

Figure 5.10 *Recorded detector output for nine concentrations of black coloured dye using an IR emitter [λ_{peak} = 880 nm]. Only the results of using black dye solutions are shown for clarity: the other dye colours produced a similar result.*

Figure 5.10 shows the most obvious result, which is that the infra-red emitter was not significantly attenuated by any of the dye solutions and so was not used for measurements. This also demonstrates that the devices are capable of operating at the longer wavelengths generated by the IR emitter (880nm) should such an excitation wavelength be required.

Figure 5.9 also shows that the optical absorption of the dyes at a given concentration varies with wavelength.

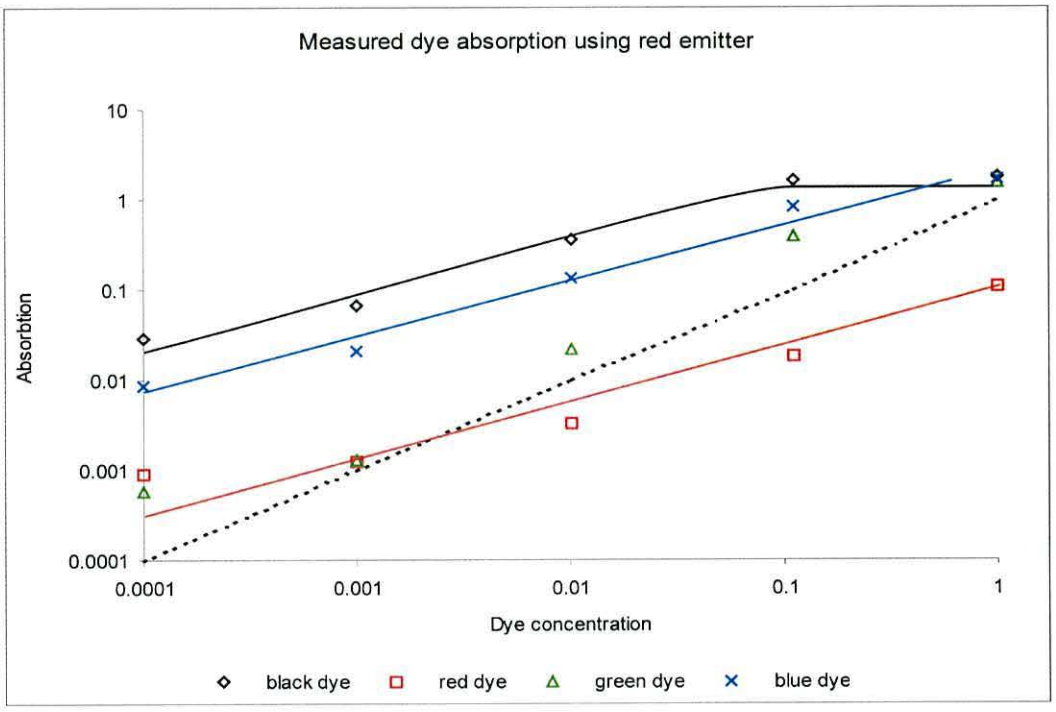

Figure 5.11 *Recorded detector output for five concentrations of four coloured dyes using a red emitter [λ_{peak} = 660 nm]*

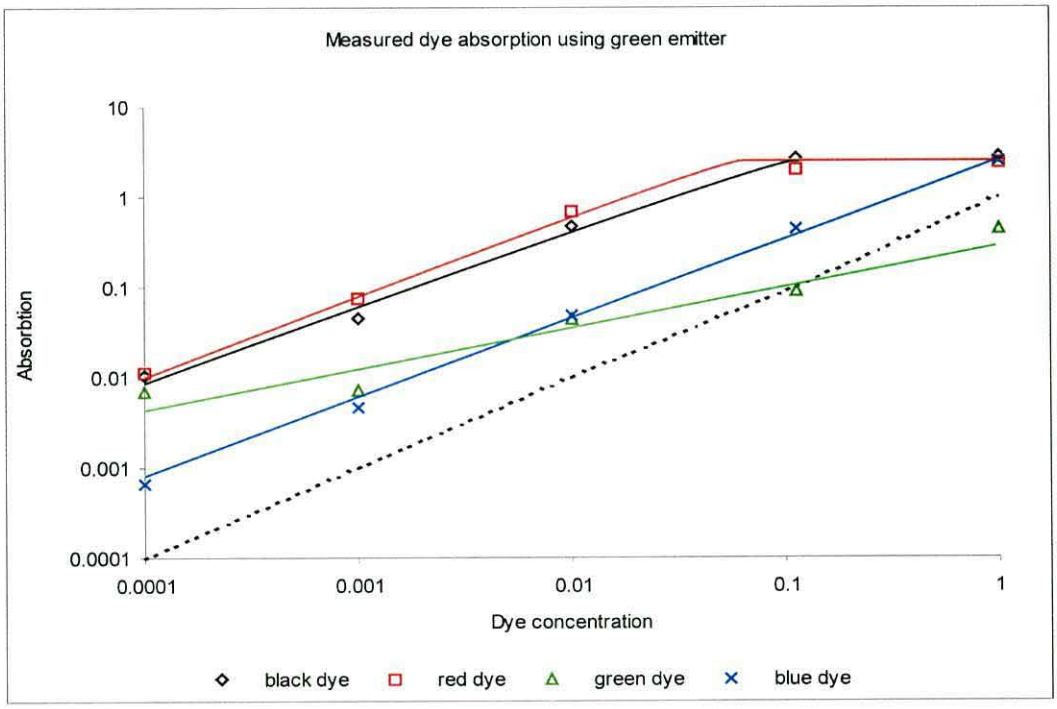

Figure 5.12 *Recorded detector output for five concentrations of four coloured dyes using a green emitter [λ_{peak} = 525 nm]*

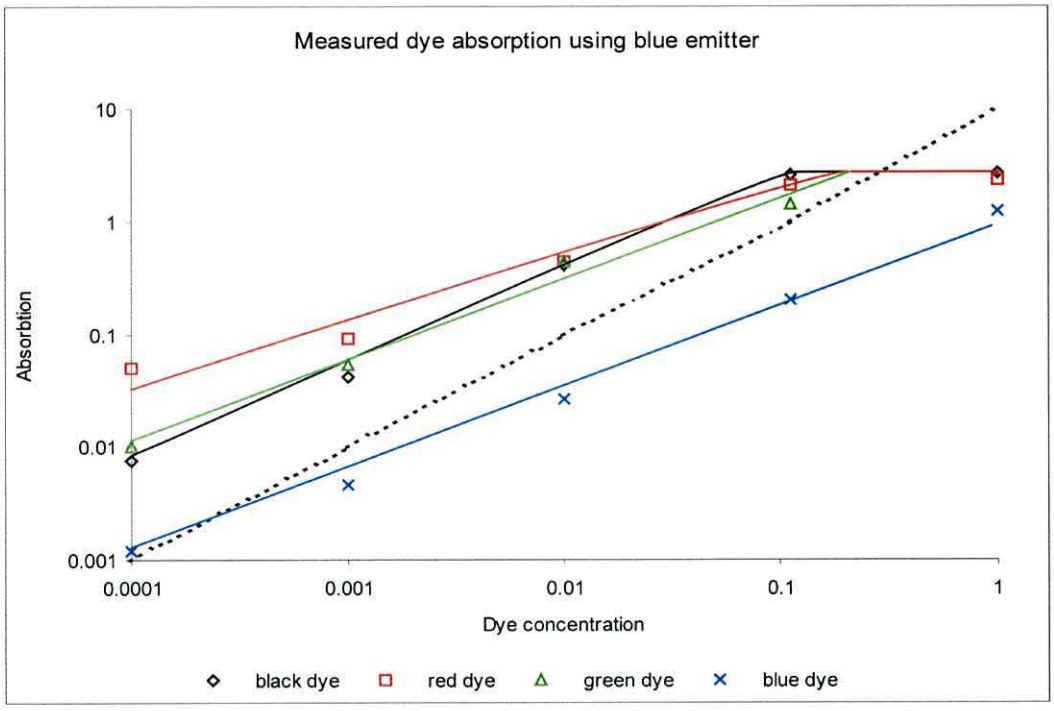

Figure 5.13 *Recorded detector output for five concentrations of four coloured dyes using a blue emitter [λ_{peak} = 430 nm]*

The dashed lines of unity slope plotted on Figure 5.11 to Figure 5.13 represent the trend of the Beer-Lambert law. As can be seen from the trendlines on each plot, the measured data does show the linear dependence on concentration with some offset present. The response can also be seen to saturate above a certain concentration, as shown in Figure 5.12 for the red dye solution.

When a red dye is used with a red emitter, or a green dye is used with a green emitter, the response is far from linear. This is probably because the incident radiation is reflected well within the solution, causing a higher degree of scattering. The most uniform response is achieved when the blue emitter is used, as all four responses appear to obey the Beer-Lambert law within the limits of the detector and the point at which the concentration is too high. It is well known that above a certain concentration the Beer-Lambert law will no longer apply and this will make predicting the device response problematical at such high concentrations.

From these results, it can be seen that the sensitivity of the device for a given colour solution can vary significantly depending on the emitter wavelength used. For example, if a chemical reaction produced colour change from clear to a red solution, then using a

red coloured emitter to detect the solution produced would not produce as sensitive an output as a green emitter.

5.3.6 Inherent limitations of fibre-based optical sensors

Although using an optical fibre based sensor allows light to be guided to the fluidic channel and the optical properties of analytes monitored, the channel height is limited by the fibre diameter. Using fibres also limits the shape of on-chip light guides, as the minimum bend radius of fibres is relatively large, typically centimetres. Splitting and joining optical paths on-chip is also difficult using fibres, because optically smooth interfaces are required. As the fibres are circular in cross-section, the sensing region is more sensitive in the centre, where the detection region is larger, compared to the top or bottom of the channel. This is not an ideal situation as events, such as a particle passing at the top of the channel, may be missed. Laser machining the fluidic channel through the optical fibre embedded in resin has however removed any problem of dead space and non-uniform flow regimes associated with manual fibre alignment in channels.

The limitations of fibre based sensors encouraged the development of a different method of on-chip light guiding using polymer based planar waveguides, as described in the next section. However, the limitations of the detection volume still apply although the light emerging from a square section waveguide will not produce conical light path, but a trapezoidal divergance in both horizontal and vertical planes due to the planar nature of the waveguide. Another significant limitation is that the detection volume is considerably larger than the particles being detected, which makes single particle detection problematical.

5.4 On-chip planar waveguide optical sensor design

Developing on-chip waveguides allows arbitrary shaped optical paths to be fabricated, including optical splitters and combination systems [5, 11]. If suitable fabrication techniques and materials are used, then the waveguides can be made square in

cross-section and the same height as the channel, allowing a uniform detection response over the entire height of the channel.

By forming the waveguide structure in a similar manner to the micro-fluidic channels, i.e. machining the thick polymer layer and injecting optical resin to form the waveguide, compatibility with existing fabrication stages is maintained. Having fabricated the optical components, the micro-fluidic channels can then be machined through the optical waveguide to produce the sensor.

As before, a 250μm diameter PMMA optical fibre was used to connect the waveguides to external light sources and the detector. By embedding one end of a polymer optical fibre [ESKA acrylic fibre, Mitsubishi] into the device, the other end can proceed off-chip to either an emitter or detector as required. This formed the required optical path between the device, emitter and detector, thus allowing optical measurement of the channel contents.

Two designs, Figure 5.14, were used to test the feasibility of the on-chip waveguide structures. Both designs are shown true size 1:1 (Figure 5.14a and Figure 5.14b) and enlarged for clarity (Figure 5.14c). These designs were created using AlphaCAM [Licom Systems, Ltd.], a 3D CAD and manufacturing program, which allowed rapid design transfer and subsequent machining of a substrate in the laser system. The two designs allowed comparison of the optical losses present in each design and the abilities of the waveguide to steer light around the device. Subsequent testing revealed that the micromachined waveguide structures produced similar results, indicating that the path of the waveguide did not affect its light carrying capability.

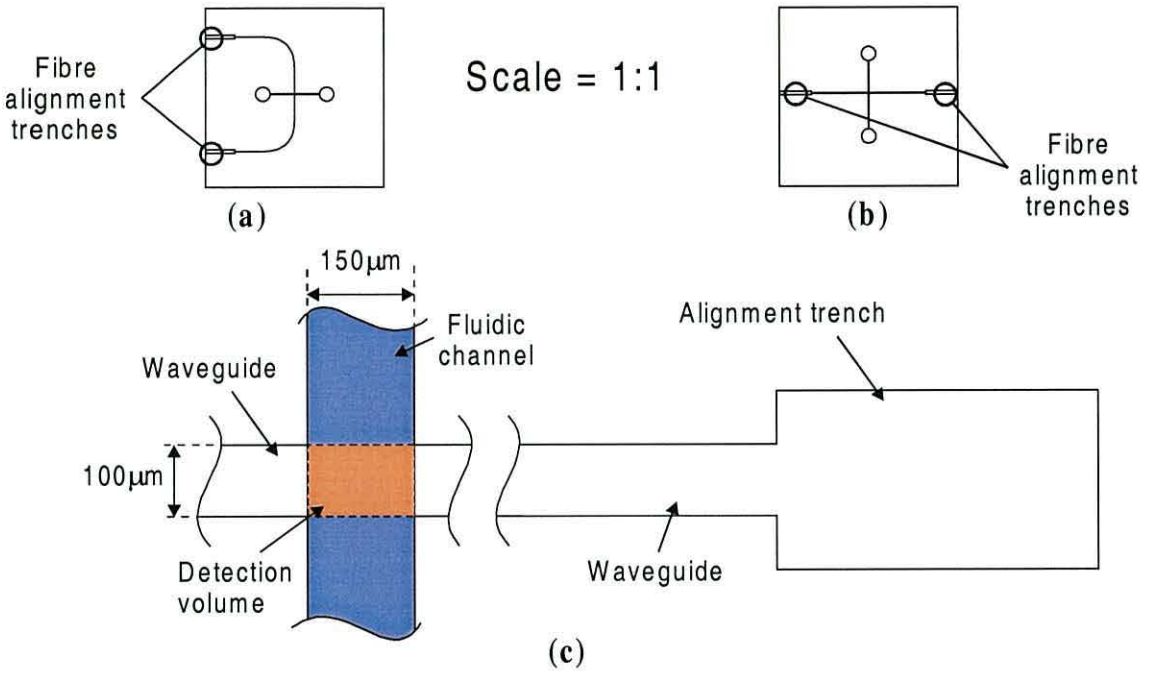

Figure 5.14 *The designs used to create the prototype optical detector devices: (a) curved waveguides, used to test the light-guiding properties of the waveguide materials, (b) straight waveguides used for comparison. (c) close-up of the intersection and fibre/waveguide connection.*

The widths of the optical waveguide and fluidic channel for the two designs were 100 μm and 150 μm respectively. The fluidic channel width was chosen to be 150 μm, as this is a reasonable approximation to the size of channels commonly used in existing devices. The waveguide width was chosen to be 100 μm, as this would allow a detection width similar to that of the channel. The height of both structures was determined by the depth to which the channels were machined into the thick polymer layer, in both cases 180μm. In order to allow maximum transmission and sensitivity across the fluidic channel, both the fluidic channel and the waveguide were machined to the same depth.

5.4.1 Planar waveguide fabrication

The excimer laser micromachining workstation (Chapter 3.1) was used to machine the thick polymer layer to produce the two designs. For this work, the excimer laser system was operated at a wavelength of 248nm with a x10 projection lens, producing a maximum energy density of 10J/cm^2 at the workpiece.

To allow optical investigation of the device during testing and to be compatible with typical fabrication techniques, the prototype device was fabricated on a glass substrate. A 180 μm thick dry-film laminate [Laminar 5038, Ozatec] was then coated onto the substrate before the optical paths were machined into it using an energy density of 1.2J/cm^2 at the workpiece. The waveguide, which was intended to have a rectangular cross-section, was machined using a square aperture. Operating in the mask dragging mode (Chapter 2.4), uniform energy deposition was achieved at the workpiece and hence a uniform machining depth across the aperture. The optical fibre alignment trenches, however, were machined by mask dragging an elliptical aperture. This had the effect of creating a non-uniform cross-section (Chapter 2.4) to allow manual alignment and insertion of the fibres into the trenches. Because the side walls of the alignment trenches were not parallel, but curved, the fibre remained in place after the insertion force was removed. This made the device fabrication process much simpler, as no fibre alignment tools were required.

After the dry-film laminate layer had been machined, the pre-cut and finished fibres were inserted into the alignment trenches. The waveguide then needed to be filled with optical resin. First a thin, transparent polymer film 20μm thick was bonded to the top of the device covering the region where the fluidic channel was to be machined through the waveguide channel. This had the effect of sealing the machined channel, forming rectangular cross-section optical paths. The thin film also kept the top surface of the device flat when the resin was added. This is beneficial when bonding the lid onto the device in order to maintain a non-leaking fluidic system.

A drop of UV curing resin (Norland 83H, Edmund Optics Inc.) was placed on the end of one of the optical fibres that had been inserted into the alignment channel. Capillary action then drew the resin into the waveguide channel. When the meniscus reached the other end of the channel, a drop of resin was placed onto the end of the second fibre. The whole device was then placed in an UV exposure cabinet and the resin cured. The hardened resin now formed the on-chip optical waveguide and provided a good degree of coupling between the fibres and the waveguides, as it removed air-gaps, as well as mechanically securing the optical fibres to the device. Figure 5.15 shows a device at this stage.

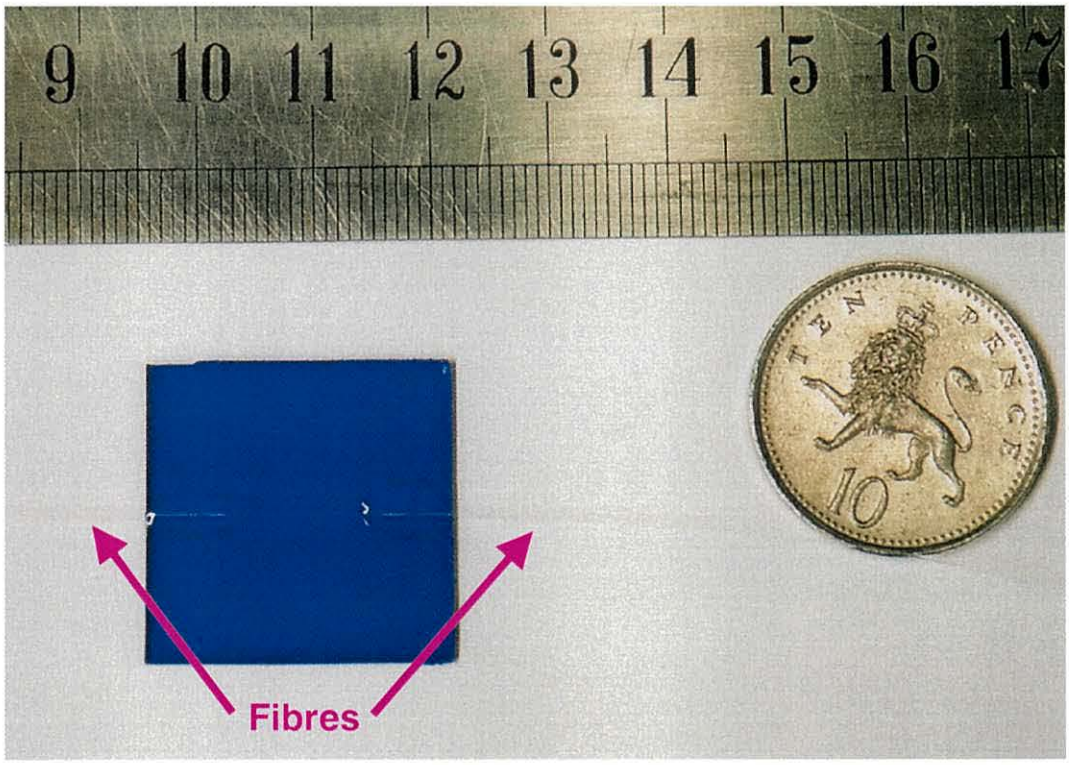

Figure 5.15 *Partially completed device where the waveguide has been machined and the optical fibres, which can just be seen running horizontally, bonded in position using optical resin.*

The optical resin used [n=1.56] had a refractive index higher than both glass and the surrounding polymer materials [n<1.56] and so will effectively act as a rectangular optical fibre.

Figure 5.16 shows the sequence of manufacturing steps used to produce the devices. Next, the fluidic system was laser machined into the polymer layer, using an energy density of 1.4J/cm^2. In this case, a simple channel with inlet and outlet wells was fabricated. The sample was replaced in the excimer laser micro-machining system, re-aligned and re-machined through the thin polymer layer, thick polymer layer and UV cured resin to form the required channel system. This ensured consistent positional and dimensional accuracy of the machined areas.

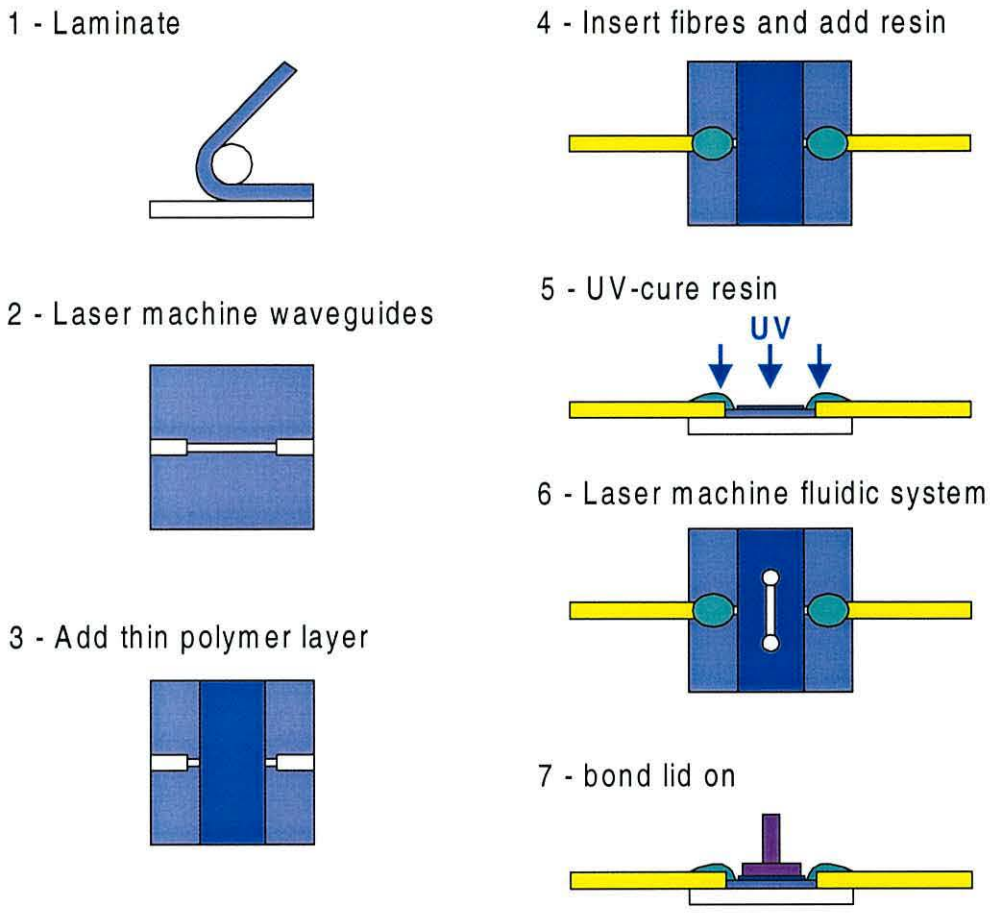

Figure 5.16 *The sequence of manufacturing steps used to fabricate the optical sensor*

It was found that the ablation threshold (Chapter 2.6) required to remove the thick polymer layer differed from that of the cured UV optical resin that made up the waveguide.

If a constant energy beam had been used to machine the fluidic channel structure, the region where the waveguide and channel intersect would have been machined to a shallower depth because the cured resin machines at a slower rate for a given laser energy density. However, it was known that machining glass was not possible at 248nm and a x10 projection lens is in use. Therefore the channel system was re-machined to completely remove all material from the fluidic channel regions. This was done three times to completely remove the cured resin from the fluidic channel and provide a constant cross section. This did not damage the glass substrate and kept the channel and waveguide depth constant throughout the device, as well as providing uniform, approximately square cross-sections throughout the fluidic channel.

Relatively high laser fluences and total energies were used for all regions machined, primarily to reduce the effects of wall angles and achieve the required channel cross-sections.

Figure 5.17 shows the device after the fluidic channels have been machined. This shows the two optical fibres, used for optical connection from the device to an emitter and a sensor. The waveguide, which runs between the fibres and across the fluidic channel, can also be seen, in this case a curved waveguide has been fabricated.

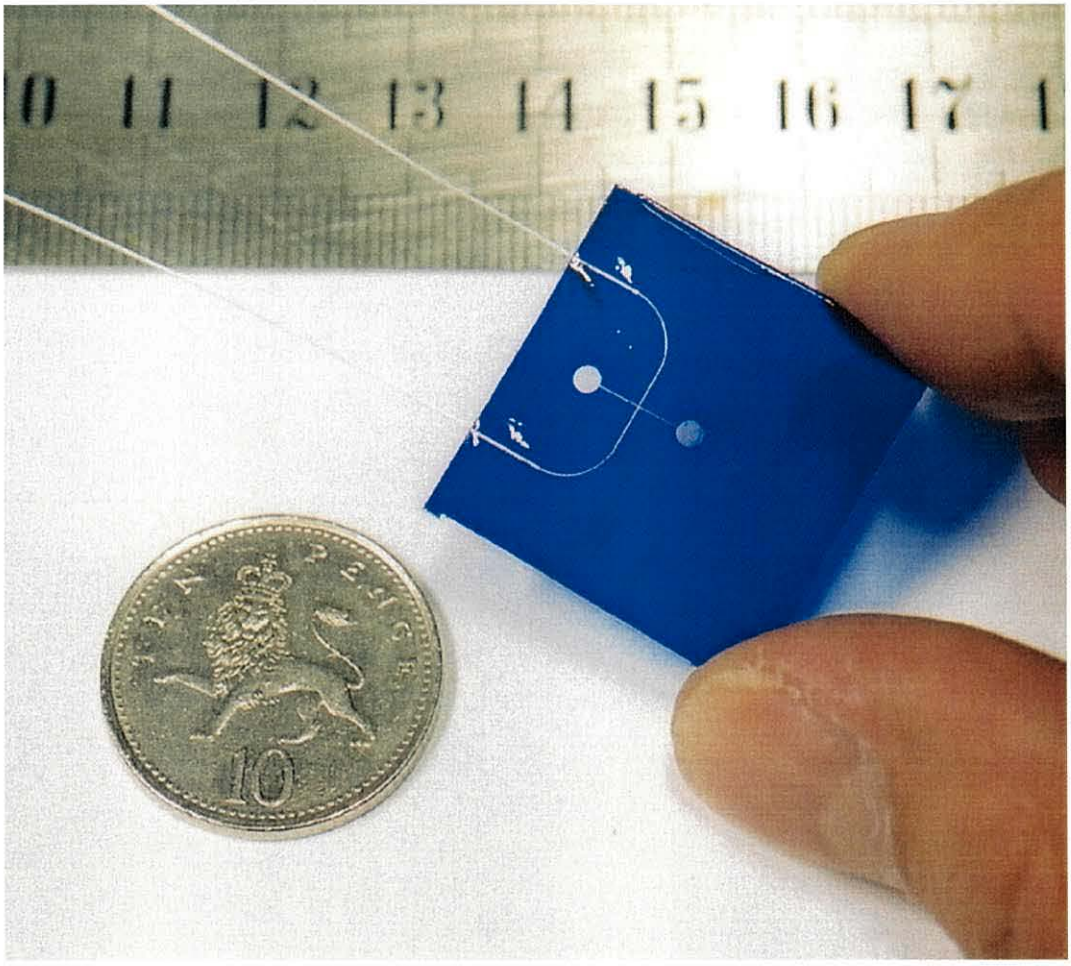

Figure 5.17 *Photograph of a machined device, prior to the lid being bonded on.*

To complete the encapsulation of the device, a transparent polycarbonate lid, with pre-fabricated fluidic inlet and outlet connections, was bonded onto the laser machined half of the device. A polycarbonate lid was used to allow rapid prototyping, as it can be cut to size using a scalpel (unlike glass that requires scribing) and does not require special drilling procedures.

A completed device, incorporating a sealed fluidic channel and on-chip optical waveguide, is shown in Figure 5.18. It would be possible to bond electrode structures, fabricated on a glass lid, onto the device to allow integration of the optical system with existing device fabrication technologies.

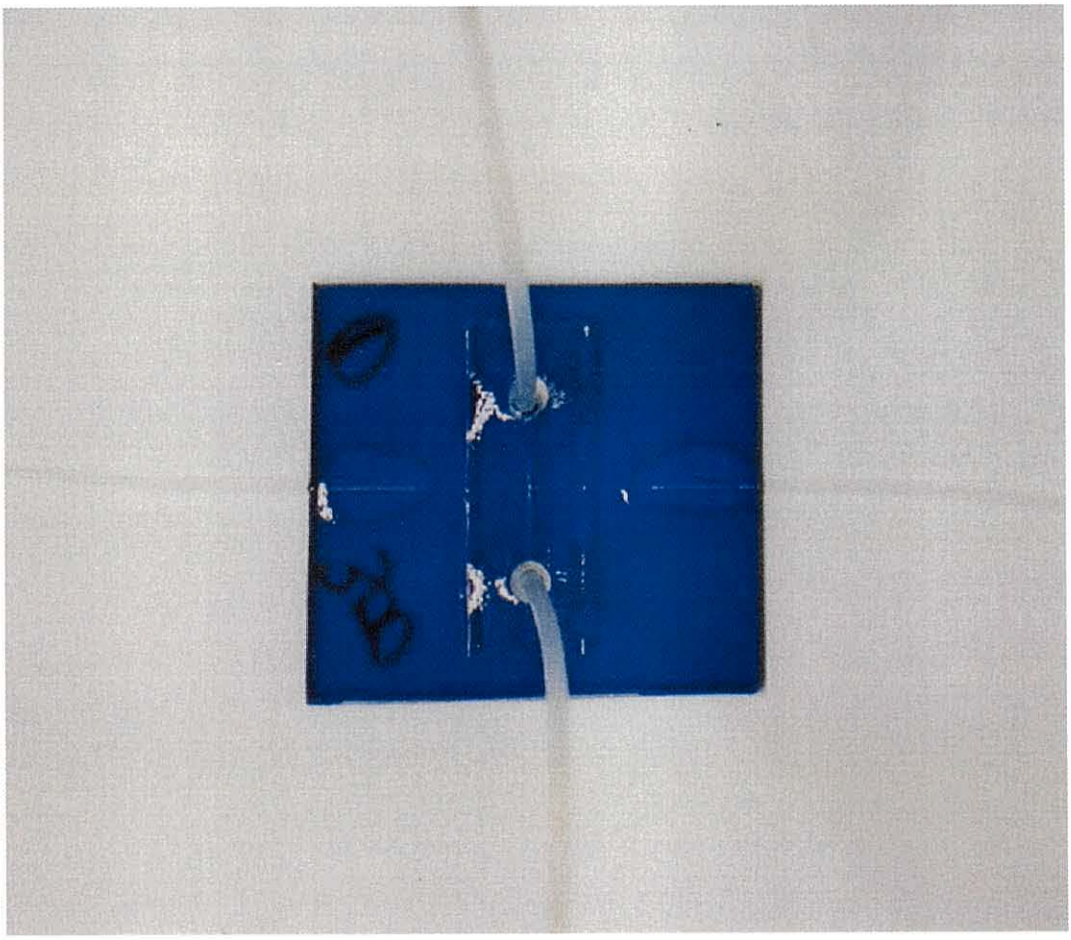

Figure 5.18 *Photograph of a completed device showing the optical and fluidic connections. The two fluidic connections are the larger pipes emerging from the top of the device and the two optical fibres can just be seen running horizontally though the device, as in this case the optical path through the device is straight.*

The polycarbonate lid seen in Figure 5.18 did not cover the optical fibre alignment trenches, as the fibres and hardened UV resin protruded tens of μm above the laminate layer, so would have impaired the bond between the lid and the device. By positioning the optical connections appropriately, for example at one side of a device, such as in the curved waveguide design, a larger lid could be used.

5.4.2 Detection and measurement of cell suspensions

Initial experiments to measure the concentration of biological cells in the sample used a red laser diode module (λ=633nm) as a light source. The laser beam passed through a lens system that focussed the beam onto the free end of the optical fibre. The lens system was attached to the laser and positioned using an adjustable clamp. The free end of the optical fibre was held in a fixed clamp, so allowing the focused laser beam to be aligned with the end of the fibre by suitable positioning of the laser.

The ability of the optical device to detect cell suspensions was tested using an aqueous suspension of yeast (*saccharomyces cerevisiae*, strain R12). Yeast was used because it is readily available and grows quickly. The cell solutions were prepared by placing a small quantity of the yeast in approximately 500 ml of Sucrose, Bacteria Peptone, Yeast Extract (SBPYE) Broth nutrient solution in a conical flask. This solution contained the nutrients required for the yeast to divide and was made by mixing the constituents shown in Table 5.2 with 1 litre of UPW.

Item	Weight used
Sucrose	50g
Bacteria Peptone	5g
Yeast Extract	5g

Table 5.2 *Components mixed to form nutrient solution to grow yeast*

The yeast/nutrient solution was left in an incubator [Labline incubator-shaker] for 48 hours at a stable temperature of 30°C and constantly agitated. Subsequently, the yeast was separated from the nutrient solution by centrifuging. The remaining pellet of yeast cells was then washed in UPW and centrifuged to re-separate the cells. This was repeated three times to remove any remaining nutrient solution. After the final rinse, UPW was added to make the remaining volume up to 5ml and agitated to form a concentrated cell solution. This solution was then diluted to create aliquots of various concentrations by adding an appropriate volume of UPW. All of the above work was carried out in a class IIa biological cabinet.

Figure 5.19 shows an optical micrograph of a completed device with yeast solution present in the channel. This image of the junction, observed from above, was captured onto a PC from a S-VHS video camera attached to a microscope [Olympus BX60]. The fluidic channel runs from the top of the image to the bottom and the waveguide crosses the channel from left to right. The light from the laser diode is being injected into the channel via the right-hand waveguide structure. The yeast cells present within the detection region are clearly seen to be scattering the incident light. Some unwanted light scattering within the channel is occurring, most likely due to the numerical aperture of the waveguide causing light to diverge from the end of the waveguide used to carry light to the channel.

If the ends of the waveguides were shaped, for example by machining a curve in the end of the waveguide to form a one dimensional lens, the divergence of light within the channel could be reduced. This could easily be done by altering the laser program used to machine the fluidic channel. However, this was not examined here, as this work concentrated on the initial feasibility study of planar waveguide fabrication and integration into existing Lab-on-a-chip technology.

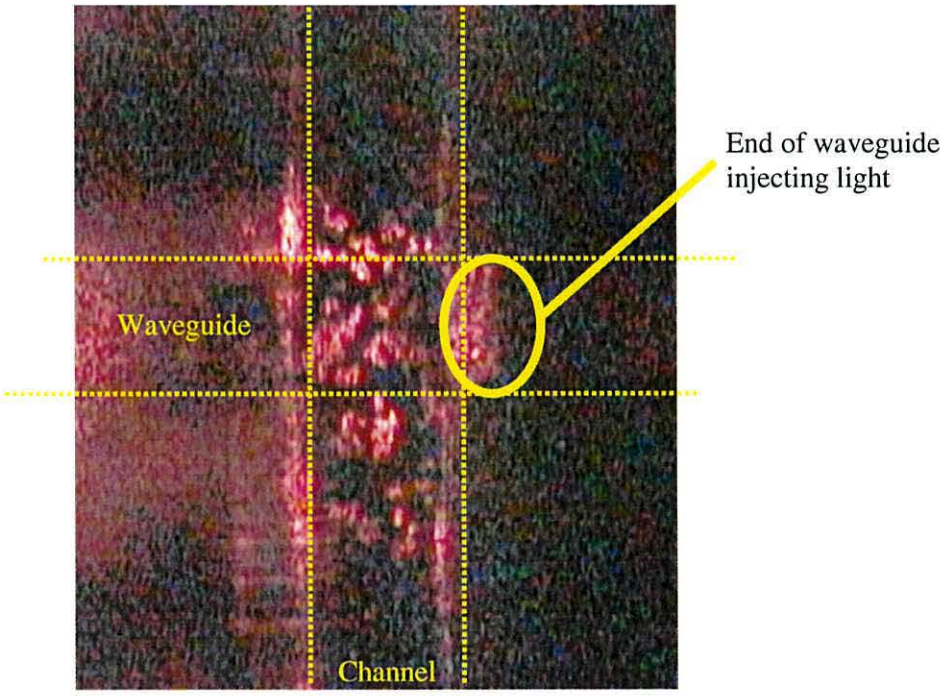

Figure 5.19 *Optical micrograph showing laser light, emitted from the end of a waveguide, being scattered by yeast cells at the intersection of the fluidic channel and the waveguide. Light scattering within the channel region can also be seen, most probably caused by reflections off the channel walls.*

The ability of the devices to measure cell concentrations was then tested. First, the fluidic system was flushed through with water. Then a 'slug' of a known cell concentration was introduced at the inlet and pushed through the device with water. Again, the concentration of the cell solutions used was measured with a haemacytometer grid [improved neubauer, Gelman Hawksley (England), B.S. 748]. By counting the number of cells within the measurement areas, with an optical microscope [Nikon Labophot II], the number of cells in each solution could be found. Figure 5.20 shows an example of the detector output vs. time when three 'slugs' of similar cell concentration were pumped through the device.

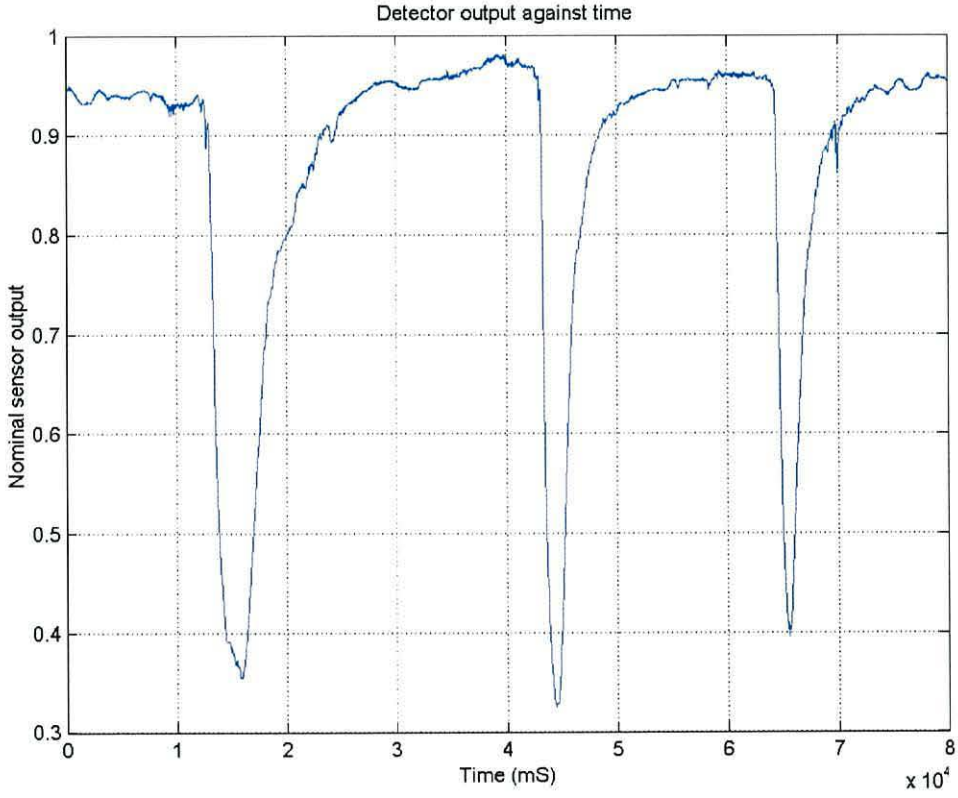

Figure 5.20 *Plot of output voltage vs. time when three cell 'slugs' are pumped through the device*

The plot shows that when only water is present in the channel, the detector output is close to maximum, as would be expected. When the yeast solution is introduced into the sensing region of the device, the output voltage falls, as the cells block/scatter the incident light. The output signal then increases back to its previous unattenuated level

as the cell concentration is diluted by the pure water flush. A similar waveform is seen when a second and a third 'slug' of cells are pumped through the device.

The detector output did not reach its minimum value instantly, because the liquid in the micro-channel is laminar and produces a curved front to the slug. Maximum attenuation occured when the entire detection volume was filled with cell solution and occurred some time after the first cells entered the detection region. Similarly, the return to maximum transmission following the water flush takes time.

Throughout this work, the performance of the sensors was measured by monitoring the fall in output from the detector. Although this is not ideal, it does allow a simple method of determining the function of such sensors with the added benefit of a minimum of detection equipment being required. A more accurate method would be to calculate the area within the region of lower output, but this would require additional computation devices and was not pursued in this initial investigation.

Figure 5.21 shows the results of three separate experiments where the highest cell concentration and two, more dilute solutions (1:9 and 1:99) were pumped through a device. In each case, the device was flushed with 25ml of UPW, before a slug of cell solution, approximately 0.25ml, was injected and pumped through the device using UPW. The measurement was repeated twice in succession for a given cell concentration. As expected, the maximum attenuation achieved reduces as the yeast solution becomes more dilute. The variation in the detector outputs at the start of each of the traces is due to slightly different laser alignment positions.

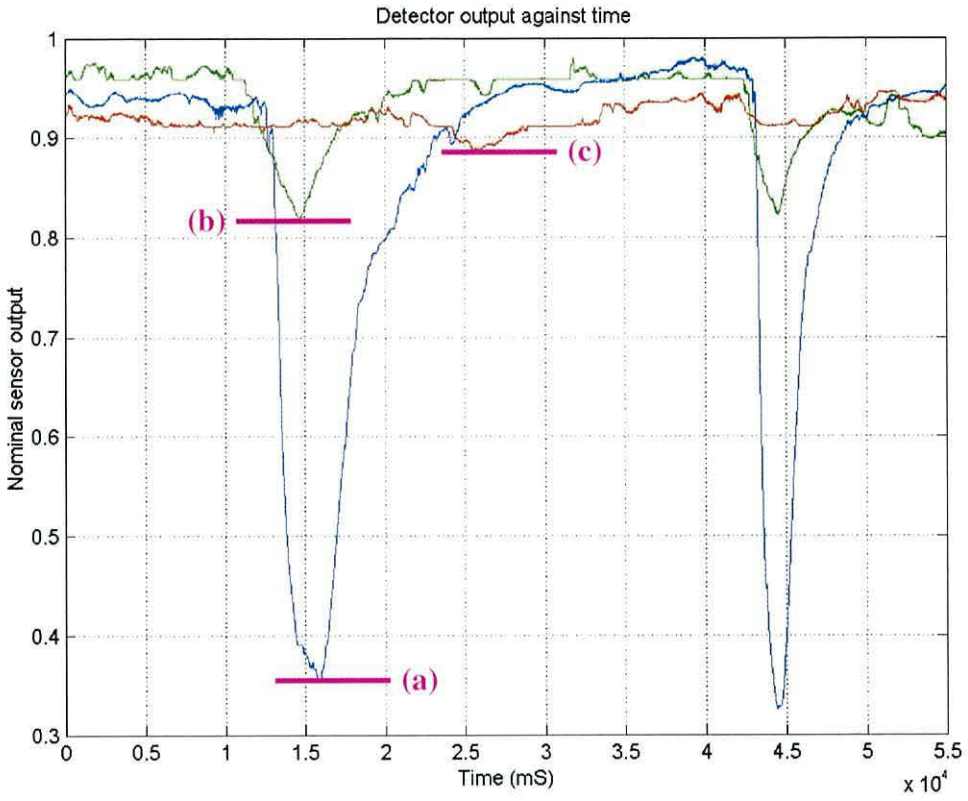

Figure 5.21 *Detector output signals when two successive slugs of (a) the original yeast solution and (b) 1:9 dilution and (c) 1:99 dilution are pumped through the detector.*

The concentration of the cell solutions measured with a haemacytometer grid are shown in Table 5.3.

	Solution 1	**Solution 2**	**Solution 3**
Measured Concentration (cells per ml)	1.44×10^7	1.44×10^6	1.44×10^5

Table 5.3 *Measured cell concentrations for the three test solutions used.*

These measurements show that although the device was able to measure cell concentrations, a relatively large number of cells were present in the test solutions used. By calculating the cell volume fraction, the relative sensitivity of the detector device can be found. The cell volume fraction is given by

$$\textit{Cell volume fraction} = \frac{\textit{Volume of cells}}{\textit{Total volume}}. \qquad (5.3)$$

Assuming that the nominal size of a yeast cell is equivalent to a 6μm sphere, the cell volume fractions can be calculated. The results are shown in Table 5.4 along with the calculated absorption (Equation 5.2).

	Solution 1	**Solution 2**	**Solution 3**
Cell volume fraction	0.5811	0.1642	0.0162
Absorption	0.43	0.077	0.011

Table 5.4 *Calculated number of cells within the detection region and absorption of the solution measured using the device*

5.4.3 Improving planar device detection sensitivity

The sensitivity of the detector is dependent upon the divergence of the light beam, the size of the detection volume and the distance that the light beam has to travel through the analyte [Equation 5.1]. In an effort to increase sensitivity, a third optical sensor was designed and fabricated in which the channel width was increased to 300 μm. Figure 5.22 shows the design used to laser machine the required waveguide and fluidic channel structures. This device was fabricated using the same methods as the first devices, with the exception of the laser program used to machine the fluidic channel. Increasing the width of the fluidic channel at the waveguide intersect, hence the cross-sectional area, will also have the effect of slowing the velocity of particles travelling through the detection region. This may also be beneficial, as any particles present in the analyte will spend more time in the detection region and events are less likely to be missed. By maintaining a smooth transition from the inlet channels to the detection region, dead space was eliminated allowing reliable flushing of the device.

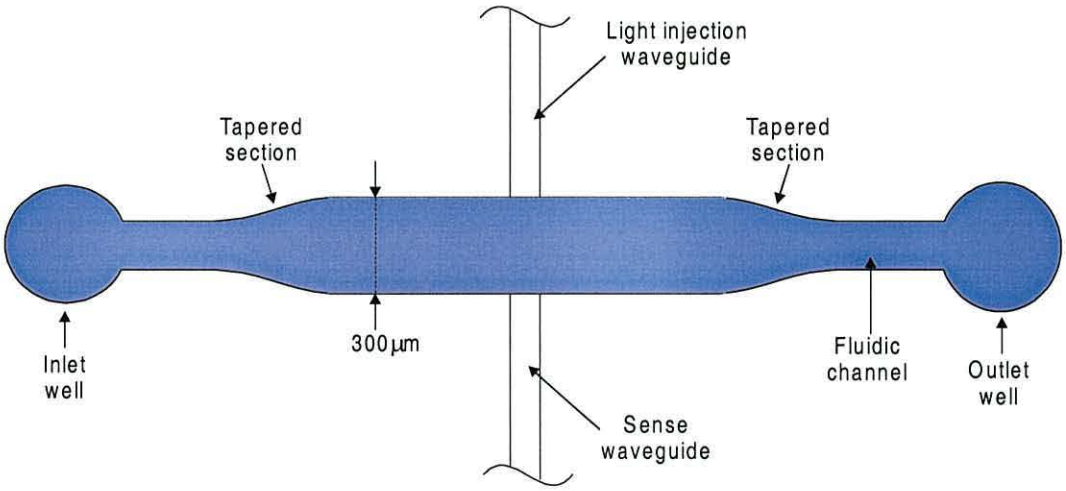

Figure 5.22 *Plan view of the fluidic channel design used to create a 300μm wide fluidic channel at the detection region.*

By doubling the width of the fluidic channel, the detection volume is also increased. Although the sensitivity of the device should be increased, it will not simply double due to the numerical aperture of the waveguides. Again, different concentrations of yeast solutions were pumped through the device and the detector output recorded in a similar fashion. The recorded sensor outputs are shown in Figure 5.23.

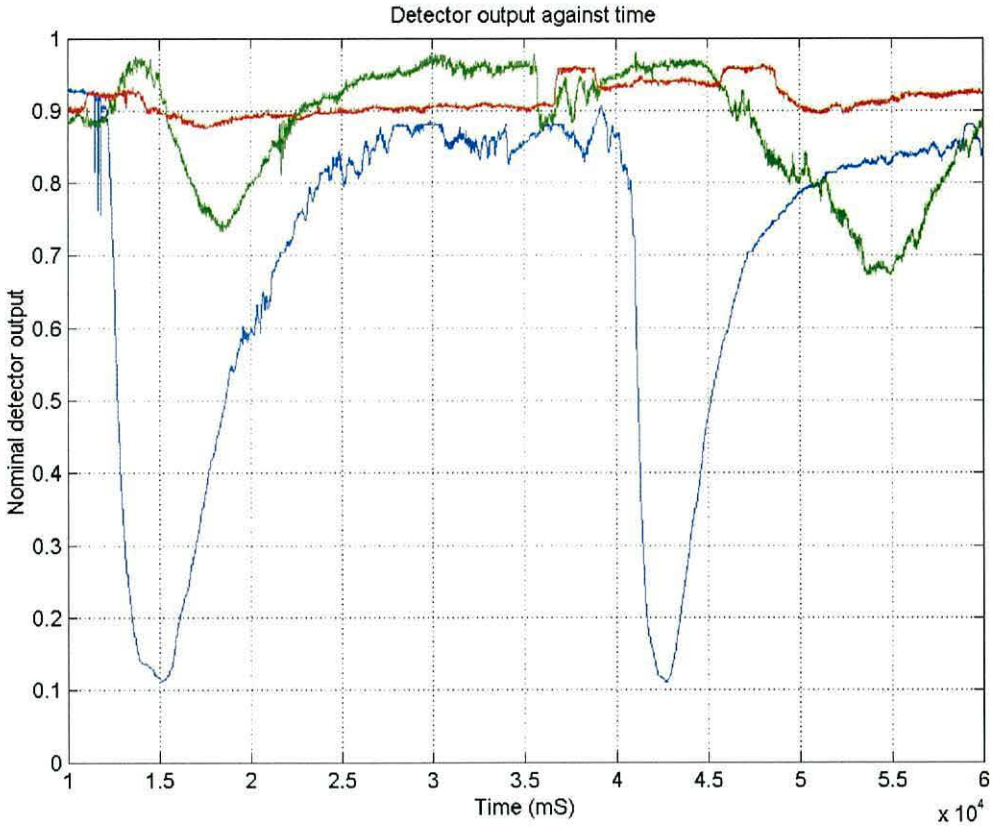

Figure 5.23 *Plot of recorded output voltage from the sensor for different cell concentrations using a device with a 300 μm wide channel.*

The results obtained are similar to those shown in Figure 5.21, although the actual yeast solutions used varied as the original yeast solutions were only viable on the day they were prepared. The concentration of the solutions was measured as before and the results are shown in Table 5.5. These are slightly lower concentrations than used in the first set of experiments and as the results obtained are similar with both devices, this indicates that the second device is more sensitive. The cell volume fractions were also calculated using Equation 5.3 for the weakest cell solution that produced a useful detector output, to allow a comparison between the devices. These results show that the 300μm device is capable of detecting a solution of cells with a lower cell fraction than the 150μm device.

	Channel width (μm)	**Cell volume fraction**
Device 1	150	0.0162
Device 2	300	0.0076

Table 5.5 *Lowest detectable cell volume fraction solution for each of the two devices*

The sensitivity variation observed as the concentrations were varied is not linear, most probably due to the high concentrations used. One possible cause of the observed non-linearity is multiple scattering events between the particles present. This makes the device response hard to predict, although using lower concentrations may improve the linearity of the device. Although the detection sensitivities were not as high as initially hoped, this initial investigation does demonstrate that optical detection systems can be integrated into existing fabrication techniques. Another factor that will affect device performance and sensitivity is background noise, which can be seen on the recorded sensor outputs (i.e. Figure 5.23).

Figure 5.24 shows the absorption responses of both devices, indicating that the 300 μm channel is more sensitive for a given cell concentration than the 150 μm wide channel. These results demonstrate the non-linearity of the devices, which can be expected as it is known that the Beer-Lambert law does not apply at high concentrations, although it should be noted that the Beer-Lambert law is not specifically intended for cell solutions.

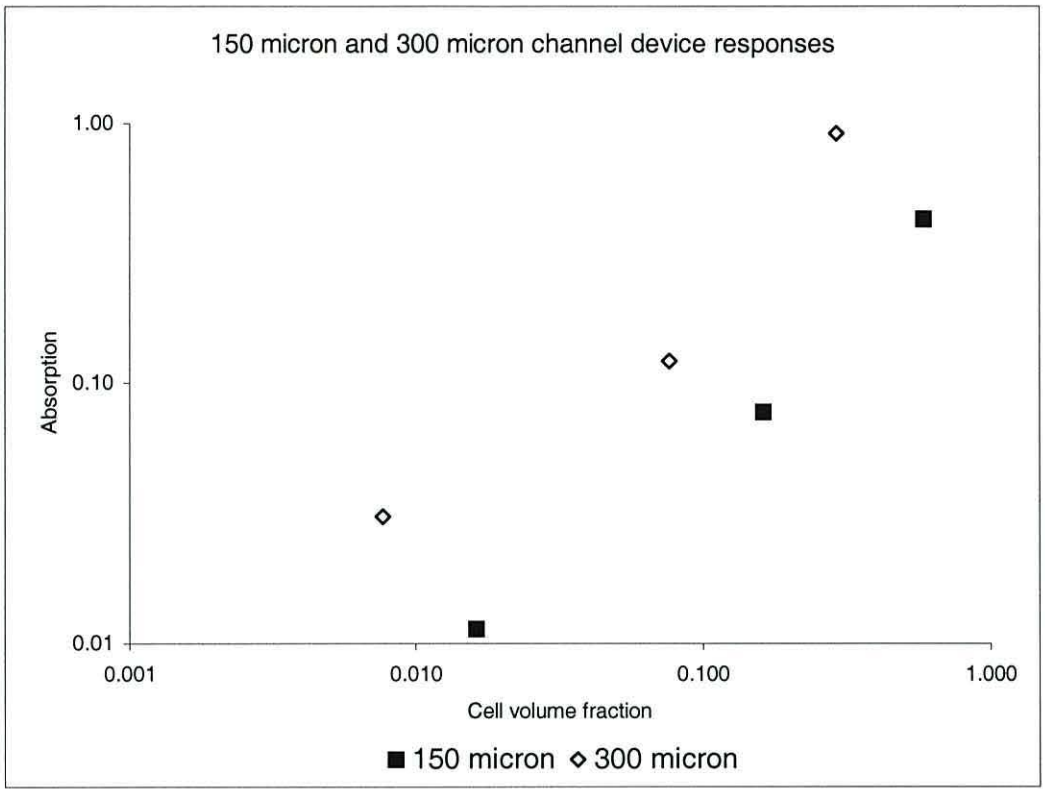

Figure 5.24 *Plot of absorption vs. cell volume fraction for the 150μm and 300μm wide detectors.*

5.4.4 Problems encountered developing planar on-chip sensors

The biggest problem encountered during the development of the experimental setup was maintaining a reliable, continuous coupling of the laser beam into the end of the inlet optical fibre of the device, as the LED emitters were glued into fibre optic cable end fittings. This made the setup very vibration sensitive, as even small impacts would cause significant variations in the output level. This in turn made accurate measurements difficult. To overcome this, a metal frame was used to hold the fibre end and laser rigidly in position, so reducing output level variations to a negligible amount. The revised setup allowed more repeatable measurements to be made and was used to obtain the results presented here. This problem could be overcome by using on-chip emitters and detectors, as then the entire system would be much less vibration sensitive.

5.5 Conclusions

Two types of on-chip optical sensor have been investigated in this work: a fibre optic and a planar waveguide based sensor, both of which can be easily incorporated into simple, low cost systems that use existing fabrication techniques.

Firstly, a novel method of fabricating optical fibre based micro-optic sensors was developed. By laser machining a fluidic channel through an optical fibre embedded in resin, device fabrication times are short and accurate alignment of the fibres is possible, as well as any dead-volumes being avoided when compared to other methods. These devices were tested using various dye and latex bead solutions.

The results obtained using the fibre-based detector show that the dyes used agree reasonably well with the Beer-Lambert law, although an offset was observed as well as saturation above a certain concentration. Particle detection was not as sensitive as had been hoped, as it was not possible to detect single particles, although it was possible to detect particle solutions. It is expected that development of the initial fibre-based design could also achieve such sensitivities, although this was not pursued. Instead, a more flexible waveguide system was developed without the limitations associated with fixed fibre diameters and limited on-chip paths.

Secondly, planar waveguide based devices were developed that were compatible with existing fabrication techniques and used to investigate the properties of cell solutions. By using excimer laser machining to define the fluidic channels, optical fibre alignment trenches and optical waveguides, great flexibility was permitted in the optical path layout of the devices. This also ensured that the structures machined were dimensionally accurate, as well as allowing fabrication of reproducible devices. As before, laser machining the fluidic channel through the optical waveguide structure created a fluidic channel with a constant cross section that had no discontinuities between the channel wall the end of the waveguide. This property is beneficial, as there is little chance of particles sticking to the joint that may be present if other fabrication processes were used. Two planar waveguide device designs were fabricated, demonstrating that arbitrary waveguide structures can be machined and successfully

used to guide light on-chip, from an off-chip source, then off-chip again to an external sensor. Another advantage of planar waveguide based devices is that they allow for the inclusion of optical splitters and re-combiners on-chip, removing the need for multiple fibre connections or additional external hardware.

However, the results of using cell slugs did not obey the Beer-Lambert Law, most probably due to the high cell concentrations used. This probably caused multiple scattering events within the analyte, decreasing the linearity of device measurement. Although cell detection was possible using the planar based devices it was not possible to detect low concentrations of cells, as was hoped. This is primarily because the cells were translucent, hence minimally absorbing, as well as being small (~6μm diameter).

Higher sensitivities can be expected if particle suspensions using light-blocking particles were used, as this would increase the attenuation per particle of the incident light beam. A more sensitive method of detecting particles would be to use light scattering, which could easily be implemented either by altering the detector design or if suitable on-chip emitters were developed.

Although the high detection sensitivities initially hoped for were not achieved during this work, the initial aim of fabricating optical detectors that can be easily integrated into existing fabrication techniques and allow flexible, arbitrary waveguide shapes has been met.

An optical detection system is also advantageous, as there is no electrical noise injected into the system that may interfere with other electrical signals used in a complete analytical device.

5.6 References

[1] 'Polymer guided wave integrated optics: an enabling technology for micro-opto-electro-mechanical systems', L. A. Hornak, K. S. Brown, B. J. Taylor and J. C. Barr, *Proc. SPIE* **3008** (1997) 124-135

[2] 'Optical particle detection integrated in a dielectrophoretic lab-on-a-chip', L. Cui, T. Zhang and H. Morgan *J. Micromech. Microeng* **12** (2002) 7-12

[3] 'Optical technique for measuring the positive and negative dielectrophoretic behaviour of cells and colloidal suspensions', M. S. Talary and R. Pethig, *IEE Proc.-Sci. Meas. Technol.* **141** (1994) 395-399

[4] 'Integrated diode detector and optical fibres for *in situ* detection within micromahcined polymerase chain reaction chips', C. G. J. Schabmueller, J. R. Pollard, A. G. R. Evans, J. S. Wilkinson, G. Ensell and A. Brunnschweiler, *J. Micromech. Microeng.* **11** (2001) 329-333

[5] 'Integrated bio/chemical microsystems employing optical detection: the clip-on', O. Leistiko and P. F. Jensen, *J. Micromech. Microeng.* **8** (1998) 148-150

[6] 'Microfluidic systems with on-line UV detection fabricated in photodefinable epoxy', R. J. Jackman, T. M. Floyd, R. Ghodssi, M. A. Schmidt and K. F. Jensen, *J. Micromech. Microeng.* **11** (2001) 263-269

[7] 'Fibre optic sensor technology: an overview', K. T. V. Grattan and T. Sun, *Sensors and Actuators* **82** (2000) 40-61

[8] 'A high density microchannel network with integrated valves and photodiodes', D. Baechi, R. Buser and J. Dual, *Sensors and Actuators A* **95** (2002) 77-83

[9] 'An optical fibre sensor for particle concentration measurement in water systems based on inter-fibre light coupling between polymer optical fibres', F. H. Zhang, E. Lewis and P. J. Scully, *Transactions of the Intitute of Measurement and Control*, **22** (2000) 413-430

[10] 'Development of Biofactory-on-a-chip technology using excimer laser micromachining', R. Pethig, J. P. H. Burt, A. Patron, N. Rizvi, M. S. Talary and J. A. Tame, *J. Micromech. Microeng.* **8** (1998) 57-63

[11] 'Polymer waveguide devices with passive pigtailing: an application of LIGA technology', H.-D. Bauer, W. Ehrfeld, M. Harder, T. Paatzsch, M. Popp and I. Smaglinski, *Synthetic Metals* **115** (2000) 13-20

[12] 'A micromachined connector for the coupling of optical waveguides and ribbon optical fibres', M. de Labachelerie, N. Kaou, V. Armbruster, J.-C. Jeannot, P. Mollier, H. Porte and N. Devoldere, *Sensors and Actuators A* **89** (2001) 36-42

[13] 'Two-step process for micro-lens-fibre fabrication using continuous CO2 laser source', A. Malki, R. Bachelot and F. VanLauwe, *J. Opt. A: Pure Appl. Opt.* **3** (2001) 291-295

[14] 'Fibre alignment – fibreoptic end-lens facilitates light coupling', R. Roux, *Laser focus World* **30** (1994) 32

[15] "*Colloid & Surface Chemistry*", D. J. Shaw, Butterworth Heinemann, 1996, Oxford, UK

Chapter 6

Development of greyscale mask micro-fabrication technology

6.1 Introduction

Conventional micromachining processes, such as photolithography and excimer laser machining, are best described as planar processes. In other words they are optimised to produce shallow structures at the surface using binary masks. While these processes are widely used in micromachining to create planar micro-structures, there is also a need to use micromachining technology to form non-planar structures, for example micro-lenses and other micro-optical components [1-10].

Although photolithography may be adapted, e.g. by increasing the exposure or development times, to produce various wall angle profiles, the effect is uniform over the entire sample [11]. Alternatively, multiple exposures can be used to create varied depth of exposure over a sample [12]. More complex patterning, however requires multiple masks coupled with several alignment steps, which increases complexity. Laser machining can be used to create non-planar structures using mask-dragging [13, Chapter 2.4.1] but more than one mask is required to change the depth of machining in different sections. Stereolithography has much greater potential for creating three-dimensional structures, although some quantisation levels are usually present [14-16] and the process requires additional hardware.

Existing equipment and processes that use binary masks to selectively pattern the workpiece can be used to fabricate non-planar structures if a suitable greyscale, or halftone mask is used. Instead of either blocking, or permitting incident radiation to pass, as is the case with binary masks, greyscale masks allow the amount of transmission to be controlled. This has the advantage of not requiring additional equipment, as well as allowing structures to be produced quickly and simply using a single mask to expose the workpiece.

During the present work, greyscale masks have been implemented successfully in both photolithographic and excimer laser fabrication processes, allowing complex three-dimensional shaping of structures. The masks used were fabricated in-house using conventional production techniques and the laser mask fabrication techniques described in Chapter 4. Greyscale masks were produced rapidly using software developed to create the required mask patterns and allowed complex topographies to be computer simulated or fabricated. For example, a micro-fluidic manifold system was designed and fabricated to demonstrate the potential of this fabrication method [17].

6.2 Greyscale masks

Both conventional photolithography and excimer laser machining are capable of patterning the workpiece using binary masks (Chapter 4). Photolithographic masks are used to selectively expose a radiation sensitive material completely, allowing subsequent chemical processing to remove either exposed or unexposed regions depending on the resist polarity. This allows selected areas of the resist to be completely removed and structures to be formed. If the exposure dosage is halved, then the exposure depth will also be halved and development will cause partial removal of material, although this will be a uniform effect over the entire surface of the workpiece. Similarly in laser machining, if the total energy applied per cm^2 is halved, the ablation depth will halve as well. Hence, by applying a suitable total illumination energy density and varying the transmission of the mask, the exposure at each point on the workpiece can be controlled. Thus by controlling the transmission across a mask, the local erosion rate can be controlled, hence allowing complex, three-dimensional structures to be created.

6.2.1 The concept of greyscale masks

The use of greyscale masks to achieve three-dimensional machining is readily described with the aid of Figure 6.1. The required structure is a 'V-groove' (Figure 6.1a), to be used for optical fibre alignment. The energy density needed to produce the structure is shown in Figure 6.1b. Maximum energy is needed at the maximum depth of the

channel, to produce the maximum erosion rate. No erosion should occur either side of the V-groove. The walls of the V-groove are angled at 45 degrees and so the energy density along the walls should increase linearly from some minimum threshold value to that required for maximum material removal. The threshold value is either the ablation threshold of the material being excimer laser machined, or the minimum exposure energy required to expose the radiation sensitive material used in a photolithographic process. Figure 6.1c shows a representation of the mask that will produce the various energy transmissions required to machine the workpiece into the V-groove structure. The areas of zero transmission are the black regions, white regions represent the areas of maximum transmission. The grey levels represent the varying transmission required to produce the transmission gradient and hence the final structure.

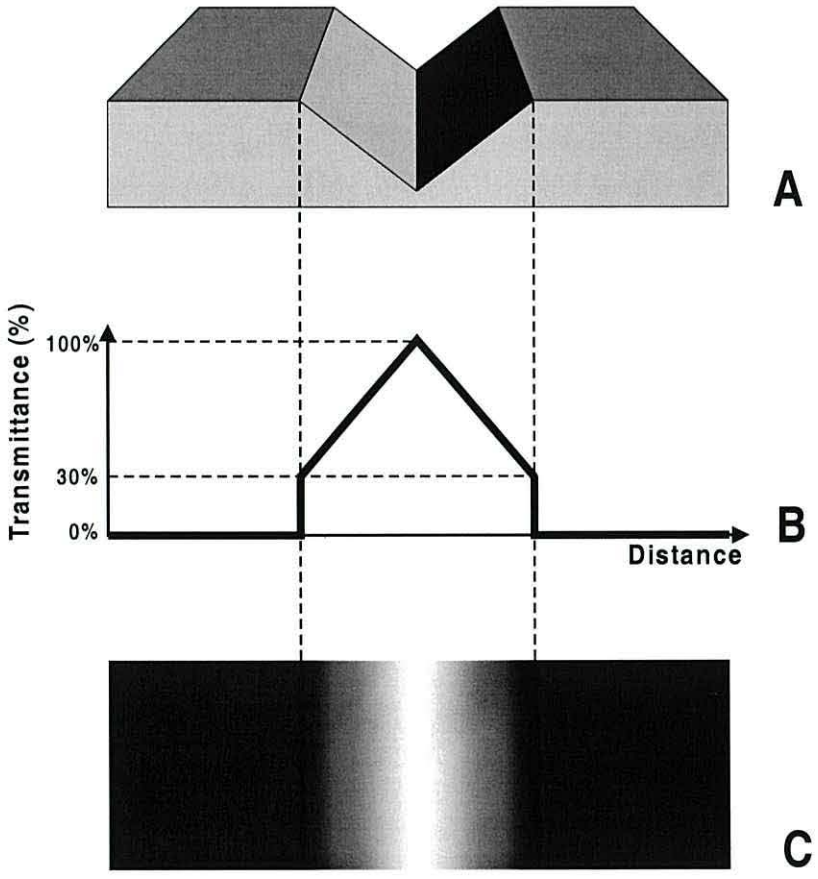

Figure 6.1 *An illustration of the function of a greyscale mask. (a) The structure to be fabricated, in this case a V-groove. (b) Plot of the energy density required to form the V-groove using a single mask process. (c) A representation of the greyscale mask required to produce the V-groove structure.*

Greyscale masks were created in this work by dividing the mask area into sub-units, ranging from 5μm to 15μm, depending on the application and altering the ratio of transmissive to non-transmissive regions of each sub-unit. This has the effect of controlling the average transmission through each sub-unit. By setting the size of the sub-unit to be below the resolution of the process in which the mask is to be used, the individual features in the sub-unit will not be resolved. Instead the workpiece would experience an average energy density, dependent on the average transmissivity of the appropriate sub-unit.

The processes used for creating greyscale masks were based on conventional binary mask technology, namely photographic mask plates (Chapter 3.5.1) and laser machined mask plates (Chapter 4). This allowed low cost masks to be produced quickly using commercially available or laser projection techniques.

6.2.2 Mask patterning options

Several methods of creating greyscale masks using various patterning techniques to produce an average transmission were considered and are described in the following. Strong emphasis was placed on ease of implementation into a computer based mask design utility. As such mask patterns are time consuming to produce manually due to the large number of elements, as well as error-prone: an algorithm that can be computer implemented is highly beneficial.

Fortunately, the expansion in the computer graphic industry in recent years has led to the publication of several dithering algorithms suitable for converting between desired image intensity and binary dot patterns, which can readily be applied to producing greyscale mask transmissions.

The common requirement of every patterning technique is that the process the mask is used in does not resolve the mask features, but approximates to an average transmission. This determines the size of the sub-units and depends on the process in which the masks are to be used.

6.2.2.1 Line / space ratio

A simple method of controlling mask transmission is to use a series of parallel lines of different width, spaced on different centres. The average percentage transmission, %T, for a series of constant line-space ratio elements is given as

$$\%T = \frac{S}{(S+L)} * 100 \qquad (6.1)$$

where L is the width of the line and S the gap between the lines. Although not ideal for a computer implemented mask design program due to the one-dimensional nature of the structure, this scheme can be implemented semi-automatically using a suitable PC based drawing package (Autosketch, Autodesk, Inc.). The designs were then plotted commercially at 4000 lpi, and used to produce greyscale masks using conventional mask fabrication techniques (Chapter 3.5.1). The maximum width of the line and space used are determined by the maximum resolution of the mask production system being used. The minimum feature that could be produced using the in-house photographic mask production system was limited to approximately 6μm by factors inherent in the process. However, producing masks by excimer laser machining allowed micron-sized features to be fabricated. This type of greyscale mask was used during the initial testing phase to determine the resolution of the photolithographic processes used.

6.2.2.2 Variable rectangular apertures

A modification of the line / space system previously described is to place another set of lines at 90 degrees to the first, so each line is on the edge of a sub-unit of the mask. This will have the effect of creating varying sized 'windows' and increase the transmission control as two factors (the thickness of the horizontal and vertical lines) now determine the transmission. This approach has been used in excimer laser machining, but the measured depth reported was not a linear function of the theoretical mask transmission used [18].

6.2.2.3 Binary dithering algorithms

Binary dithering algorithms are well documented and are commonly used in computer graphics applications to provide an approximation to a grey tone level on binary devices, such as laser printers. These algorithms are optimised for computer based implementation by controlling the spatial density of the bilevel display used [19-21]. This makes such algorithms ideally suited to creating the mask patterns required for greyscale masks. Furthermore, many of the problems anticipated in greyscale mask fabrication are common to and have been overcome in the algorithms developed for greyscale printing.

The visual appearance of an image, a relatively subjective quantity, is of great relevance in computer graphics and associated displays – regardless of the viewer, the image must be acceptable [22, 23]. The appearance is not critical, however, to the task in hand. The requirement is simply that the average energy density transferred by the greyscale mask to the workpiece corresponds to an intended energy density, without any mask features being resolved. This consideration negates the issues applied to generate visually acceptable images, as well as those of luminance [22] and reflectance correction for various forms of display and output devices, area of interest in computer graphics. In particular, the size of the screen pitch used in printing must be as small as possible to increase the aesthetic quality of the image. In greyscale mask patterning on the other hand, the only criterion is that the pitch must be smaller in dimension than the resolution of the machining process. Another property considered in computer graphics is the shape of the display elements used. As no such elements exist for the purposes of this work, these too are unimportant. This allows the shape of pixels and the screen angle (the angle between vertical and the grid defining the elements) to be chosen to allow simple implementation, so greatly simplifying the choice of algorithm used.

Square elements on a regularly spaced grid were used in the present work, so that the dithering process remained simple but with sufficient resolution to allow greyscale masks to be created without the individual pixels being resolved. The algorithm used is considered in the next section where the emphasis is on simple processing operations due to the large amount of data generated when producing such masks.

6.2.2.4 Clustered-dot-ordered-dither

The clustered-dot-ordered-dither (CDOD) algorithm [24] is a widely used halftoning technique. It is optimised to produce the appearance of grey levels on devices such as printers where producing grouped pixels is easier than producing discrete pixels, as is the case in a printing press [25]. Hence, the CDOD algorithm is also ideally suited to photographic mask production techniques, as grouped elements will be produced with less error (caused by diffraction) than a series of discrete features. When the greyscale patterns are created on the masks, reproduction accuracy is crucial, as the patterns determine the effective mask transmission. The method is also well suited to computer generation of the mask pattern and has been used successfully in both investigations.

The algorithm allows an approximation of a continuous tone picture to be displayed on a binary output device by controlling the ratio and organisation of the number of pixels per area that are 'on', compared to those that are 'off'. Throughout this work, a screen angle of 0° was used, as opposed to the standard 45° screen angle used in the printing press due to the spatial frequency response of the human eye. The algorithm converts continuous tone grey levels into binary patterns by comparing the actual level to a series of thresholds contained in a matrix. When the appropriate threshold value has been determined, halftoning using the clustered-dot-ordered-dither algorithm is extremely simple. It is because of this that the algorithm is widely used in other applications.

The original image is divided into a series of discrete levels, which can then be represented by the relevant number of pixels using a common 'threshold matrix' that determines the position of the 'on' pixels, in this case non-transmissive mask regions. A similar approach was used to create the greyscale mask patterns, except that the required height map of the surface replaced the continuous tone picture. The output of the algorithm is predetermined, with the relationship of each of the levels 'on' pixels close to the previous levels, as opposed to a random process that will distribute the pixels, which is not optimum for photographic mask manufacture. The output level generated for each sampled pixel of the design is not dependent on any other sample area, greatly simplifying the greyscale pattern generation step. No storage or subsequent processing is required, which is not the case when error diffusion algorithms are implemented.

The CDOD algorithm was applied to create greyscale mask patterns by subdividing the sub-units into an n by n grid. The algorithm was then used to determine which elements of the grid were filled and which were left clear. The connectivity between filled elements of the grid is maintained at all times. Figure 6.2 shows an example of a 36-element threshold array, where the numbers are arranged to provide a transmission corresponding to pixels 1 to 11 being set to 'on'. The pre-determined arrangement of the pixels allows simple computer implementation to create the greyscale masks by converting the required structure height into a percentage of the deepest feature and using an appropriate look-up table.

In the case of Figure 6.2, n=6 which produces 37 discrete transmission levels (i.e. n^2+1 grey levels) in the mask. The number of transmission levels can of course be changed by changing n.

35	30	18	22	31	36
29	15	10	17	21	32
14	9	5	6	16	20
13	4	1	2	11	19
28	8	3	7	24	25
34	27	12	23	26	33

Figure 6.2 *36 element threshold array, formed by a 6 x 6 grid (n = 6). This allows 37 separate transmission levels, each allocated to a range of approximately 2.7%.*

Quantisation errors will be unavoidable. For example, if a transmission of 32% is required then a choice must be made between level 11 which corresponds to approximately 30.6% in a 6 x 6 level grid and level 12 corresponding to 33.3%. Normally the lower level is taken. It should be noted that the inverse of the graphics dithering process, where the set number of pixels are turned 'on' to represent the grey

level of the original, is also used in creating greyscale mask patterns. The polarity of the dithering algorithm is determined by the process the mask is to be used in. If creating greyscale masks for use with the photolithographic process when using photonegative materials, the pixels are cleared from a normally non-transmissive state. However, if photopositive materials are being used or the mask was to be implemented in the laser system, the inverse of this process is used, as the less light transmitted, the more material remaining. The mask transmission generated at level l using an n x n grid can be determined, for a photolithographic greyscale mask used to expose a photonegative material, by:

$$\%T = 100 - \left(100 * l * \frac{1}{n^2} \right) \tag{6.2}$$

And for exposing a photopositive material or as use as a laser greyscale mask by:

$$\%T = 100 * l * \frac{1}{n^2} \tag{6.3}$$

Quantisation errors can be reduced by increasing n. However, there will be a maximum limit governed by the minimum resolvable feature size of the process the mask is used in and the smallest feature that can be created.

6.2.2.5 Periodic grids

An alternative method of creating greyscale masks relies on placing suitably sized elements on a regular, periodic grid to create an average transmission. Others [3, 26] have used this method in various forms including variable sized dots, or apertures on a grid [26] and variable dimension squares on a regular grid [3]. However, the result is the same in that the dimension of the mask features are below that which the process can resolve.

Implementing greyscale transmission by varying the diameter of the elements (dots or apertures) on a regular grid was also tested in the present work. Figure 6.3 shows,

diagrammatically, the layout of the elements considered in the work as well as the measurements used to define the element diameter and the grid pitch. Here, the arrangement used consists of non-transmissive 'dots' on a clear mask background, although the inverse can also be used, in which case the elements are apertures on a non-transmissive mask background.

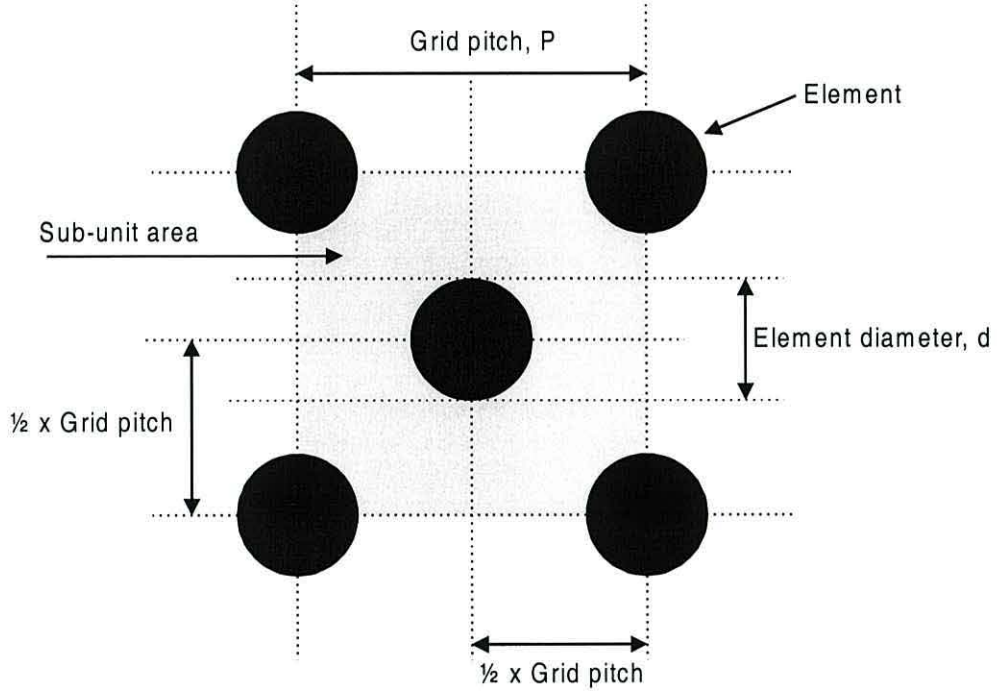

Figure 6.3 *Diagram showing the layout of the elements on the grid and the associated spacings used. This method was successfully used to control mask transmission. The elements are defined as apertures on a non-transmissive background and non-transmissive 'dots' on a clear background.*

The relationship between the percentage transmission, %T of the mask, the grid pitch, P and the element diameter, d, is given by

$$\%T = \left(1 - \frac{2\pi\left(\frac{d}{2}\right)^2}{P^2}\right) * 100 \qquad (6.4)$$

However, if apertures are used instead of dots, Equation 6.4 becomes

$$\%T = \left(\frac{2\pi\left(\frac{d}{2}\right)^2}{P^2} \right) * 100 \qquad (6.5)$$

Figure 6.4 shows a plot of the average mask transmission obtained when the grid pitch is constant, in this case $P = 8$, but the elements used, which can be either apertures or dots, are varied in diameter. The units used are arbitrary and would in practice depend on the resolution of the process used, although the relationship is the same.

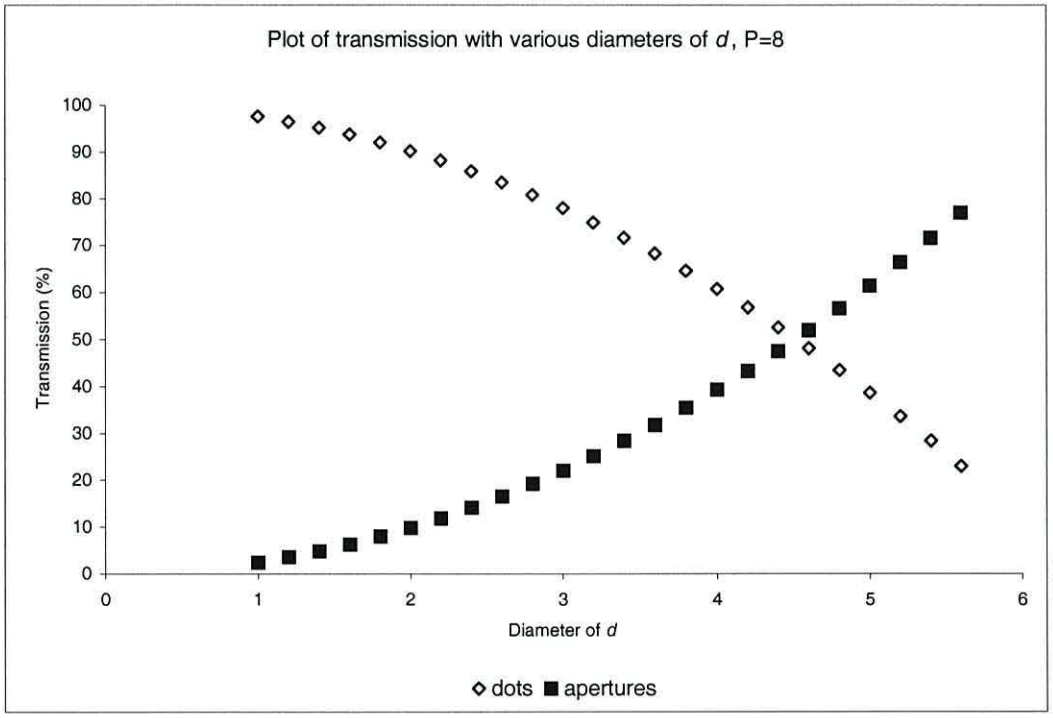

Figure 6.4 *Plot of the average transmission of a mask consisting of variable diameter dots on a constant grid spacing, P=8 (arbitrary units).*

The plots show that where the elements are variable diameter apertures cut into a non-transmissive background, good control of transmission is possible between 0% transmission and approximately 50%. Although a mask with transmissions above 50% can be fabricated using this system, better resolution is obtained using non-transmissive elements on a clear background for this range. It should also be noted that if d is increased beyond a certain point, the dots will overlap and Equation 6.4 and Equation 6.5 are no longer valid. However, this was not found to be a problem as it was

not necessary to exceed such a dot diameter to obtain a complete range of transmissions. In the case considered here, d ~5.65.

When the diameter, d, of a single element was kept constant, in this case d=1, but the pitch, P, of the grid was varied, the variation in transmission is shown in Figure 6.5. Again, transmission over the whole range is best controlled using a combination of transmissive and non-transmissive elements, as before. Here, Equations 6.4 and Equation 6.5 are valid as long as P is larger than 1.42.

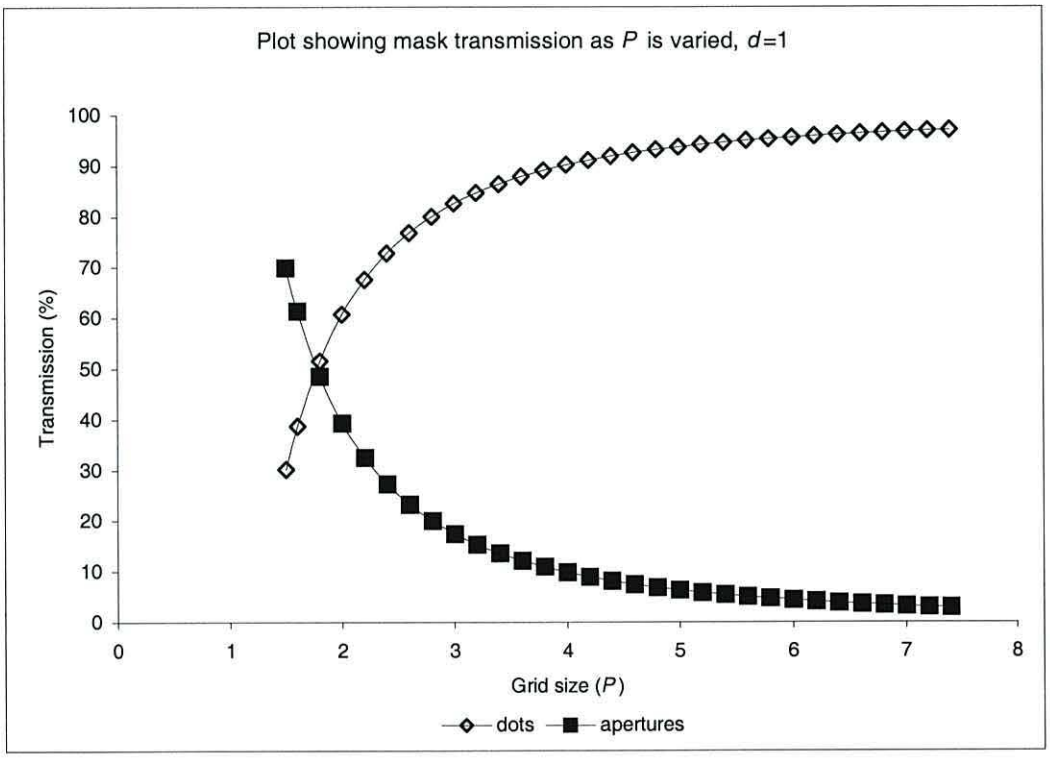

Figure 6.5 *Plot of transmission using a variable pitch grid and constant diameter elements.*

Although this process of greyscale mask patterning was used to produce varying amounts of exposure, it was still preferable to use the clustered-dot-ordered-dither algorithm or mask pattern generation due to the simpler implementation process.

6.3 Implementing greyscale masks in photolithography

Utilising greyscale masks in photolithographic processes allows the production of complex three-dimensional structures in a single exposure. Others have reported the

use of greyscale (or halftone) masks to create micro-components and structures in thick photoresists [1, 3-7, 11, 27, 28]. Typically the process used chrome on quartz masks which were created using E-beam lithography [1, 27, 29-32]. This type of mask fabrication process allows very high-resolution masks to be fabricated, with nanometer resolution. They are, however, expensive to manufacture with an associated long turnaround time, because a very small beam has to cover a much larger area. As it is expensive to produce such masks, cheaper photographic plate masks were used in this work.

The requirements of such masks and the relationship between exposure fluence and exposed depth for different materials were investigated and three-dimensional structures, including a fluidic manifold, fabricated in a single exposure.

6.3.1 Mask requirements

To implement greyscale masks with the existing photolithographic process requires knowledge of several factors. The smallest feature that can be resolved and the relationship between exposure fluence and exposure depth in the photosensitive material are important. The structures to be fabricated were tens of microns deep so that conventional photoresists were too thin, e.g. S1818 is typically 1.5μm thick. Therefore, the structures were fabricated either in a dry-film laminate (Laminar 5038, Ozatec) or in a high build photosensitive epoxy such as SU8 (Microlithography Chemical Corporation). Dry-film laminate is available in a range of thicknesses up to 100μm and is simple to use – it requires only a substrate pre-clean prior to lamination. SU8 is a well-known and well-characterised high-build, photodefinable epoxy compound commonly used in microstructure fabrication [33, 34].

Preliminary experiments were undertaken to determine the minimum amount of energy required to polymerise the complete thickness of the relevant photosensitive layers. The glass substrates used were cleaned (in a class 10,000 cleanroom) prior to coating to remove any particulate or grease contamination from the surface. This provided a suitable surface onto which the photosensitive materials could be applied.

The photosensitive materials were characterised by exposure to the collimated (1:1) UV source of the Tamarack MAS12 mask aligner. Incremental increases in exposure over the sample surface was achieved by setting a constant total exposure time and revealing the surface in 1mm strips by manually moving a blanking sheet over the surface. The procedure produced strips of higher and higher exposure which when developed produced a staircase structure (Figure 6.6).

The developer used for the dry-film laminate was 1% sodium carbonate in water. The solution was heated to 30°C and continuously sprayed at low pressure onto the sample using a Girojet II (CIF, France) PCB development tank. The SU8 was developed for 7 minutes in propylene glycol methyl ether acetone (PGMEA) to reveal the material polymerised by exposure to the UV source.

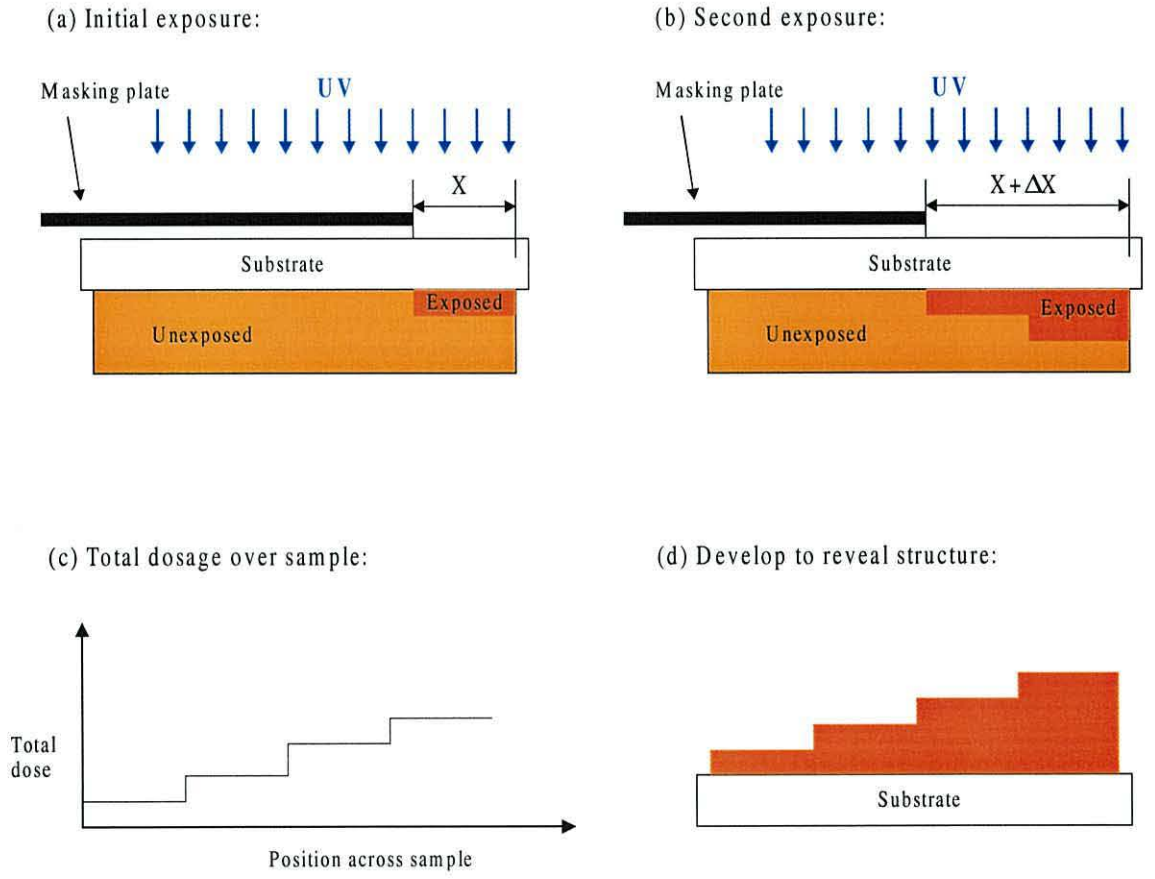

Figure 6.6 *Calibrating the relationship between exposure dose and exposure depth. (a) the first exposure (b) the next exposure (c) the dose profile and (d) the structure produced by developing photoresist.*

The staircase structure allowed the total exposure dose to be correlated with height of the material remaining. Repeat experiments confirmed that the process was both reliable and repeatable. Figure 6.7 shows the results of these experiments for the dry-film laminate. The results of the SU-8 experiments are shown in Figure 6.8.

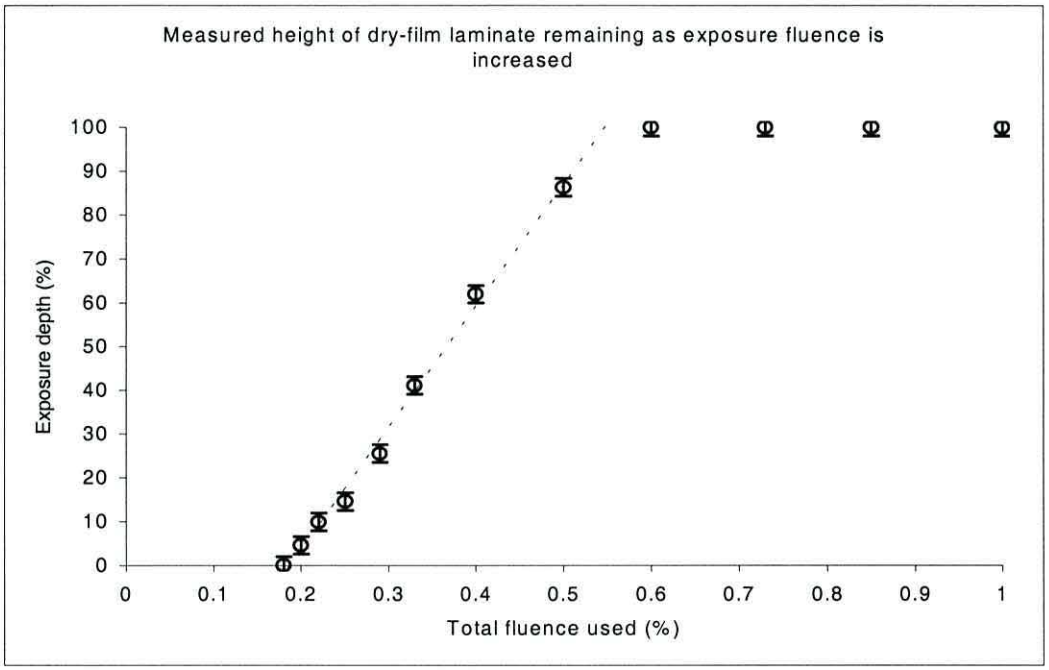

Figure 6.7 *Plot showing the relationship between exposure fluence and exposure depth, shown in normalised form.*

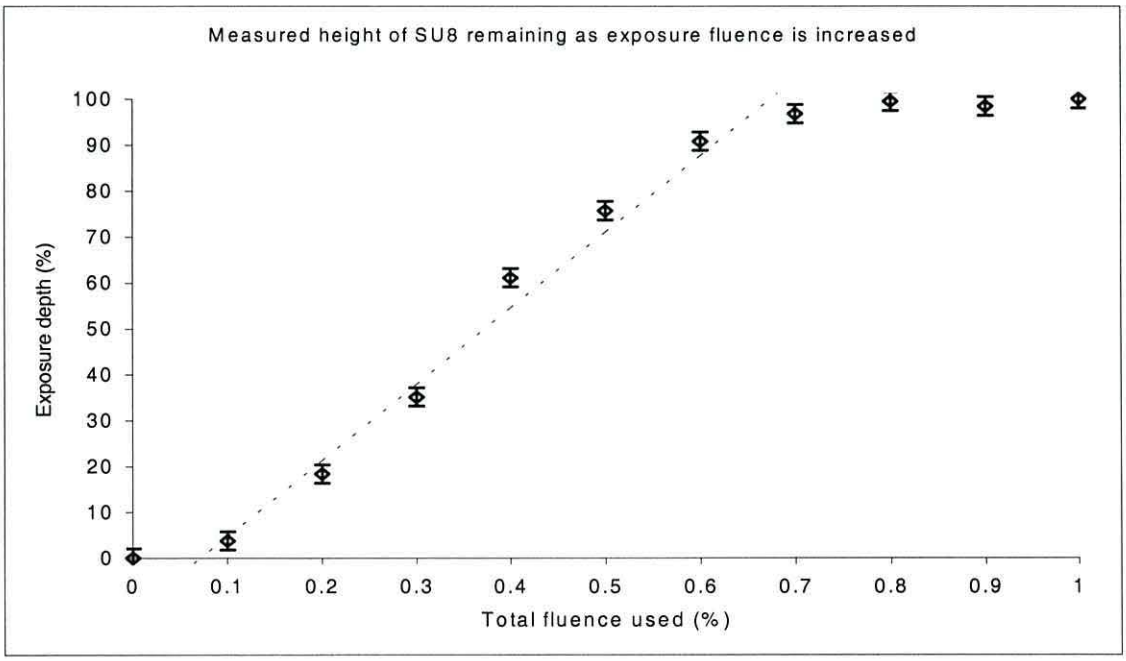

Figure 6.8 *Plot showing the relationship between curing depth of SU8 epoxy and applied total energy, in normalised form.*

From these results it can be seen that the response is linear with a least-squares fit to the linear regions of both plots yielding a correlation coefficient, R^2, of 0.9948 for dry film laminate and 0.9811 for SU-8. A threshold energy level can be seen in both cases, below which there is no effect on the photosensitive material. Saturation occurs when the complete thickness of the photosensitive layer has been exposed. For the case of Laminar 5038 dry film photoresist, 100% exposure fluence is 85 mJ/cm^2. The graph shows zero exposure below a threshold of 30% (approximately 25 mJ/cm^2). Above the threshold, depth is a linear function of fluence until complete exposure occurs when the entire depth of the material is exposed. Again, a threshold value exists and exposure depth is a linear function of fluence until the complete layer is exposed, in this case 100μm. From the above data, it can be concluded that by varying the transmission of a mask to provide local exposure dosages lying between the threshold and saturation, the amount of photosensitive material remaining after developing can be controlled to reasonable accuracy.

To find the resolution limits of the photosensitive materials, test masks consisting of a series of lines of different widths, ranging from 4μm to 64μm (separated by different width gaps) were created using a CAD package (Autosketch, Autodesk, Inc.). The design was plotted commercially and the patterns photographically reduced and transferred onto photographic plates in-house. These masks were then used to expose the photosensitive layers. After development, the narrowest resolvable line was ~10μm which is much larger than the smallest feature that can be produced on a photographic plate. Figure 6.9 shows another example of one of the manually created test masks used to determine the resolution limits, in this case a range of varying size squares on a fixed grid.

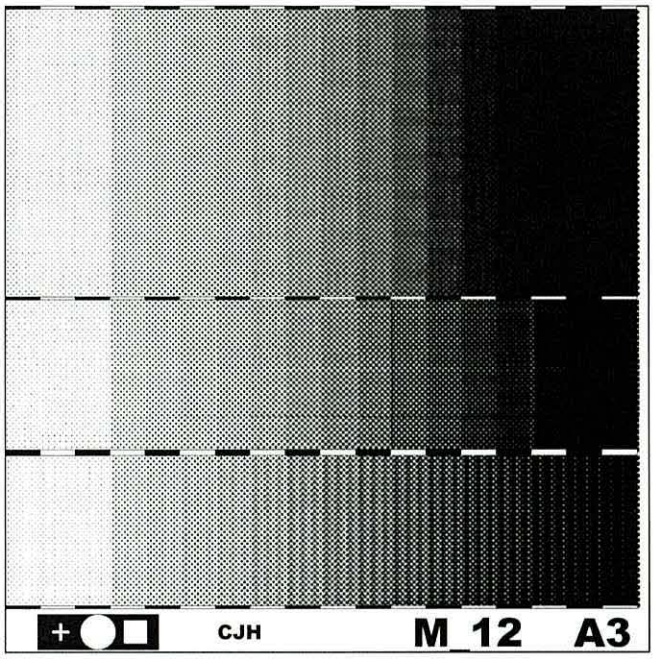

Figure 6.9 *One of the manually created test mask designs used to find the resolution limit of the photolithographic process when SU8 and dry-film laminate resists are used*

The collimation of the exposure source was measured to be approximately 3°, by exposing a wide channel and measuring the wall angle obtained. This, combined with the thickness of the resist layers used explains the relatively poor minimum resolution of the photosensitive layers.

Using the information derived above, greyscale masks were created which allowed three-dimensional structures to be fabricated in a single exposure.

6.3.2 Creating three-dimensional test structures in a single exposure

Several masks were drawn in order to test the suitability of various greyscale patterning options. Figure 6.10 shows an optical micrograph of a section of a photographic mask plate with a line-space greyscale test pattern on it. The section shown is an area of constant transmission, in this case 33% where the line widths are 10μm and the spaces are 5μm. The mask plate was photograhpically produced and is shown backlit.

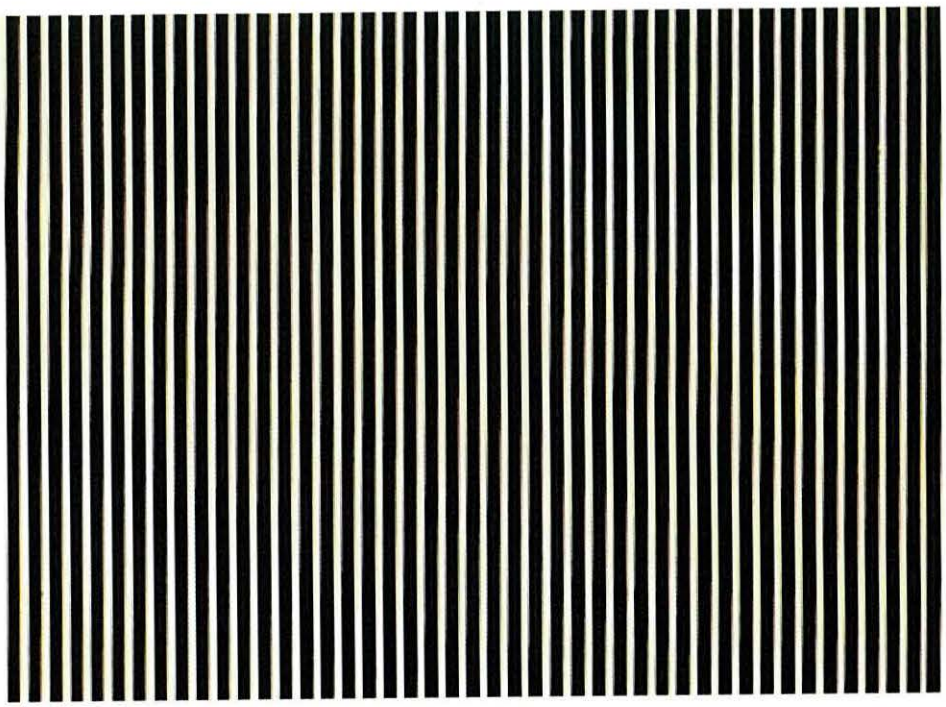

Figure 6.10 *Optical micrograph of a photoplate mask with a 33% transmission greyscale test pattern on it. The photoplate is backlit, so regions that transmit incident radiation are shown as bright areas, whereas dark areas are regions that block incident radiation.*

The actual transmission of the masks was determined by digitally capturing the image, using a digital camera attached to the microscope, and importing it to a computer. The image was then loaded into Matlab [Mathworks, Inc.] where the transmission was found by comparing the number of lit pixels to the number of dark pixels. By repeating this several times and averaging the result a good approximation to the actual mask transmission was obtained.

The correlation between the designed and actual transmission through the masks was not perfect. A constant error was present (~2.4%), which probably arose from the resolution limit of the photographic reduction system used. By compensating for the error at the design stage, the final machined features were produced to the correct dimensions.

The test masks were used to expose both dry film laminate and SU8 photosensitive layers. The experiments revealed that the greyscale masks produced the intended structures, which, in the case of the initial test masks, were flat plateaus at different heights. The measured heights of the test structures produced corresponded well with

what would be expected from the designed transmission through the mask. For example, Figure 6.11 shows the height of laminate remaining after a single exposure through a greyscale mask. In this case, 90μm of laminate was coated onto a glass substrate. The mask consisted of a series of adjacent stripes of increasing transmission, producing a staircase similar to the characterisation experiments (Figure 6.6). The various transmissions were created using the CDOD algorithm to pattern the various areas.

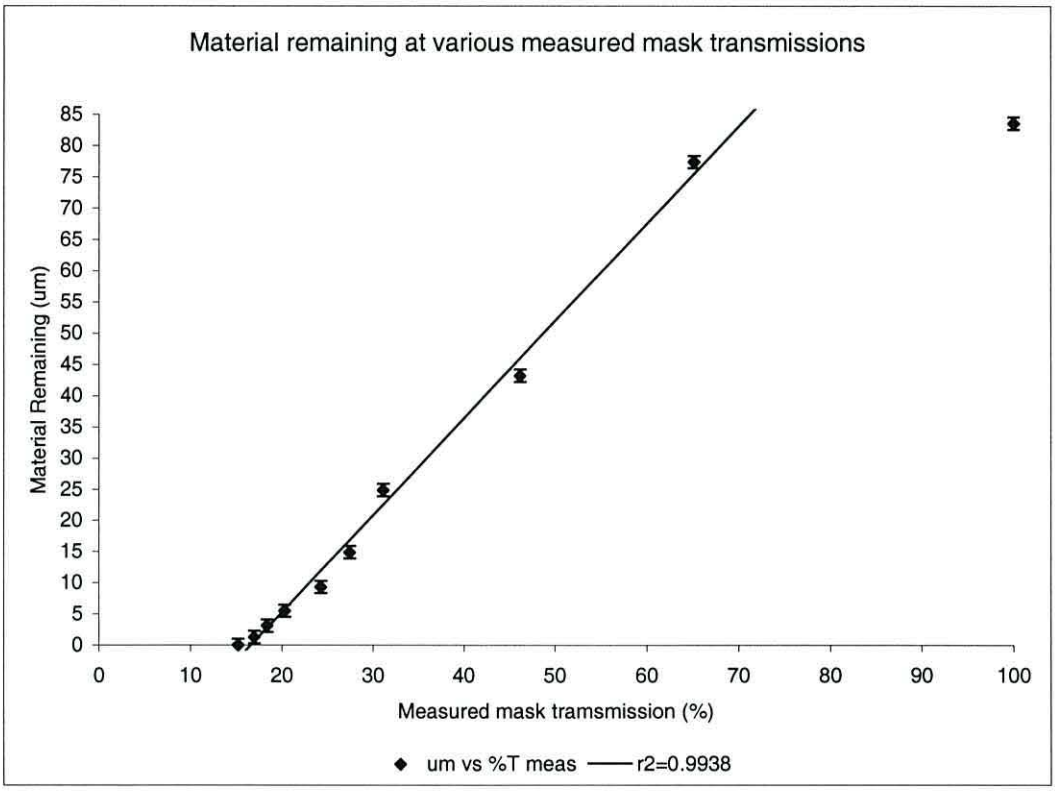

Figure 6.11 *Plot showing the height of laminate remaining after development as a function of the measured mask transmission used to expose the laminate. The various heights were produced using a single exposure of 90μm thick laminate on glass with an n=5 CDOD patterned greyscale mask that consisted of a series of increasing transmission stripes.*

The mask design was based on an n=5 clustered-dot-ordered-dither algorithm, which allowed 26 discrete levels and a pixel size of 2μm. The least squares fit to the linear portion yielded a correlation coefficient R^2 = 0.9938 indicating a high degree of linearity. Any inaccuracies present are likely to arise from the unevenness in the surface of the dry-laminate film. The surface unevenness was measured to be up to 3μm on this sample.

Having demonstrated the feasibility of using photographic mask plates as greyscale masks, a series of simple designs were drawn using Autosketch. All the designs compensated for the errors arising later during the production of the photographic plate. Various test structures were produced in the two photosensitive materials. For example, Figure 6.12 is a simulation of the greyscale mask used to create a 'spiral staircase', shown in Figure 6.13, in a 60μm thick dry-film laminate layer. The final structure is 400μm in diameter and the step heights range from 5μm to 15μm and are within 3 μm of the designed heights. The maximum height variation of each plateau is less than 1μm. Supplementary experiments were used to confirm that the orientation of the lines relative to the workpiece was unimportant.

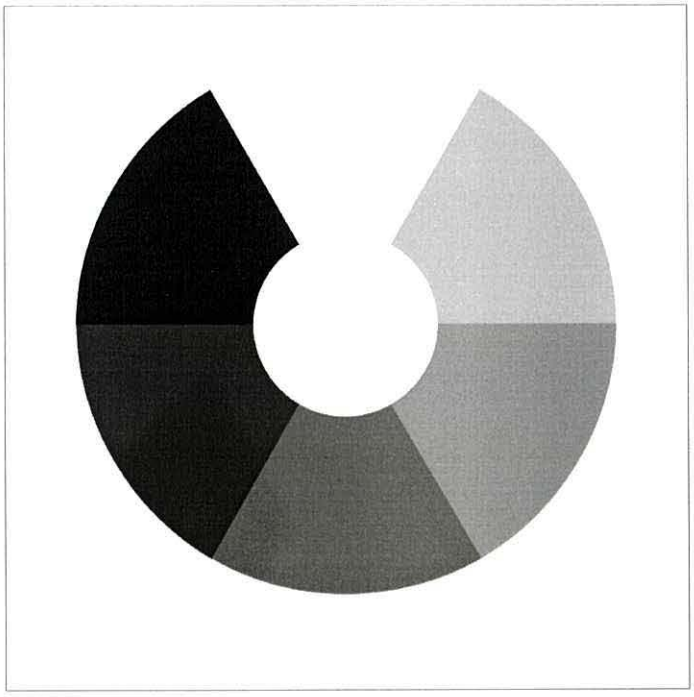

Figure 6.12 *A simulation of the transmissions in a mask used to produce a 'spiral staircase'. Black indicates zero transmission, white indicates 100% transmission. The method of transmission control implemented used vertically oriented variable mark-space ratio lines and gaps.*

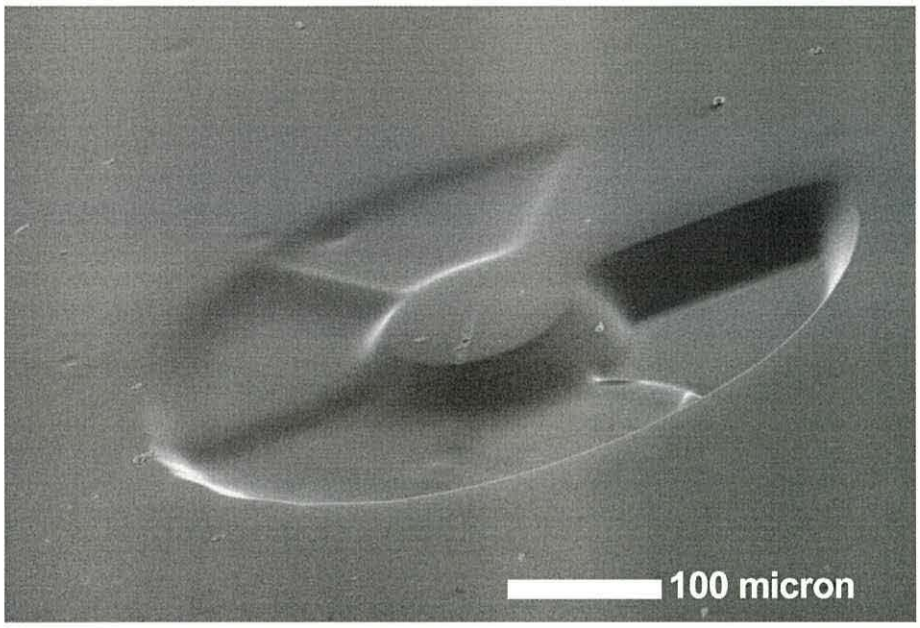

Figure 6.13 *SEM micrograph of the final 'spiral staircase' structure fabricated in a 60μm thick layer of dry film laminate using the mask design in Figure 6.12. The 'steps' are flat, with less than 1μm unevenness.*

Figure 6.14 is a SEM micrograph of a linear ramp, fabricated in a 60μm thick SU8 layer. This structure could form a micro-mirror if a suitable reflective coating, such as an evaporated metal layer, was applied to the surface.

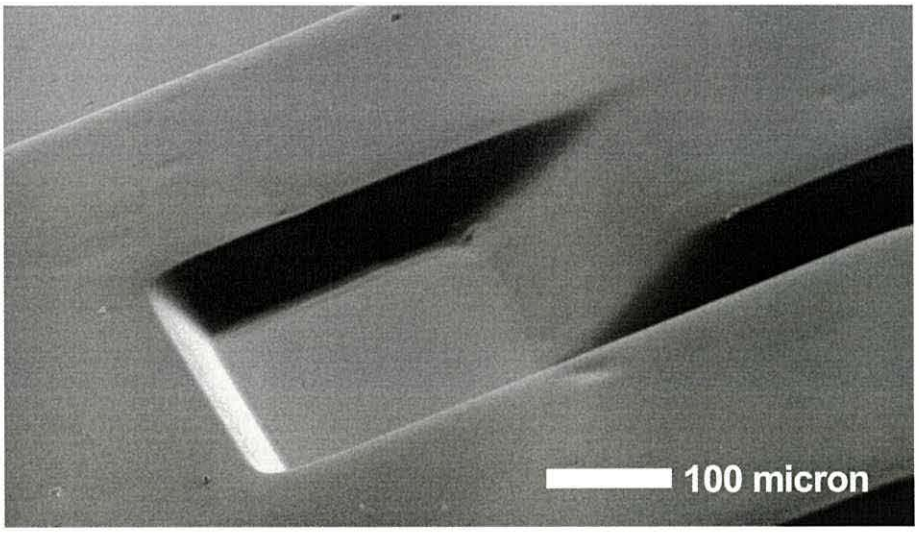

Figure 6.14 *Scanning electron micrograph of a linear ramp fabricated in SU-8. This was intended to act as a micro-mirror when coated with a reflective metal layer.*

In order to test the accuracy of the greyscale process further, a mask was designed using the CDOD algorithm, to create two constant slope ramps. Figure 6.15 shows (a) a

visualisation of the mask transmission pattern and (b) the final structure, consisting of two back to back ramps.

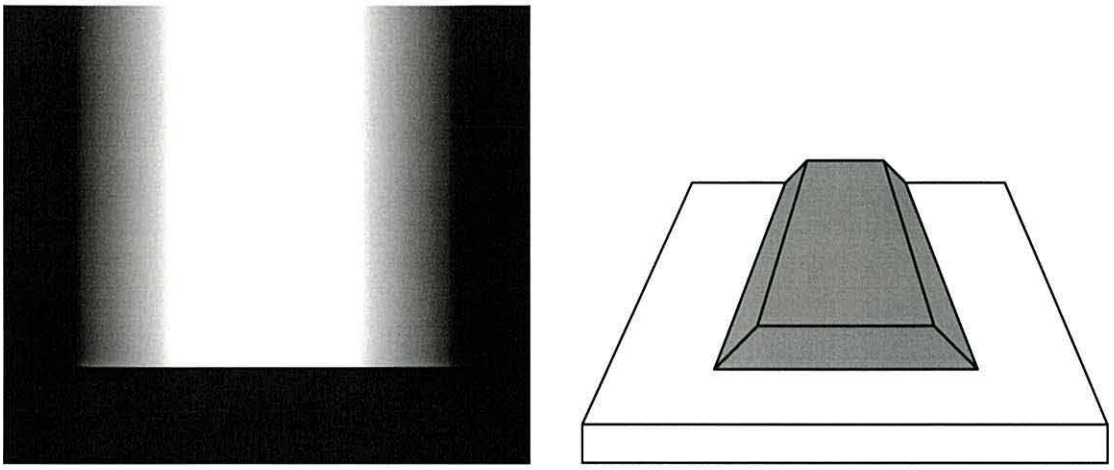

(a) **(b)**

Figure 6.15 *(a) Visualisation of the greyscale mask, with white areas being areas of 100% transmission and black areas being areas of 0% transmission. (b) Diagram of the intended final structure.*

The mask design shown in Figure 6.15 was then used to fabricate the structure shown in Figure 6.16, which is a view of one end of the two adjacent ramps with the intended design overlaid on the SEM micrograph. This was produced in a 90μm thick dry-film laminate film using a single exposure of the greyscale mask, followed by standard development.

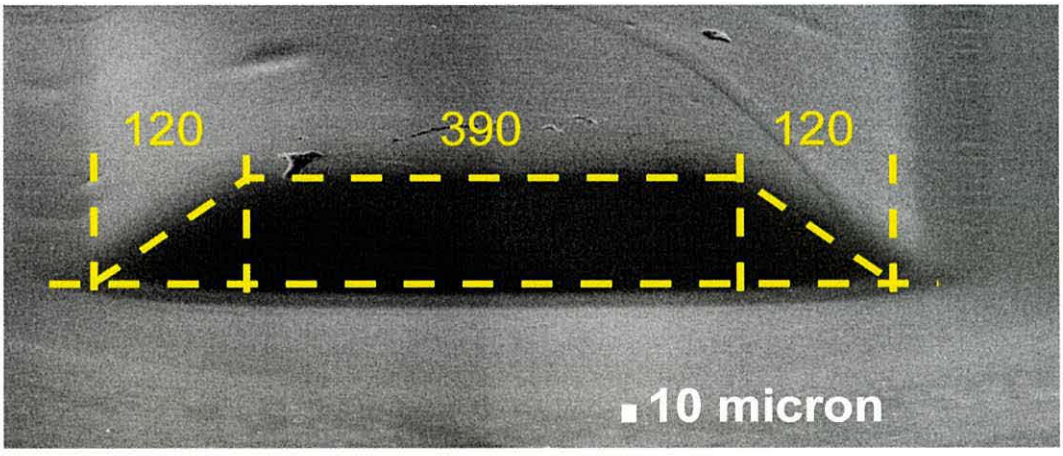

Figure 6.16 *Scanning electron micrograph of the structure fabricated from the mask shown in Figure 6.15 The ramps were produced in a 90μm thick dry film laminate. Superimposed on the SEM image is a profile of the original design.*

From Figure 6.16 it can be seen that there is a high degree of correspondence between the design and the structure produced. Although some rounding of the corners is present due to the chemical development process used, the overall shape of the structure was correctly reproduced. This is a good demonstration of the suitability of this process for accurately creating three-dimensional structures.

It was also observed that the type of greyscale mask patterning used had no detectable effect on the resulting structure: if the patterns used are below the resolution of the photosensitive material then they are not resolved and the energy transmitted per unit area is averaged. This is an important observation, as the implementation of a computer generated mask is preferable, as the mask design can be obtained faster and more accurately. If the patterns used are not important, then the algorithm used to create the dither patterns can be optimised for computational efficiency, which is beneficial. Computer mask generation also allows more complicated and larger area masks with smaller pixel sizes to be created quickly with less error, so increasing the number of transmission levels and hence vertical resolution possible.

Having produced working criteria for creating greyscale masks that allow controllable patterning of photosensitive materials, a Matlab computer program was written that can generate the required greyscale mask pattern, so removing the manual mask drawing stage. By altering the number of pixels used in each unit on the mask, it is possible to determine the number of discrete levels that can be attained. However, care must be taken to ensure that the individual pixels are not resolved. So, if the number of pixels is reduced, the dimension of each sub-unit has to decrease. Figure 6.17 shows an optical micrograph of a section of an n=6 greyscale mask. This mask was created using the Matlab program, whose output was plotted to acetate, before being photographically reduced. The individual elements used are 10μm in size and was used to pattern S1818 spin coated onto quartz. This allows 2.5μm sized elements when laser projected using a x4 projection lens, suitable for use as a photolithography greyscale mask (Chapter 4).

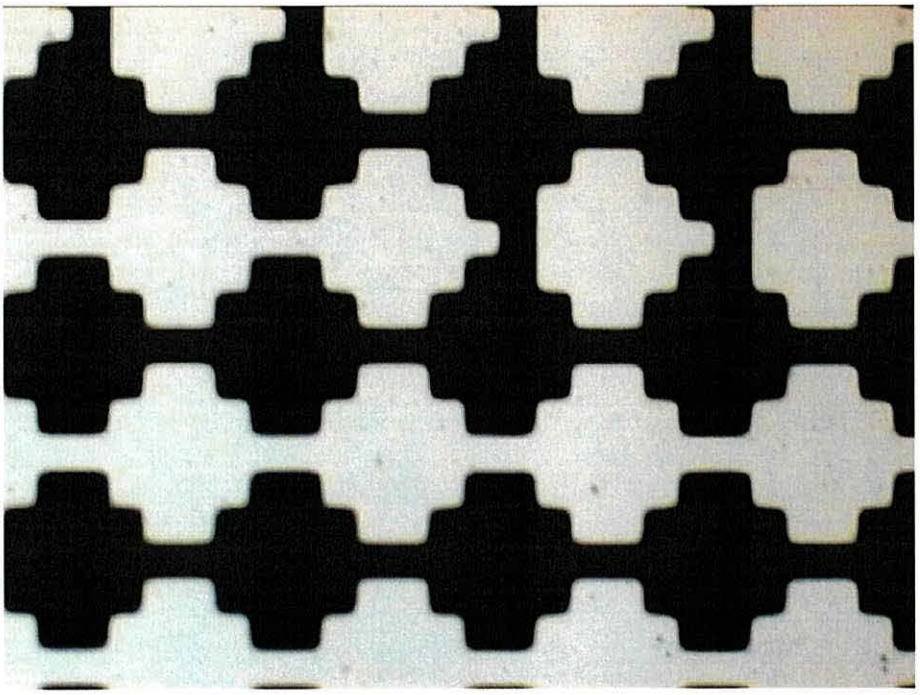

Figure 6.17 *Example of an n=6 CDOD output generated from the Matlab program.*

Although externally plotted acetate based masks could be plotted at a resolution of 4000lpi (approximately 6μm), these masks could not be used directly. Attempts to reproduce the required mask patterns were not successful, as individual 6μm features were not resolved correctly. This is most likely due to quantisation levels of the plotting process.

Computer simulation of the structure that should result from using the greyscale mask is also important in the design and development of new structures. Consequently, another Matlab program was written, which used a greyscale mask design to create a three-dimensional representation of the final structure. The three-dimensional simulation can be rotated through 360° around all three axes of rotation, to allow any area to be viewed at any angle, as demonstrated in Figure 6.18. Here, a simulated 3D view of a 4x4 microlens array is shown (Figure 6.18a), as well as the side profile (Figure 6.18b), plan view (Figure 6.18c) and a view of the structures surface from below (Figure 6.18d). The view of the structure from below is useful when the fabricated structure is to be moulded, as the moulded structure profile can also be viewed.

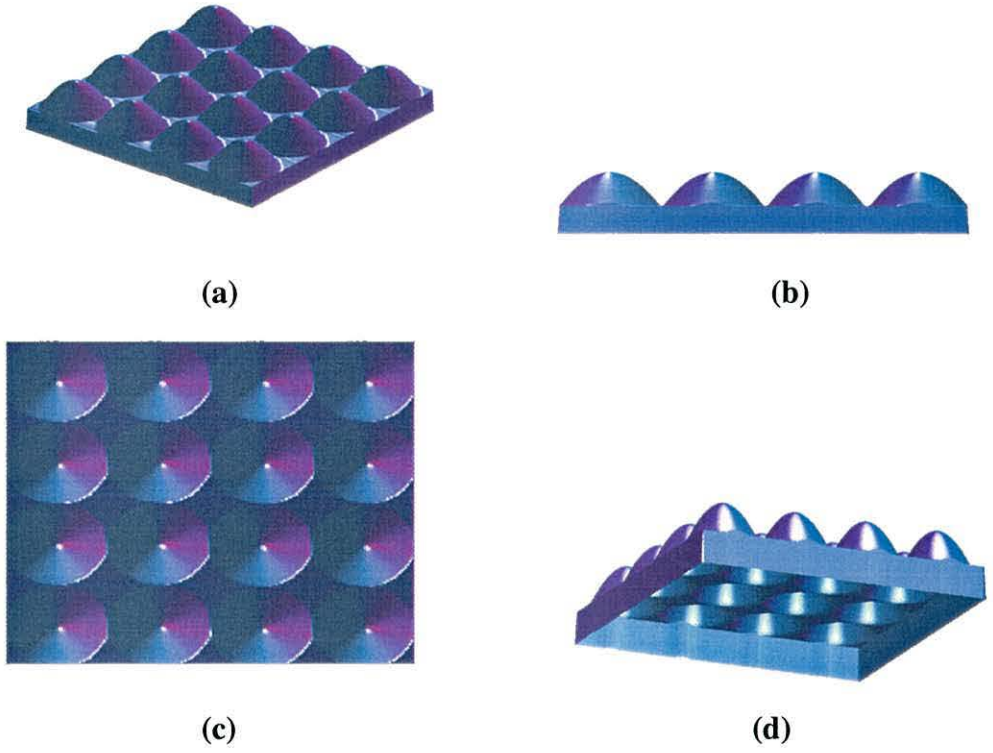

Figure 6.18 *Example of the simulation program output from a microlens array greyscale mask design. (a) 3D rendered view of the surface, (b) side profile, (c) plan view, (d) view of the surface from below the sample, useful if the structure is to be moulded.*

6.3.3 Fabricating a fluidic manifold

The ability of greyscale masks to produce complex structures accurately was further tested by fabricating a circular cross-section fluidic manifold with a controlled profile [17]. This allowed two designs to be created: (a) channels of constant cross-sectional area from two inlets through the junction to the outlet and (b) one in which the channel cross-section varied.

Figure 6.19a shows a scanning electron micrograph of a section of the first type of fluidic channel. The circular well structures, ~200μm in diameter, at the end of each channel form part of an inlet or outlet port. Contoured channels lead from the inlet and outlet ports to the 'Y' junction. This forms one half of the fluidic channel system; the complete structure is formed by bonding two such structures face-to-face to create an enclosed channel. Figure 6.19b shows the Matlab simulation for comparison. The two

images show that there is a good correlation between them. The simulated channel appears slightly shallower due to the orientation of the two images not being the same. The two projections into the channel at the junction region were intended to induce a small amount of sample mixing.

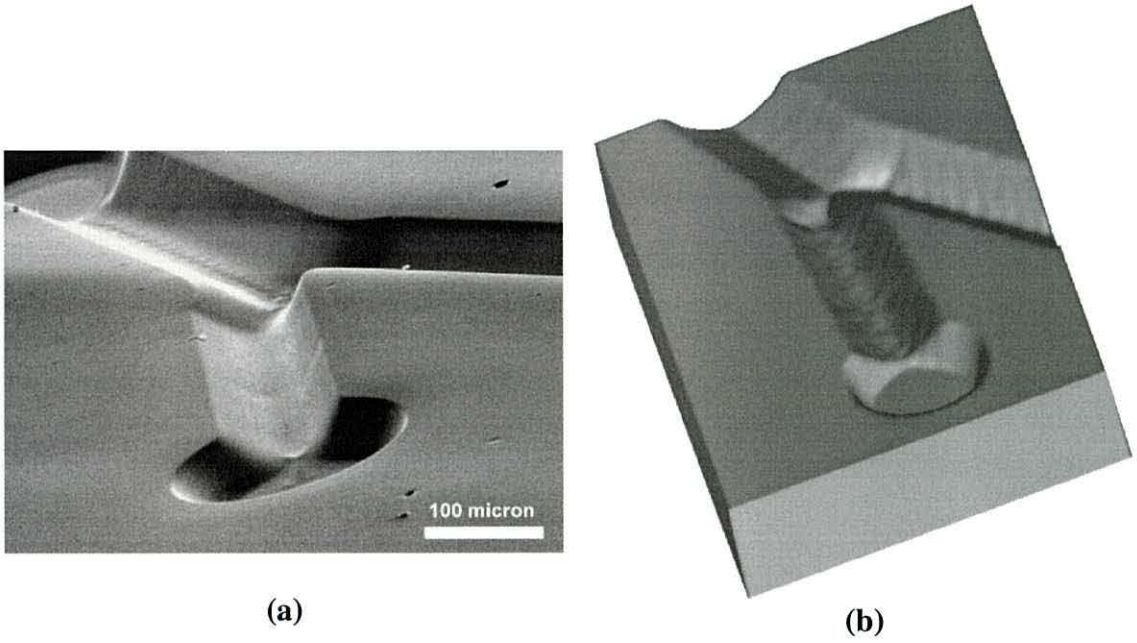

Figure 6.19 *A comparison of an actual and modelled three-dimensional structure. (a) A simple fluidic device, where the rounded channels are approximately 100μm wide and the associated inlet and outlet ports at the end of each fluidic channel are 200μm wide. (b) An image of the graphical model of the fluidic system produced by the Matlab using the greyscale mask dither patterns.*

The single exposure mask used to create the manifold in Figure 6.19 was also used to create clear UV-curing resin halves, one half having embedded hypodermic needles providing fluidic connection to the inlet and outlet wells. The two halves were then bonded together to form the final system(s) shown in Figure 6.20.

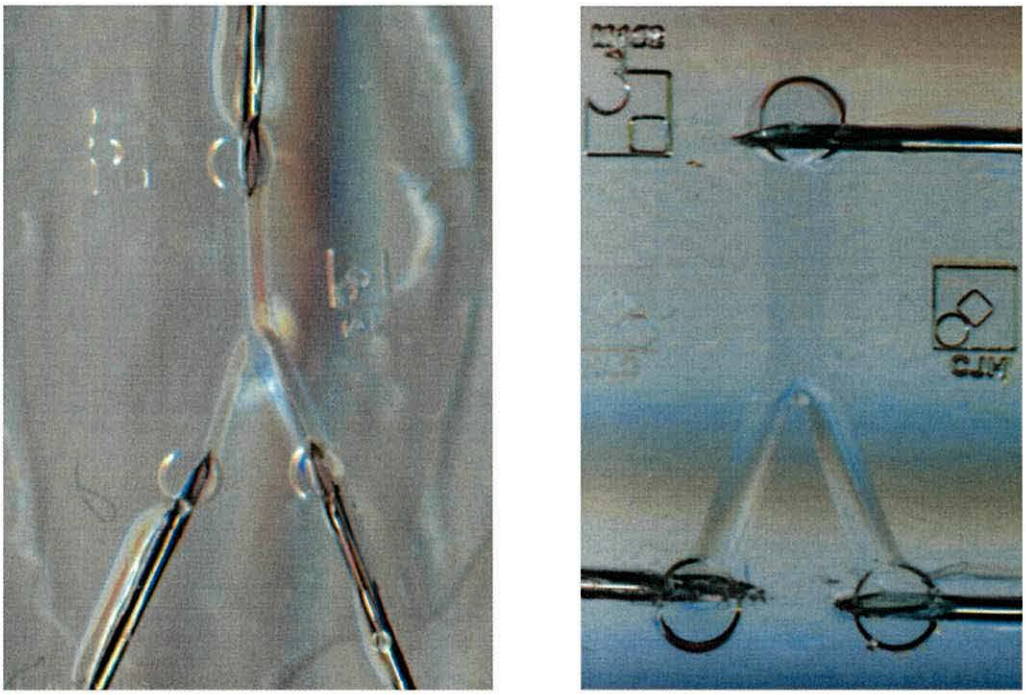

Figure 6.20 *Two examples of micro-fluidic channel systems fabricated in transparent resin to allow microscopic investigation of particle flow through the channels.*

When the micro-channel was completed, a solution containing a suspension of 25.7μm latex beads (Sigma Aldrich Co., Ltd., UK) particles was pumped through the system. The flow of the suspension was recorded for subsequent analysis onto S-VHS video tape via an optical microscope and CCD camera. The complete experimental setup is shown in the diagram in Figure 6.21. Thus it was possible to track sets of particles and measure the distance travelled between particular frames and hence deduce their average speed.

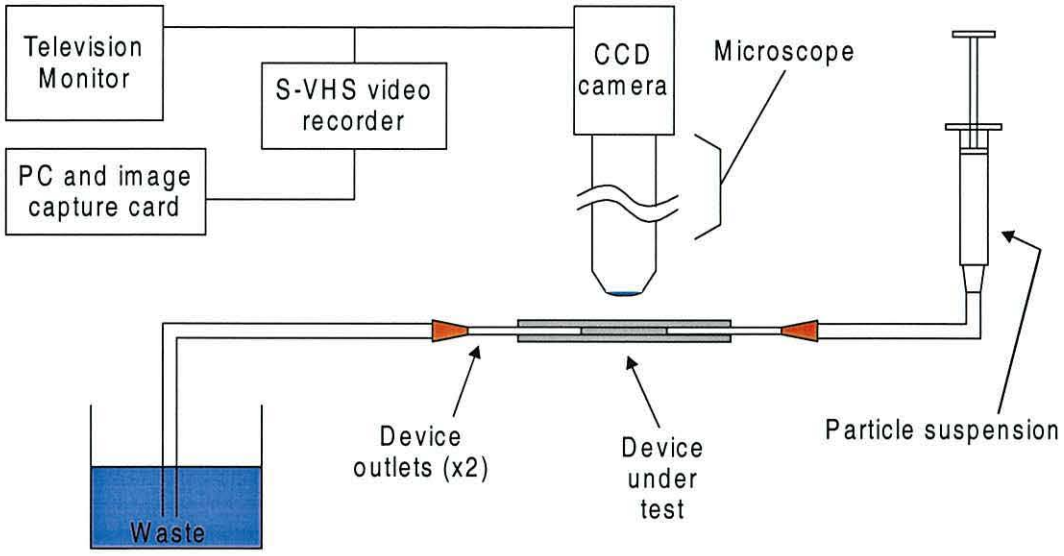

Figure 6.21 *Experimental setup used to record the particle flow data. The devices were mounted on a microscope slide, allowing observation. A particle suspension was then injected into the device under test and flow in the channel structure recorded onto S-VHS video via a CCD camera. This could then be analysed using a computer capture system, allowing particle progression to be monitored at a rate of 25 fps.*

Figure 6.22 and Figure 6.23 show the average speed of 10 particles through (a) the constant cross-section and (b) the variable cross-section micro-channels. From this it can be seen that particles in manifold (a) travel approximately the same distance between each frame, whereas the particles in manifold (b) do not. This is to be expected, since the local, linear flow velocity of an incompressible fluid will adjust to the channel cross-section so as to maintain a constant volume flow rate. This has the effect of increasing the velocity of fluid flow when a cross sectional area decreases as seen in Figure 6.23.

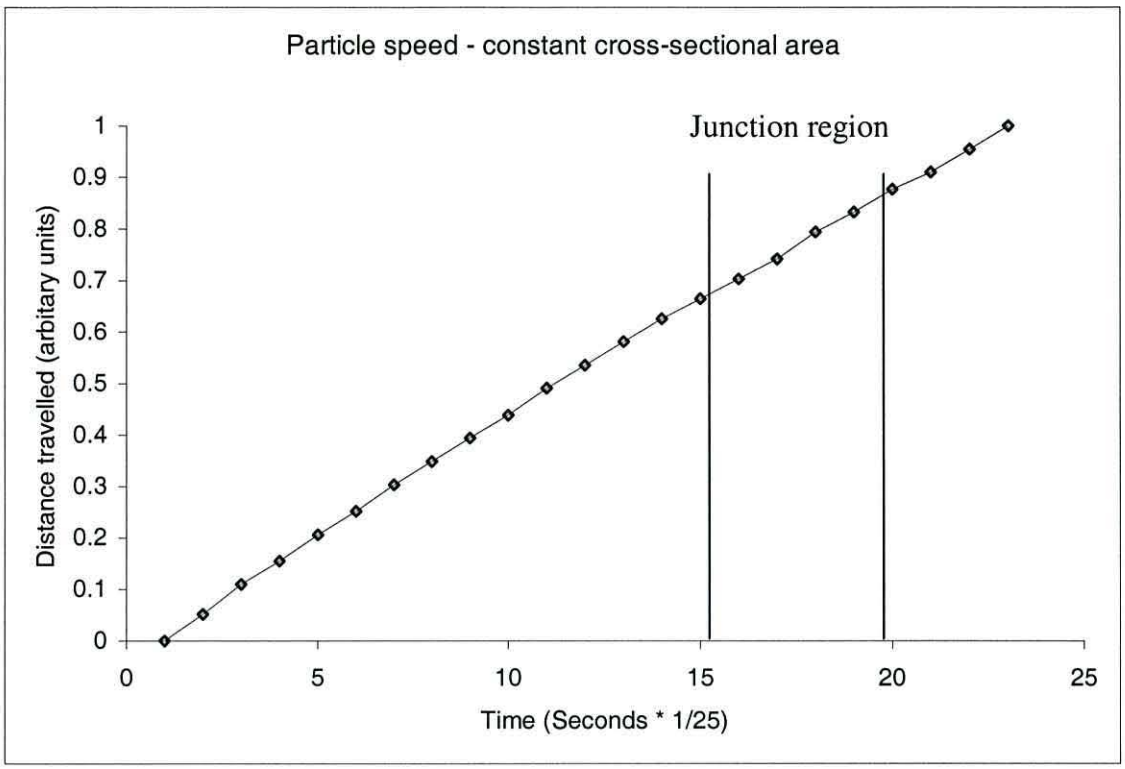

Figure 6.22 *A graph showing the progression of particles down a constant cross-sectional area manifold. The two vertical lines represent the start and the end of the junction region.*

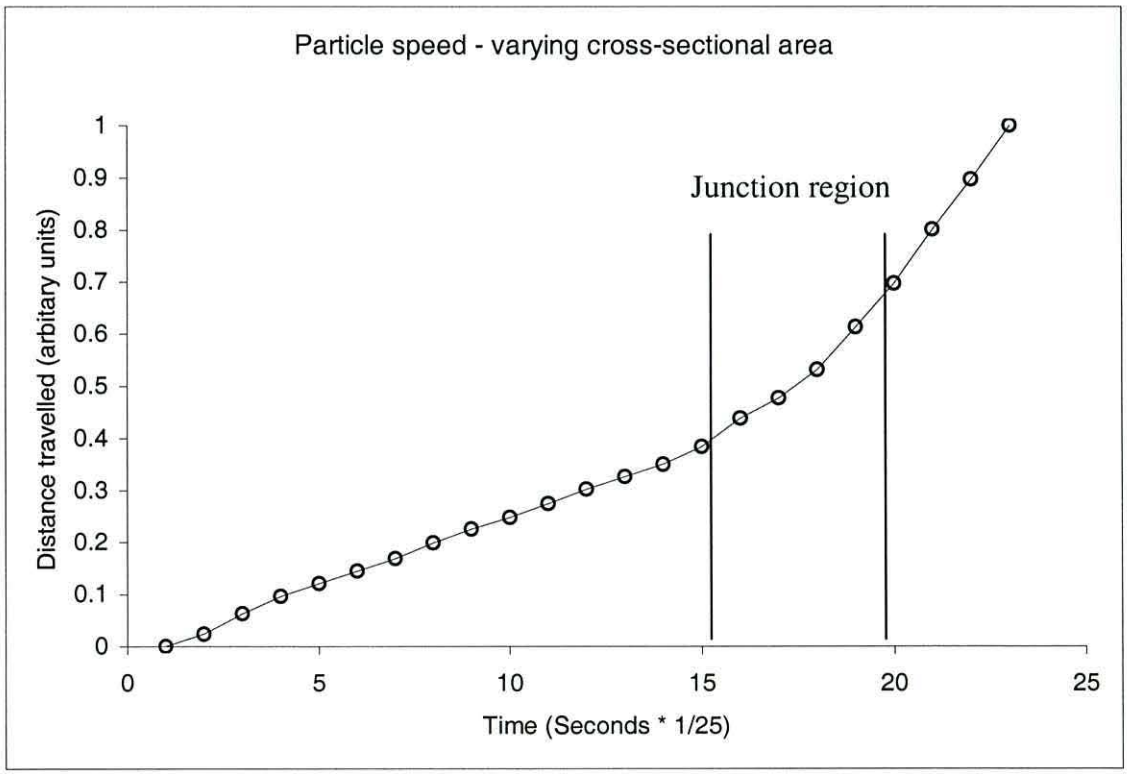

Figure 6.23 *A graph showing the progression of particles down a non-constant cross-sectional area manifold. The two vertical lines represent the start and the end of the junction region.*

The fact that the flow velocities either side of the 'Y' junction are constant provides good evidence for the high degree of control that is possible in the machining of micro-channels using greyscale masks.

During these experiments the flow was laminar, although it was possible to induce turbulent flow around the inlet and outlet wells if high enough flow rates were used. However, it is unlikely that this would be a problem where the manifolds are incorporated into analytical devices, as such high analyte flow rates would not be used.

The three-dimensional structures fabricated using greyscale masks are well suited to act as masters for polymer duplication techniques such as hot embossing and injection moulding [35-38]. These fabrication methods require robust negative moulds to be created at a suitable spatial resolution, for example by electroplating a micromachined substrate to form a metal mould [39, 40]. Structures formed in SU8 have been reported as being capable of patterning polymer materials in a hot embossing system so long as production runs are short [33]. Figure 6.24 shows the SU8 hot embossing masters that were created in the present work to fabricate fluidic manifold halves. Figure 6.24b is a close up view of the junction area. The smooth curved surfaces that are created by the greyscale production process can clearly be seen.

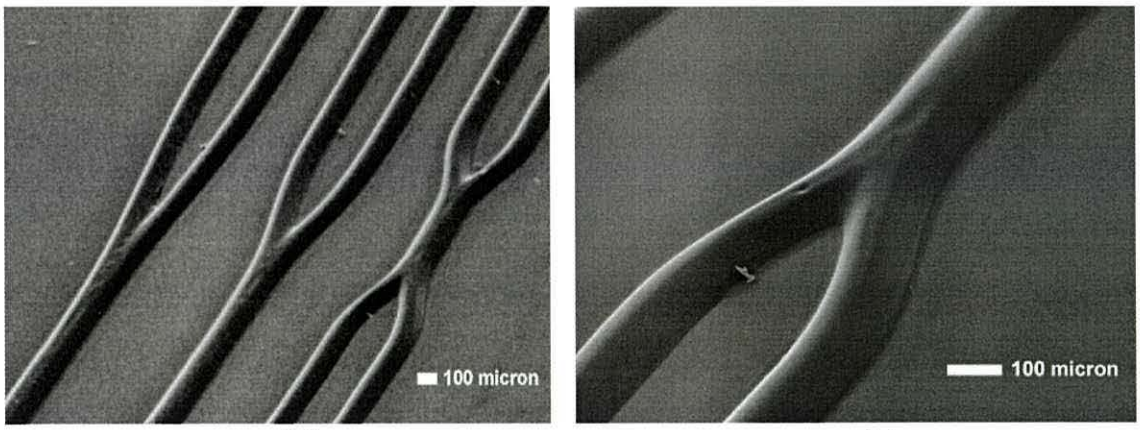

(a) **(b)**

Figure 6.24 *Electron micrographs of greyscale-mask produced microfluidic manifold structures suitable for use in duplication processes such as hot-embossing and injection moulding. The structures were fabricated in SU8 photosensitive epoxy and show channels with diameters of 100μm.*

6.4 Excimer laser machining using greyscale masks

Combining greyscale masks with excimer laser machining allows complex topographies to be created in a single machining process in a range of materials, such as polymers, glass and ceramics, in addition to photosensitive ones. Successful implementation of greyscale masks has already been reported using excimer laser ablation to produce diffractive optical elements [18], although the depth of machining was limited and the machining characteristics were not ideal. The structures were machined using e-beam fabricated masks which are costly and relatively fragile. They have a limited life-span when used in an excimer laser machining system, as well as limiting the maximum laser energy that can be used without rapid degradation. The next section describes a study undertaken to investigate the possibility of producing low cost masks using resist-coated quartz plates to create greyscale masks for use in the excimer laser system (Chapter 3.5.3).

6.4.1 Laser mask requirements

Greyscale masks for use in the excimer laser system were fabricated by patterning a layer of S1818 that had been spin-coated onto a quartz substrate. It has already been demonstrated (Chapter 4.3) that such structures worked well in the laser system. The S1818 masks were created directly by laser machining or by photolithography using a suitable binary mask.

The range of laser energy densities used at the mask is determined by two factors - the ablation threshold of the material being ablated and the fluence at which significant mask erosion occurs. The ablation threshold is a physical characteristic of the workpiece material and will occur at a given energy density, depending upon the laser wavelength used (Chapter 2). Below this threshold energy, no laser ablation will occur, although photo-bleaching of the material may be evident. Hence, the minimum laser energy density present at the workpiece must be above its ablation threshold if material is to be removed. The maximum laser energy that can be used will be limited by the erosion rate of the mask (Chapter 3.4.2). Using high energies will cause more material

to be removed from both the mask and the workpiece, whereas if the energy is too low for the particular greyscale mask design being used, areas of low transmission may be below the ablation threshold, so producing distorted structures. Using too high an energy may also cause unwanted distortion due to heating effects in the workpiece as well as the mask. Hence, choosing the appropriate laser energy density to use is critical and must be considered carefully when fabricating greyscale masks.

However, the laser system differs from the photolithographic contact exposure mode process, in that any mask pattern is transferred to the workpiece via a demagnification projection lens. Because of this, the maximum mask feature size used in laser greyscale masks is determined by the properties of the demagnification lens used, not by the resolution of a photoresist, as is the case when implementing photolithographic greyscale masks. Hence the maximum feature size that can be present in a laser greyscale mask is limited by the minimum feature size that the optical projection system can resolve (Chapter 2.5).

From Table 2.2 the maximum mask feature size when using the laser system at 193nm with a x10 demagnification projection lens must be ~10μm.

This poses no problem because masks with smaller feature sizes are readily created using either photographic or laser machining based fabrication methods. Hence suitable greyscale mask patterns can be created that will not be resolved when used in the laser system.

6.4.2 Excimer laser greyscale mask creation

Others [8, 18] have used different methods to those used here to control the effective transmission per unit area of the mask. For example, a combination of E-beam lithography and RIE were used to produce diffraction gratings on a mask, so allowing control of the mask transmission [8]. However, the relationship between the grating duty-cycle and the ablated depth was found to be non-linear. Another method used was to divide the mask into equally sized areas, then control the transmission through each area by altering the size of a single window [18]. This was repeated on a regularly

spaced grid and allowed very accurate theoretical control of the masks transmission, as described in Section 6.2.2.2. However, the relationship between mask transmission and the measured depth of the machined region was found to be non-linear. It is believed that the method used to create the various greyscale transmissions, namely repeating similarly sized elements, allowed diffraction effects to influence the actual mask transmission so that it varied in the non-linear manner observed.

In the present work, a binary dither algorithm was used instead to create the greyscale mask patterns. When implementing greyscale masks in the photolithographic process (Chapter 6.3), it was found that the actual dithering pattern used had no observable effect on the mask transmission. In light of this, the clustered-dot-ordered-dither (CDOD) was again used because a computer based mask creation system had already been implemented by the time this part of the work was undertaken.

The laser greyscale mask patterns were created using a modified version of the Matlab program described in Section 6.3.2, but modified to meet the resolution requirements calculated above.

Two methods of producing the masks were investigated: (a) direct laser machining of the mask and (b) commercially plotting the designs, which were then photographically transferred onto a S1818 layer on quartz, before being projection-reduced using the laser optical system to create the final laser mask.

Laser machining the greyscale mask patterns directly, using a similar approach to that described in Chapter 4, allowed very high-resolution masks to be fabricated over a large area. Figure 6.25 shows an optical micrograph of a section of a machined mask. An additional Matlab program was written to provide rapid transfer between the Matlab generated mask design and the PC controlling the laser thereby automating the production of the final masks.

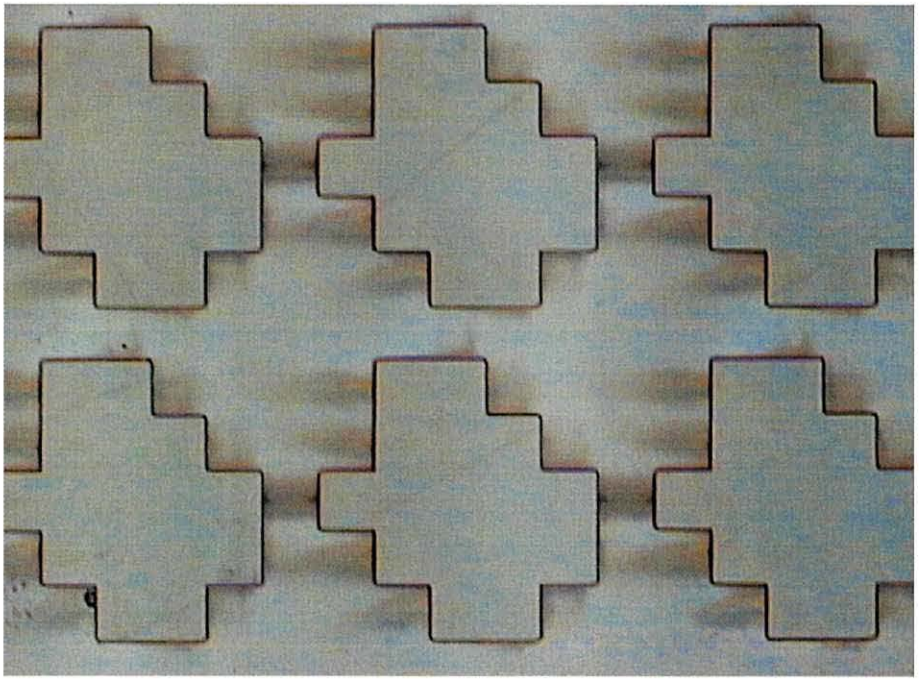

Figure 6.25 *Optical micrograph of a laser machined mask, formed in a 1.5μm thick S1818 layer on a quartz substrate. A section of a x10 mask to create the required laser mask consisting of a n=6 clustered-dot-ordered-dither pattern is shown.*

Transferring the plots photographically, then using the laser to projection-reduce the pattern allowed much more rapid production of masks, but the size of mask that could be produced was limited by the final reduction possible, i.e. the size of mask that could fit into the laser mask stage. However, the resolution of these masks was also high, as the projection-reduction step allowed high-resolution machining from a low-resolution mask, as has been demonstrated in Chapter 4.

6.4.3 Implementing test masks

To allow initial characterisation of the ablation process when using greyscale masks, a simple test mask was created with regions of constant transmission. The CDOD algorithm was used, where n=3, allowing 10 discrete transmission levels. The first material machined was a 90μm thick dry-film laminate layer on a glass substrate. The ablation threshold for this material is 350 mJ/cm^2, which equates to an energy density of ~7 mJ/cm^2 at the mask plane when using the x10 de-magnification lens, which is sufficiently low to prevent erosion of the S1818 on quartz laser mask used.

The energy actually used for the characterisation experiments was 875 mJ/cm^2 at the workpiece, which is both below the mask erosion threshold and above the ablation threshold for dry-film laminate, so allowing the effectiveness of varying transmissions to be investigated. A transmission of ~35% corresponds to the ablation threshold of the laminate when using the setup described and since the test mask consisted of various transmissions between 0% and 100%, no machining was expected below ~40% transmission.

A visualisation of the mask used is shown in Figure 6.26, where the various regions of transmission are separated by regions of maximum transmission. Here, the transmission increments used were 11%, which correspond to the measured data points.

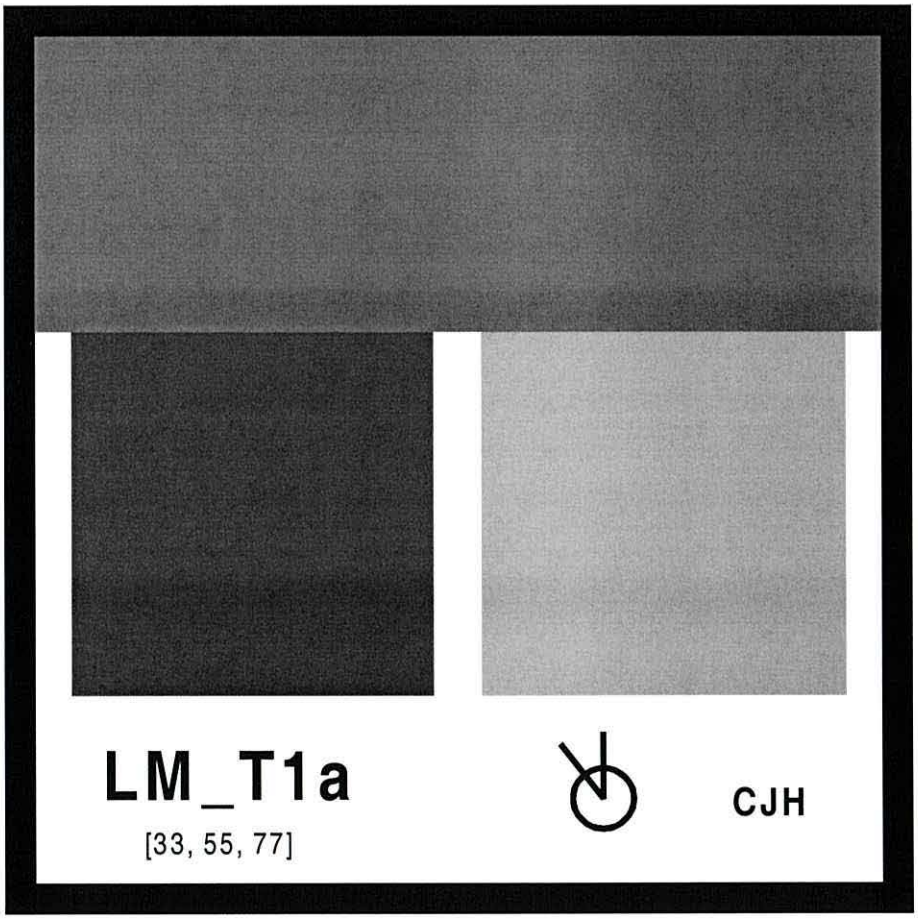

Figure 6.26 *Visualisation of the simple laser greyscale test masks used initially, allowing process viability to be investigated*

The laser greyscale test mask was used to machine dry-film laminate layers using the x10 demagnification projection lens, using various laser fluences and number of laser

pulses. The machined areas were then compared to reveal the depth of the machined areas, allowing comparison between the different settings used. Figure 6.27 shows the measured machined depth vs. mask transmission produced.

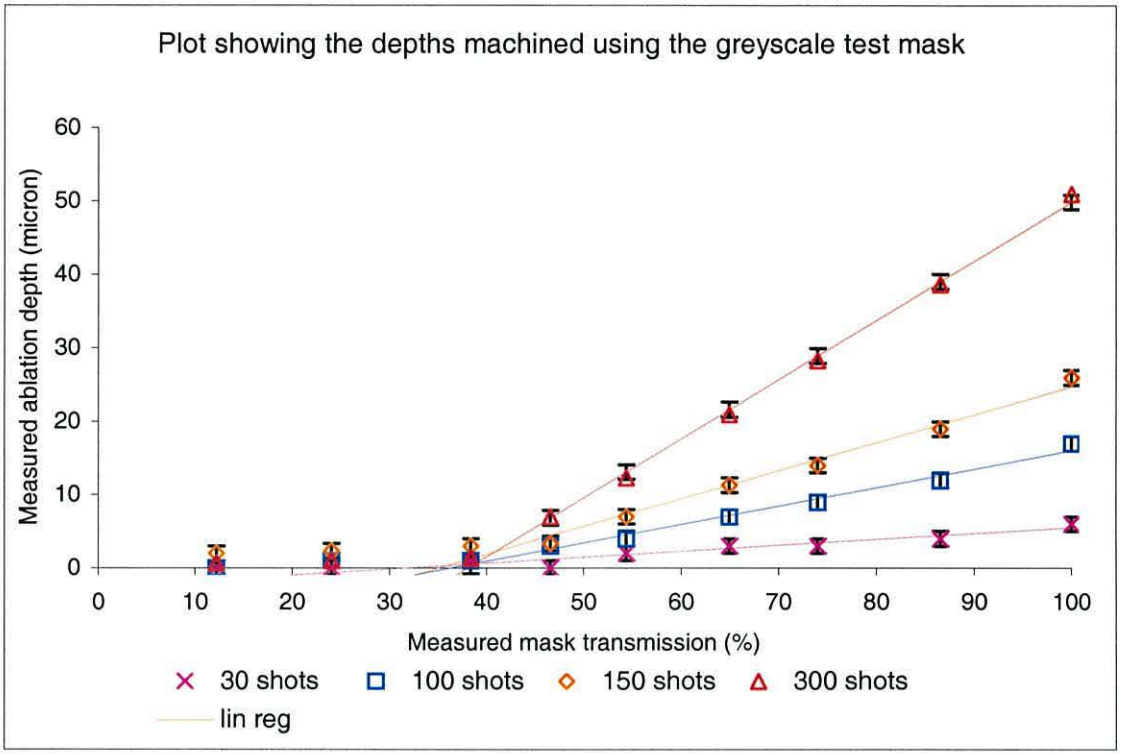

Figure 6.27 *Plot of mask transmission vs. depth machined for various total number of laser shots fired.*

This indicates that the process is linear at the energies investigated, and the relationship between the number of shots fired and material removed is also linear at various energies. A least squares fit to the data yields a correlation coefficient R^2 =0.991 or higher for the measured data sets. This agrees well with the data obtained, showing that doubling the number of shots fired, using a similar laser fluence, doubles the machined depth as the total energy density is doubled. This was expected, as the ablation process is known to be linear [41]. It also indicates that other processes, such as mask-generated diffraction effects, are not influencing the machining significantly.

It should also be noted that machining depths in the order of hundreds of microns are possible, which is significantly more than reported by others [18]. No noticeable deterioration was found during visual inspection of the S1818-quartz laser mask after any of the machining processes.

Having machined a simple test mask to confirm that the process was viable, more complex masks were developed and the machining of other materials was investigated. Figure 6.28 shows another test mask, in this case n=6 (CDOD), which allowed for 37 discrete transmission levels. This allowed a reasonable approximation to a transmission gradient, seen as the linear ramp at the top of the mask. Here, regions of constant transmission were separated by regions maximum transmission.

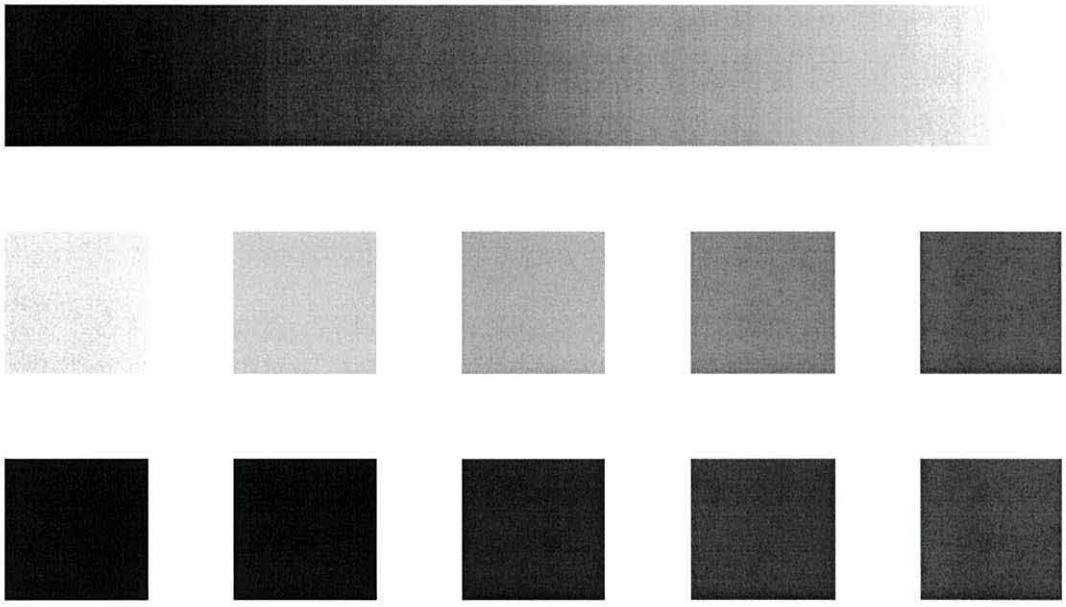

Figure 6.28 *Visualisation of laser greyscale test mask used to allow process characterisation*

This mask was used to machine a 150μm PET film and produced the structures shown in Figure 6.29. Although the areas corresponding to the various mask transmissions are present, the surface quality is not high due to the machining characteristics of the material (Chapter 2.1).

The measured machining depth is plotted in Figure 6.30 at the various mask transmissions and laser fluences used.

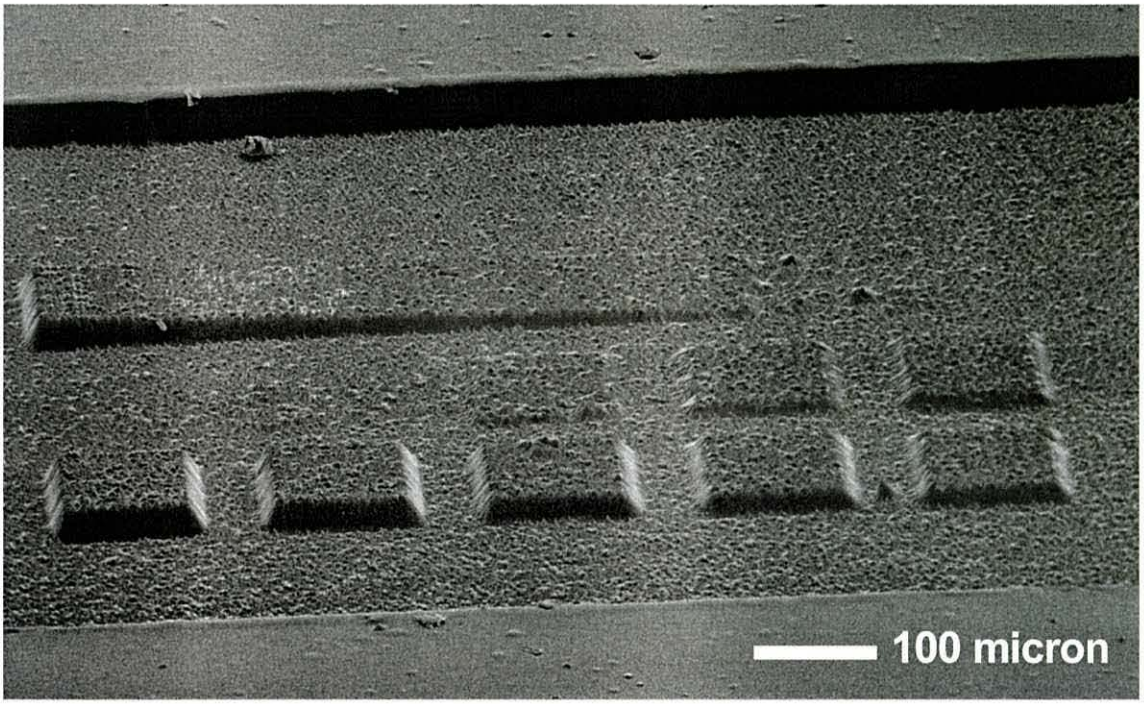

Figure 6.29 *SEM of the structures produced using the greyscale mask shown in Figure 6.28*

The data presented in Figure 6.30 also confirms that the relationship between machined depth and mask transmission is a linear one, for a given fluence, when the ablation threshold is exceeded. This is confirmed by the smallest value of R^2, the correlation coefficient, being 0.996.

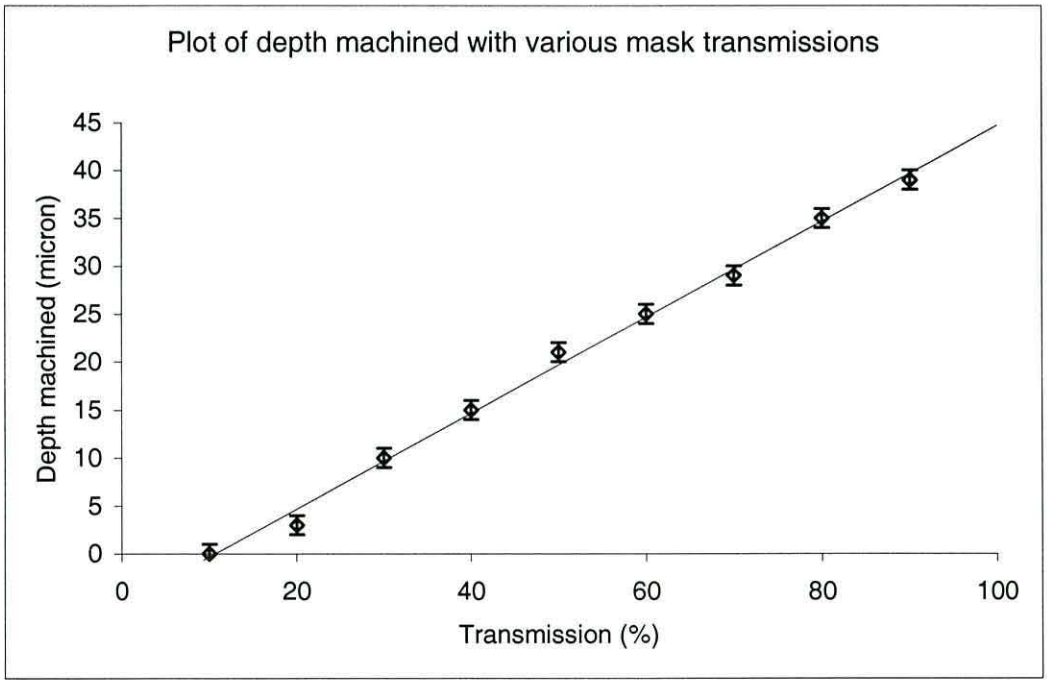

Figure 6.30 *Plot of the depth machined at various mask transmissions using different laser fluences*

6.4.4 Results of using ill-matched mask dimensions

For this investigation, the laser system was operated at 193nm and both x4 and x10 demagnification projection lenses were used. The x10 lens was used both to machine greyscale masks and also to project the greyscale laser mask onto the workpiece, so allowing differential machining rates. Only the x4 lens was used to produce the laser greyscale masks from the photographically produced masks.

The effect of using a mask where the patterning is too large (~30μm sub-units) is shown in Figure 6.29, where a linear ramp design was machined into a 30μm thick dry-film laminate layer on glass. Although the basic ramp shape is visible, some of the properties of the mask patterns used to determine the transmission can be seen as a series of ripples throughout the ramp region.

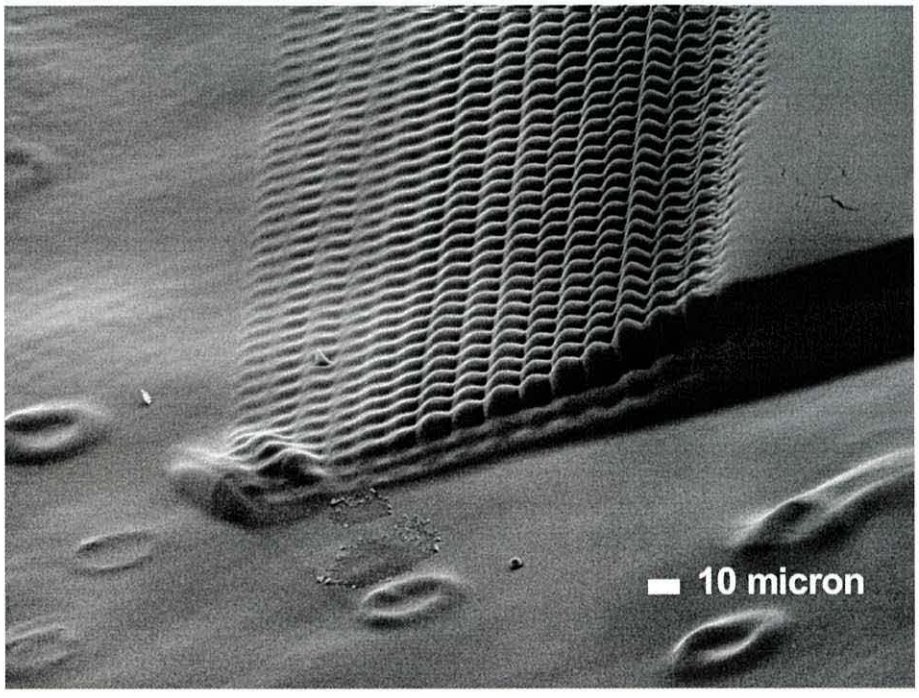

Figure 6.29 *Scanning electron micrograph showing the effects of machining a linear ramp using a greyscale mask where the patterning features are larger than the resolution limit of the optical system. In addition to the ripple-like diffraction pattern in the ramp, the effects of debris on the surface of the sample prior to machining can also be seen.*

The 'doughnut' shaped features to the left and bottom of the ramp are due either to adventitious particles present on the surface prior to machining or to impurities in the dry-film laminate [42]. The ripple-like interference and diffraction patterns present at

the edge of the ramp can be explained by the presence of third and fifth harmonics resulting from the features used being too large. Diffraction also explains the ripples, as the unit areas of the mask are arranged in a linear array. Although there is a gradual increase in the height of the ramp, this is not suitable for the smooth contouring required in fluidic channels and micro-optical components.

6.4.5 Machining glass using greyscale masks

The greyscale masks were also used in attempts to machine glass. Figure 6.30 is an example of a level machined in a 300μm borosilicate glass cover-slip using an energy density of 4.97J/cm^2 at the workpiece. To form the structure some 150 shots were fired. While it proved possible to machine glass to a depth of ~10μm, the high energy density necessary had caused visible deterioration of the laser mask.

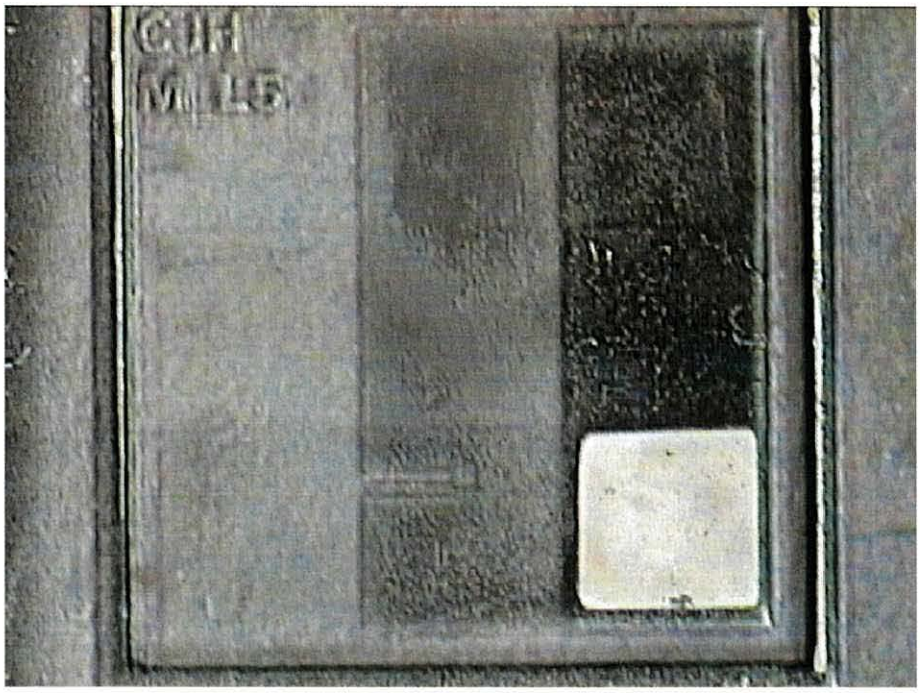

Figure 6.30 *Micrograph showing the result of machining glass using greyscale masks*

The quality of the machined surface is inherent to machining glass at the laser wavelength used, as the ablation process tends to rely on the formation and accumulation of defects within the ablated region [43, 44]. This results in the surface having a roughened appearance, as can be seen in Figure 6.30, although it has been

reported that the surface quality can be improved by subsequent processing [43]. However, greyscale masks may not be well suited to machining glass, as the high fluences required shorten mask longevity and the ablation process has also been reported to be fluence independent [43]. This is due to initial pulses, whose fluence is above the ablation threshold of glass, forming sufficient defects in the ablated area for subsequent material removal at much lower energies

Figure 6.31 shows the machined depths measured at various mask transmissions, again indicating that the machined depth is a linear function of the mask transmission over the conditions used. Here the linear correlation coefficient, R^2, is 0.974. The relatively large error bars are to allow for the surface variation due to recast ablation generated debris. A total of 75 laser pulses were fired to achieve these data.

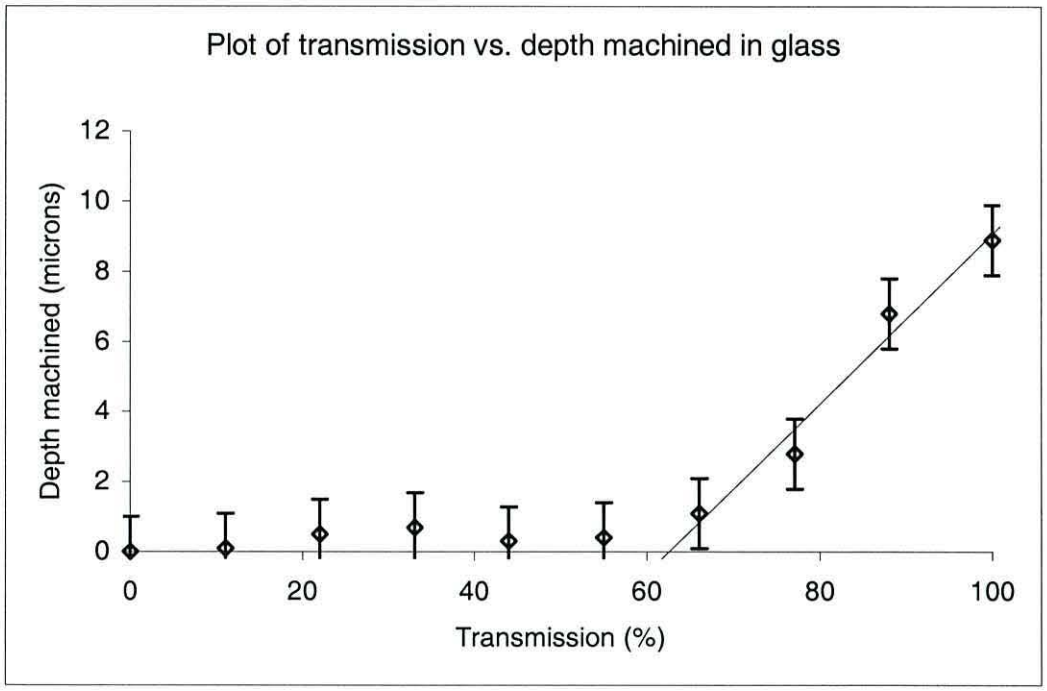

Figure 6.31 *Plot of the measured machined depth in glass and the corresponding mask transmission.*

6.4.6 Creating complex three-dimensional structures

After determining the relationship between greyscale mask transmission and depth of material removed, it became possible to create accurate three-dimensional structures.

This was accomplished using Matlab, both to generate the final mask design and to convert the design to the laser code required for machining the greyscale laser mask. The material machined was a 1.5μm spin coated S1818 layer on a quartz mask plate, as detailed in Chapter 4.

Initially, a simple geometric structure, consisting of a 1000μm circle inside a 1500μm square was designed, each having opposing gradients, as shown in the Matlab simulation in Figure 6.32.

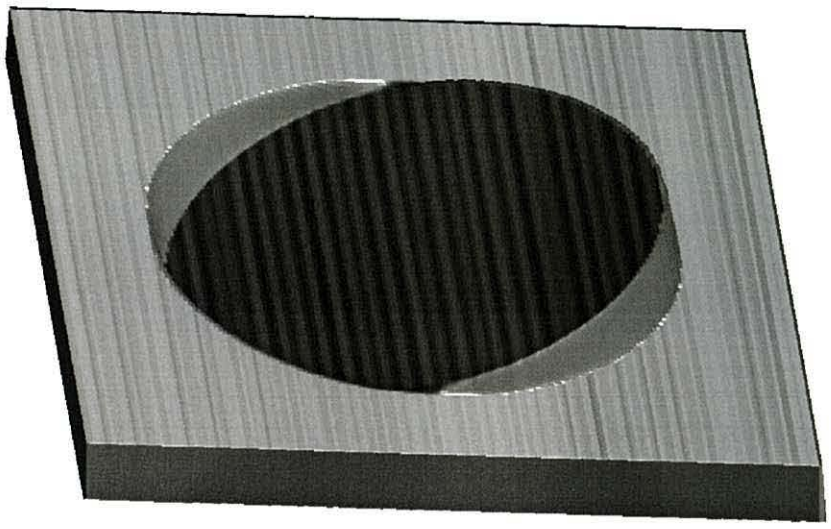

Figure 6.32 *Matlab simulation of the simple geometric structure*

Figure 6.33 shows the structure machined in PET using this mask. Again, surface irregularities can be seen due to the machining characteristics of the material. Steps can be seen in both of the notionally flat surfaces because the number of transmissions available (n=5) was insufficient to create such a shallow gradient smoothly. The average height should change smoothly by approximately 50μm over the length of the 1500μm wide square.

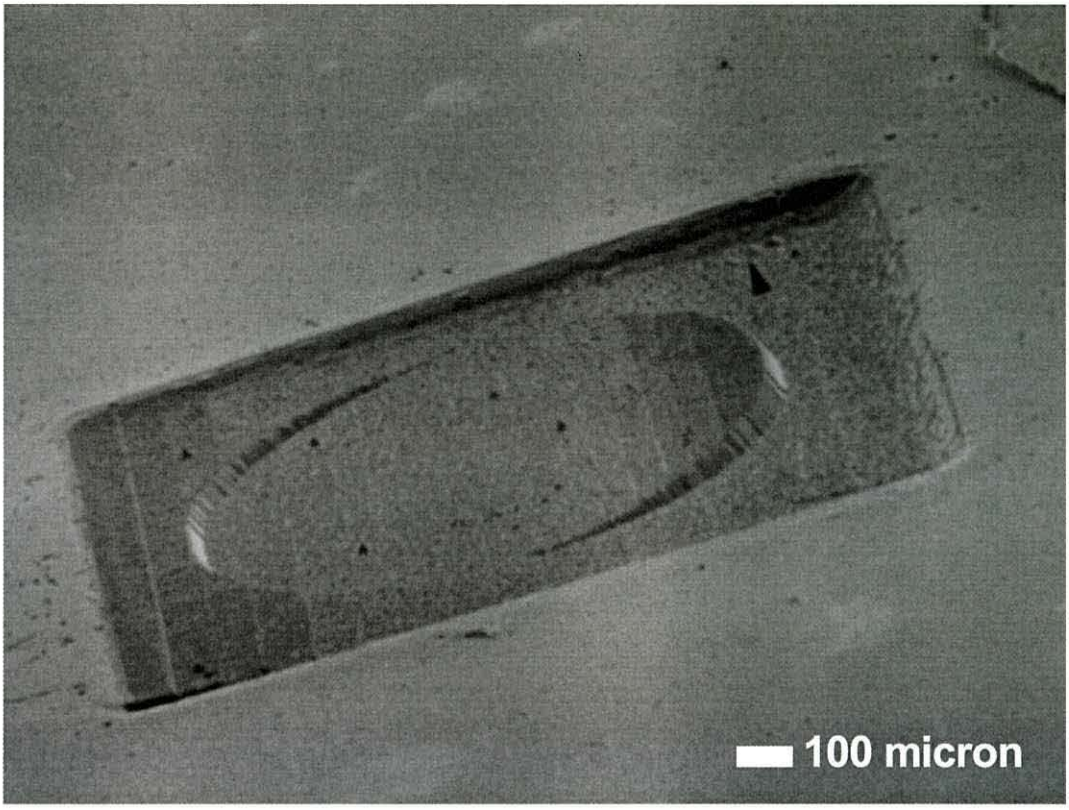

Figure 6.33 *Structure produced using the mask shown in Figure 6.32.*

The second structure to be fabricated consisted of a circular channel with varying cross-section. Figure 6.34 is a Matlab simulation of the structure while Figure 6.35 is a visualisation of the greyscale mask required.

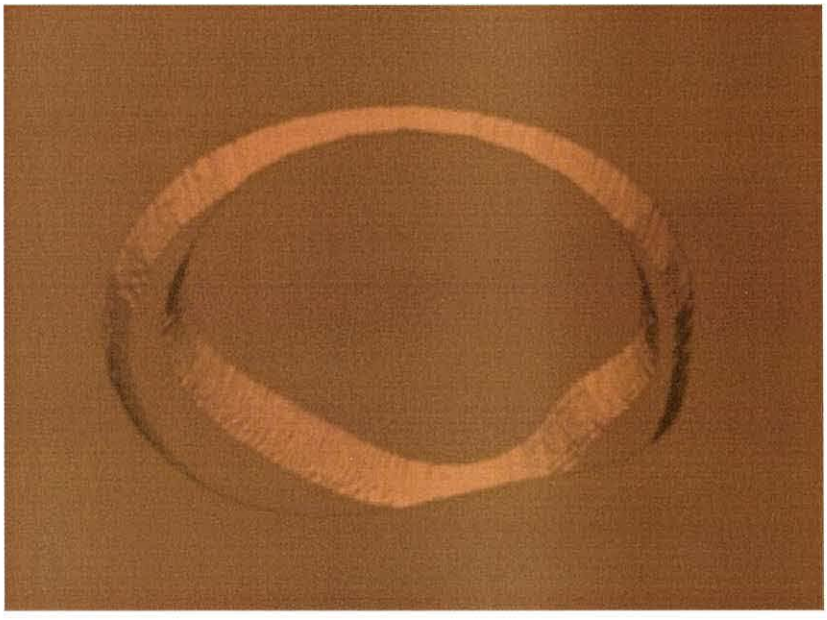

Figure 6.34 *Matlab simulation showing the circular, varying cross-section channel*

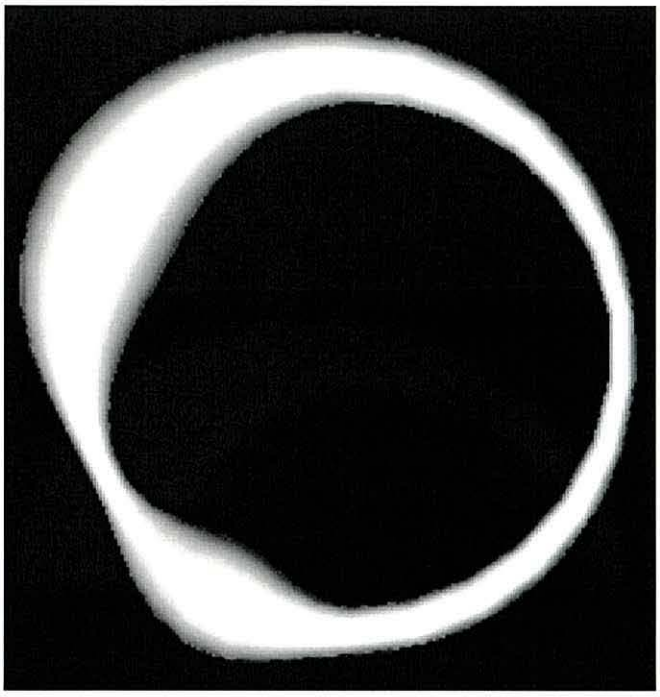

Figure 6.35 *Visualisation of the greyscale mask design produced to fabricate the structure in Figure 6.33.*

The resulting structure, laser machined in a dry-film laminate film is shown in Figure 6.34. An enlarged section is shown in Figure 6.36. The structure was machined approximately 50μm into a 90μm thick dry-film laminate.

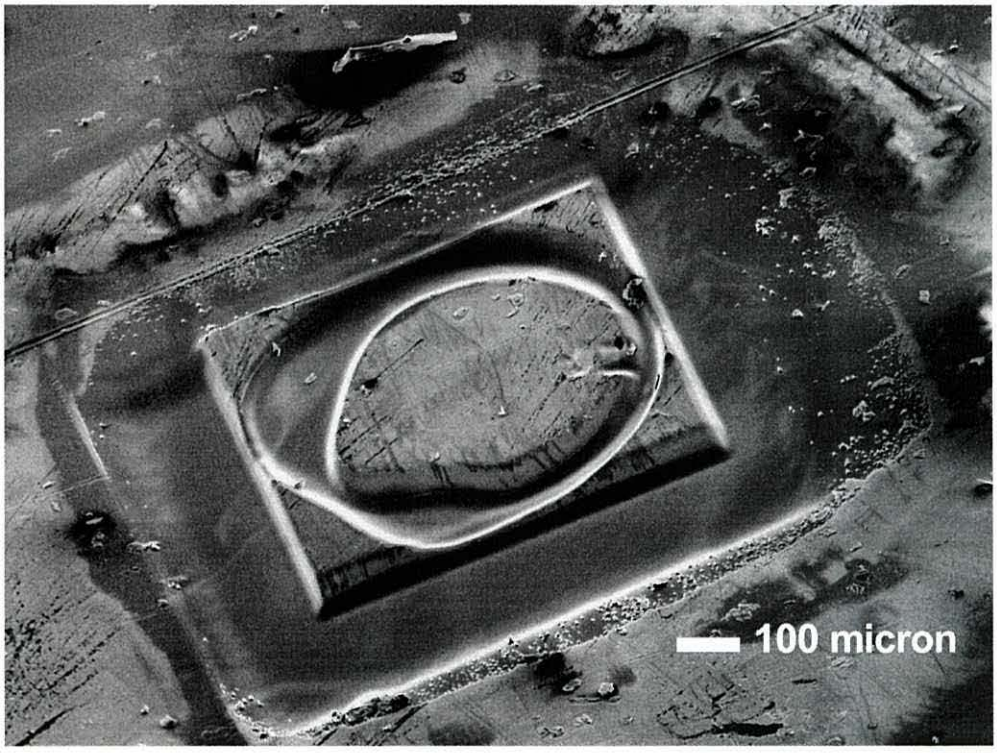

Figure 6.36 *Scanning electron micrograph showing the structure machined.*

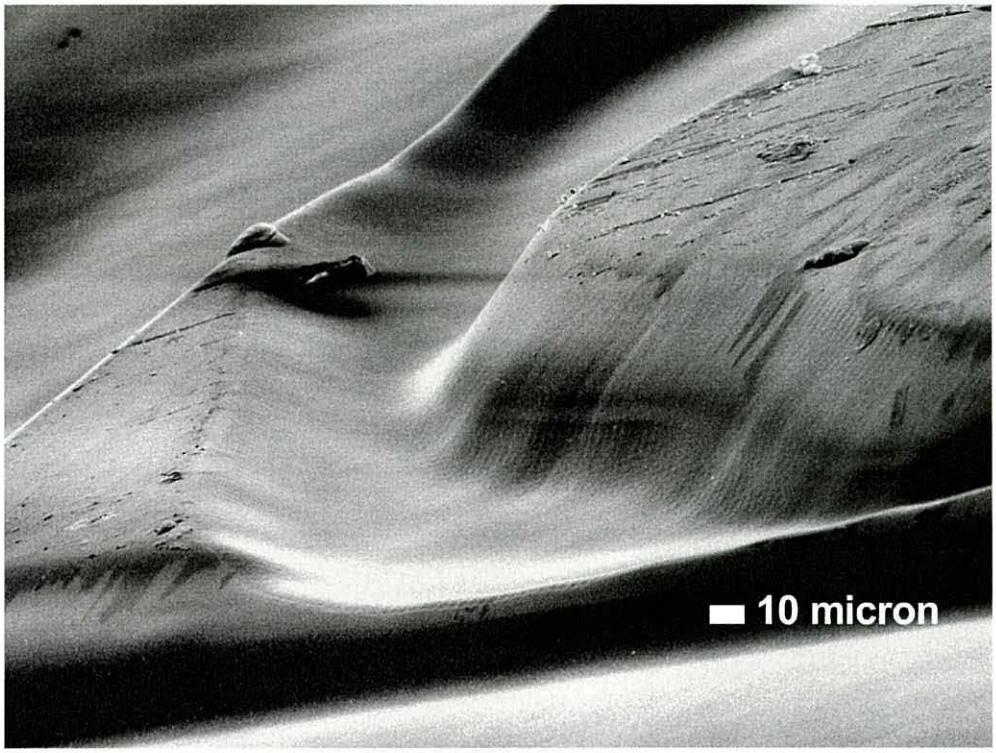

Figure 6.37 *Scanning electron micrograph of a section of the machined structure. The curved sidewalls can be seen to be smooth, with no sign of the mask features being resolved. This indicates that the process is successful.*

The structure produced can be scaled in the Z direction by altering the number of laser shots fired, but maintaining a constant fluence. Altering the laser fluence used to machine the structures significantly will cause distortion in the contours produced, the effects of which are demonstrated in this section.

Smooth transitions between machined and unmachined regions, for example where the channel depth approaches zero at the right of Figure 6.37, were achieved by producing laser fluences that dropped from above, to below the ablation threshold. This had the effect of removing abrupt changes in the depth machined, as the fluence at the workpiece fell gradually, avoiding sudden changes in machined depth.

Lowering the laser fluence significantly would cause a distortion in the structure produced, as only the higher mask transmissions would produce fluences capable of machining the workpiece. This would result in a 'clipped' appearance, where regions of lower transmission were not machined as the fluence produced at the workpiece are below the ablation threshold.

However, if the laser fluence used were increased significantly, the gradual fall in fluence at the workpiece to below the ablation threshold would not occur. Instead, the higher fluence used would cause every transmission of the mask to produce fluences that were above the ablation threshold of the material at the workpiece. This would cause a step to develop at the border between machined and unmachined regions. Figure 6.38 shows an example of increasing the fluence used, showing the much deeper channel that has been produced with steeper walls, although contouring is still present.

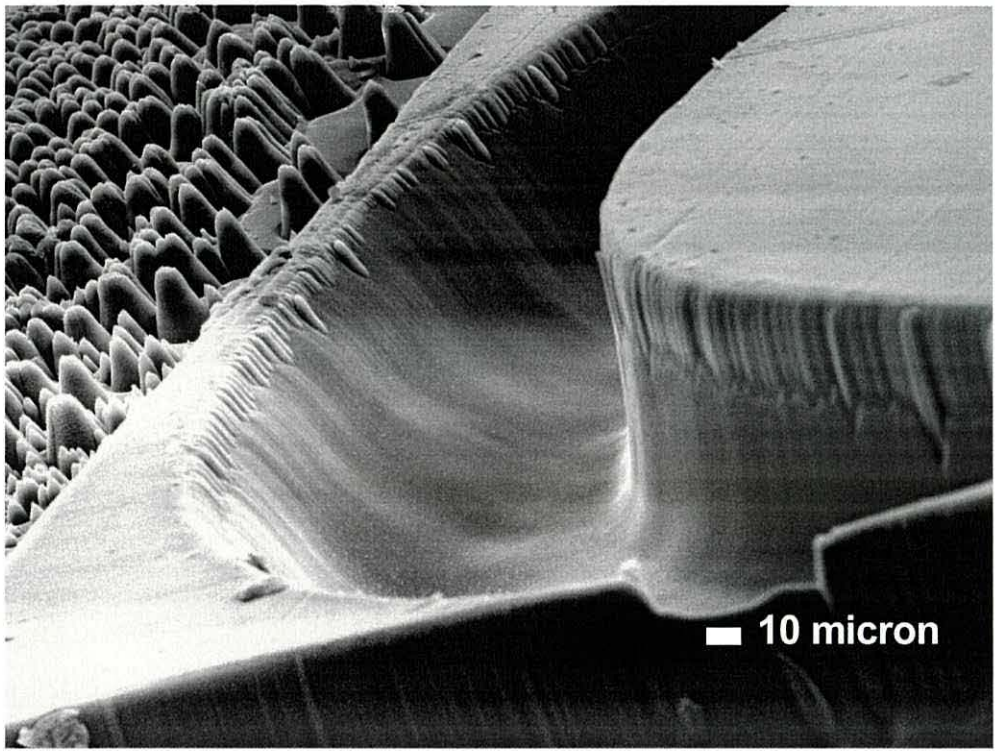

Figure 6.38 *Scanning electron micrograph showing a section of the contoured channel structure, machined using a higher fluence. The sidewalls, although still curved, are much steeper that those in Figure 6.36, but are still smooth. The effects of increasing the energy can be seen at the junction between the machined and unmachined regions, as there are now steps apparent instead of a contour.*

However, instead of a smooth transition between machined and unmachined regions, a step is present. This is because the higher fluence used has caused all transmissions of the mask to be above the ablation threshold of the workpiece. If the fluence used is increased still further, the effects are exaggerated, as shown in Figure 6.39. Here, the entire thickness of the dry-film laminate layer has been removed from most of the channel regions and the contouring is much less noticeable.

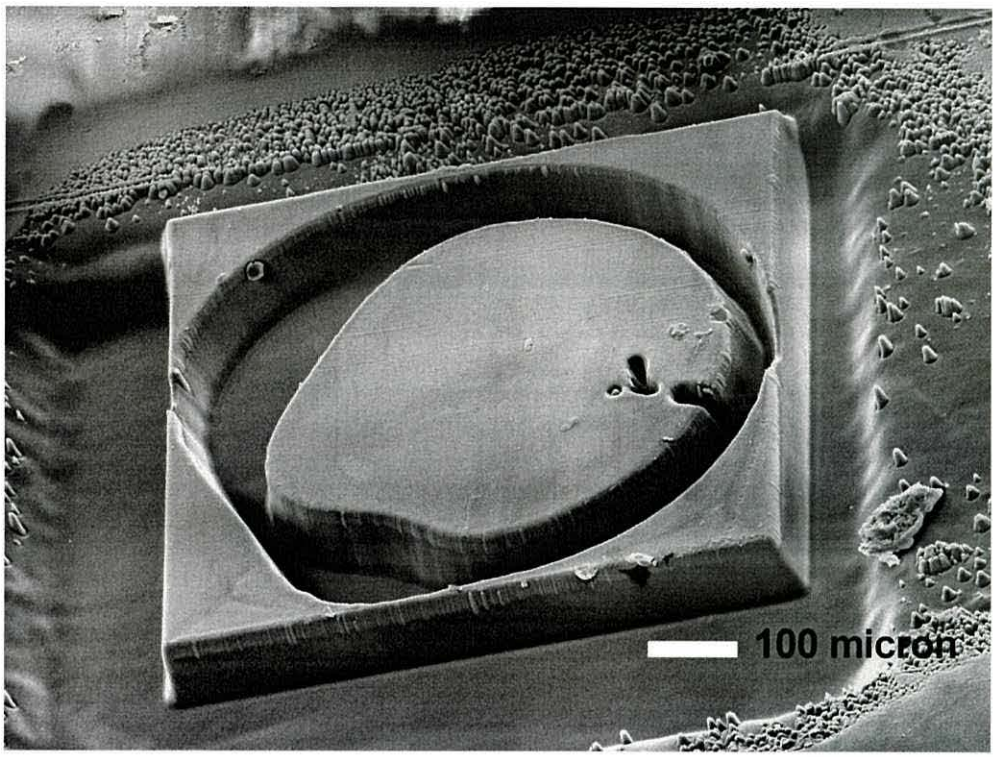

Figure 6.39 *Scanning electron micrograph showing the result of increasing the laser energy used to machine the structure shown in Figure 6.35. The channel walls are much steeper and there is little curvature present at the bottom of the channel, as the 90μm thick dry-film laminate layer has been completely removed. Regions of the mask that have been damaged can also be seen at the right of the structure, where machining has occurred unintentionally.*

6.5 Conclusions

Several methods of creating an effective average mask transmission have been examined, although many other methods exist. All allow the average transmission of a set area to be controlled by varying the ratio of transmissive to non-transmissive regions. Most of the computer graphics based algorithms considered have been developed for use in displaying variable tone images on bi-level computer displays and outputs, such as laser printers. Devices such as printers are not necessarily good at printing discrete pixels, or 'dots' and this is also inherent in the photographic mask production system. This allows similar algorithms to be implemented. Unlike computer-based graphical outputs, the aesthetics of the greyscale mask pattern generated are not important, instead the effective transmission must be as required. This is why other more complex algorithms that address qualities such as aesthetics have not been considered.

The clustered-dot-ordered-dither algorithm, originally developed for displaying continuous tone images on bi-level displays, is ideally suited to creating the mask patterns required for this work. This algorithm is also well suited to producing outputs for devices, including the photographic mask production system, where discrete elements are hard to produce. An additional consideration that has to be catered for when producing greyscale masks is the lower energy threshold not present with image processing, as well as any possible non-linearities present in the photosensitive material. Providing the feature sizes used are not resolved by the process, this method of creating greyscale masks has been used to achieve automated production of three-dimensional structures with good correlation to the original design requirements.

However, the limitation of any mask patterning method is the smallest feature size that can be created using standard photographic mask production techniques, which is approximately 6μm. Laser machining allows much smaller features, in the order of 1μm and below, although there is an increase in the processing time if the laser is used to serially machine the mask pattern. Instead, photographic masks were made and then photolithographically reproduced onto suitable laser masks (Chapter 3.5.1) and the laser micromachining system used to machine greyscale masks in a similar manner to that described in Chapter 4. This allowed the rapid production of greyscale masks with micron-resolution that could be used in both processes.

Computer generation of greyscale masks has also been demonstrated. These Matlab programs allow rapid mask creation from a design file – a useful feature for developing new designs and refining existing ones. This process is several orders of magnitude faster than manual mask design and also allows for much more complex designs with no decrease in accuracy due to mask design errors. The computer generated mask files can also be simulated to allow previewing of a design to check the resultant structure for any errors. The simulation program provides a three-dimensional view that can be manipulated on the computer to allow any part of the design to be analysed. It has also been shown that the results of the computer simulation correlate well with the structures manufactured using the greyscale mask produced from the design.

Greyscale masks have been successfully implemented into an existing photolithographic process to allow the fabrication of complex three-dimensional structures in a single exposure. The results obtained show that the process is accurate, reliable and repeatable. The greyscale masks used were fabricated in-house using a combination of photographic reduction and laser machining. Several materials have been patterned successfully using greyscale masks, including dry-film laminate, SU8 photodefinable epoxy, UV curing resin and UV curing glues. This indicates that if a suitable greyscale mask is used, most photodefinable materials are compatible. Micro-moulds have also been fabricated in a variety of materials for use either as hot-embossing moulds or for moulding liquid structures, such as PDMS. Here, good surface quality of the mould is important, which is met using greyscale masks.

Fluidic manifolds have also been fabricated and tested using particle suspensions to measure the flow rate through the manifold junction. These results show that if the cross-section of the manifold remains constant, particle speed will remain constant, however if the cross-section changes, then particle speed will also change. The observed constant particle speed indicates that there is a good degree of control possible using greyscale masks, as the cross-sectional area remains constant as intended in the original design.

Greyscale masks have also been successfully used with excimer laser machining. The required masks were created quickly and cheaply in-house using both photolithographic processes and the laser system. These masks have been used in the laser system for several hours at high energy densities with no visible deterioration. This in turn allowed machining of structures hundreds of microns deep in thick film polymer layers, which is not known to have been reported previously. Glass was also machined using greyscale masks, although the quality of machining was not as high as for polymers, most likely due to the mechanisms inherent to the glass machining process. Mask erosion was also evident when machining glass, due to the higher energy densities required to machine glass and the mechanisms causing material removal may limit the application of greyscale masks to machining arbitrary shapes in glass.

The processes developed are well suited to allow controlled, three-dimensional structuring in a wide variety of materials. Structuring photosensitive materials using

photolithography is a simple and fast procedure requiring a single exposure in a standard process and non-photosensitive materials can be patterned using excimer laser ablation. Apart from the mask used, which can also be fabricated quickly and cheaply using mainly in-house methods, the fabrication processes remain unchanged, which is beneficial for any mass-production environment.

6.6 References

[1] 'Fabrication of complex micro-optic components using photo-sculpting through halftone transmission masks', D. R. Purdy, *Pure Appl. Opt.* **3** (1994) 167-175

[2] 'Excimer laser micromachining and replication of 3D optical surfaces', A. Braun, K. Zimmer, B. Hosselbarth, J. Meinhardt, F. Bigl and R. Mehnert, *Applied Surface Science* **127-129** (1998) 911-914

[3] 'Microfabrication of complex surface topographies using grey-tone lithography', B. Wagner, H. J. Quenzer, W. Henke, W. Hoppe and W. Pilz, *Sensors and Actuators A* **46-47** (1995) 89-94

[4] 'One level grey-tone design – mask data preparation and pattern transfer', K. Reimer, W. Henke, H. J. Quenzer, W. Pilz and B. Wagner, *Microelectronic Engineering* **30** (1996) 559-562

[5] 'Coding grey-tone mask for refractive microlens fabrication', J. Yao, J. Su, J. Du, Y. Zhang, F. Gao, F. Gao, Y. Guo and Z. Cui, *Microelectronic Engineering* **53** (2000) 531-534

[6] 'Design of hybrid micro optical elements with coded grey-tone mask', J. Yao, Z. Cui, F. Gao, Y. Zhang, F. Gao, J. Du, J. Su and Y. Guo, *Microelectronic Engineering* **57-58** (2001) 793-799

[7] 'Refractive micro lens array made of dichromate gelatin with grey-tone photolithography', J. Yao, Z. Cui, F. Gao, Y. Zhang, Y. Guo, C. Du, H. Zeng and C. Qiu, *Microelectronic Engineering* **57-58** (2001) 729-735

[8] 'Diffractive grey-tone masks for laser ablation lithography', C. David, J. Wei, T. Lippert and A. Wokaun, *Microelectronic Engineering* **57-58** (2001) 453-460

[9] 'Continuous profile writing by electron and optical lithography', E. Kley, *Microelectronic Engineering* **34** (1997) 261-298

[10] 'Fabrication of waveguide tapers by semitransparent mask photolithography', J. Wengelink and H. Engel, *Microelectronic Engineering* **30** (1996) 137-140

[11] 'Photoresist parabolas for curved micromirrors', S. K. Rotich, J. G. Smith, A. G. R. Evans and A. Brunnschweiler, *J. Micromech. Microeng.* **8** (1998) 108-110

[12] 'A novel micro-machining method for the fabrication of thick-film SU-8 embedded micro-channels', F. E. H. Tay, J. A. van Kan, F. Watt and W. O. Choong, *J. Micromech. Microeng.* **11** (2001) 27–32

[13] 'Combination of contour and half-tone masks used in laser ablation', A. Braun, K. Zimer and F. Bigl, *Applied Surface Science* **168** (2000) 178-181

[14] 'Micro-stereolithography of polymeric and ceramic microstructures', X. Zhang, X. N. Jiang and C. Sun, *Sensors and Actuators* **77** (1999) 149–156

[15] 'Stereolithography and microtechniques', S. Zissi, A. Bertsch, J.-Y. Jezequel, S. Corbel, D. J. Lougnot and J.C. Andre, *Microsystem Technologies* **2** (1996) 97-102

[16] 'Microstereolithography using a liquid crystal display as dynamic mask generator', A. Bertsch, S. Zissi, J. Y. Jezequel, S. Corbel and J. C. Andre, *Microsystem Technologies* (1997) 42-47

[17] 'Fabrication of fluidic manifold systems using single exposure greyscale masks', C. J. Hayden, J. P. H. Burt, *Proc. SPIE* **4404** (2001) 231-237

[18] 'Multilevel diffractive optical element manufacture by excimer laser ablation and halftone masks', F. Quentel, J. Fieret, A. S. Holmes, S. Paineau, *Proc. SPIE* **4274** (2001) 420-431

[19] 'An optimum algorithm for halftone generation for displays and hard copies', T. M. Holladay, *Proceedings of the SID* **21** (1980) 185-192

[20] *"Computer Graphics principles and practice"*, J. D. Foley, A. vanDam, S. K. Feiner and J. F. Hughes, *Addison-Wesley Publishing Company*, 1991, Massachusetts

[21] 'Digital halftones by dot diffusion', D. E. Knuth, *ACM Trans. Graph.* **6** (1987) 245-273

[22] 'The effect of dither on luminance quantisation of pictures', B. Lippel and M. Kurland, *IEEE Trans. Commun. Tech.* **19** (1971) 879-888

[23] 'Design of dither waveforms for quantised visual signals', J. O. Limb, *Bell Syst. Tech. J.* **48** (1969) 2555-2582

[24] 'A survey of techniques for the display of continuous tone pictures on bilevel displays', J. F. Jarvis, C. N. Judice and W. H. Ninke, *Computer Graphics and Image Processing* **5** (1976) 13-40

[25] *"Digital halftoning"*, U. Robert, *Halliday Lithographic*, 1987, USA

[26] 'Fabrication of grey-tone mask and pattern transfer in thick photoresists', S. Nicolas, E. Dufour-Gergam, A. Bosseboeuf, T. Bourouina, J-P. Gilles and J-P. Grandchamp, *J. Micromech. Microeng.* **8** (1998) 95-98

[27] 'Development of the dispersive microlens', G. Gal, B. Herman, W. Anderson, D. Shough, D. Purdy and A. Berwick, *Pure Appl. Opt.* **3** (1994) 97-101

[28] 'Semitransparent mask technique for relief type surface topographies', J. Wengelink, H. Engel and W. Doldissen, *Microelectronic Engineering* **27** (1995) 247-250

[29] 'Simulation assisted design of processes for grey-tone lithography', W. Henke, W. Hoppe, H. J. Quenzer, P. Staudt-Fischbach and B. Wagner, *Microelectronic Engineering* **27** (1995) 267-270

[30] 'Grey-tone lithography and dry etching technique for the fabrication of integrated spot size converters', S. Ullerich, R. Steingruber and A. Umbach, *Microelectronic Engineering* **46** (1999) 303-306

[31] 'Continuous profile writing by electron and optical lithography', E.-B. Kley, *Microelectronic Engineering* **34** (1997) 261-298

[32] 'Optical proximity correction by grey tone photolithography', Z. Cui, J. Du, Q. Huang, J. Su and Y. Guo **53** (2000) 153-156

[33] 'Polymerisation optimisation of SU-8 photoresist and its applications in microfluidic systems and MEMS', J. Zhang, K. L. Tan, L. J. Yang and H. Q. Gong, *J. Micromech. Microeng.* **11** (2001) 20-26

[34] 'SU-8: a low-cost negative resist for MEMS', H. Lorenz, M. Despont, N. Fahrni, N. LaBianca, P. Renaud and P. Vettiger, *J. Micromech. Microeng.* **7** (1997) 121-124

[35] 'Hot embossing – the moulding technique for plastic microstructures', M. Heckele, W. Bacher and K. D. Muller, *Microsystem technologies* **4** (1998) 122-124

[36] 'Modular moulding equipment for quasi monolitic integration of micromechanical and microelectronic components', M. Heckele, W. Bacher, *proceedings of the 3rd France-Japan Congress & 1st Europe-Asia Congress on Mechatronics*

[37] 'Micro moulding – a powerful tool for the large scale production of precise microstructures', L. Weber, W. Ehrfeld, H. Freimuth, M. Lacher, H. Lehr, B. Pech, *Proc. SPIE* **2879** (1996) 156-167

[38] 'Microlens array produced using hot embossing process', N. S. Ong, Y. H. Koh and Y. Q. Fu, *Microelectronic Engineering* **60** (2002) 365-379

[39] 'Micro heat flux sensor using copper electroplating in SU8 microstructures', S. H. Oh, K-C. Lee, J. Chunn, M. Kim and S. S. Lee, *J. Micromech. Microeng.* **11** (2001) 221-225

[40] 'Patterning, electroplating and removal of SU8 moulds by excimer laser micromachining', M. K. Ghantasala, J. P. Hayes, E. C. Harvey and D. K. Sood, *J. Micromech. Microeng.* **11** (2001) 133-139

[41] 'Multishot ablation of polymer and metal films at 248nm', E. Hunger, H. Pietsch, S. Petzoldt and E. Matthias, *Applied Surface Science* **54** (1992) 227-331

[42] 'The effects of debris formation on the morphology of excimer laser ablated polymers', R. S. Taylor and K. E. Leopold, *J. Appl. Phys.* **64** (1988) 2815-2818

[43] 'Excimer laser micro machining of inorganic dielectrics', J. Ihlemann and B. Wolff-Rottke, *Appl. Surf. Sci* **106** (1996) 282-286

[44] 'Femtosecond and nanosecond pulse laser ablation of bariumalumoborosilicate glass', P. Rudolph, J. Bonse, J. Kruger and W. Kautek, *Appl. Phys. A* **69** (1999) S763-S766

Chapter 7

Stereolithography using excimer laser exposure

7.1 Introduction

There are many applications that require the fabrication of three-dimensional microstructures that cannot be produced in a single process using conventional machining techniques [1-3]. Greyscale masking does, however, extend the capabilities of such techniques, allowing structures such as lenses to be fabricated [4, 5]. Although greyscale masking is fast and simple to implement with no additional equipment requirements, it is of limited application. For example, an enclosed fluidic channel or freely moving object [6] cannot be created in a single photographic exposure. Such objects would require exposure through a series of masks resulting in alignment errors and problems relating to coating uniformity and development of the exposed regions.

Stereolithography [6-22], on the other hand, allows more flexibility in the structuring of materials because any part within the volume of a suitable material can be addressed during the manufacturing process. Instead of exposing or removing varying amounts of material, as is the case with greyscale masks, stereolithography polymerises a liquid material by illuminating it with a suitable source, such as an UV lamp or a laser [7, 10]. If the illuminating source can be focused, shaped, positioned and moved accurately enough, then high-resolution structures can be created [6]. Stereolithography also allows high aspect ratio structures [10], as well as overhangs and hence enclosed channels, to be fabricated in one process [6], which is not possible with other single-process methods. However, the main disadvantage of implementing stereolithography is that specialist materials and extra manufacturing equipment are normally required. Despite this, the process is of interest in the context of the current work, because of the potential it has for producing complex structures suitable for Lab-on-a-chip devices, such as encapsulated channels. Of special interest is the feasibility of using the existing laser system for fabricating microscale artefacts using stereolithography.

It is known that the excimer laser micromachining system is capable of high-resolution machining, positioning and alignment of samples over a large area (Chapter 4, 25). If the existing system could be implemented to act as an exposure source, primarily by lowering the energy density at the workpiece to a suitable level, then it would be possible to define micron-resolution structures over large areas. This has the advantage of using existing equipment, i.e. the laser and associated optical system to provide the illumination source and the precision motion stages for accurate positioning of the workpiece. The following describes a feasibility study into the application of the laser system for the production of miniature, three-dimensional structures using stereolithography.

7.2 Principle of Stereolithography

Stereolithography can be implemented in various ways, for example using a light source and suitable dynamic mask [12, 17, 18], two scanning laser beams [15] or a single laser beam and an elevation stage [7]. These processes create structures from a liquid medium that polymerises when irradiated with an energy density above some threshold level. Typically, a photosensitive liquid epoxy resin is used in conjunction with a laser whose wavelength is suitable for activating the polymerisation process. Structures can then be created either by scanning the radiation source over the surface, or moving the sample relative to the laser beam [10, 16].

A single source can be used to create structures by patterning thin layers of polymerisable material one at a time, which are built up to form the required shape. Initially a substrate is loaded onto a vertical elevation stage and flooded with a thin layer of photosensitive liquid. The illumination source, commonly a focused laser beam, is then used to expose and hence polymerise selected areas of the liquid polymer layer. When the entire layer has been patterned as required, the elevation stage is lowered, causing a second layer of photosensitive material to cover the initial layer. This layer is then patterned in a similar manner to the first layer. If a beam of suitable profile and energy density is used, then only the thickness of the uppermost layer will be exposed, leaving unpolymerised regions under the top layer unaffected.

By repeating this process, it is possible to fabricate complicated, true three-dimensional structures that can incorporate overhanging regions, such as enclosed channels. However, additional specialised equipment is required and the process may not be very rapid [23, 24], depending on the resolution required of the final structure and the material properties. Figure 7.1 shows two diagrams of typical stereolithography fabrication systems where (a) the illumination source is scanned over the sample surface and (b) where the sample is moved relative to the beam.

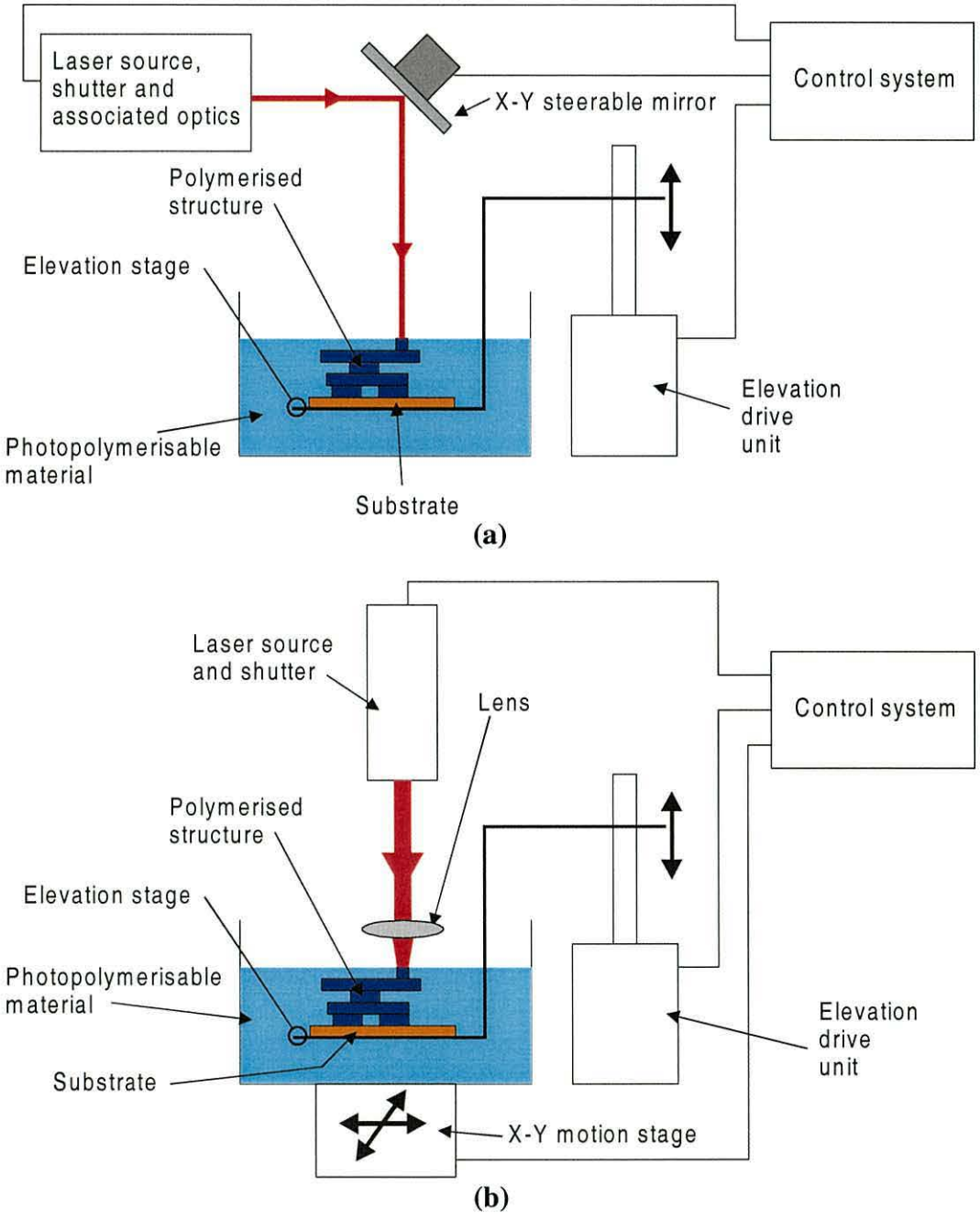

Figure 7.1 *Diagrams of typical stereolithograpical fabrication systems, where the liquid resin is polymerised in 'layers' using a single illumination source.*

Other methods allowing faster patterning of each layer have been reported where dynamic mask generators have been used [12, 17, 18]. An alternative method, that does not require an elevation stage, uses two perpendicular scanning laser beams to define the structure. Here, the energy density of one laser beam is lower than the polymerisation threshold of the photosensitive liquid used, but where the two beams intersect, the total energy density present exceeds the polymerisation threshold and the material is polymerised. This allows a controllable volume of material to be polymerised and structures to be defined by scanning the two beams. The technique avoids limitations on the minimum dimension of the structure that can be fabricated. Using such a system the beam profiles and movement determine the size of the polymerised region, rather than the thickness of the polymerisable layers. The higher resolution that is possible, compared to a layer approach, comes with the added cost of either a second radiation source or additional optical components to generate the second beam, e.g. a beam splitter and associated control systems. A typical arrangement for such a setup is shown in Figure 7.2. It should be noted that it is also possible to implement this process by moving the sample relative to two stationary laser beams.

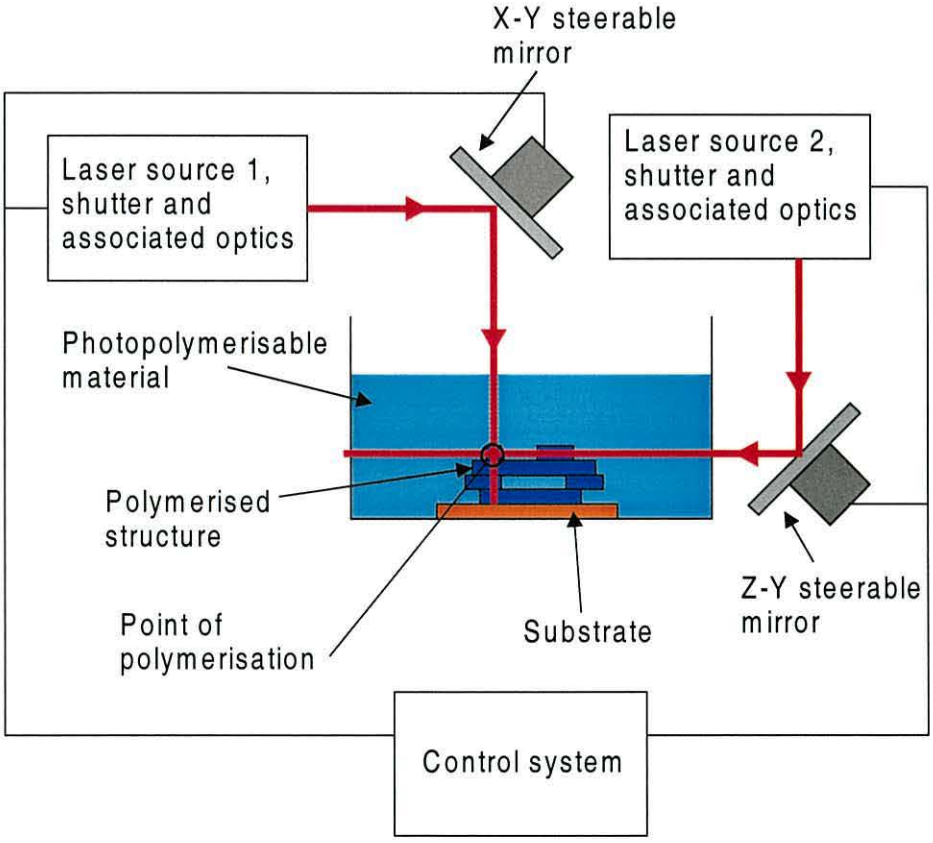

Figure 7.2 *Diagram of a typical stereolithograpical fabrication system using two scanning laser beams to create the required structure.*

In both cases, when the required structure has been defined, a suitable solvent is used to rinse off the unpolymerised material, leaving the finished structure.

Initial trials were undertaken using the laser to pattern a thin layer of material, applied by spin-coating a uniform layer of photosensitive resin onto a glass substrate. When the exposure parameters had been defined, stereolithographic fabrication was attempted.

7.3 Experimental setup

The liquid resin material used was an UV curing acrylate resin, type 30/63, supplied by Epigem Ltd. specifically for this work. The material was specially formulated to contain photo-initiators, that start a polymerisation reaction when exposed to 248nm wavelength light. The resin could therefore be cured using light generated by the excimer laser.

The substrates used for this work were covered with an evaporated gold layer to allow accurate focusing of the sample using the height measurement facility of the laser system. An important consideration during this work was that, although the material was stable and could be handled at normal atmospheric conditions, it could only be polymerised in an inert atmosphere. This was accomplished by flooding the work area with nitrogen during exposure experiments.

7.3.1 Initial characterisation investigation

The substrate and liquid resin were contained within a miniature aluminium container, shown in Figure 7.3, for initial trials to avoid contaminating the laser system. The base of the container was machined down to ~400μm so as to avoid adding unwanted height to the laser chuck. The laser system elevation range was limited to 5mm, hence focusing could become problematical if a standard container were used.

First attempts to form a thin layer of material, by spin-coating the resin onto a glass substrate, were not successful. Although the resin could be spin-coated into a thin layer,

if left for a period of several hours, it pulled away from the edges of the substrate and formed holes in the coating. This was most likely due to the inherent properties of the material, namely surface tension, viscosity and wetting. An attempt to overcome these problems, using an HDMS prime process, did not produce a noticeable improvement in the coatings. Although not very satisfactory, experiments could be undertaken if the sample was processed within an hour of coating.

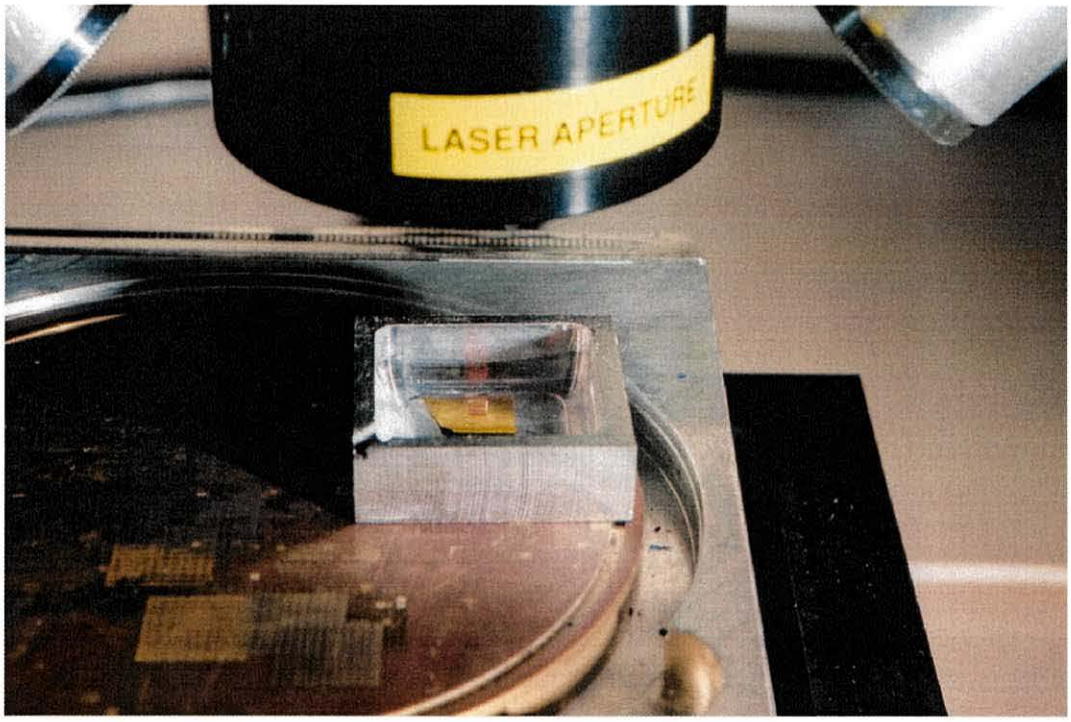

Figure 7.3 *Photograph showing the aluminium container used for initial experiments in place on the laser chuck, complete with sample present. The laser chuck vacuum retention system was found to be adequate for holding the container in place.*

Subsequent laser exposure at a range of energy densities was then used to find the point at which polymerisation of the UV resin occurred. To do this, a thin layer of resin, approximately 10μm thick was spin-coated onto a glass substrate. It was not possible to create thinner coatings that were useable due to the poor wetting properties of the resin. The layer was then exposed using the laser and the unpolymerised material rinsed off with acetone within 15 minutes to reduce resin shrinkage to a minimum. A range of laser pulse energies and total energies were investigated. This was achieved using a laser control program that constructed a 10 by 10 grid of exposed regions. The laser energy density used was increased from a set minimum to a set maximum down each column, with the number of shots fired increasing between adjacent columns. Thus a characterisation grid was created and the curing threshold of the material found.

This revealed that an energy density of 0.245mJ/cm^2 was required at the workpiece to polymerise the resin, above which no effect was observed; the resin was very sensitive to the incident radiation and has a relatively low polymerisation threshold. Dielectric coated quartz plates attenuated the laser beam to 35% of the intensity of the unattenuated beam used for machining. This allowed the laser attenuator to be operated at a reasonable level.

During these experiments, it was found that high nitrogen flow rates were not required to maintain a suitable atmosphere over the sample surface. Indeed, if the pressure and flow rates used were too high, ripples and other distortion of the surface of the liquid resin occured. This can be seen in Figure 7.4, which shows a section of a calibration grid made by exposing a 10μm thick spin-coated layer, using a 500μm square beam at the workpiece. The effects of using high nitrogen flow rates have caused some of the polymerised regions to 'drift'. However, this does indicate that very thin layers of material can be selectively polymerised. To avoid distortion of the surface it was found necessary to keep the gas supply pressure below approximately 2psi. The reduced flow rate was still sufficient to maintain the inert atmosphere to allow polymerisation to occur.

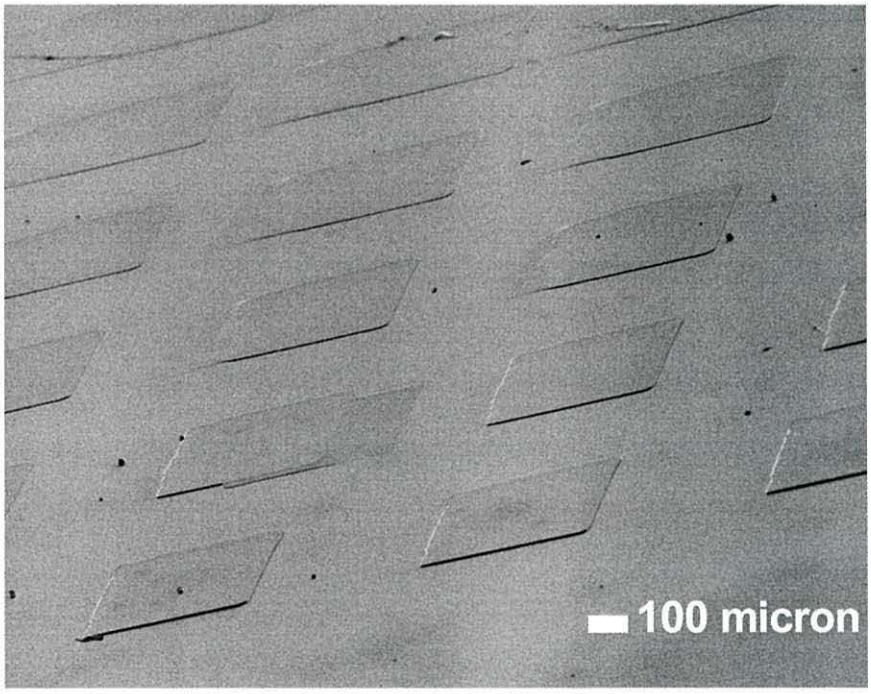

Figure 7.4 *Scanning electron micrograph showing part of a calibration grid used to determine the polymerisation threshold of the resin.*

An example of the results obtained using a lower gas supply pressure is shown in Figure 7.5, where a rectangular aperture was used to expose the resin. The rough edge at the left of the polymerised feature is due to the exposed region extending beyond the edge of the resin layer.

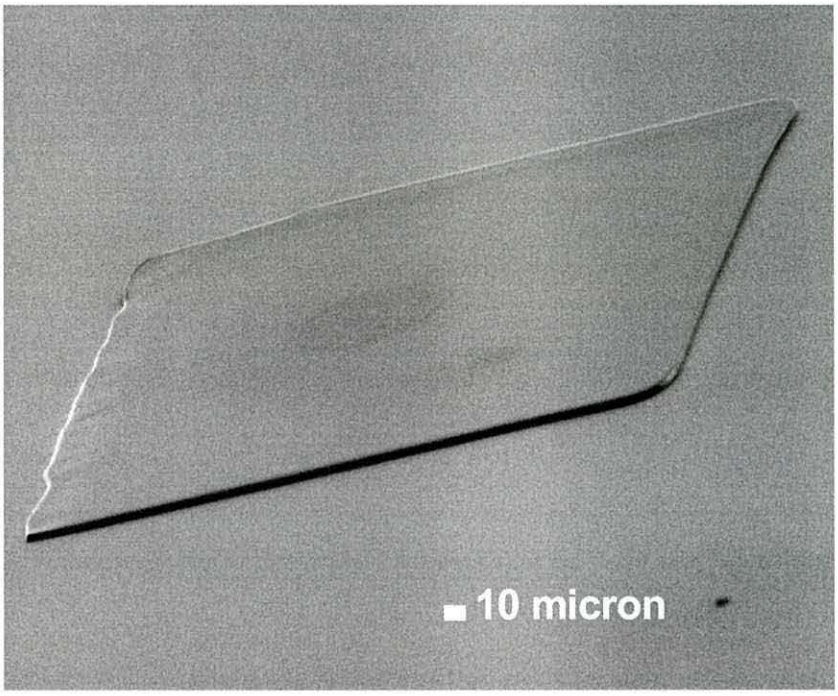

Figure 7.5 *SEM showing the effects of reducing the nitrogen supply pressure and flow rate so that it would not cause disturbance to the resin surface.*

It was intended to use various thickness resin films to find the point at which complete polymerisation of the resin layer ceased. This would allow the depth of polymerisation per shot to be measured. However, useable layers thinner than ~10μm could not be produced which limited the investigation into the depth polymerised per shot, as well as the linearity of the polymerisation process. Another problem was that the resin coating was found to vary several microns in thickness over the surface of the sample. This was most likely due to the poor wetting properties of the resin causing varying amounts of retraction in the time taken to expose the layer. Furthermore, the non-ideal low spin-coating speed used to achieve a complete coating may also have caused ripples in the layer. It was anticipated that if the substrate could be submersed in the liquid resin and the gas supply pressure was suitable, then the uniformity problems encountered spin-coating a resin layer would be avoided. Therefore an initial attempt was made with a layer ~10μm thick to establish such a relationship.

7.4 Results of suitability trials

The approximate depth of curing was investigated by spin-coating a glass substrate with a layer of resin approximately 10μm thick and measuring the depth exposed below the surface. By exposing the resin using various laser energies and masks, the minimum exposure depth for a given energy density was determined approximately. It was found that a single exposure was capable of polymerising a thin layer of material, but this could not be accurately measured as it was not attached to the substrate and retaining the polymerised regions undamaged while removing the surrounding unpolymerised material was not successful.

The first exposure was found to polymerise a thin layer at the surface of the resin layer leaving unpolymerised regions beneath. Subsequent shots then polymerised progressively further into the resin layer, until eventually the whole thickness was polymerised. The progressive polymerisation into the depth of the layer probably comes from the lower absorption of the polymer film compared with the unpolymerised fluid. Consequently, the greatest absorption will occur in the fluid just below the interface with the polymerised material.

Figure 7.6 shows the result of incomplete polymerisation through the resin thickness. As can be seen, not all regions are attached to the substrate. In both cases, the polymerised layer has distorted and lifted from the substrate in some regions, but has remained attached in others. This is most likely due to the uneven thickness of the spin-coated layer used, resulting in only some exposed areas polymerising down to the substrate.

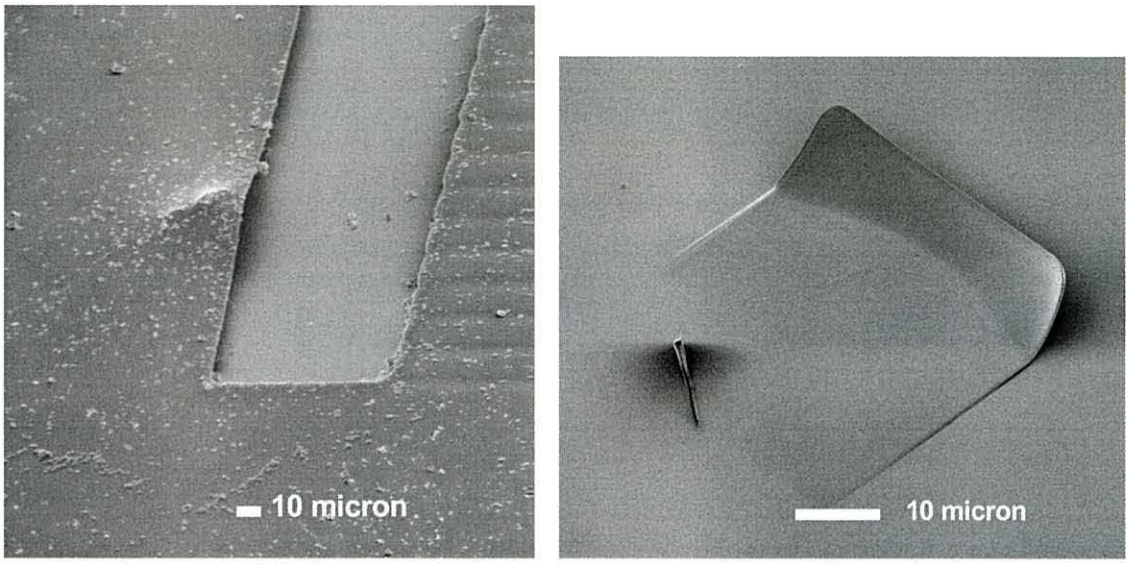

(a) **(b)**

Figure 7.6 *SEMs showing the incomplete attachment of polymerised regions (a) lifting around the edge of a poymerised region and (b) distortion of a calibration square. Both are due to uneven resin layers.*

By increasing the number of exposure 'shots', the resin could be polymerised through its complete thickness. An example is shown in Figure 7.7. Here, the complete thickness of the resin layer, which was measured to be approximately 6μm, has been exposed. Noting the results in Figure 7.6 and Figure 7.7, it may be deduced that the resolution possible using the laser as an exposure source is probably sub-micron – 15 shots were required to completely polymerise the spin coated resin layer to produce the structure in Figure 7.7. This is consistent with problems experienced previously, where structures fabricated using a single shot were not attached to the substrate, i.e. when a layer thinner than the resin coating had been polymerised at the surface.

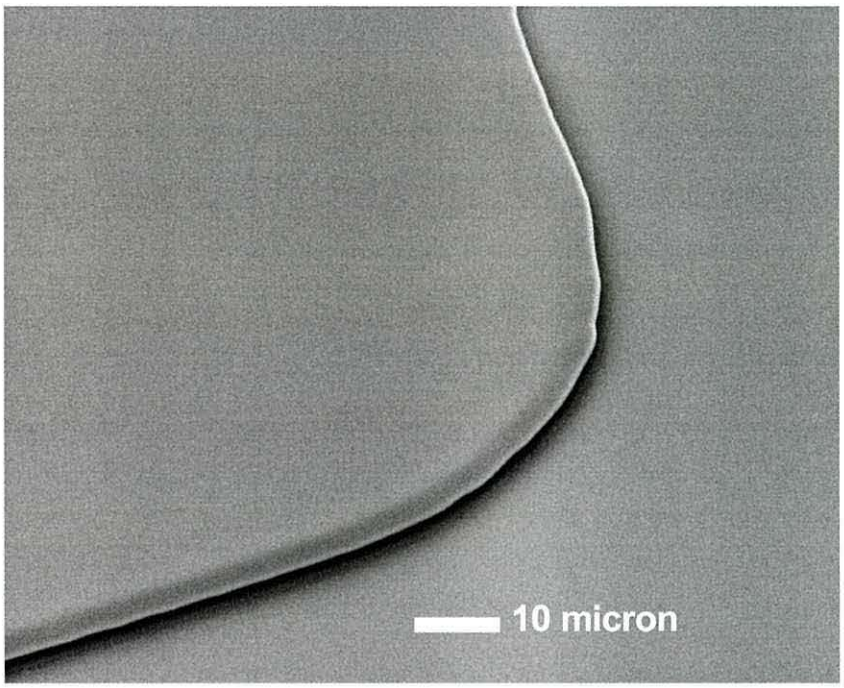

Figure 7.7 *SEM showing the edge of a region of resin where the complete thickness has been polymerised using 15 shots.*

Figure 7.7 also shows that the upper surface of the polymerised region is in good accordance with the intended mask aperture (chemically etched copper berillium sheet, Chapter 3.5.1) and has polymerised throughout the depth of the resin layer. With a low gas supply pressure, no ripples or drifting were present in the sample. The slight roughness around the edge was also observed in the mask used.

Figure 7.8 shows a magnified section of the polymerised region shown in Figure 7.7, showing that the surface layer shape extends for approximately 2μm below the surface of the resin, the underlying area being polymerised in subsequent shots. The effect of using a focused laser beam can also be seen below the surface of the resin as the structure formed is tapered. Hence it is feasible that the laser system could be used to pattern layers under 1μm thick using a single shot, if a suitable resin coating were produced, or if the substrate were submerged in a vat of resin.

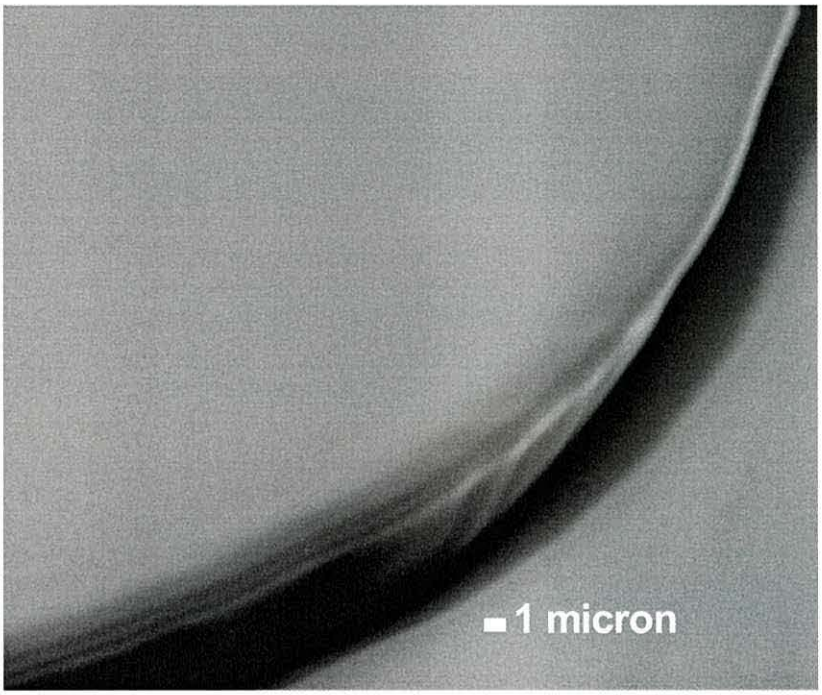

Figure 7.8 *Scanning electron micrograph showing the edge of a polymerised region where the complete spin-coated layer has been polymerised.*

Figure 7.9 shows the result of using a 'finger-electrode' mask for fabricating travelling wave electrode tracks [25]. The mask consisted of alternate regions of 40μm wide transmissive and non-transmissive stripes. The structure was then reproduced in a 20μm thick resin layer using approximately 100 laser shots to completely polymerise the layer. Although the pattern is visible, it is not very well defined. This is probably due to the large total energy required to polymerise the complete resin layer used in this sample, causing over-exposure, as well as problems associated with maintaining laser focusing on the top of a varying thickness resin layer. A very thin layer of polymerised resin can be seen between the exposed regions, which is a good indication that the resin is capable of high-resolution patterning. The tapered structure produced beneath the surface is most probably due to the focused laser beam used. This is consistent with the wall angle obtained when deep structures are machined (Chapter 2.5.3). It also demonstrates that the entire thickness of the resin layer can be polymerised.

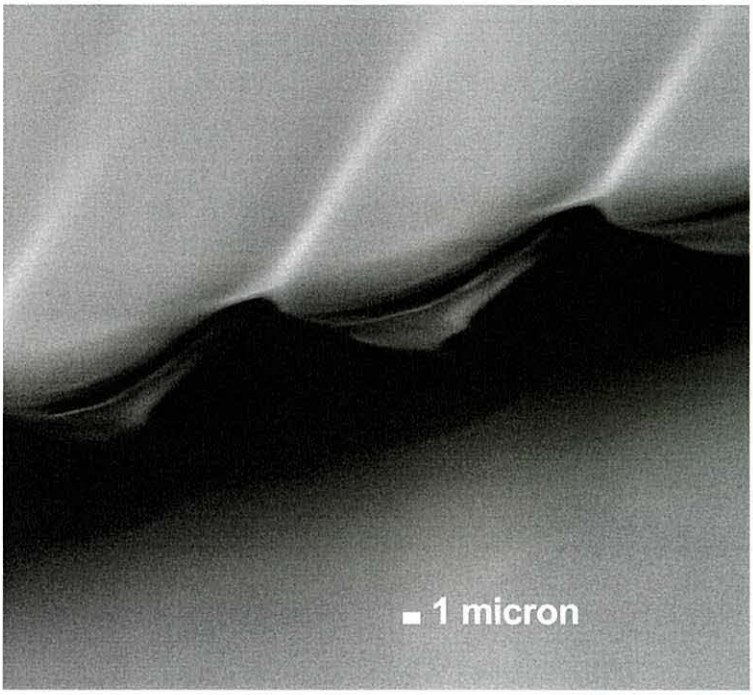

Figure 7.9 *SEM showing the material polymerised beneath the surface of a thick resin layer when 100 shots were fired. The tapered appearance is most likely due to the laser beam profile inherent to the focused optical system used.*

7.5 Investigation to create three-dimensional structures

In order to fabricate three-dimensional structures, a method of adding a fresh layer of resin on top of a previously exposed layer was required. A simple manually adjustable elevation stage was fabricated to allow initial investigation into altering the height of the substrate within a container of liquid resin, so removing the need for spin-coating layers of resin and avoiding the associated problems of wetting and layer uniformity.

This approach has the advantage of only needing to focus the laser on the surface of the liquid resin in a suitable container once during the fabrication process, as the liquid level will not vary significantly during the process. Initially, the sample was submerged, then raised to a point where it was a known distance below the surface of the liquid resin. This formed the start layer to be patterned using the laser system. Figure 7.10 shows the elevation stage used to raise the height of the sample. The thumb-wheel was used to manually alter the height of the elevation stage and had a reference marker scribed on it. The scale used divided one revolution of the thumb-wheel into various units, corresponding to a minimum height change of

approximately 10μm. The vertical thicknesses of the components were as thin as possible to maximise the height of structures that could be fabricated with the limited laser elevation range available. The base of the container was 350μm thick and the height of the elevation stage was 400μm. The components were machined out of aluminium, which is inert to the solvents present in the liquid resin. The platform allowed manual control of the sample height, which although not ideal due to positional errors, the fabrication process could be evaluated. Including an accurate servo system into a dedicated laser chuck is relatively easy.

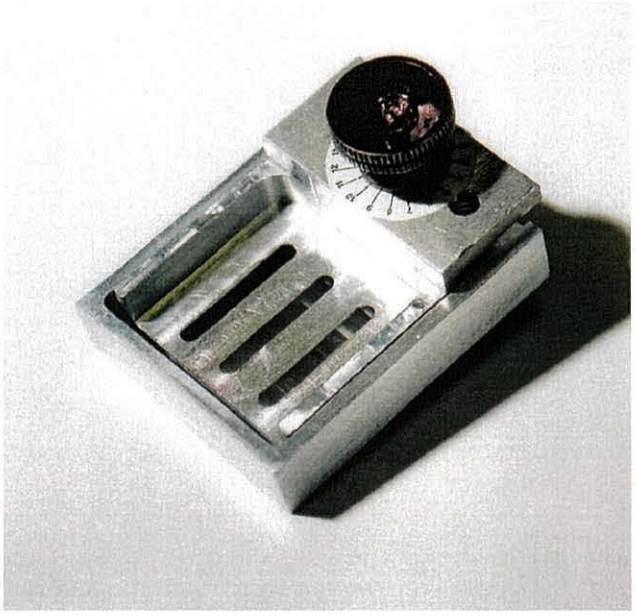

Figure 7.10 *Photograph of the manual elevation stage fabricated to allow manual height adjustment of the sample within a volume of liquid resin.*

The positional accuracy and repeatability of the manual stage was measured using the optical height measurement facility of the laser system by placing a glass substrate, with an evaporated gold coating, on the stage. This allowed the sample holder height to be measured with minimal influence on the stage height, using the reflective surface of the gold. The calibration curve for the elevation unit are shown in Figure 7.11. The error present in the measured stage height is probably due to the non-parallel motion of the stage (the construction was simple with no slider bars) coupled with the dimensional errors present in the scale used, which was printed using a laser printer.

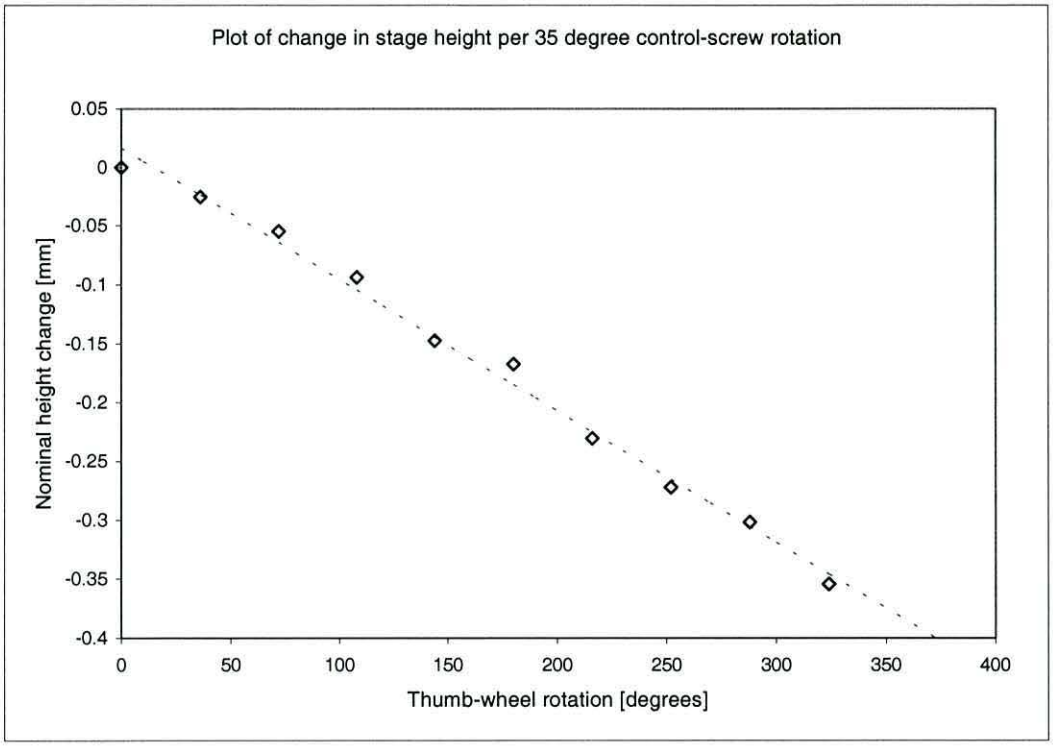

Figure 7.11 *Plot showing the measured height and height deviation when manually adjusting the miniature elevation stage.*

To obtain these results the control screw was turned in 18 degree increments, indicated on the rotary scale by a single division. Additional rotary scales were used with various graticules, typically 5 degree increments that allowed ~10μm height steps. The screw thread used in the elevation stage was known to have a pitch of 0.7mm per revolution. This equated to a theoretical change in height of 35μm per 18 degree revolution of the control screw, although mechanical backlash, rotary scale alignment errors and non-uniformity of the thread were likely to distort the actual height change of the stage.

The substrate height was varied over a distance of 350μm, as this would be sufficient to create test structures. This was repeated five times and the average height change per indicated 35 degrees of rotation of the control screw calculated. The average change in substrate height achieved was found to be 35.4μm, which correlates well with the designed value. The maximum error between the measured and theoretical values, however, was 5μm. Linear regression of the recorded data reveals that the linear regression coefficient, R^2, is 0.993 as would be expected from a linear screw thread. Although the maximum amount of error is significant at 5μm, initial trials using the stage were possible, as it was found that the viscosity of the resin prevented resin layers

below 10μm to 15μm from being formed so larger step increments were generally required.

7.6 Results

The elevation stage was used in an attempt to fabricate a 'staircase', where a square aperture was used to polymerise a layer of resin, the sample then lowered and the workpiece stage moved before another 'step' was created, partly overlapping the first. It was found that the resin was too viscous to cover the surface of the sample in thin layers, as the resin meniscus prevented it from flowing over the surface of the sample unless it was several hundred microns below the surface of the resin. Attempts to dilute the resin using acetone, which was used to remove the unpolymerised material, proved unsuccessful, as the resin was still far too viscous and also failed to polymerise.

In light of this, an alternative approach was adopted, where the elevation stage was used to position the height of the sample relative to the laser beam focal plane. Then a fixed volume of resin (typically 10 μl, depending on the sample surface area) was dispensed onto the surface of the sample using a guilson to form the layers. Although the layers formed were still relatively thick (between 5μm and 15μm), it did allow the creation of structures using the resin to be investigated.

Figure 7.12 shows the result of altering the sample elevation stage height and then dispensing a small volume of resin onto the surface prior to each set of exposures. The manual elevation stage was at its highest point at the top right of the structure and at its lowest at the lower left of the structure. The debris that can be seen came from cutting the glass substrate in order to view the structure in the SEM. The laser stage was also moved down and left 10μm in each direction between exposures to create the structure shown. A 50μm square beam was used to expose the resin at an energy of 0.280mJ/cm^2, with 14 shots fired at each of the ten locations to ensure complete polymerisation of the resin down to underlying polymerised material. The sample height decrement was approximately 5 microns between each set of exposures. Although the structure made was relatively coarse, compared to the minimum depth of

exposure possible and not as well defined as was hoped, it does demonstrate proof of principle.

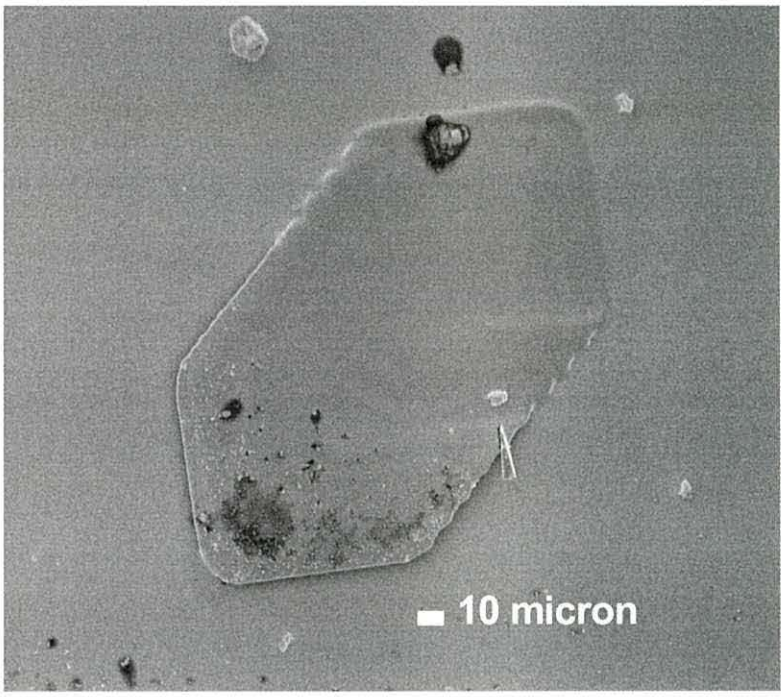

Figure 7.12 *SEM showing the result of multiple laser exposures of the liquid resin at various sample heights and positions.*

Figure 7.13 shows a magnified view of the edge of the structure, seen at the lower left of Figure 7.12, where a thin layer of material has successfully been polymerised, with no material present below the exposed layer. This is a good indication that high-resolution stereolithography should be possible using the excimer laser. The polymerised region is approximately 4μm thick, although it should be noted that the repeatability of this process is limited by the inherent properties of the resin and the manual stage used.

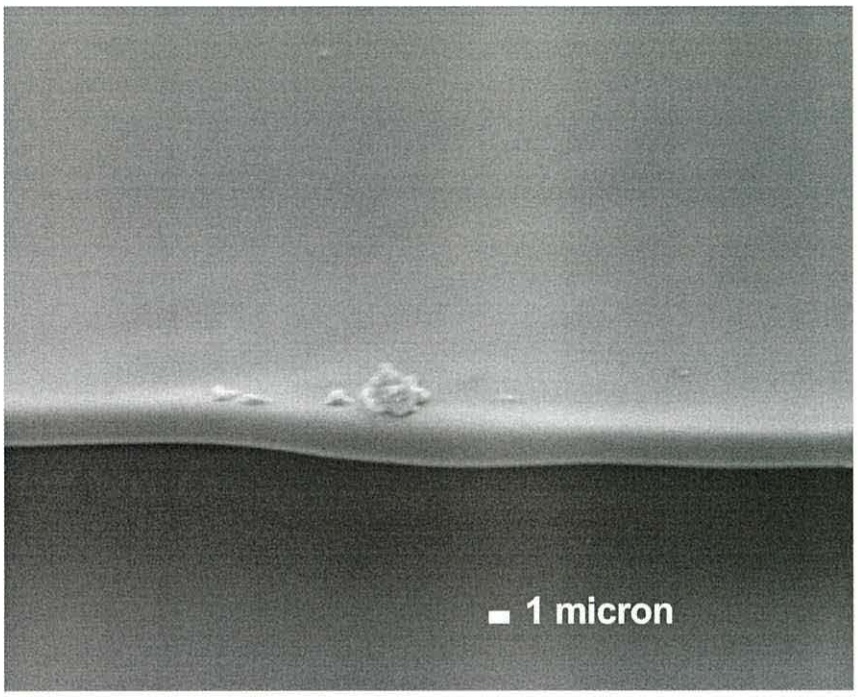

Figure 7.13 *Scanning electron micrograph showing an enlargement of the edge of a 50μm square polymerised region that is elevated above the surface of the substrate with no material present under it.*

The section shown in Figure 7.13 is suspended ~35μm from the substrate and is part of a flat region of polymerised resin that was approximately parallel to the substrate surface with no signs of distortion to the final structure. This indicates that the overhang present is unlikely to have been generated by the resin lifting from the surface due to gas flow or handling and is caused be the exposure process, as intended.

In order to allow more accurate dispensing of the resin, a precision dispensing system was developed, consisting of a PIC micro-controller, power driver section and stepper motor driven screw drive that controlled the position of a syringe plunger to within 1.25μm.

The actuator stage consisted of a high quality stepper motor capable of 0.9 degree steps, connected to a precision screw thread. The motor and thread were fixed, but a nut was attached to a linear slider block causing it to move when the thread was rotated. Using these components allowed the slider block to move in 1.25μm steps per 0.9 degree step of the motor. When a 1ml syringe was attached to the device, the system accurately displaced 21.5 nl of fluid. An overview of the system is shown in Figure 7.14.

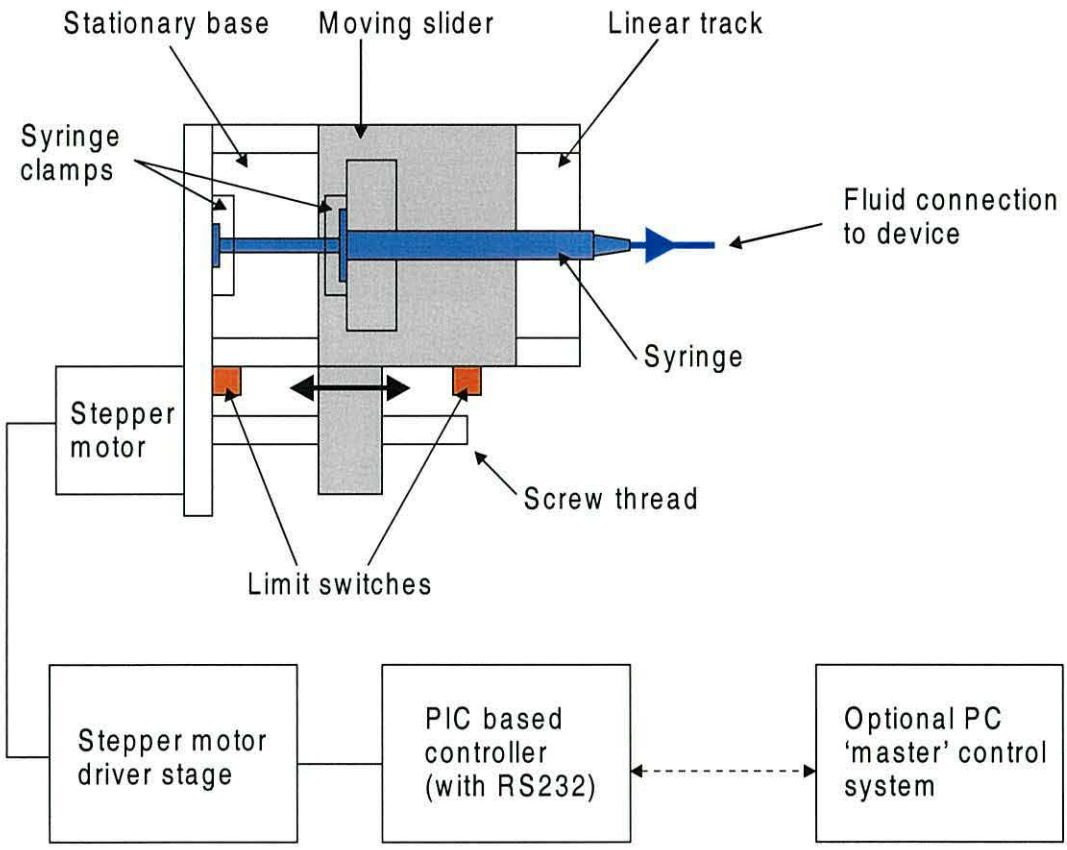

Figure 7.14 *Overview of the precision pump system developed.*

The prototype pump attached to a 1ml syringe was tested by using it to control the position of 6.4μm latex beads (Sigma Aldrich Co., Ltd., UK) within a known cross-section channel. A test channel was fabricated that was mounted in a re-useable clamp [Appendix IV] containing a micro-fluidic channel 80μm wide, 30μm high. The beads were displaced approximately 10μm per motor step, corresponding to a volume change of 24nl, which is in good accordance with the calculated fluid volume change. The repeatability of the device was examined by moving a stationary particle along the channel by turning the motor through a series of discrete steps. When the motor rotation direction then reversed, the particle returned to almost exactly the same position, as shown in the frame sequence in Figure 7.15. This indicated that minimal backlash was present in the system. The pump was designed to allow syringes of various volumes to be fitted, so allowing the total dispensing volume and accuracy to be tailored to the task in hand. Table 7.1 shows the pump input / output volumes theoretically obtainable per motor step for various sized syringes, although for the present work, a 1ml syringe is sufficient.

Syringe volume	Approximate plunger travel for full output [mm]	Theoretical volume change per mm of plunger movement	Theoretical volume change per motor step
1ml	58	17.24 μl	21.6 nl
500ul	60	8.33 μl	10.4 nl
250ul	60	4.17 μl	5.2 nl

Table 7.1 *Theoretical pump input / output volumes obtainable per stepper motor step.*

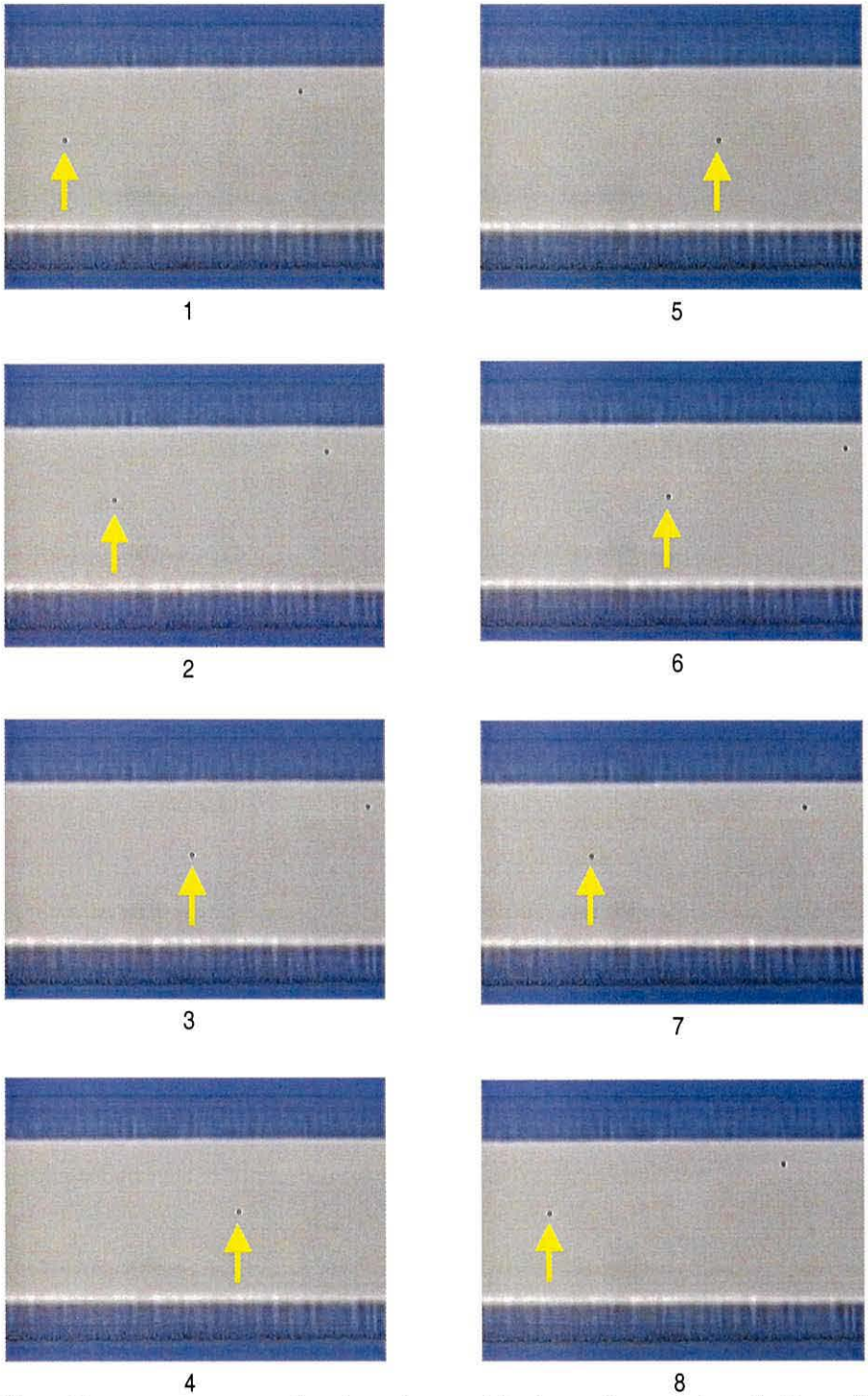

Figure 7.15 *Frame sequence showing the positioning of particles (indicated) within a micro-channel. This shows a high degree of repeatability of the pump.*

To date the pump has not been implemented in the stereolithography experiments.

The system that has been developed to control the pump stepper motor is capable of driving up to four stepper motors simultaneously and can be controlled remotely if required, via a serial port. This could form a useful part of a future stereolithography system, as it could be used to control a liquid resin dispensing system, as well as a dedicated sample elevation stage driver. Both of these components could be mounted on a suitable laser chuck and used in place of the conventional laser machining chuck. If the laser control PC were interfaced to the stepper motor driver system, then the entire system could be fully integrated to provide a micro-stereolithography fabrication system.

Alternatively, a completely separate stereolithography fabrication system could be created using the stepper motor controller unit and a PC based controller. This could consist of an elevation stage as well as an X-Y positioning stages, similar to the prototype pump assembly, all of which could be PC controlled in conjunction with a simple laser emitter.

7.7 Conclusions

It can be seen that the excimer laser system is an ideal exposure source with minimal modification to the optical system and can be used for stereolithographical production of basic three-dimensional structures. However, the properties of the resin initially obtained were not ideally suited to the application in hand and limited the quality of the results. Although the laser system could be used to successfully pattern the resin to high-resolution, the material viscosity was too high and the wetting ability was poor. This caused problems when attempting to create uniform layers of resin that were less than 10μm to 15μm thick. The wetting properties of the material were also poor, so producing a uniform layer of material proved to be problematical, as the resin tended to creep away from the edges of the substrate and holes developed if left for a prolonged period of time. These properties were not ideal when attempting to characterise the resin layer, as non-uniformities in the coating layer limited the amount of work that

could be done. Ideally, micron or even sub-micron thick layers would be required to produce micro-components. The resin was also too sensitive to the incident radiation, as any spurious reflections, not normally apparent during laser ablation, caused unwanted polymerisation of the resin.

It was found that the laser system was capable of polymerising a 6μm thick layer of resin using 15 laser pulses, which equates to ~3 pulses per micron. This also indicates that thinner, sub-micron layers could be produced, although it was not possible to produce examples during this investigation. It has also been shown that complex, overhanging structures can be produced, without polymerising underlying material. The process is also relatively rapid, as few exposures were required to polymerise the resin.

The resin was also found to be very sensitive to incident radiation, requiring that all experiments were conducted with yellow filters over any light sources. A more significant problem was that reflected laser light from almost any surface caused polymerisation of the material. This required additional shuttering to be put in place during the experiments, which was not needed when a material was being ablated. The high sensitivity of the resin also required that multiple attenuation plates were used in the laser system to reduce the laser energy density at the workpiece to a sufficiently low level. This was not ideal, since an additional setup task was required.

These problems were reported to Epigem and an alternative mixture was obtained. However, there was insufficient time to conduct detailed exposure characterisation experiments using the new mixture. Initial inspection revealed that the second resin mix had a much lower viscosity than the first mixture and was not as sensitive to incident radiation, as it could not be polymerised with attenuation plates present in the laser beam. The resin also had improved wetting capability and did not shrink back from the edges of the substrate and holes did not develop in spin-coatings. This resin seems to be much better suited to stereolithography as it addresses the major shortfalls of the first resin mix used for this work.

Manual alteration of the sample height also incurred large positional errors in all three axes, although it did allow proof of principle. A servo actuated precision stage would

overcome these problems, producing minimal disturbance of the sample, so allowing faster throughput and synchronised, autonomous operation. If there had been time to fully test the second resin mix and it proved successful, an additional elevation stage was to be added and integrated into the existing laser control system. This could be accomplished relatively easily by removing the laser system chuck normally used and replacing it with a suitable custom made unit. This would remove the need to spin-coat samples with resin, as the substrate could be suspended in a liquid medium and lowered sequentially as required. A suitable actuation mechanism would be a linear screw drive system, similar to that used in the development of the precision syringe pump. Combining this with the precision dispensing pump is an important goal in the next phase of the work.

7.8 References

[1] 'Rapid prototyping (stereolithography) in the management of intra-articular calcaneal fractures', G. M. Kacl, M. Zanetti, M. Amgwerd, O. Trentz, B. Seifert, H. Stucki and J. Hodler, *Eur. Radiol.* **7** (1997) 187–191

[2] 'Stereolithography: application to neurosurgery', M. Foroutan, B. Fallahi, S. Mottavalli and M. Dujovny, *Crit Rev Neurosurg* **8** (1998) 203–208 203

[3] 'A novel micro-machining method for the fabrication of thick-film SU-8 embedded micro-channels', F. E. H. Tay, J. A. vanKan, F. Watt and W. O. Choong, *J. Micromech. Microeng.* **11** (2001) 27–32

[4] 'Fabrication of complex micro-optic components using photo-sculpting through halftone transmission masks', D. R. Purdy, *Pure Appl. Opt* **3** (1994) 167-175

[5] 'Development of the dispersive microlens', G. Gal, B. Herman, W. Anderson, D. Shough, D. Purdy and A. Berwick, *Pure Appl. Opt* **3** (1994) 97-101

[6] 'Submircon stereolithography for the production of freely movable mechanisms by using single-photon polymerisation', S. Maruo, K. Ijuta, *Sensors and Actuators A* **7** (2002) 1-7

[7] 'Distributed MEMS phase shifters by microstereolithography on silicon substrates for microwave and millimeter wave applications', T. S. Ji, K. J. Vinoy and V. K. Varadan, *Smart Mater. Struct.* **10** (2001) 1224–1229

[8] 'Feasibility of Design in Stereolithography', B. Asberg, G. Blanco, P. Bose, J. Garcia-Lopez, M. Overmars, G. Toussaint, G. Wilfong, and B. Zhu, *Algorithmica* **19** (1997) 61–83

[9] 'Femtosecond two-photon stereo-lithography', M. Miwa, S. Juodkazis, T. Kawakami, S. Matsuo and H. Misawa, *Appl. Phys. A* **73** (2001) 561–566

[10] 'Micro-stereolithography of polymeric and ceramic microstructures', X. Zhang, X. N. Jiang and C. Sun, *Sensors and Actuators* **77** (1999) 149–156

[11] 'Stereolithography and microtechniques', S. Zissi, A. Bertsch, J.-Y. Jezequel, S. Corbel, D. J. Lougnot and J.C. Andre, *Microsystem Technologies* **2** (1996) 97-102

[12] 'Systems control for a micro-stereolithography prototype', S. Huang, M. I. Heywood, R. C. D. Young, M. Farsari and C. R. Chatwin, *Microprocessors and microsystems* **22** (1998) 67-77

[13] 'Optical microstructures fabricated by femtosecond laser two-photon polymerisation', L. Luo, C. Li, S. Wang, W. Huang, C. Wu, H. Yang, H. Jiang, Q. Gong, Y. Yang and S. Feng, *J. Opt. A: Pure Appl. Opt.* **3** (2001) 489-492

[14] 'Processing and characterising photo-sensitive polymer in the rapid protptyping process', J. Y. H. Fuh, L. Lu, C. C. Tan, Z. X. Shen and S. Chew, *Journal of Materials Processing Technology* **89-90** (1999) 211-217

[15] 'A biphotonic process in stereolithography', J.-J. Clair, *Pure Appl. Opt.* **2** (1993) 169-172

[16] 'Manufacturing of three-dimensional micro-parts by UV laser induced polymerisation', T. Nakamoto, K. Yamaguchi, P. A. Abraha and K. Mishima, *J. Micromech. Microeng.* **6** (1996) 240-253

[17] 'Microstereolithography using a liquid crystal display as dynamic mask generator', A. Bertsch, S. Zissi, J. Y. Jezequel, S. Corbel and J. C. Andre, *Microsystem Technologies* (1997) 42-47

[18] 'Study of the resolution of a new 3D microfabrication process: the microstereolithography using a dynamic mask-generator technique', A. Bertsch, J. Y. Jezequel and J. C. Andre, *J. Photochem. Photobiol. A: Chem.* **107** (1997) 275-281

[19] '3D microfabrication by combining microstereolithography and thick resist UV lithography', A. Bertsch, H. Lorenz and P. Renaud, *Sensors and Actuators* **73** (1999) 14-23

[20] 'Over-curing reduction of parts fabricated by the solid laser-diode plotter rapid prototyping system using the taguchi method', J.-Y. Jeng, Y. S. Wong and C. T. Ho, *Int. J. Adv. Manuf. Technol.* **18** (2001) 683-691

[21] 'Microprocessing at the fingertips', G. Thornell and S. Johansson, *J. Micromech. Microeng.* **8** (1998) 251-262

[22] 'Laser fabrication and assembly processes for MEMS', A. S. holmes, *Proc. SPIE* **4274** (2001) 297-306

[23] 'A study of the build-time estimation problem for Stereolithography systems', J. Giannatsis, V. Dedoussis and L. Laios, *Robotics and Computer Integrated Manufacturing* **17** (2001) 295

[24] 'A process planning method for improving build performance in stereolithography', A. P. West, S. P. Sambu and D. W. Rosen, *Computer-Aided Design* **33** (2001) 65-79

[25] 'Development of Biofactory-on-a-chip technology using excimer laser micromachining', R. Pethig, J. P. H. Burt, A. Patron, N. Rizvi, M. S. Talary and J. A. Tame, *J. Micromech. Microeng.* **8** (1998) 57-63

Chapter 8

Conclusions and suggestions for future work

8.1 Conclusions

The aim of this work was to develop flexible micro fabrication techniques, allowing the development of polymer-based Biofactory components. All the techniques were based on an excimer laser micromachining system that permitted micron resolution patterning of a wide variety of materials, either by ablation or exposure. The results obtained during this work demonstrate the flexibility of the excimer laser micromachining facility when used in micromachining processes, as several advancements have been made, including high resolution mask fabrication, greyscale mask based laser machining and the associated design and simulation software. Another significant experimental result was that laser ablation generated debris, that can be problematical in some situations, was removed with no effect on the sample by an electrostatic debris collection system.

High accuracy machining of a range of materials over large areas has been achieved, including fabricating photolithographic masks that can be used in a contact exposure process (Chapter 4). The maximum measured error of these masks was 95nm over an area of 81mm^2. The features of these masks were measured to be in very good accordance with the design dimensions and were used to produce microelectrode arrays for cACEOP pumping. These masks can be fabricated quickly, typically in 15 minutes, so allowing the rapid production of disposable, high-resolution masks, ideal for a contact imaging process and the inherent eventual mask damage. This type of mask fabrication system, which allows the rapid development and production of contact masks, is not known to have been reported previously. Other methods, such as direct electrode machining and the patterning of etch resistant layers have also been investigated to produce microelectrode devices directly, thus removing the photolithographic step normally required. Although operational cACEOP devices were fabricated, the results obtained with these methods were not as consistent or as

high-quality as those obtained using photolithography, due to the machining characteristics of metal films, inherent to the machining process.

Micro-channels and optical waveguide structures were also created using excimer laser ablation to pattern a thick polymer layer and allow on-chip detection to be integrated into existing production techniques. By defining the waveguide using laser machining, much greater flexibility has been achieved in the path of the waveguides. Various designs were tested and the path of the waveguide had little effect on the light-guiding properties of the device. Such a system also allows the integration of on-chip optical splitters and re-combiners relatively simply – the only difference being the design used. Although the cell detection sensitivity of such devices was not as high as had been hoped, basic optical measurements were performed. It should also be noted that the aim of this initial investigation was the fabrication of planar optical waveguides that could be integrated into Lab-on-a-chip devices.

Greyscale masks have been successfully created by and implemented in the laser system, as well as by a conventional photolithographic process. Laser machined masks allowed micron resolution features in addition to rapid mask production using projection-reduction techniques, similar to those used to fabricate the cACEOP devices. It was found that if the mask features were below the resolution of the system in which the masks were implemented, the actual method of creating the transmission patterns had little effect. This allowed a simple computer algorithm to be used to create the required transmission. Two computer programs were written, one allowing computer-based generation and the other simulation of greyscale masks. This has the advantage of being considerably faster than manual mask creation and is less error prone, as well as allowing the structure that would be produced using a particular mask to be simulated prior to fabricating it.

Photolithographic greyscale masks were used to fabricate various structures, including fluidic manifolds, allowing precise, well defined structuring as the relationship between total energy and material remaining for the materials used was found to be linearly dependent. Various photosensitive materials were used, including SU8, dry-film laminate and UV curing resins. This allowed the rapid production of complex structures

in a single exposure, requiring no additional equipment and using an existing process, so is ideally suited to mass-production of Bio-factory and micro-components.

Implementing greyscale masks in laser machining allows a wider range of materials to be structured, as photosensitive materials are not required. Again, high-resolution structures were fabricated with good accordance to the original design and were fabricated in various materials, including dry-film laminate and glass. Structures several tens of microns deep were machined into materials using laser greyscale masks, with little mask damage. As far as is known, this is the first report of such deep machining. The process was also found to have a linear relationship between transmission and machined depth, contrary to the reports of others. The mask generation process is therefore greatly simplified.

Although designed primarily for laser ablation, the system has also been used successfully as a precise exposure source using the deep UV radiation produced by the excimer laser. This allowed an initial investigation of the excimer laser micromachining system for stereolithographic production of structures. Unfortunately, the results produced during this investigation were not optimal due to the characteristics of the UV resin used. An alternative material was developed by the supplier, which seemed to have the necessary properties to overcome the problems encountered but was not fully tested. However, it was deduced that micron resolution patterning, or better, can be achieved using the laser system as an exposure source.

8.2 Suggestions for future work

While considerable progress has been made, the work undertaken during the current programme has highlighted a number of issues that need to be addressed in order to further improve the micro fabrication flexibility of the excimer laser system.

8.2.1 Mask fabrication process

Although laser machining was successfully implemented in mask fabrication, it may be preferable to use the laser as an exposure source for directly patterning a photoresist material. This would remove the need for contact exposures and any inaccuracies that may be incurred, for example the mask not contacting the photoresist completely or the collimation of the exposure source not being ideal. As shorter wavelengths are used in the laser, compared to the aligner, and high-resolution optics are present, the resolution obtainable using this technique should far exceed that of contact exposure using the existing in-house photolithographic system.

8.2.2 On-chip optical detector

Although a successful waveguide fabrication technique and a method of coupling an optical fibre to the on-chip waveguides has been developed, the measured performance of the devices was not as high as was hoped. The performance of the optical detector (Chapter 5) could be improved if the light source and detector were incorporated on-chip. As well as removing the need for external equipment and optical connections that are mechanically weak and susceptible to breaking, this would allow a more portable device to be built. It would also remove the problems of optical alignment and fibre coupling losses incurred in the current system. Clearly improving the sensitivity of the device is an important area for future development.

Shaping the waveguide ends may also be beneficial in reducing the amount of light scattering observed in the channel when simple, square ended waveguides are used. This could easily be implemented by laser machining the required contour at the channel/waveguide intersection which should have little effect on fluid flow within the channel if the deviation is small. Although the detection of low cell concentrations was not obtained, it may become possible with suitable development of the design and the manufacturing process used. Detecting a single translucent cell using optical detection may be best suited to other optical methods not considered here, such as light scattering, where the signal to noise ratio is significantly improved.

8.2.3 Machining with greyscale masks

Greyscale masks allow the effective transmission per unit area to be accurately controlled and such masks have been implemented in both photolithographic and excimer laser machining processes. However, the range of materials that can be processed using such techniques is limited to those normally patterned, such as photoresists and polymers. Femtosecond laser machining is capable of machining almost any material and if such masks could be applied to such a machining process, greater flexibility could be obtained. However, the suitability of greyscale masks to such a machining system would depend upon the optical setup used and the application in-hand.

8.2.4 Development of a stereolithography micro-fabrication system

Using a suitable UV curing resin is vital to the resolution properties and quality of the stereolithography process. The development of additional hardware to allow the laser system to be used as a stereolithography fabrication tool was started during this investigation and will no doubt bring improvements when completed. Initial results indicate that it should be possible to produce high-resolution, true three-dimensional structures rapidly, using a suitable UV curing liquid resin and the excimer laser system with minimal disturbance to the micromachining system, as only the chuck requires changing. This task can normally be completed in under half an hour, so would allow rapid changing between the possible roles of a micro-stereolithography fabrication system and an excimer laser ablation system. It is envisaged that a computer controlled elevation system would greatly improve matters, as more accurate and repeatable results could be obtained. Using the new resin mix supplied, which appeared far more suitable for the task in hand, should also allow improvements in the resolution and quality of structures produced.

Alternatively, a dedicated micro-stereolithographical system could be fabricated if the stepper motor controller unit were used to control additional X-Y motion stages as well as the substrate elevation stage. If these systems were linked to a control PC along with

a suitable illumination source, an integrated and automated system could be produced, without the setup requirements incurred when using the excimer laser micromachining system as a stereolithographic exposure source.

Appendix I

Data used to obtain the required thickness SU8 coatings, obtained from the EPON SU8 datasheet (Microlithography Chemical Corp., Shipley).

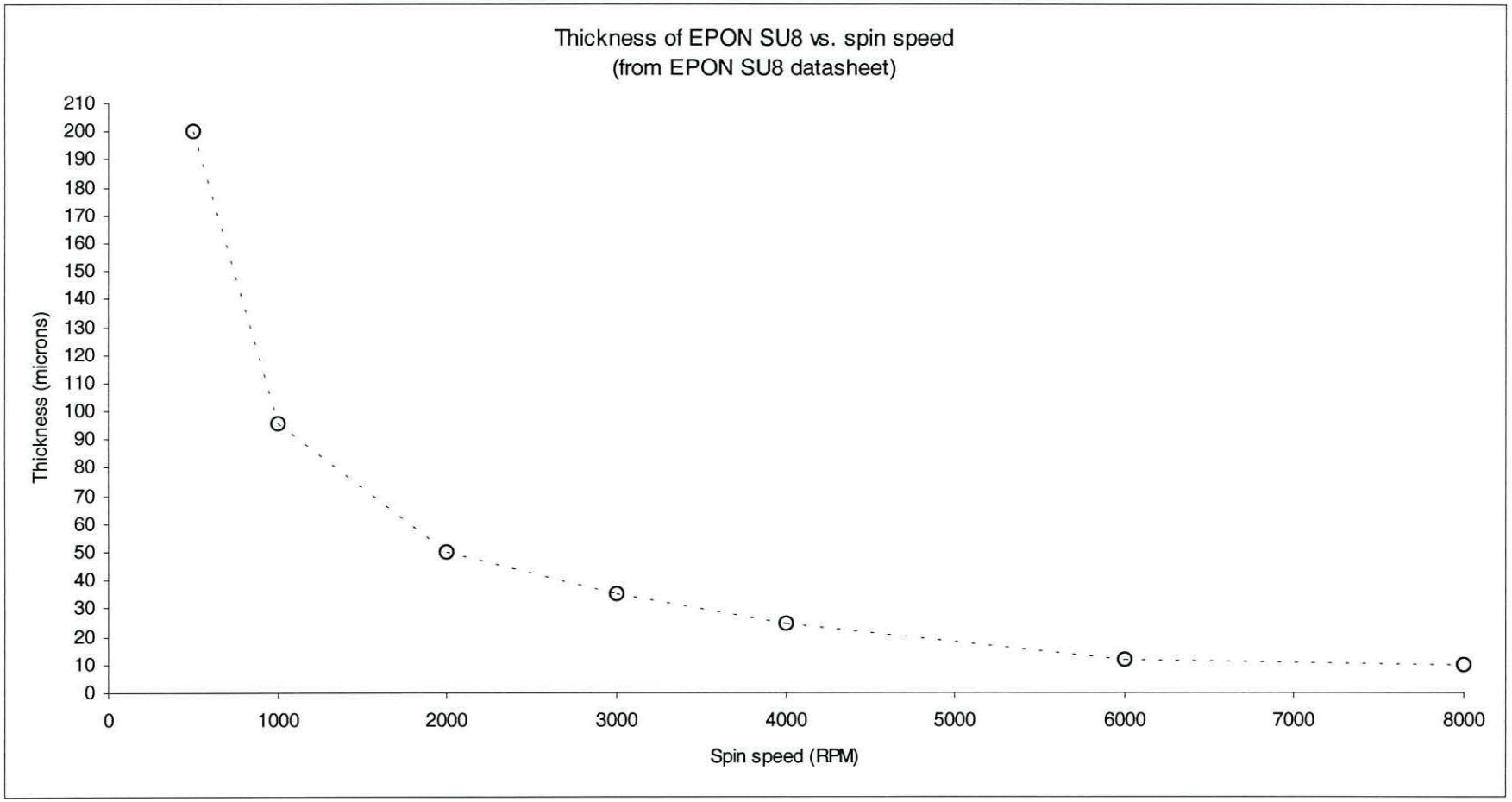

Appendix II

Listing of laser code used to implement mask scanning

```
; mask scanning program, to machine 4" plate to produce cEHD pump
electrodes
; last update:    21-01-2002, CJH

WAIT ALL

v1=50                              ; Mask speed in mm/sec
v2=5                               ; Number of shots per area
v3=10.0195                         ; Current projection lens
demagnification value
v4=77.5                            ; Mask start position Z
v40=180                            ; Mask start position U
v5=$xap/10000                      ; Workpiece start position is current
                                   ; X position
v50=$yap/10000                     ; Workpiece start position is current
                                   ; Y position
v6=140                             ; Size of mask scan in the U direction
v61=105                            ; Size of mask scan in the Z direction
v7=14                              ; Height of the beam at mask (in U
direction)
v70=14                             ; Step along long axis of the beam at
mask
v8=V61/(V70*2)                     ; Number of times that the unit loop
repeats
v90=V1*V2/V7                       ; Determine the laser repetition rate
(Hz)
V10=-V6/V3                         ; Distance the workpiece moves during
scan
V12=V1*60*SQR(1+(1/(V3^2)))        ; Speed of the workpiece (mm/min)

Wa on                              ; wait

g90                                ; Motion is absolute
pr me                              ; Units are metric
v15=1000*v70*3.14159/v1            ; Rounding-off time in ms
PSOF,0
g1 z=v4 u=v40 x=v5 y=v50 f1000     ; Move mask and workpiece to their
start positions

wa on                              ; wait
m0                                 ; prompt user to continue
g91                                ; Relative mode
ME DI "Mag %.4fv3"                 ; Display lens demagnification being
used
PSOP,1,0,50,0                      ; set laser firing pulse timing
settings
PSOD,0,(v7*10000/v2)               ; Laser fires every (V7*10000/V2)
                                   ; machine steps
```

```
PSOF,3,u                          ; Laser fires during u motion only



; ########################  Scanning rountine bit
##########################

ramp 500                          ; Set ramp time (mS)

:DOROUND
ROUNDING ON                       ; Rounding on
ROUNDING v15

LOOP v8                           ; Machining loop

g91 g1 u=v6 y=v10 F=v12/5         ; Mask and workpiece motion control
g91 g1 z=v70 x=-v70/v3 F=v12/10   ; Defining mask scanning
g91 g1 u=-V6 y=-v10 f=v12/5
g91 g1 z=V70 x=-v70/v3 f=v12/10
wa on                             ; wait
NEXT                              ; Repeat until all of mask scanned

; ########################  end of scanning motion
##########################

ROUNDING OFF                      ; Rounding off
PSOF,0                            ; laser off
g90                               ; absolute mode
g1 z=v4 u=v40 x=v5 y=v50 f1000    ; return mask and workpiece to start
positions

wa on                             ; wait
exit                              ; exit program
```

Listing of laser code used to create calibration grid

```
; A program to create a 10x10 array of holes, varying energies and number
of shots, to form a calibration grid

; CJH 2000


pr me                                          ; metric mode
g90                                            ; absolute mode
wa all                                         ; wait all


; ****************** variable definitions ******************

V1=231.6851                                    ; Z position of mask
V2=239.7281                                    ; U position of mask
V3=$xap/10000                                  ; X position of workpiece
V4=$yap/10000                                  ; Y position of workpiece

V5=0.1                                         ; attenuator start setting
V6=0.02                                        ; attenuator step size
V7=50                                          ; laser repetition rate (Hz)

V8=5                                           ; starting number of shots
V9=5                                           ; number of shots added

V10=0                                          ; column number
V11=0                                          ; row number
V17=1000                                       ; set stage feed rate

; ************** start position of mask and workpiece **************

bo 1                                           ; board 1
g90 g1 z=v1 u=v2 f=V17                         ; move mask
g90 g1 x=v3 y=v4 f=V17                         ; move
wa on                                          ; wait

; ****************** laser ablation routine ******************

loop 10                                        ; loop to create 10 columns
bo 1                                           ; select board 1
g90 g1 x=v3+(0.08*v10) y=v4 f=V17              ; move workpiece to start
position & x+50um
bo 2                                           ; select board 2
g90 g1 x=v5+(v6*v10) f10                       ; set energy to start
wa on                                          ; wait

loop 10       ; loop to create 10 rows (increasing number of shots)
bo 1                                           ; select board 1

g90 g1 x=v3+(0.08*v10) y=v4+(0.08*v11) f=V17       ; move workpiece
wa on                                          ; wait
PSOF,0                                         ; disable laser
```

```
PSOP,1,0,50,(10000/v7)-50                ; set laser pulse
PSOF,2,v8+(v11*v9)                       ; laser on

dw (1000/V7)*((V11+1)*V9)
wa on                                    ; wait
v11=v11+1                                ; increment row counter
next                                     ; end of row loop
v11=0                                    ; reset row counter
v10=v10+1                                ; increment column counter
next                                     ; end of column loop
v10=0                                    ; reset column counter

; ident

g90 g1 x=v3+(0.08*12) f=V17              ; move
PSOF,2,50                                ; laser on
dw (1000/V7)*50                          ; wait

psof,0                                   ; laser off
exit                                     ; exit
```

Appendix III

Figure III.1 shows the circuit used to produce an electrical output from the light emitted by the on-chip optical sensor.

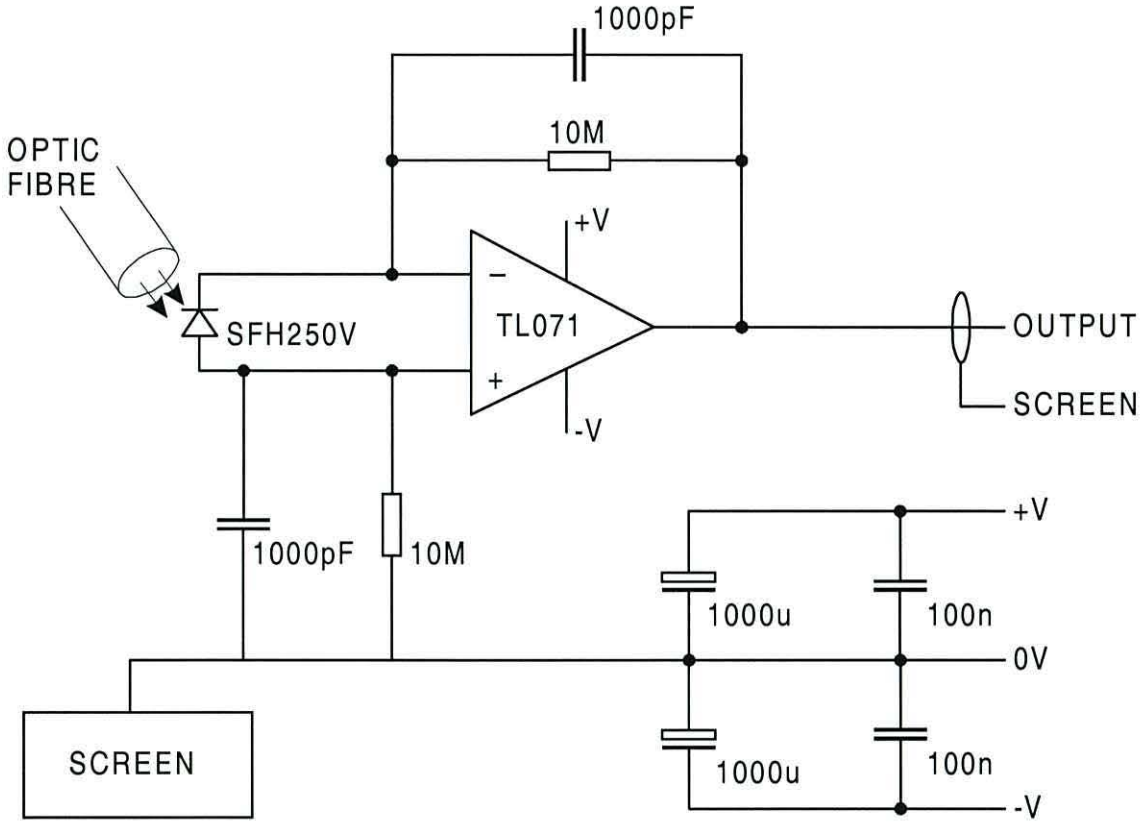

Figure III.1 *Circuit used to amplify the photocurrent generated by the photodiode used to detect the optical output from the on-chip optical detectors.*

Appendix IV

Re-useable device mount

IV.1 Introduction

A re-useable device mount design is presented here, which allows the rapid insertion and removal of micro-devices while still maintaining reliable fluidic connections. The method used to hold the device and provide fluidic connections is to physically clamp the device between rubber 'O' rings, providing mechanical integrity and good sealing, typically better than other methods commonly used. This approach is well suited to a mass-manufactured, disposable device providing a single, reliable fluidic connection method for such devices, although electrical connectivity to the devices could easily be included.

IV.2 Re-useable device mount

The first problem to be addressed was rapid insertion and removal of devices, while still providing reliable fluidic and electrical connections. Compressive force was used not only to hold the device firmly, so allowing optical inspection, but also to provide fluidic sealing. This was accomplished using rubber 'O' rings to maintain a good fluidic connection between the device and the mount. In order to allow a repeatable fluidic connection, a two port [inlet and outlet] pattern was devised that allowed electrical connections to be brought to the edge of the device and allowed enough room for the sealing mechanism. This fixed the position of two fluid ports, typically drilled through the glass substrate of the device, relative to a corner of the device, allowing simple alignment. Figure IV.1 shows the design used and a section through the clamping assembly. The fluid inlet and outlet port positions are marked accordingly, as well as the position of the electrical connections. The initial design was for 16 separate electrical connections, allowing some flexibility in the design of any device electrode connection routes.

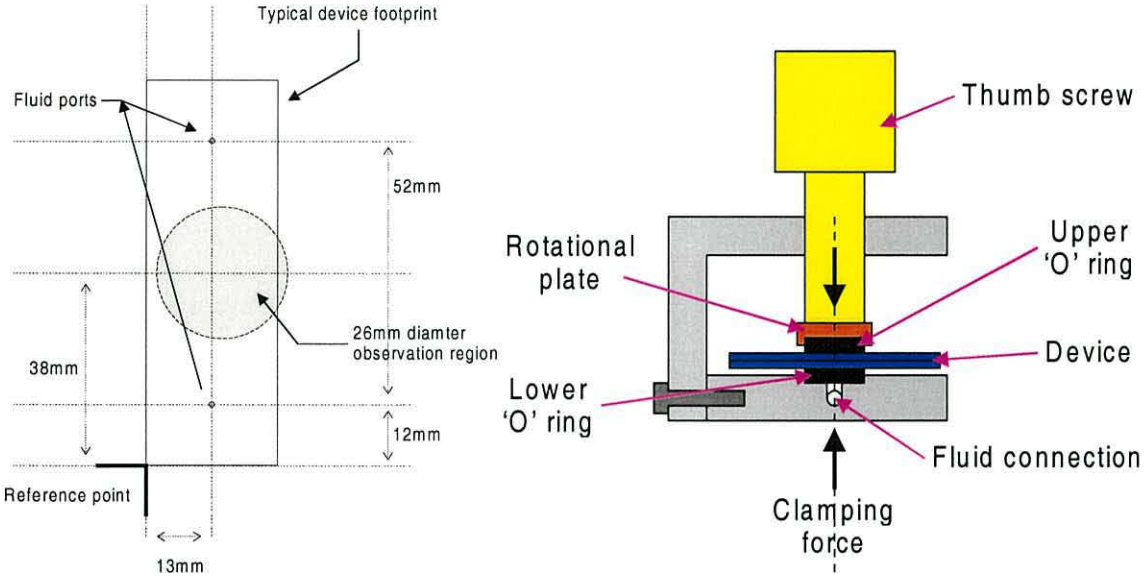

Figure IV.1 *Pattern used to maintain repeatable connections to devices (a) and section through the clamping system (b).*

It was envisaged that the electrical connections to the devices in the mount would be provided using miniature spring-loaded contacts, although this has not yet been implemented. The materials used to fabricate the mount were chosen to be inert and also to allow sterilisation in an autoclave, should this be necessary. The baseplate of the mount was machined from stainless steel and contained the fluidic connections needed to connect the device to external sources. Alignment studs were also fitted to the baseplate for alignment of the device relative to the fluid ports. Two rubber 'O' rings were mounted in a recessed region of the baseplate using an interference fit, i.e. the diameter of the recessed region was ~50μm smaller than the diameter of the 'O' ring. This caused the device to be elevated from the baseplate by approximately 1mm.

A backplate, attached to the baseplate, held two thumb-screws which were positioned over the fluidic ports in the baseplate. These were fitted with independently rotating bases and additional 'O' rings, also held in place using an interference fit.

By clamping the device, which commonly contained brittle glass layers, between rubber 'O' rings, any slight inaccuracies in the device or the mount machining and the glass layers can be tolerated. Positioning the thumb-screw clamps over the lower ports also

avoids damaging the device, as most of the materials used in devices, namely glass, are strong in compression. Other advantages of clamping the devices was that they were electrically isolated from the mount by the rubber 'O' rings and the compressive force used to provide the fluidic seal and hold the device also reduced the risk of the device bursting, as it was physically held together. Figure IV.2 shows a series of photographs of the mount that was fabricated. The stainless steel tubing used to connect the device to external sources was sealed into the stainless steel base using silver solder.

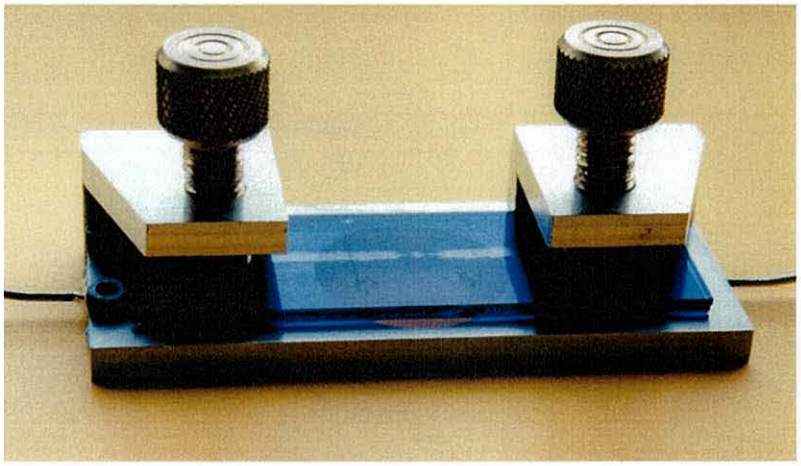

(a)

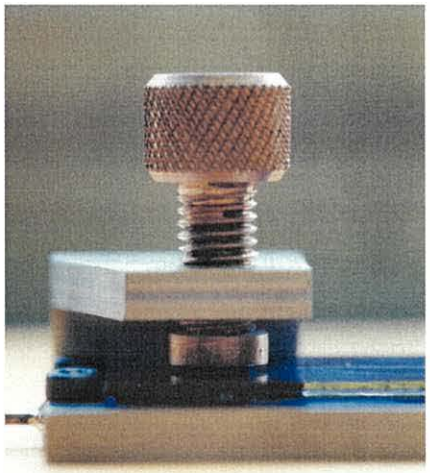

(b)

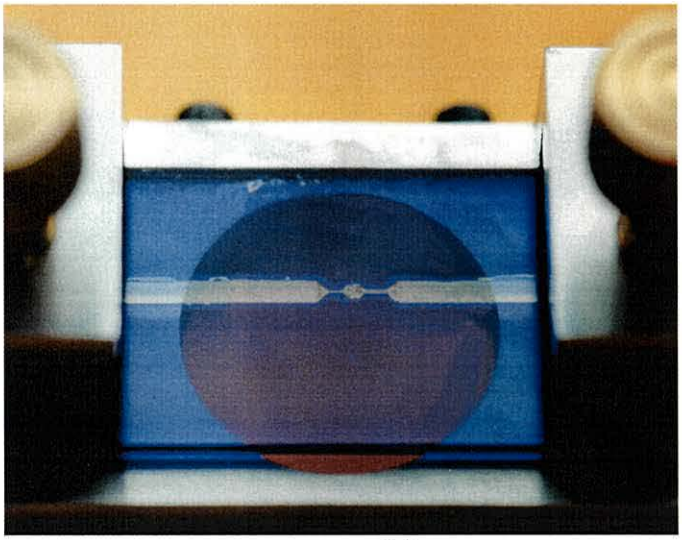

(c)

Figure IV.2 *Photographs of the mount fabricated: (a) view of the complete mount with test device in-situ. The two pipes at either side of the mount are inlet and outlet connections. (b) detail of the compression port seal, (c) view of the observable region of the device mounted, in this case a channel with two constrictions for testing the precision pump.*

The large circular hole that can be seen in the baseplate allows the condenser lens of a microscope to approach the back of the device. This is useful when observing certain particles, such as cryptosporidium, using phase-contrast lighting. The cut-out between the two knurled thumb-screws is to allow movement of the device on a microscope stage without obstructing the objective lens. The device construction allowed either chemical sterilisation of the mount or autoclaving and the 'O' rings used (Viton™ (Dupont), RS Components) were capable of withstanding elevated temperatures without degrading.

Devices were tested using this mount and it was found virtually impossible to cause a leak between the device and the mount. Instead, either no effect was observed, the fluidic system would fail elsewhere, or the device itself would fracture. The pressures used were high, typically in the order of 500psi, which is several orders of magnitude higher than would be required during normal operation of a device. This proved that the mount was capable of maintaining fluidic seals to the device at higher pressures than would normally be used.

The feasibility of using the mount during microscope observation was also tested using a simple device consisting of a micro-fluidic channel with a narrowed region in the centre. The motion of latex beads was observed and recorded to S-VHS video using a precision micro-pump also developed [Chapter 7.6], as the mount provided a convenient method of attaching the test device to a microscope and the pump. This demonstrated that little flexing of the fluidic system was present, as the latex beads could be repeatably moved and then returned to a start position.

However, it was noticed that observation at other than the centre of the device was limited by the clamp mechanism and that the mount required better securing to the microscope table. These requirements were addressed by re-designing the mount specifically for operation on a microscope.

IV.3 Revised device mount

The design used to create the second mount varied significantly from the first. The second version was specifically designed to be mounted on a microscope, allowing full X-Y movement for observation of the whole device, while maintaining a low profile to allow optical observation.

The problem of the previous clamping system being too bulky was addressed by replacing the two thumb-screws with countersunk screws that held the upper clamp unit to the base plate and secured the device. An advantage of this is that multiple fluid ports are now possible. The base plate was machined from aluminium and incorporated X-Y sliders. The fluidic connections consisted of stainless steel inserts, shown in Figure IV.3, that can be removed for sterilisation without dismantling the whole assembly. This also allowed multiple ports to be incorporated, should they be needed.

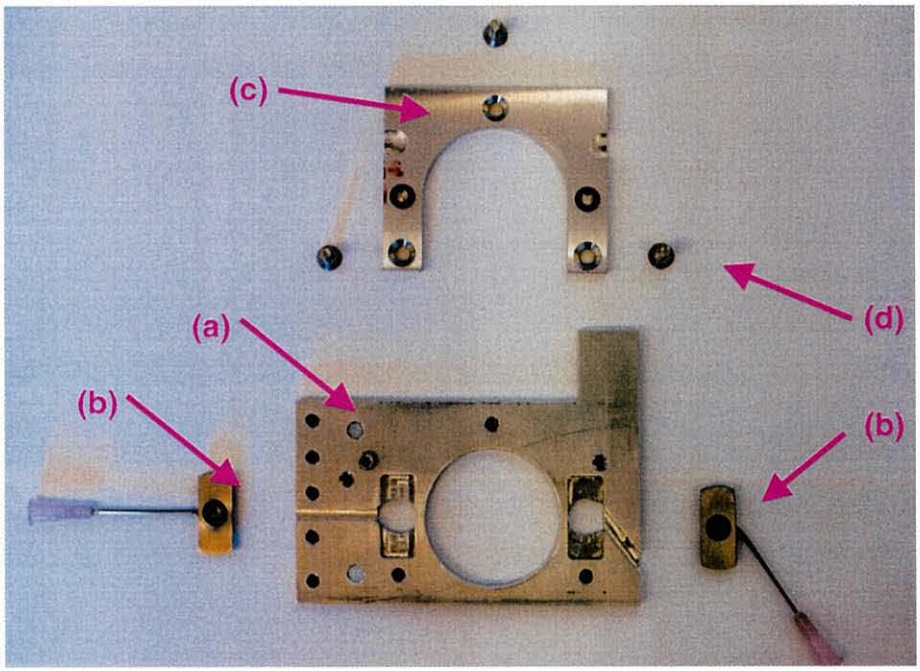

Figure IV.3 *Plan view of the revised device mount design, showing the mobile device clamp assembly components. (a) lower half, (b) fluid connection ports with 'O' rings in place, (c) upper half of clamp, (d) fixing screws*

The upper and lower clamp assemblies were held onto a custom-made microscope table using two leaf springs. These provided some stiffness to the mobile clamp stage and allowed simple and accurate adjustment using the X and Y adjuster screws. Figure IV.4

shows a plan view of the moveable device mount assembly and the complete unit is shown in Figure IV.5.

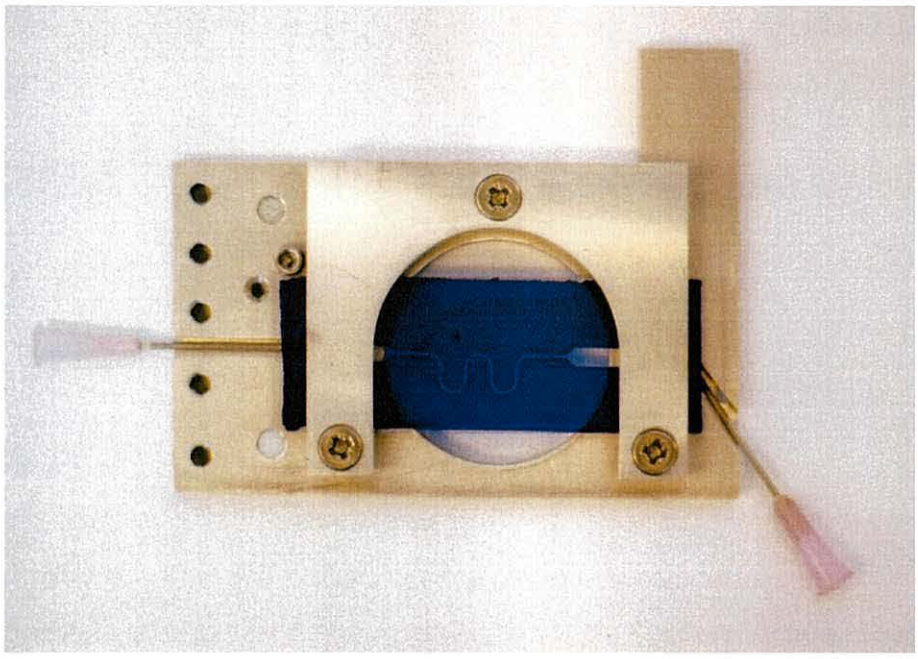

Figure IV.4 *Picture of the assembled mobile device mount assembly, complete with a test device*

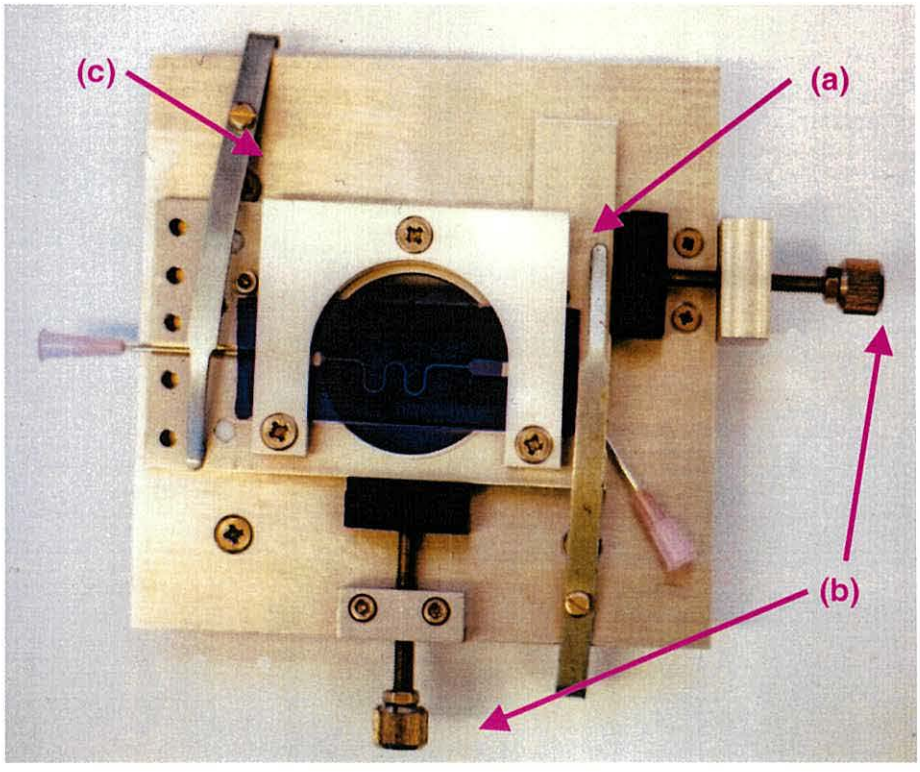

Figure IV.5 *Plan view of the complete device mount design, showing (a) the mobile device clamp assembly in place on the base, (b) the X-Y adjusters and (c) the retention springs.*

Flexible fluidic connection to the device was made using 1mm bore PEEK tubing (BDH Laboratory Supplies, Dorset, UK), which minimised pressure variations when using the micro-pump and helped to maintain rigidity of the motion stage.

Fabrication of this device was completed and fluidic connection to a test device was examined as before. The revised clamping method, which required a screwdriver to change devices, was not found to add an excessive time penalty in changing devices. Pressure testing revealed results similar to the first mount, in that no leaks occurred between the device and clamp mount. Instead, the device fractured or the external connections failed. The removable fluidic connections also simplified cleaning the unit. When the device was clamped into the mount, it could be positioned accurately to allow viewing of a large area of the device. Figure IV.5 shows a picture of the mount attached to a Nikon Labophot II microscope.

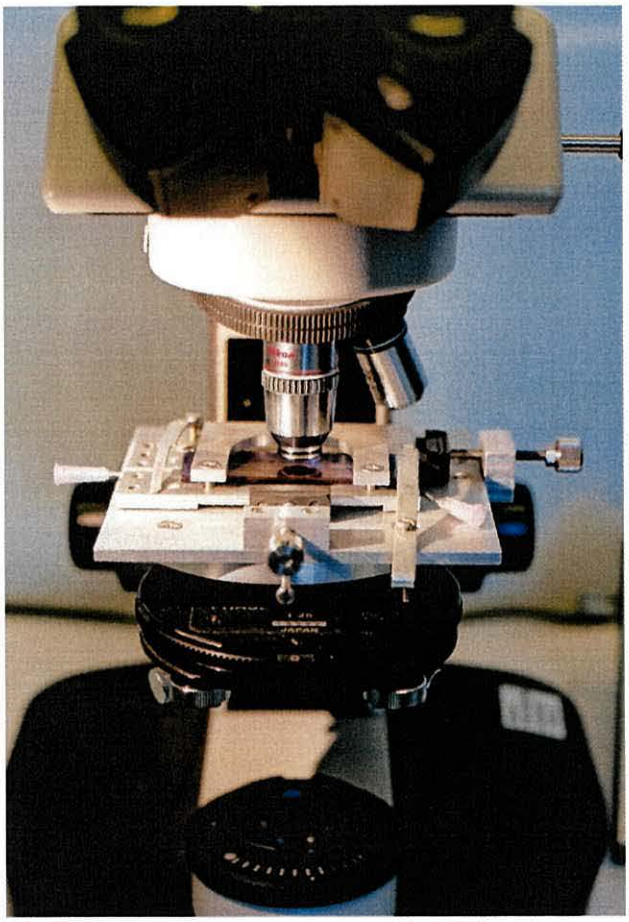

Figure IV.6 *Picture of the revised device mount, attached to a Nikon Labophot II microscope.*

IV.4 Conclusions

Two device mounts, allowing repeatable fluidic connection to Lab-on-a-chip devices have been developed that maintain high-pressure fluidic connection to devices. When high pressures were used, the seals between the device and the mount did not fail, instead either the device would fracture or the external fluidic connections failed.

The first version fabricated, although not well suited to microscope observation, would be ideally suited to automated operation of a device which, for example, used optical particle detection instead of manual observation. A second device has been developed that was designed for use on a microscope stage, allowing easy manual observation over a larger area of the device. This is well suited to non-automated applications, as the device characteristics are similar to the first device, in that good fluidic seals are maintained, as well as the accurate X-Y position adjustment possible. Such a device would be well suited to laboratory use, allowing simple and reliable connection to prototype devices under test.

Completion of the electrical connection system provide reliable device mounts that can be used to connect disposable Lab-on-a-chip devices to external electrical and fluidic systems quickly and repeatably. An improvement to the mounting system could be implemented by using a lever to lock the devices in place. This would be relatively simple to implement and allow much faster device insertion and removal times when using either version of mount.

Appendix V

Published work

Papers published and presentations given during the course of this work:

'An AC magnetohydrodynamic micropump for chromatographic applications', J. C. T. Eijkel, C. Dalton, C. J. Hayden, J. P. H. Burt and A. Manz, *Submitted to MEMS, May 2002.*

'A circular AC electroosmotic micropump for chromatographic applications', S. Debesset, C. J. Hayden, C. Dalton, J. C. T. Eijkel and A. Manz, *Submitted to uTAS 2002, May 2002.*

'Laser micromachining of Biofactory-on-a-chip devices', J. P. H. Burt, A. D. Goater, C. J. Hayden and J. A. Tame, *Proc. SPIE, Photonics West, San Jose, USA (Invited presentation / paper)*, (2002) *In press*

'Fabrication of fluidic manifold systems using single exposure greyscale masks', C. J. Hayden, J. P. H. Burt, *Proc. SPIE*, **4404** (2001) 231-237

'Development of a micro system for circular chromatography using wavelet detection', J. C. T. Eijkel, C. Dalton, C. J. Hayden, Y. C. Kwok and A. Manz, *Micro Total Analysis Systems 2001* (2001) 541-542

'Electric Field Interaction with Debris Generated by Laser Ablation of Polyimide Films', C. J. Hayden, R. Pethig and J. P. H. Burt, *Electrostatics 1999, Inst. Phys. Conf. Ser.* **163** (1999) 261-264

'Electrostatic field interaction with debris generated by laser ablation of polyimide films', *Oral presentation, Electrostatics '99, 10th International Conference (IoP), March 1999, Cambridge, UK*

'Fabrication of fluidic manifold systems using single exposure greyscale masks', *Oral presentation, Proc. SPIE, Lithography for Semiconductor Manufacturing II, Edinburgh, May 2001*

'Three Dimensional Microfabrication using greyscale masks applied to lab-on-a-chip technology', *Oral presentation, European Workshop on Electrokinetics and Electrohydrodynamics in Microsystems, Glasgow, September 2001*

Laser Micromachining of Biofactory-on-a-Chip Devices

Julian P. H. Burt, Andrew D. Goater, Christopher J. Hayden and John A. Tame
Institute of Bioelectronic and Molecular Microsystems, University of Wales, Bangor, Dean Street, Bangor, Gwynedd, LL57 1UT United Kingdom

ABSTRACT

Excimer laser micromachining provides a flexible means for the manufacture and rapid prototyping of miniaturised systems such as Biofactory-on-a-Chip devices. Biofactories are miniaturised diagnostic devices capable of characterising, manipulating, separating and sorting suspensions of particles such as biological cells. Such systems operate by exploiting the electrical properties of microparticles and controlling particle movement in AC non-uniform stationary and moving electric fields. Applications of Biofactory devices are diverse and include, among others, the healthcare, pharmaceutical, chemical processing, environmental monitoring and food diagnostic markets. To achieve such characterisation and separation, Biofactory devices employ Laboratory-on-a-Chip type components such as complex multilayer microelectrode arrays, microfluidic channels, manifold systems and on-chip detection systems. Here we discuss the manufacturing requirements of Biofactory devices and describe the use of different excimer laser micromachining methods both in stand-alone processes and also in conjunction with conventional fabrication processes such as photolithography and thermal moulding. Particular attention is given to the production of large area multilayer microelectrode arrays and the manufacture of complex cross-section microfluidic channel systems for use in sample distribution and device interfacing.

Keywords: Excimer, Laser, Micromachining, Biofactory, Laboratory-on-a-Chip

INTRODUCTION

In recent years microfabricated devices, or microsystems, have found applications in areas as diverse as the aerospace, automotive, environmental, healthcare, pharmaceuticals, chemical processing, biotechnological and food industries. A major area of expansion for microsystems technology has been in the areas of chemical and biochemical analysis that play a routine part of many industries. These microsystems, known generally as Laboratory-on-a-Chip devices, offer many advantages over conventional laboratory apparatus. The small internal volumes of such devices can lead to reduced reagent and sample costs whilst at the same time benefiting from faster reaction times. In addition, the small internal dimensions of these devices allows accurate control of environmental parameters such as temperature and pressure. The integrated nature of Laboratory-on-a-Chip devices allows multiple processes to be carried out within a single device giving rise to increased ability to automate complex analytical and production processes. Whilst a single device may be limited in the reagent volumes it can process, the small physical dimensions of Laboratory-on-a-Chip devices provide the possibility of employing many devices operated in parallel arrays to provide the production throughput of conventional apparatus. Additionally, with judicious choices of construction materials and manufacturing processes, such devices can also offer the advantages of lost-cost, single use disposable units to ensure process quality control and to eliminate concerns of inter-process contamination.

Laboratory-on-a-Chip devices have employed a wide range of techniques to provide on-chip processing. Many of these techniques can be considered as macroscopic technologies that are miniaturized to provide additional functionality. Examples of such devices are those that employ techniques such as capillary electrophoresis for separations or labelling processes for identification. In these devices the reduced physical dimensions of Laboratory-on-a-Chip devices allow, in the case of capillary electrophoresis, increased separation resolution or, for labelling methods, increased signal to noise ratios during detection. An increasingly important group of Laboratory-on-a-Chip devices are those that employ processes that function optimally in miniature systems. Biofactory-on-a-Chip devices are an exemplar of such devices

and are capable of performing a wide range of complex diagnostic tasks in a single, miniaturised, low-cost package. Such devices have the advantage of being automated systems capable of the rapid analysis of small volume samples and have applications in the fields such as medical and single cell diagnostics, chemical detection, water quality control and food analysis. The phenomena utilised in Biofactory-on-a-Chip devices exploit the dielectric properties of particles and the electric field induced motion caused by the following AC electrokinetic processes:

(1) Dielectrophoresis (DEP), the translational motion induced when particles are exposed to stationary, non-uniform, electric fields.

(2) Electrorotation (ROT), the rotational motion induced in particles when exposed to rotating electric fields.

(3) Travelling Wave Dielectrophoresis (TWD), the translational motion induced when particles are exposed to travelling electric fields.

For these AC electrokinetic phenomena to operate, the geometries of strong AC electric fields need to be accurately controlled over dimensions of the same order as the size of the particles to be processed. The combination of the required electric field strengths and geometric control make exploiting such phenomena problematic on a macroscopic scale. The background theories of these AC electrokinetic processes and perceived biotechnological applications are described elsewhere[1,2]. Here, we discuss the design and manufacturing issues of Biofactory on-a-Chip type devices. To illustrate the manufacturing processes, examples have been taken from a recently completed device for the detection and viability analysis of parasites known to contaminate water supplies.

EXAMPLE BIOFACTORY-ON-A-CHIP DEVICE

Central to the Biofactory concept is the use linear arrays of electric field producing electrodes allowing particles to be transported around Biofactory devices using travelling wave dielectrophoresis[3]. The speed and direction of travel is dependent on the dielectric properties of the particles and the suspending medium along with the frequency and strength of the travelling electric field. Figure 1a shows an illustration of the multilayer construction of such electrode arrays. Field producing electrodes form the lowest layer and are partially covered with a thin insulator. The insulator is patterned with an array of via holes that expose the underlying electrodes in defined regions. A series of four bus-bars form the top layer of the structure and are positioned to allow every fourth field-producing electrode to be connected together, with adjacent field producing electrodes being connected to adjacent bus-bars. Energising the

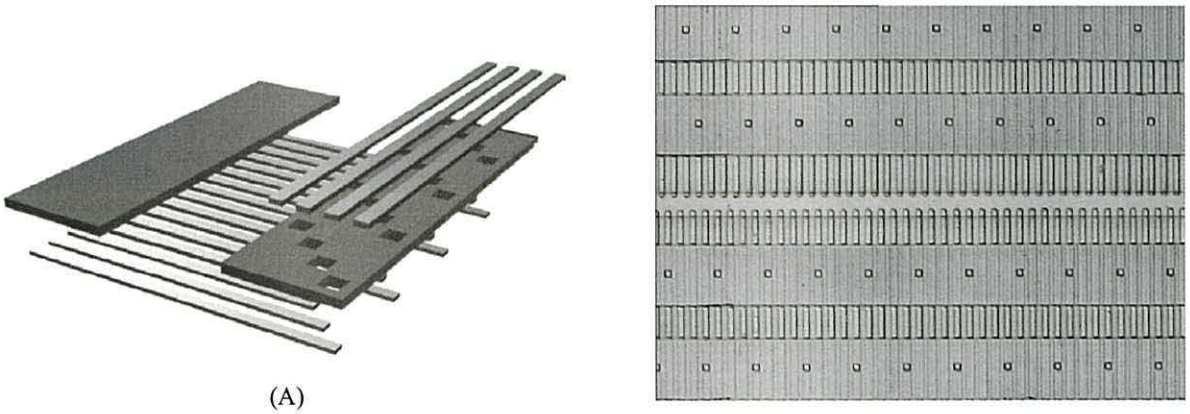

(A) (B)

Figure 1. (A) Illustration of multilayer electrode arrays used in the construction of Biofactory devices. (B) A multilayer electrode array for the transport and selective trapping of particles in Biofactory devices.

Bus-bars with quadrature sinusoidal voltages produces a travelling electric field along the length of the electrode array. The use of a multilayer structure for such electrodes allows arbitrary length electrode arrays to be constructed whilst requiring only four external electrical connections.

Figure 2 shows an image of an unencapsulated example Biofactory-on-a-Chip device for the detection and viability analysis of oocysts of the water borne parasites *Cryptosporidium parvum* and *Giardia lamblia*. The presence of such parasites, even in very low concentrations, in drinking water has led to outbreaks of human infection that occurs as self-limiting diarrhoea in healthy adults but may lead to death in infants and immuno compromised people. Since these oocysts do not multiply outside their hosts, conventional microbiological procedures are not applicable for their detection. The Biofactory device shown in figure 1 can be considered in two sections. The first section, forming the upper half of figure 1, is an array of external electrical connections to allow control of the Biofactory device. These connections are arranged in blocks of four electrodes allowing the individual sections of the device to energised independently using quadrature sinusoidal voltages. The nine blocks of four electrodes signify that this device contains nine independently controllable regions. The second section of the device covers the lower half of figure 1. Here a series of conveyor tracks can be seen forming a network of analysis tools. A raw water sample, filtered to both remove large debris and concentrate particulates is fed into inlet port A1. At the same time, a sample of latex beads coated in an antibody targeted to a specific microorganism is fed into inlet port A2. Water sample particles travel along TWD conveyor electrode arrays or 'tracks', similar to B, through the junction structure, C and arrive at a dielectrophoretic particle trap, D. Latex beads travel along conveyor track, B, and also arrive at the trap D. At this point, antibodies on the latex beads will react with any of their targeted microorganisms if present. The result of this is the binding of latex beads to the microorganism to form a complex particle. This complex particle will have different electrical properties to the unreacted microorganisms and so will move along conveyor tracks with a different velocity. Energising the conveyor track to the right of the dielectrophoretic trap causes all particles to move along the track. Energising different junction branches within the device allows unreacted latex beads to be directed back to dielectrophoretic trap whilst unreacted microorganisms can be directed to one of the outlet ports A3 or A5. Bead/microorganism complexes are directed to the electrorotation analysis unit, E, where the microorganism complexes are made to rotate under the influence of a rotating electric field. Observation of the speed and direction of rotation for a range of electric field frequencies, allows microorganism presence and viability to be detected. Finally, analysed complexes can be removed from the device through outlet port A4. Therefore, through the appropriate application of electric fields and detection of rotation, it is a simple matter to enumerate the number of a specific organism present as well as calculate their viability.

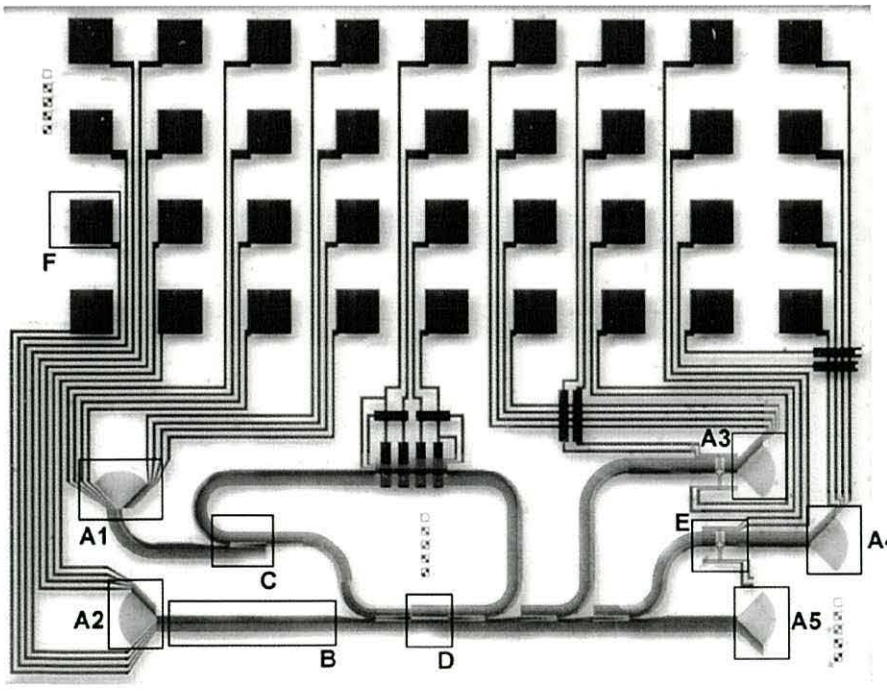

Figure 2. Image of an example Biofactory-on-a-Chip device. Six key elements are employed in the device.

A Inlet/outlet ports.

B Travelling wave dielectrophoresis conveyor tracks.

C TWD conveyor track junctions.

D Dielectrophoretic particle trap units.

E Electrorotation analysis units.

F External electrical connection contacts.

MATERIALS AND METHODS

MATERIALS

A diverse range of materials has been used for the fabrication of Laboratory-on-a-Chip devices. In Biofactories, the choice of materials is governed by the device's application area. In general, Biofactories are intended to be used as low-cost, single or low usage, devices. As such, chosen materials must have low volume costs and be applicable to simple, inexpensive, large scale manufacturing processes. Being essentially planar devices, Biofactories are fabricated as a series of thin layers on a supporting substrate. This substrate must be rigid and optically clear to allow observation of processing within the Biofactory. In current work, thin glass substrates have been employed although it is also possible to use transparent polymers such as polycarbonate and PMMA. Microelectrode arrays within Biofactory devices must be capable of providing controlled electric fields in a diverse range of sample media. Therefore, electrode arrays are primarily constructed from inert metals such as thin, thermally evaporated, gold films typically 100nm thick. To assist in adhesion to different substrates, a 5nm seed layer of chrome is often deposited prior to gold deposition[4]. The insulating material used between the field producing electrodes and bus-bars in multilayer electrodes is a critical part of Biofactory devices. Current work employs a series of different insulators depending on the Biofactory application. For the majority of devices, polyimide films are used to isolate different conducting layers within devices. These films are deposited by spin coating followed by a series of patterning and baking stages to produce robust isolating layers. Other Biofactory devices have made use of the photosensitive epoxy resist SU-8. An important feature of SU-8 is its ability, under correct conditions, to produce contact type bonds between layers of SU-8[5]. This is particularly useful when encapsulation layers are fabricated from SU-8. Encapsulation layers are used to define microfluidic channels over the microelectrodes arrays and so confine analysis samples to defined areas of the Biofactory devices. A wide range of materials can be used for this stage. For low-cost development work, the popular mouldable elastomer polydimethylsiloxane (PDMS) has been successfully used. For untreated, clean surfaces, PDMS forms a weak, releasable, bond on contact with materials such a glass and so allows fluidic distribution systems to be evaluated on a single standard electrode array. More permanent bonding of encapsulation layers has employed thermoplastic polymers such as polycarbonate. Fluidic channel structures are thermally embossed into polymer sheets and bonded to the electrode bearing substrate using a range of adhesives. The advantage of such encapsulation layers is the ability to mould external inlet and outlet ports into the encapsulation layer allowing easy interconnection with other laboratory equipment.

EXCIMER LASER ABLATION

A key factor in developing Biofactory-on-a-Chip technology is the ability to employ a wide range of low-cost production processes in the bulk production of such devices. Examples of this include photolithography for the patterning of microelectrode arrays and thermal embossing or injection moulding for the production of encapsulation layers. However, in the design stage there is a need to employ flexible microfabrication processes that allow rapid development of devices whilst interfacing directly with final production processes. Excimer laser ablation and laser based micromachining is an ideal method for this design stage. Thin metal films can be patterned directly by laser ablation without the need for the multistep processes of mask preparation, resist coating, exposure, developing, etching and resist removal involved in photolithography. At the same time, to interface with bulk production using photolithography, an excimer laser can also be used as a highly controllable, deep ultra violet (UV) light source for high-resolution photolithographic patterning. In addition, excimer lasers are ideal for the accurate patterning of polymers both in thin film form and as bulk materials. In this way, both the insulation layers used in multilayer electrodes and encapsulation layers used to control sample position can be directly machined using excimer lasers.

The laser system used for this work was an Exitech Series 8000 microfabrication workstation (Exitech Ltd, Oxford, UK) incorporating a Lambda Physik Compex 110 excimer laser configurable for operation at either 248nm or 193nm. In this system, beam delivery optics contain beam shaping and homogenisation components to create a uniform intensity beam at the plane of a mask held on a CNC controlled XY stage. The double 6x6 (36 element) homogeniser arrays produced a 12mm x 12mm uniform illumination at the mask plane with an intensity variation of ± 5% RMS. A projection lens was used to transfer the pattern on the mask to a workpiece mounted on precision, air-bearing, XY stages. The demagnification factors of the projection lenses allow low-resolution mask patterns to be used to produce

high-resolution structures on the workpiece. Demagnification factors of 4x, 10x and 30x provided workpiece fluences of 1.5 Jcm^{-2}, 5 Jcm^{-2} and 60 Jcm^{-2} respectively.

The main workpiece XY air-bearing stages (Aerotech inc. ATS80020) employed brushless linear servomotors giving 200mm x 200mm travel with 100nm resolution. Mask stages (Aerotech Inc. ATS34030) also used brushless servo drives to give 300mm x 300mm travel with 100nm resolution. Additional stages provided workpiece elevation and rotation control at similar resolutions. All stages were controlled through standard CNC control programming. Stages and beam delivery optics were mounted in a single enclosure with a damped frame to reduce vibrational coupling between the mask and workpiece stage sets. To reduce errors due to thermal expansion of the mechanical systems, the laser machining workstation was housed in a temperature controlled (± 1°C) semi-clean environment.

The stages of the laser micromachining workstation were controlled by two PC-based motion controllers (Aerotech Inc. Unidex 500), one of which was coupled to a laser-firing interface. The flexibility of this control system allowed the system to operate in one of two modes. Serial write mode projected the beam through a fixed mask aperture and moved the workpiece stages to serially write a pattern onto a workpiece sample. Control of stage movement was achieved either through CNC program commands or directly from graphical computer design files using a CAD/CAM software interface (AlphaCAM, Licom Systems Ltd UK). In this mode, the maximum ablation area was defined by the beam width and the write rate was limited by the laser repetition rate (100 pulses sec^{-1}) and the number of laser pulses required to produce the pattern. The second mode of operation employed the synchronised movement of both mask and workpiece stage sets. In this scanning mode, large area mask patterns could be transferred onto a workpiece at a rate that depended mainly on the number of laser pulses required to pattern a workpiece area equivalent in dimensions to the unapertured beam.

To achieve accurate laser machining, high quality masks were required. For long-term, frequent use applications such as beam aperturing, conventional 4" chrome-on-quartz plates were used. These were commercially produced using electron beam based lithography and could sustain mask beam fluences of up to 0.1 Jcm^{-2} without damage. Such masks, whilst providing excellent quality, suffer from a high individual cost and relatively long production and delivery times. To allow rapid development of Biofactory concepts, low-cost, limited lifetime, masks were also used produced using the laser mciromachining workstation. These masks exploited the fact that most polymers are strong absorbers of deep ultra violet radiation at 248 nm and 193 nm. Masks were produced by spin coating a quartz plate with a thin layer of photoresist and then directly ablating the resist with an apertured beam. Mask patterns were drawn using a low-cost CAD package (Autosketch, Autodesk Inc.) and serial laser writing of the mask pattern was controlled through the CAD/CAM interface provided by AlphCAM. Using a 1μm thick resist layer (Shipley 1818) these masks could be patterned at a resolution of 0.8 μm. Since this limitation appeared to be governed by the resolution of the projection lens used in the writing process, the masks produced, when placed in the mask stages, allowed the system to operate at its full resolution. Resist based masks were capable of sustaining higher initial beam fluences than conventional chrome masks. However, after prolonged use at fluences greater than approximately 0.05 Jcm^{-2}, gradual degradation of the mask pattern was observed. Durability of the masks could be improved by adjusting baking the resist and the addition of a thin evaporated chrome film over the resist prior to ablating the mask pattern.

BIOFACTORY DEVELOPMENT

MICROELECTRODE ARRAYS

Microelectrodes are essential for the operation of any Laboratory-on-a-Chip device employing AC electrokinetic processes. In Biofactory devices, the movement, separation and characterisation of biological particles is achieved using electrode arrays that impart travelling wave dielectrophoretic or electrorotational movement in bioparticles. An important factor to note is that in Biofactory devices, particles are made to move directly rather than as a result of general fluid motion. To produce controlled motion of particles in a Biofactory device linear, multilayer, electrode arrays that form travelling wave dielectrophoresis conveyor tracks are required. An example travelling wave conveyor track is shown in figure 1. Field producing electrodes are formed on the first layer of the multilayer structure whilst bus-bar connecting electrodes are fabricated on a second, insulating, layer with interconnecting via holes to allow every

fourth electrode to be connected together. Since these electrode arrays are typically used to create AC electric fields in conducting aqueous media, and hence, in total, must be able to carry up to 100mA of electrical current, the reliable production of such arrays poses two challenges. First, the rapid production of the field producing electrodes, typically 10μm in width, using laser micromachining and the second, the production of reliable interconnecting via holes in the insulating layer.

Several methods were investigated for the production of field producing electrodes. The first of these was direct, single pulse, ablation of thin, evaporated, chrome-gold films on a glass substrate using scanning mode ablation through a large area mask[6]. Using a wavelength of 248nm and a fluence of 200 $mJcm^{-2}$ electrode structures with widths >25μm were successfully produced. However, for smaller electrodes with widths of the order of 10μm, poor edge quality was observed. The laser ablation of metal films is a complex process involving a combination of the rapid thermal expansion and melting of the metal film and a shock wave associated with the delivery of high energies in the short, typically 20ns, laser pulse. In the case of fine electrodes, the shock wave caused the lifting of the thin chrome-gold metal film from the glass substrate. To provide additional mechanical rigidity to the metal film and to damp shock wave effects, a second approach was to coat the metal film with a thin, baked, polyimide layer. Electrodes were then formed by ablating through both the polyimide and the gold film prior to the chemical removal of the polyimide. Using this method, improved edge definition was observed. Figure 3 shows a series of 5μm wide electrodes on a glass substrate produced using this improved direct ablation process.

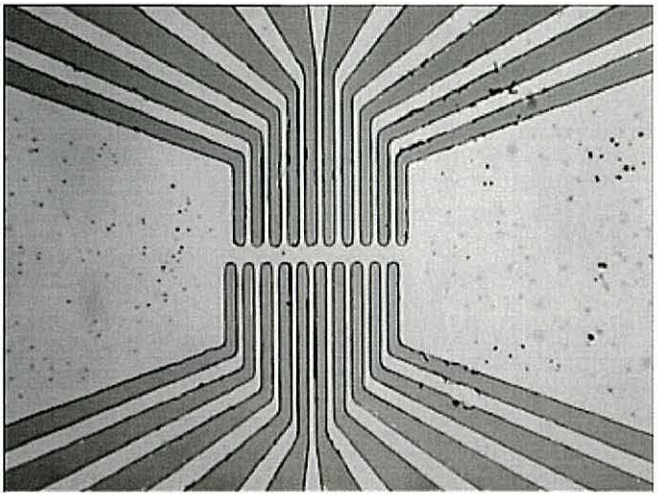

Figure 3. An example of laser patterned microelectrodes for travelling wave dielectrophoresis.

Also visible in figure 3 is a significant amount of debris caused by the recasting of material from the ablation process. This debris is an undesirable by-product of clearing large areas of unwanted metalisation. This form of debris can largely be removed by rinsing in a solvent such as propanol. A better approach to high-resolution electrode manufacture is to avoid debris contamination all together. This was achieved using a third production technique that employed the excimer laser workstation as a deep ultra violet exposure source. In this case, the thin chrome-gold film was coated with a 248nm resist (UVIII, Chestech Ltd UK) which was exposed using synchronised scanning of the mask and workpiece stages with a fluence of 15 $mJcm^{-2}$. Following development of the resist the exposed gold and chrome was etched to produce high quality electrode arrays. Electrodes produced using this process achieved a resolution of 1.25μm being limited by the optical resolution of the 4x demagnification projection lens used to transfer the mask pattern to the workpiece.

Having established a reliable method of producing microelectrodes capable of producing strong AC electric fields, a method for producing reliable inter-layer electrical connections was investigated. The insulator used to separate the field producing electrodes from the busbar electrodes was a spin coatable polyimide (Dupont) that produced a 3μm thick film over the electrodes. Excimer laser ablation has the ability to machine a wide range of polymers with the depth of the ablated structure being controlled by the fluence of the beam and the number of laser pulses received by the workpiece. Therefore, excimer laser ablation can be used to produce via holes only with careful control of the machining process. Figure 4 shows the ablation properties of a 3μm polyimide film. The ablation depth for a single laser pulse is a linear function of the beam fluence. Also shown in figure 4 is the threshold of damage for a thin gold film similar to that used in Biofactory electrode arrays. From the graph it can be seen that using fluences less than 180 $mJcm^{-2}$ will allow the polyimide film to be fully ablated whilst preventing any damage to the underlying electrodes. In this work, a fluence of 100 $mJcm^{-2}$ was chosen to minimise the chance of damaging the electrodes through either

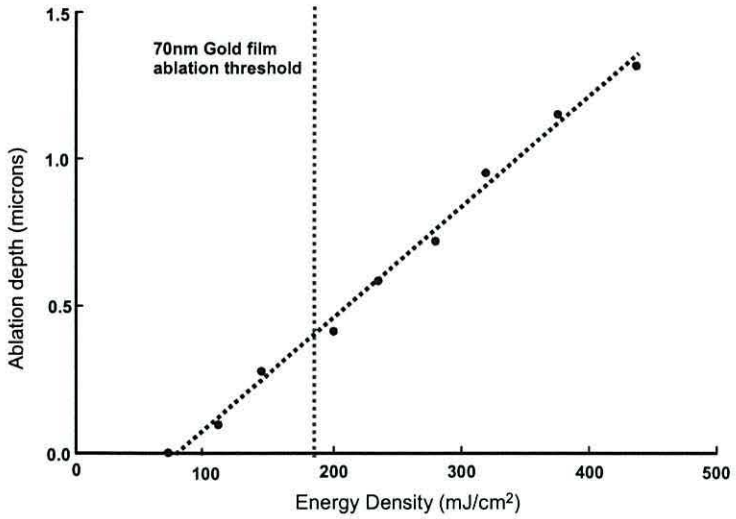

Figure 4. The ablation characteristics of a 3μm thick polyimide film

ablation or thermal stress while maintaining a reasonable rate of machining. Under such conditions, via holes could be produced reliably with 60 laser pulses.

Using either serial writing or scanning machining modes, electrodes via hole arrays were produced with minimal recasting of debris. The excimer laser ablation machining process produced via holes with sidewalls angles of approximately 20° from vertical. However, experimental evaluation of electrode arrays fabricated in this manner revealed an unacceptable level of failed or unreliable via hole connections. Following electron beam microscopy investigation, it was found that, due to the near vertical nature of the sidewalls, via holes appeared to be receiving poor metal coatings during the evaporation of the bus-bar connecting electrodes. To improve the metalisation, the sidewall angle of the via holes had to be increased in a controlled manner to around 70^0. To achieve this sidewall angle, the via holes were machined with a series of steps. Having produced a normal 10μm wide via hole using the previously described method, the workpiece was moved by 1.4μm to one side of the via hole and the workpiece was exposed to a further 8 laser pulses. Repeating this a further 6 times produced a wall profile consisting of 7 steps. Due to the 20° wall angle, these steps tended to merge into one continuous slope. Repeating the process on the opposite side of the via hole produced a reliable through connection between bus-bars and the underlying field producing electrodes. Figure 5 shows a demonstration via hole containing 4 sidewall steps on the front and rear walls of the via hole. These faces correspond to the direction of the bus-bar connecting electrodes.

FLUIDIC CONTROL AND DISTIBUTION

Microfluidic channel systems form an important role in the encapsulation of Biofactory devices. In general, the modular microelectrode arrays used in Biofactories are planar structures, confinement of a sample to the active regions of these electrode arrays occurs at the encapsulation stage through the use of fluidic channels formed in a rigid, optically transparent, encapsulating layer. Fluidic channel systems in encapsulating layers have been formed using several processes including the direct serial writing of channels using excimer laser ablation. Since fluid motion within Biofactory devices is limited, such channels can be of simple rectangular cross section without the concern of particle trapping as a result of fluidic flow profiles. However, of more importance is the interconnection of Biofactory devices with external laboratory equipment. In general, laboratory fluidic interconnection employs circular cross section tubing. Therefore, manifolding components are required to convert circular cross section inlet and outlet ports to rectangular cross section channels within Biofactories. In addition, such manifolds may also be required for the distribution of particle suspensions to multiple Biofactory devices on a single substrate. To allow easy interconnection of fluidic components with arbitrary cross sections, a process for laser ablation based micromachining using greyscale or grey tone masks has been developed.

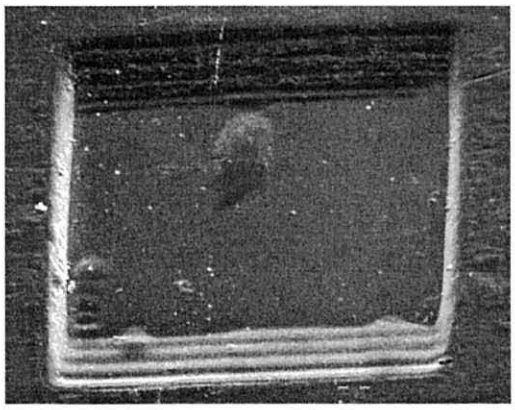

Figure 5. A demonstration via hole with 4 sidewall steps on the front and rear walls.

Conventional laser patterning processes make use of 'binary' masks. These simple masks consist of regions where light is either fully transmitted through the mask or completely blocked. Since

the mask is binary in nature, all exposed regions are illuminated with the same fluence. Therefore, equal amounts of the material are removed in all illuminated regions and the mask pattern is accurately transferred. Greyscale masks, as the name suggests, permit controlled amounts of light to be transmitted allowing a workpiece sample to be exposed to a range of beam fluences. As shown in figure 4, above a threshold of ablation, there is a linear relationship between the depth of ablation and the beam fluence. Therefore, spatially controlling the fluence at a workpiece allows the direct transfer of three-dimensional structures in a simple machining step. Figure 6 illustrates this concept. Here a V-groove structure is to be produced in a polymer workpiece sample. Figure 6b shows the energy profile required to produce the V-groove through the control of ablation depth. At the edges of the groove, no illumination occurs whilst at the centre of the groove, the material is fully illuminated. The V-groove walls are produced using a linear gradient of fluence from the ablation threshold to 100% of the beam fluence. Figure 6c shows schematically the greyscale mask required to produce this fluence gradient. Here it can be clearly seen that zero illumination occurs where the mask is black, 100% illumination occurs where the mask is clear and levels of grey are used to produce a the controlled fleunce gradient.

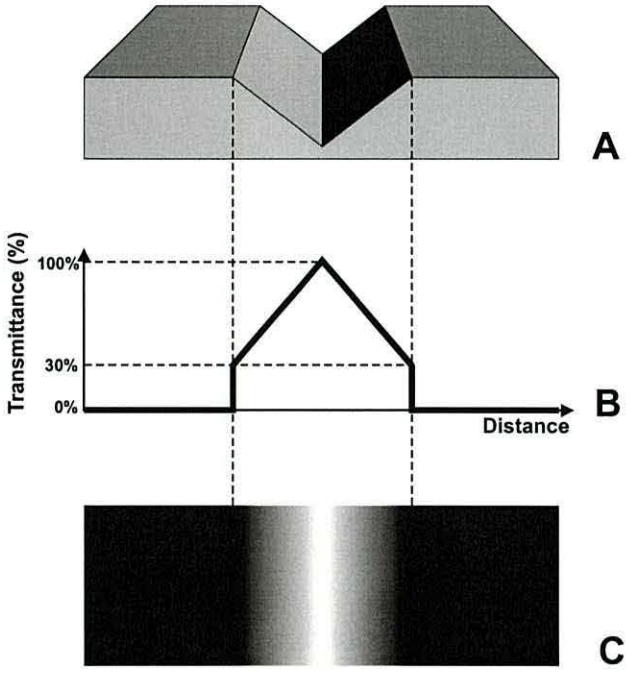

Figure 6. An illustration of the function of a greyscale mask. (a) The structure to be machined. In this case a simple V-groove (b) The exposure fluence required to create the V-groove through a single ablation process. At the apex of the groove the material is fully illuminated, whilst at the edges of the groove zero exposure occurs. A linear fluence gradient is required from the ablation threshold to full illumination to create the linear walls to the groove. (c) An illustration of the greyscale mask used to produce the V-groove structure. Where zero illumination is required the mask is black, where full exposure is required the mask is clear. The fluence gradient is achieved by applying a dithering process to produce a reduction in the mask transmittance. With dither pattern elements much smaller in size than the smallest feature resolvable by the beam delivery optics, a smooth wall surface is achieved.

To allow low cost greyscale based laser micromachining, greyscale masks need to be created using conventional binary mask technology. This can be achieved using binary dithering techniques similar to those used in printing and computer graphics applications. The dithering process controls the average transmittance of the mask over a defined unit area by using a series of dot patterns as shown in figure 7. If the dimensions of the unit area are below the maximum resolution of the beam delivery optics, the individual features of the unit will not be reproduced but instead the ablation depth will depend on the average intensity of the light transmitted through each unit of the mask. The expansion of the computer graphics industry in recent years has lead to the publication of many dithering algorithms suitable for converting between desired image intensity and binary dot patterns. In this work, the clustered dot ordered dither algorithm[7] has been used.

Figure 7 illustrates the output of this algorithm. In summary, each mask unit area is subdivided into an n x n grid. The algorithm determines which elements of this grid are filled and which are left clear with particular attention being paid to the connectivity between filled elements of the grid. A filled area indicates a black (zero transmittance) region of the mask and a clear region indicates a clear (full transmittance) region of the mask. In the case of Figure 7, $n = 3$ resulting in 10 discreet grey levels in the mask. The number of grey levels can be increased by increasing n. Using this technique with a binary mask production process, the number of grey levels is given by n^2+1.

Laser greyscale masks for this work were produced in-house either using a standard photolithographic process or using the resist

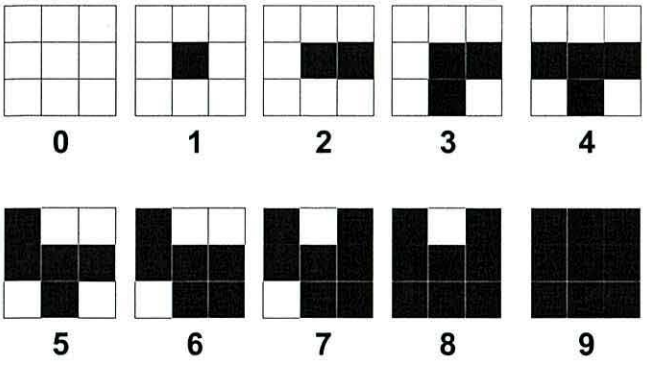

Figure 7. An illustration of the output of the clustered dot ordered dither algorithm used to produce varying transmittance in greyscale masks. The small regions of the mask are subdivided into n by n grids, in this case n=3 leading to 10 discreet grey levels, the algorithm determines which elements of the grid are filled and which remain clear. In the algorithm, particular attention is paid to the connectivity between filled elements of the grid.

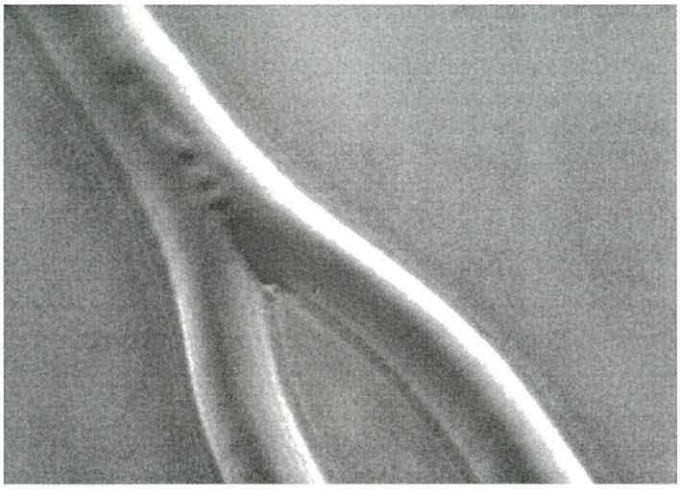

Figure 8. Electron micrograph of a 100μm microfluidic manifold moulding tool microfluidic produced in SU-8 using greyscale masking techniques.

mask production process described previously. In both cases the demagnification factor of the projection lens allowed mask dither features to be larger than the optical resolution of the projection lens. Optimum greyscale reproduction was achieved using a 10x projection lens with a resolution of 0.8μm.

Greyscale laser micromachining has been used in two ways. The first was for the direct machining of channel and manifold structures in polymers such as polycarbonate and PMMA. Here manifolds were constructed in two symmetrical halves that were bonded together using either adhesive, solvent or thermal bonding processes to form a complete manifold. The second application of greyscale machining was the fabrication of moulding tools for the production of multiple manifold systems using thermal embossing processes. Figure 8 shows a simple manifold moulding tool produced using the photosensitive epoxy-based resist SU-8. The channel structure is shown as a positive, raised, feature in the tool. When embossed into a polymer substrate such as polycarbonate, the tool produces a half channel which can be solvent bonded, using ethylene chloride, to a matching half channel producing a full channel with arbitrary symmetrical cross sectional geometry. It is of interest to note in figure 8 the smooth surface quality of the semicircular manifold mould tool. In this case, the inlet side of the manifold (top) has a cross-sectional area twice that of the outlet channels (bottom).

Associated with fluidic distribution in Biofactory devices is the need to provide fluidic isolation of portions of Biofactory devices. This is achieved through the use of microfabricated valve devices as illustrated in figure 9. These use a structure similar to that proposed by Quake[8]. The sidewalls and floor of a microfluidic channel are fabricated in a flexible, easily deformable, material such as rubber or thin PDMS. Beneath the floor of the channel is a second, fluid filled, chamber containing a thin microelectrode on a rigid, glass, substrate. On passing a current through the electrode, heat is produced which causes the fluid in this lower chamber to expand. The separating layer between the upper channel and lower chamber is graded in thickness to allow controlled deformation of the floor of the upper channel. Pressure from the expanding fluid in the lower chamber causes the floor of the channel to extend until it completely blocks the channel so providing fluidic isolation. To provide a strong seal, the ceiling of the upper channel can also be contoured to match the deformation of the channel floor. The use of flexible, deformable, materials makes this form of valving ideal for use with particulate suspensions. Contouring of the channel floor and ceiling can be achieved either using greyscale masking techniques or by the simple machining of concentric circles increasing the

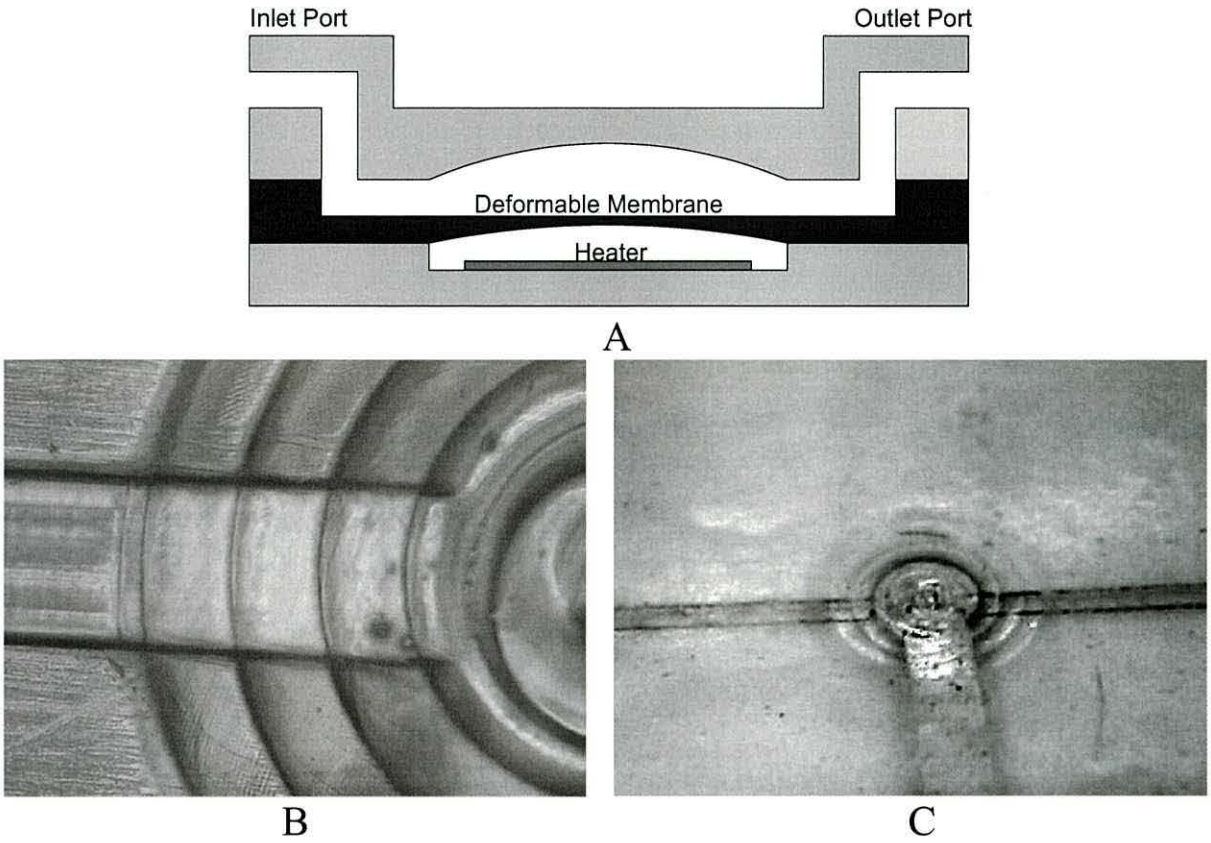

Figure 9. Laser micromachined membrane valves. (A) The floor and sidewalls of a fluidic channel are formed from a flexible material such as rubber or PDMS. The ceiling of the fluidic channel contains a dome structure. Below the flexible floor is a fluid filled chamber containing a heater. The flexible floor has a graded thickness over the heater chamber. On energising the heater, fluid in the heater chamber expands and deforms the flexible floor of the upper channel until the upper channel is blocked. Contouring of the ceiling of the upper channel allows the formation of a good fluidic seal. (B) A close up image of the thinned deformable floor. Thinning is achieved by machining concentric circles of decreasing depth in the floor material using a wavelength of 193nm. The fluence of the laser beam determines the depth of ablation. (C) An overall view of a microvalve showing the inlet to outlet channel running left to right with the heater chamber extending to the lower edge of the image.

depth of machining with reducing circle radii. For the valve shown in figure 9, the flexible material was a 100μm thick rubber film formulated to combine strength and deformability. Machining used a serial writing mode with a wavelength of 193nm. A 200μm aperture mask was projected through a 10x demagnification lens to provide a 20μm beam at the workpiece. A beam fluence of 1 Jcm^{-2} was used with the depth of ablation being controlled by the number of laser pulses incident per unit area of the workpiece. Figure 9b and 9c show optical micrographs of a sample valve system. The overall thickness of the device is approximately 200μm with a diameter of 200μm.

EXTERNAL FLUIDIC INTERFACES

The success of many miniaturised Laboratory-on-a-Chip systems will depend on their ability to reliably interface with conventional, larger, laboratory equipment. Laser micromachining has also been successfully applied to the creation of microfluidic interconnection ports for Biofactory devices. Biofactory devices employ low-pressure fluid flow and only at the time samples enter or leave a device. Interconnection ports have been designed to allow low cost single or

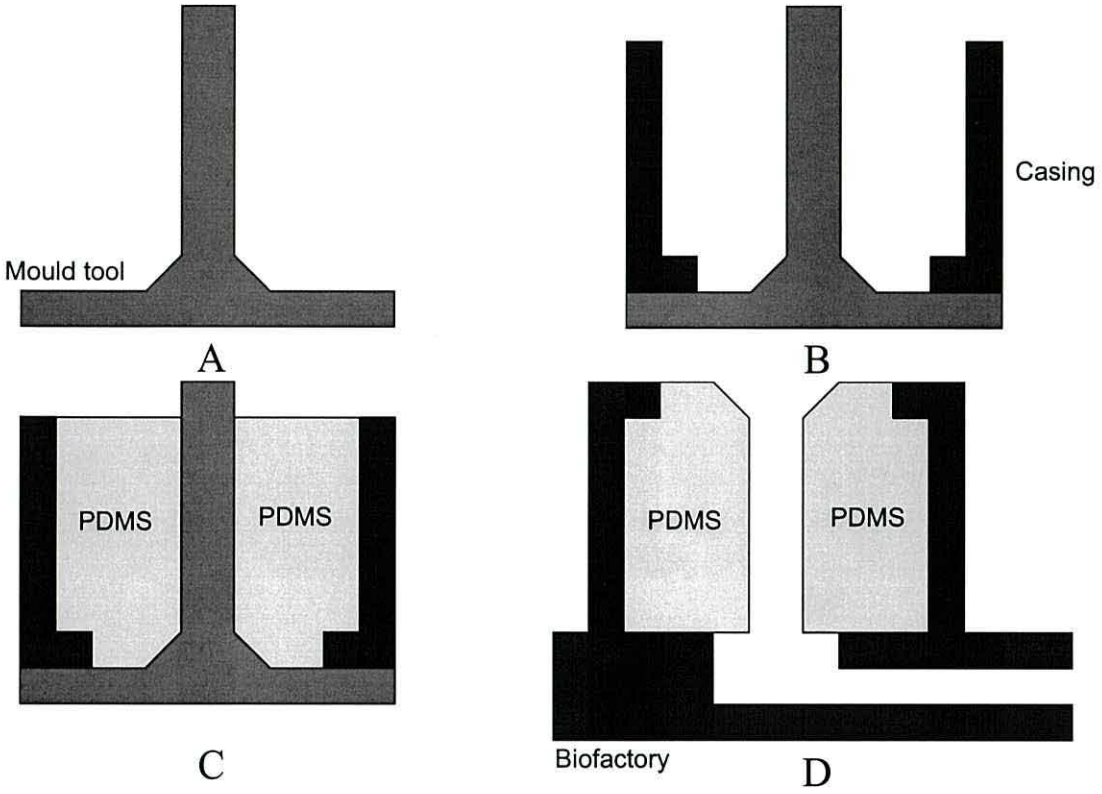

Figure 10. Micromoulding for external fluidic interconnects. (A) A substrate is laser micromachined to produce a negative mould tool of the final PDMS structure. (B) The mould tool is mounted on the inverted outer casing of the inlet port component. (C) PDMS is poured into the cavity formed by the tool and casing until the PDMS reaches the level of the upper wall of the casing. (D) When set, the polymer mould tool is removed and the combined casing and PDMS structured port is inverted and bonded to the interconnection region of a Biofactory device.

multiple use connections suitable for use in automated sample distribution equipment. Such equipment typically uses rigid thin-walled metal tubing to deliver known volumes of a sample onto analytical tools such as multi-well plate arrays. To allow these systems to distribute samples to Biofactory devices, interconnection ports must be able to accept and form a seal around the metal tube. Flexible, mouldable materials such as PDMS[9] are ideal for this purpose. Figure 10 illustrates how laser micromachining can be used for the production of micromoulds for structuring PDMS. Excimer laser ablation based micromachining is used to produce a negative of the structure to be imprinted in the PDMS. In this case the structure consists of a vertical pillar with a cone-shaped base. The mould structure is then mounted on the inverted casing of the interconnection port and PDMS in a liquid state is poured into the cavity created from the mould tool and casing. The PDMS is then allowed to cure before the mould tool is removed. The PDMS insert and casing can then be inverted and bonded to the interconnection region of a Biofactory device.

There are several factors to be considered in fabricating the Biofactory interconnection ports. The first is the choice of materials for the mould tool and outer casing. The mould tool material should possess low adhesion to PDMS in its cured form. Experimentation has shown that the epoxy based photoresist SU-8 to be a suitable material for the mould tool. Conversely, the outer casing of the interconnection port should have good adhesion to cured PDMS. This allows a firm bond between the casing and PDMS insert so assisting the sealing of the port whilst providing mechanical strength. The design of the mould tool is also critical for the operation of the interconnection port. The cone shaped base of the tool is intended to provide a tapered entrance to the port and hence assist in guiding a thin-walled metal tube into the

body of the port. The diameter of this cone is controlled by the positioning accuracy of the automated delivery system and the flexibility of the delivery tube. The fluidic seal of the port is formed by the compression of PDMS onto the outer wall of the delivery tube when it is inserted into the body of the port. Therefore, the diameter of the pillar of the mould tool has to be carefully chosen to be slightly smaller than the diameter of the metal tube but allowing both a good seal and easy insertion and removal. A secondary factor in determining the diameter of the pillar is the composition of the PDMS used as the port insert. PDMS is a two part, addition curing, clear potting compound. Mixing the two parts in different ratios allowed control of the flexibility of the cured PDMS. In this work, a range of mix ratios ranging from 3:1 to 30:1 were used depending on the width and material of the automated delivery tube. PDMS curing was achieved by heating the sample at 80°C for 15 minutes.

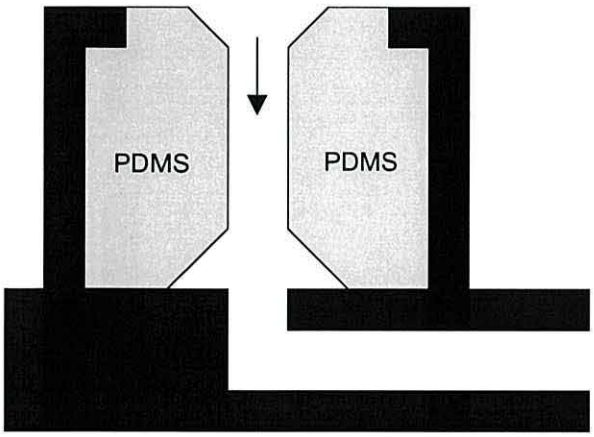

Figure 11. Illustration of a single use interconnection port. The flared exit to the body of the port mates with the flared end of a sample delivery tube to lock the delivery tube in position.

In the case of the interconnection port shown in figure 10d, a multiple insertion design is illustrated. By employing a two part mould tool allowing a cone-shaped entrance and exit to be imprinted in the PDMS insert, a single use interconnection port can be fabricated. The design of such a port is shown in figure 11. Here, the delivery tube possesses a flared end that matches the cone-shaped exit of the PDMS insert. When the tube is inserted into the port, the PDMS stretches to allow the tube to pass along the body of the PDMS insert. When fully inserted, the flared end of the tube mates with the flared exit of the PDMS insert to lock the tube in position. In this construction, any backpressure created within the Biofactory device pushes the flared end against the bulk of the PDMS and increases the strength of the fluidic seal.

CONCLUSIONS

This work has demonstrated that excimer laser ablation based micromachining has a useful role to play in the development of miniaturised Laboratory-on-a-Chip technologies such as the Biofactory devices described here. Examples have been presented to illustrate the use of excimer lasers in the fabrication of complex multilayer microelectrode arrays allowing electrokinetic phenomena such as travelling wave dielectrophoresis to be exploited in micro devices. Of particular importance is the use of laser micromachining to produce accurately profiled electrical via holes in multilayer devices. In addition, the flexible nature of laser micromachining has been demonstrated through examples of fluidic distribution and control components which interface with larger scale production processes such as thermal embossing and injection moulding. This work has culminated in the production of a fully integrated miniaturised Biofactory-on-a-Chip device for the analysis of water borne parasites (figure 2).

ACKNOWLEDGEMENTS

We acknowledge the UK Engineering and Physical Sciences Research Council (EPSRC) and Biological and Biotechnological Research Council (BBSRC) for supporting this research work over a number of years. We thank R. Pethig, M. S. Talary, J. A. Tame, Xiao-Feng Zhou, J. P. Kerslake, J. Drysdale and C. Dalton for their useful discussions and assistance during this work. We also thank N. Rizvi of Exitech Ltd. (UK) for technical assistance and guidance in excimer laser micromachining.

REFERENCES

1. R. Pethig, Dielectrophoresis, "*Using Inhomogeneous AC Electrical Fields to Separate and Manipulate Cells.*" Critical Reviews in Biotechnology **16** (4) 331-348, 1996
2. A.D. Goater and R. Pethig, "Electrorotation and Dielectrophoresis." Parasitology 117 177-189, 1998
3. R. Pethig, J.P.H. Burt, A Parton, N. Rizvi, M.S. Talary and J.A. Tame, "Development of Biofactory-on-a-Chip Technology Using Excimer Laser Micromachining." J. Micromech. Microeng. **8** 57-63 1998
4. M.S. Talary, J.P.H. Burt, J.A. Tame and R. Pethig, "Electromanipulation and Separation of Cells using Travelling Electric Fields." J. Phys. D: Appl. Phys **29** 2198-2203, 1996
5. J. Zhang, K.L. Tan, G.D. Hong, L.J. Yang and H.Q. Gong, "Polymerization Optimization of SU-8 Photoresist and its Application in Microfluidic Systems and MEMS." J. Micromech. Microeng. **11** 20-26, 2001
6. N.H. Rizvi, E.C. Harvey, P.T. Rumsby, J.P.H. Burt, M.S. Talary, J.A. Tame and R. Pethig, "An Excimer Laser Micromachining System for the Production of Bioparticle Electromanipulation Devices." Proc. Int. Soc. Opt. Eng. **3224** 255-272, 1997
7. C. J. Hayden and J.P.H. Burt, "Fabrication of Fluidic Manifold Systems Using Single Exposure Grayscale Masks." Proc. SPIE **4404** 231-237, 2001
8. M.A. Unger, H-P Chou, A. Scherer and S.R. Quake, "Monolithic Microfabricated Valves and Pumps by Multilayer Soft Lithography." Science **288** 113-116, 2000
9. B. Xu, F. Arias, S.T. Brittain, X-M Zhao, B. Grzybowski, S. Torquato and G.M. Whitesides, "Making Negative Poisson's Ratio Microstructures by Soft Lithography." Advanced Materials **11** 1186-1189, 1999

Fabrication of Fluidic Manifold Systems Using Single Exposure Greyscale Masks

C J Hayden and J P H Burt

Institute of Molecular and Biomolecular Electronics
University of Wales, Bangor, Gwynedd LL57 1UT, U.K.

Abstract

Lab-on-a-chip devices are currently being developed at the University of Wales, Bangor. These devices can be used to manipulate and characterise bio-particles suspended in a fluid medium. For precise operation, accurate fluidic transport within these devices is required, for example at channel junctions where flow rates or mixing must be controlled. We present a technique for the production of varying cross-section channels and fluidic manifolds by photolithographic exposure of greyscale masks. This technique is ideally suited to the rapid prototyping and production of lab-on-a-chip devices, since a single exposure system is both faster and simpler than other methods currently available.

Keywords: Lab-on-a-chip, manifold, bio-particle, greyscale

Introduction

Over the past decade, there has been an enormous growth in the development of miniaturised analytical devices, so called Laboratory-on-a-chip devices, based around semiconductor and related microfabrication technologies. In addition, work at the University of Wales, Bangor has recently developed a related technology, named Biofactory-on-a-chip [1]. This employs the electrokinetic phenomena of dielectrophoresis, electrorotation and travelling wave dielectrophoresis to manipulate, separate and characterise particulates such as biological cells, viruses and macromolecules in miniaturised lab-on-a-chip type devices containing arrays of microelectrodes. A common feature of many of these forms of devices is the need to move samples through different microfluidic channel systems. Often, an important factor in moving these samples is the degree of control given to sample velocity, pressure and flow profiles. With sufficient control, samples can be merged, mixed, separated, concentrated and diluted within the fluidic channel systems. Additionally, fluidic channels systems must also be immune from blocking or the presence of dead flow zones where valuable sample volumes can become trapped and hence lost from any subsequent processing. To address these issues, several microfabrication processes have been employed by device developers. Many of the processes used represent a compromise between desired fabrication resolutions, cost of fabrication and required geometry. At the largest scale, micromechanical milling has been used where, like conventional milling, mechanical cutters are moved in a serial manner to cut channel structures in a given substrate. Higher resolution fluidic channels have also been produced using high-resolution excimer laser ablation [2]. In this method, two machining routes are available. In the first, fluidic channels are directly machined by serially writing using an apertured beam. The shape of the aperture used determines the cross-sectional profile of the channel. In the second method the laser beam is used in a similar manner to that of a conventional milling tool, allowing three-dimensional structures to be created by machining a series of contours. Photolithography is probably the most popular method for producing fluidic channel systems. Projecting the desired channel pattern onto a photosensitive material through a photo mask followed by subsequent developing and optional etching allows complex, high-resolution, channel systems to be produced with high reliability. However, each of these methods has limitations. In micromechanical milling, dimensions are limited by the combination of the cutting tool cross-section and the cutting speed of the tool. Excimer laser machining is slow and relatively expensive due to the serial nature of both laser machining methods. Although channels with a degree of circular geometry can be produced by experimenting with developing and etching rates, photolithography typically produces microfluidic channels with square cross-sections.

For accurate control of fluid movements within Laboratory-on-a-chip devices, high-resolution microfluidic channels with controllable cross-sectional geometries are required. Greyscale masking techniques offer one solution to these

requirements. Generated using conventional mask production techniques, this fabrication method allows the production of three-dimensional structures through a low cost, single exposure process. Here we describe the use of greyscale photo masks to produce a range of microfluidic channels and manifolding systems suitable for incorporation into laboratory-on-a-chip devices.

Methodology

Conventional patterning processes for photosensitive materials make use of "binary" masks. These simple masks consist of regions where light is either fully transmitted through the mask or light is completely blocked. When used to process a photosensitive material, such as a photoresist, the mask pattern is projected onto the surface using a radiation source such as an ultra-violet lamp. Areas of the material corresponding to regions on the mask where light is fully transmitted become exposed and the material changes structure. Subsequent chemical processing is then used to differentially remove either the exposed or unexposed regions depending on the material. Since the mask is binary in nature, all exposed regions are illuminated with the same energy fluence. Therefore, in the developing stage of the process, equal amounts of material are removed and the mask pattern is accurately transferred. The linearity and reproducibility of this process is an essential feature of conventional photo processing and is responsible for the high reliability of photolithographic processes.

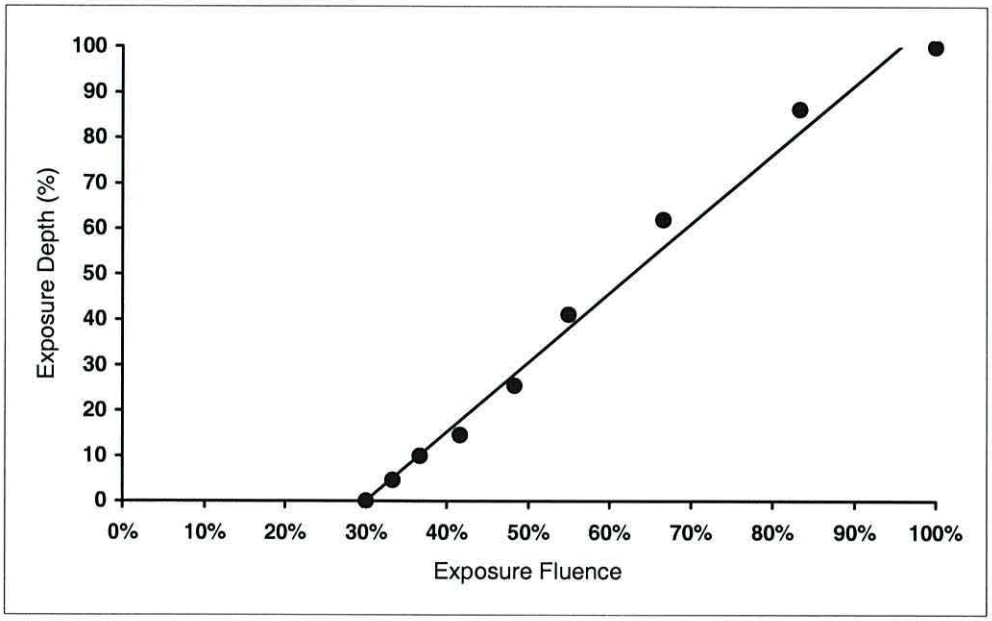

Figure 1

A typical relationship between exposure fluence and exposure depth shown in normalised form. For the case of Laminar 5038 dry film photoresist, 100% exposure fluence is 85 $mJcm^{-2}$. The graph shows zero exposure below a threshold of 30% (approximately 25 $mJcm^{-2}$). Above this threshold exposure doseage, depth is a linear function of fluence until complete exposure occurs.

Greyscale masks, as the name suggests, allow controlled amounts of light to be transmitted. This, in turn, allows photosensitive materials to be exposed to a range of energy fluences. A typical photoresist will be sensitive to light once the fluence is above a threshold value. At this threshold fluence, only the surface of the photoresist will be affected. Since the exposed photoresist will absorb a proportion of the incident light, a larger fluence is required to achieve a greater depth of exposure. Figure 1 shows a typical exposure depth to fluence relationship for a photoresist. Above the exposure threshold the depth of exposure is a linear function of fluence. A plateau is reached when the photoresist is either fully exposed or the exposed photoresist absorbs all the incident radiation. The principle of greyscale masks is to generate a controlled transmission of light through the mask and hence allow the depth of exposure of a photosensitive material to be accurately controlled. If this is the case then, after the developing stage where exposed or unexposed material is removed, a three-dimensional structure will be revealed in the material. This concept is illustrated in Figure 2. Here a V-groove structure,

shown in Figure 2a, is to be produced in a photo-positive material where exposed material is removed at the developing stage. Figure 2b shows the energy profile required to produce the V-groove through the control of the exposure depth. At the edges of the groove, no exposure occurs whilst at the centre of the groove the material is fully exposed. The V-groove walls are produced using a linear gradient of energy from the exposure threshold to 100% of the exposure fluence. Figure 2c shows schematically the greyscale mask required to produce this energy gradient. Here it can be clearly seen that zero exposure occurs where the mask is black, 100% exposure occurs where the mask is white and the levels of grey are used to produce the controlled energy gradient.

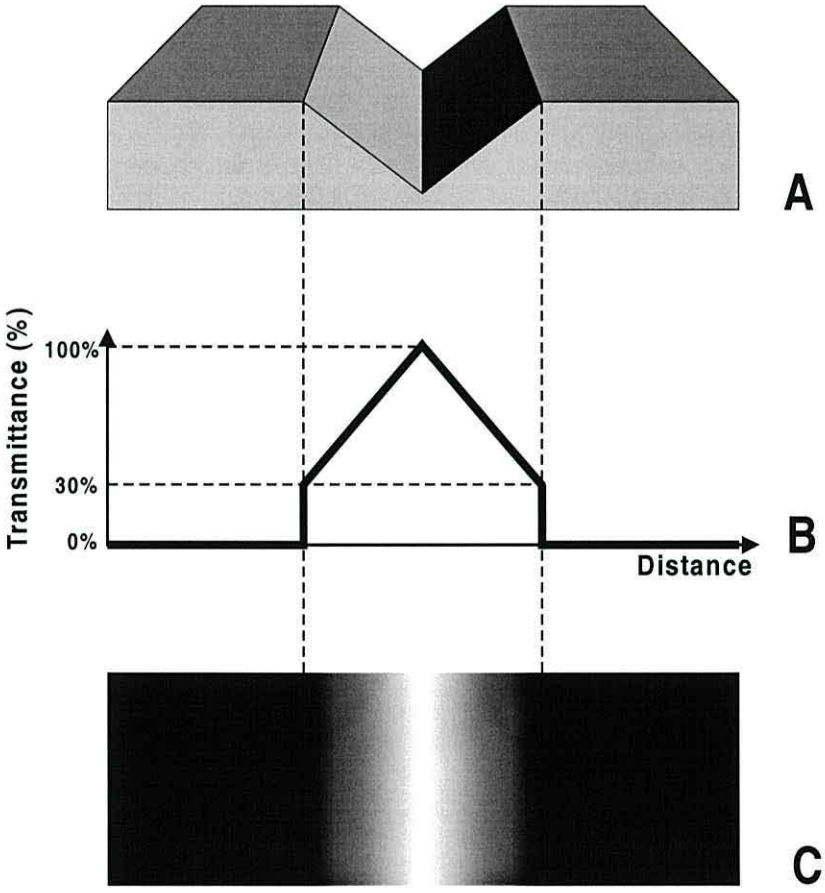

Figure 2

An illustration of the function of a greyscale mask. (a) The structure to be machined. In this case a simple V-groove in a photosensitive material. (b) The exposure fluence required to create the V-groove through a single exposure process. At the apex of the groove the material is fully exposed, whilst at the edges of the groove zero exposure occurs. A linear fluence gradient is required from the exposure threshold to full exposure to create the linear walls to the groove. (c) An illustration of the greyscale mask used to produce the V-groove structure. Where zero exposure is required the mask is black, where full exposure is required the mask is clear. The fluence gradient is achieved by applying a dithering process to produce a reduction in the mask transmittance. With dither pattern elements much smaller in size than the smallest feature resolvable by the photosensitive material a smooth wall surface is achieved.

To allow low cost greyscale exposure, the greyscale mask needs to be created using conventional binary mask technology. This can be achieved by employing binary dithering techniques similar to those used in printing and computer graphics applications. The dithering process controls the transmittance of the mask over a defined unit area by using a series of dot patterns as shown in Figure 3. If the dimensions of the unit area are below the maximum resolution of the photosensitive

material, the individual features of the unit will not be reproduced but instead the material will respond to the average intensity of the light transmitted through each unit of the mask. The expansion in the computer graphic industry in recent years has lead to the publication of several dithering algorithms suitable for converting between desired image intensity and binary dot pattern. In this work, the clustered dot ordered dither algorithm [3] has been used.

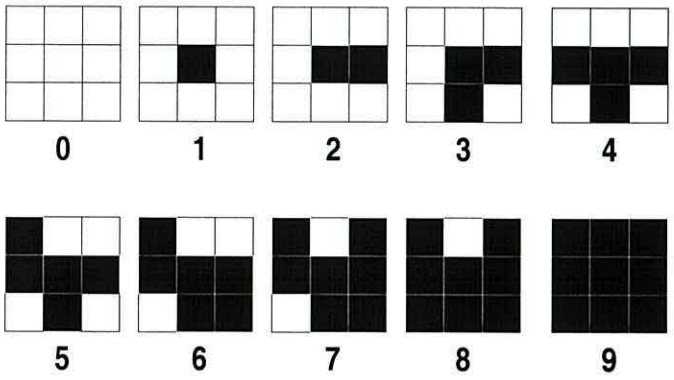

Figure 3

An illustration of the output of the clustered dot ordered dither algorithm used to produce varying transmittance in greyscale masks. The small regions of the mask are subdivided into n by n grids, in this case n=3 leading to 10 discreet grey levels, the algorithm determines which elements of the grid are filled and which remain clear. In the algorithm, particular attention is paid to the connectivity between filled elements of the grid.

Figure 3 illustrates the output of this algorithm. In summary, each mask unit area is subdivided into an n by n grid. The algorithm determines which elements of this grid are filled and which are left clear with particular attention being paid to the connectivity between filled elements of the grid. A filled area indicates a black (zero transmittance) region of the mask and a clear region indicates a clear (full transmittance) region of the mask. In the case of Figure 3, n=3 resulting in 10 discreet grey levels in the mask. The number of grey levels can be increased by increasing n. In general, using this technique with a binary mask production process, the number of grey levels is given by n^2+1.

Results and Discussion

An essential part of many Laboratory-on-a-chip devices is the distribution of liquid samples to designated parts of the device. Often, this should be achieved with minimum disturbance to fluidic flow properties such as flow profile, rate and pressure. Abrupt changes in microfluidic channel cross-sectional profile are known to cause disruption to the normal flow profile. Whilst in many cases these disturbances appear not to enter a turbulent regime, they are undesirable and may lead to quantities of a sample being trapped within the fluidic channel system. This is particularly significant if the sample analyte appears in low concentrations as, for instance, is the case when analysing parasites within water supplies. Using greyscale masks, microfluidic channel systems were created where the cross-sectional profile could be accurately controlled. This allowed the smooth transition between different channel geometries as well as the creation of microfluidic manifolds to divide or combine fluids during sample distribution.

Essential information required prior to the design of greyscale masks is the resolution limit of the photosensitive material to be processed and the exposure energy to exposure depth characteristics for the material. In this work, two photosensitive materials were used. The first was a 50 μm thick dry film photo resist (Laminar 5038, Ozatec), typically used in the manufacture of printed circuit boards, which was laminated, either in single or multiple layers, onto a glass substrate. The second material was the photosensitive epoxy SU-8 (Microlithography Chemical Corporation) which was spin-coated onto glass substrates at thicknesses up to 100 μm. Test binary masks where employed to determine the resolution of each of these materials followed by exposure with a calibrated, high-resolution, greyscale mask containing transmission regions varying from 0% to 100% in 5% steps. Exposure was carried out using a mask aligner (Tamarack MAS12) that allowed 1:1 collimated ultra-violet exposure at a wavelength of 365 nm. Results from these exposure tests revealed that both materials have a resolution limit of around 10 μm and a linear relationship between exposure energy and exposure depth (as shown in

Figure 1). Using this information, masks were produced with a grid element size of approximately 1 μm and greyscale dithering commencing at the threshold of exposure.

In this work, dither patterns were laser plotted at 25x size at a resolution of 4000 lines per inch to create an enlarged master of the final mask. Photographic reduction by a factor of 25 was then employed to produce a final mask. In this process, the final size of the individual grid elements was approximately 1 μm. Using this method represented a significant cost advantage over E-beam and other commercially produced masks that have been used by other workers in this field [4-6]. Additionally, high-resolution rapid prototyping masks were also produced using direct excimer laser abalation of the photographic emulsion on an exposed glass photo mask plate. Using an Exitech Series 8000 Micromachining Workstation (Exitech Ltd., UK) mask feature sizes of 0.8μm could be readily produced so allowing higher accuracy greyscale reproduction.

The numerical analysis package Matlab (Mathworks Inc.) was used to calculate optimum dither patterns for mask creation. Microfluidic channel system geometries were drawn in a commercial 3D CAD/CAM package (AlphaCAM, Licom Systems Ltd.) and subsequently transferred to Matlab for greyscale dither pattern calculation. Figure 4a shows a scanning electron micrograph of a section of a fluidic channel system designed to combine two separate sample types. The circular well structures, approximately 200 μm in diameter, at the end of each channel form part of an inlet or outlet port. Contoured channels lead from the inlet/outlet ports to a Y-junction where slight constrictive projections into the channel promote a degree of sample mixing. This structure forms one half of a full fluidic channel system. A second identical section bonded face-to-face with the existing section can be used to form the complete, enclosed, channel structure. As well as calculating the dither patterns for mask production, the numerical and visualisation features of Matlab were used to produce a three-dimensional graphical representation of the structure the mask would produce. Figure 4b shows the graphical model produced for the example fluidic channel system. Within the resolution limits of the model simulation and the experimental error of the exposure process, the model shows excellent agreement with the actual device. Not only are the three-dimensional profiles of the contoured channel and inlet/output ports reproduced but the constrictive projections for sample mixing can also be seen close to the Y junction in the model.

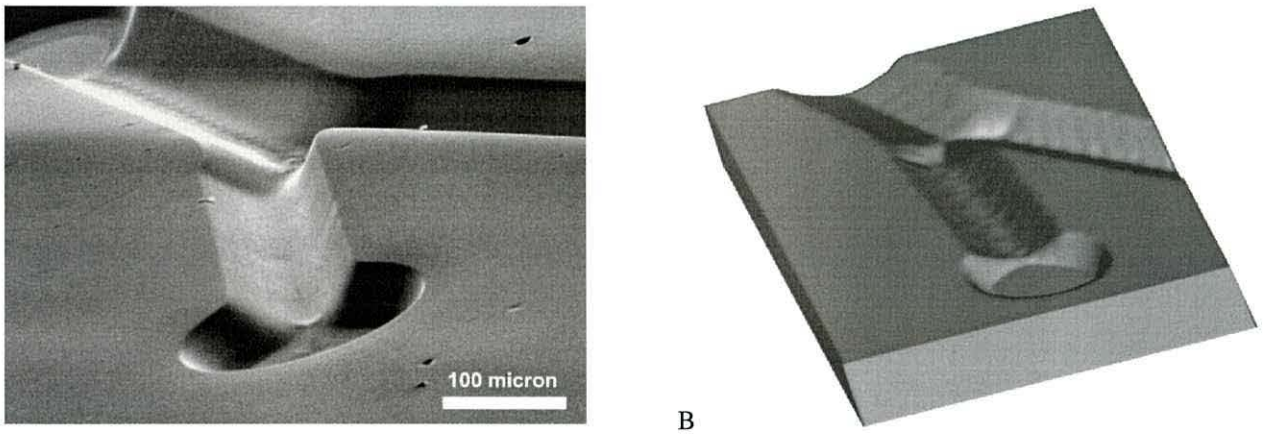

Figure 4

A comparison of an actual and modelled three-dimensional contoured microfluidic system. (a) A simple fluidic device for sample combination and simple mixing. The rounded channels in this device are approximately 100 μm wide with an inlet/outlet port at the end of each fluidic channel. Combination and mixing occurs at the junction of the three channels. (b) An image of the graphical model of the fluidic channel system produced during the Matlab calculations of greyscale dither patterns. Within the errors and resolution limits of the modelling and fabrication process, excellent agreement exists between the model and the final device.

The use of greyscale masks provides a means of producing complex three dimensional structures in photosensitive materials using a single-step exposure process. However, whilst the process is a relatively low cost one, the fabrication requires a number of complex chemical developing steps that are undesirable in the large scale production of devices. A more

acceptable method for large-scale production could utilise well-established polymer duplication techniques such as embossing and injection moulding. Use of such technologies requires the manufacture of a robust "negative" of the desired channel system. Typically, these negative "masters" of the structures are produced in a metal substrate using either a conventional direct metal milling process or a electroforming process from a metal substrate. Greyscale masking can, for small production runs where degradation of the master is minimal, be used to produce the negative for an embossing process. Figure 5 shows the negative master of an array of fluidic manifolds for the combination and separation of fluidic samples within Laboratory-on-a-chip devices. These masters can be used to produce symmetrical fluidic channel sections which, when bonded together form a fully enclosed manifold. Figure 5a shows two sample splitting manifolds on the left hand side and a simple sample combining and splitting unit which can be used to mix two samples together. Figure 5b shows a close up view of the mixing unit to emphasise the smooth curved surfaces that are created by the greyscale production process.

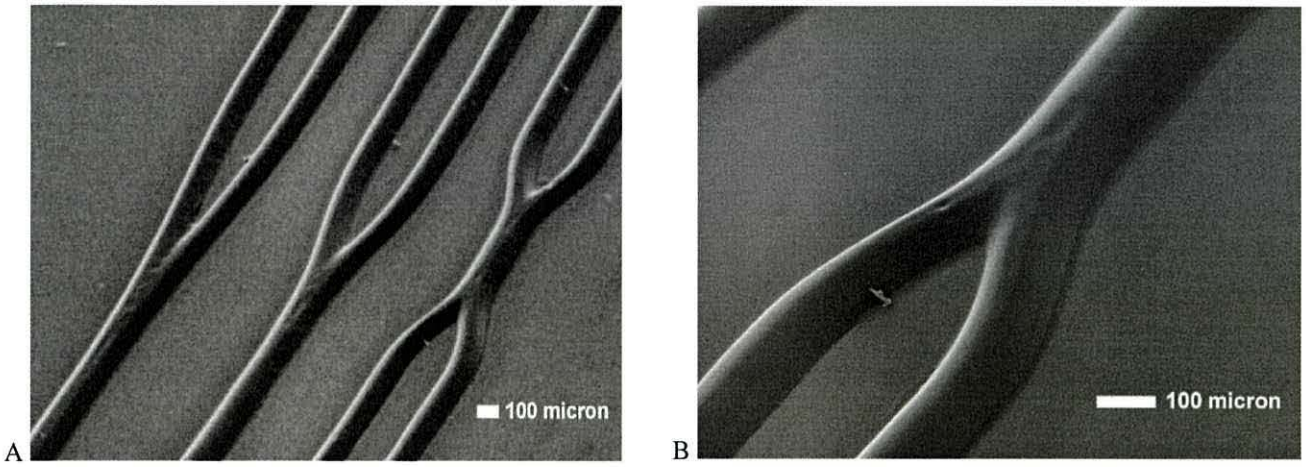

Figure 5

Electron micrographs of greyscale-mask produced microfluidic manifold structures suitable for use in duplication processes such as embossing and injection moulding. The structures were fabricated in SU-8 photosensitive epoxy and show channels with diameters of 100 μm.

Conclusion

Greyscale masking techniques have been successfully used to produce a range of microfluidic channel and manifold structures. The low cost methods of mask production and the use of established computer algorithms for calculating mask greyscales have, through computer modelling, been shown to be both accurate and reproducible. Therefore, with the growing importance of fluidic control within Laboratory-on-a-chip devices we envisage that greyscale fabrication processes will become an increasingly popular form of microfabrication.

Acknowledgements

We acknowledge the UK Engineering and Physical Sciences Research Council (EPSRC) for the provision of a research studentship for C J Hayden. We also thank A D Goater, J A Tame and Xiao-Feng Zhou for useful discussions and assistance during the experimental stages of this work.

References

1. R Pethig, J P H Burt, A Parton, N Rizvi, M S Talary and J A Tame "Development of biofactory-on-a-chip technology using excimer laser micromachining" *J. Micromech. Microeng.*, **8,** pp. 57-63 1998

2. M C Gower, E C Harvey, N H Rizvi, P T Rumsby, J P H Burt, M S Talary, J A Tame and R Pethig "Manufacture of Miniature Bioparticle Electromanipulators by Excimer Laser Ablation" *SPIE Proceedings* **3274** pp. 152-160 1998

3. Holladay, T.M., "An Optimum Algorithm for Halftone Generation for Displays and Hard Copies" *Proceedings of the society for information display* **21(2)** pp. 185-192 1980

4. S K Rotich, J G Smith, A G R Evans and A Brunnschweiler "Photoresist parabolas for curved micromirrors" *J. Micromech Microeng.* **8** pp. 108-110 1997

5. S Nicolas, E Dufour-Gergam, A Bousseboeuf, T Bourouina, J-P Gilles and J-P Grandchamp "Fabrication of a gray-tone mask and pattern transfer in thick photoresists" *J. Micromech and Microeng* **8** pp. 95-98 1998

6. B Wagner, H J Quenzer, W Henke, W Hoppe, W Pilz "Microfabrication of complex surface topographies using grey-tone lithography" *Sensors and Actuators A* **46-47** pp. 89-94 1995

DEVELOPMENT OF A MICRO SYSTEM FOR CIRCULAR CHROMATOGRAPHY USING WAVELET TRANSFORM DETECTION

J.C.T.Eijkel[1], C.Dalton[2], C.J.Hayden[2], J.A.Drysdale[2], Y.C.Kwok[1], A.Manz[1]
[1]AstraZeneca SmithKline Beecham Centre for Anal. Science, Imperial College, London, UK
[2]Institute of Bioelectronics and Molecular Microsystems, University of Wales, Bangor, UK

Abstract
Two components of a circular chromatography system are demonstrated: a magnetohydrodynamic micropump and wavelet transform detection.

Keywords: Magnetohydrodynamic pump, circular chromatography, wavelet transform

1. Introduction

When chromatography is performed in a circular channel with detection at some point(s) along the channel, it is possible to vary the analysis time at will. The plate number will be proportional to analysis time, enabling the generation of extremely high plate numbers for difficult separations but also the reduction of analysis time for simple separations. A pumping method is needed that is suitable for circular channels. Also, a sensitive detection method is needed. Both elements are presented here.

2. Magnetohydrodynamic micropump

When perpendicular magnetic and electrical fields are applied to an electrolyte solution, a Lorentz force on the electrolyte ions results, propelling the solution. Lemoff and Lee constructed the first practicable circular magnetohydrodynamic pump applying ac fields to reduce electrolysis [1]. The present device is based on the same principle but has a much smaller channel depth, necessitating the application of a strong magnetic field and a high current density at high frequency (10-100 kHz). The device (Fig.1) consists of a glass/gold/laminate/glass sandwich with a 30 μm deep and 400 μm wide circular channel of 1 cm radius as well as injection channels defined in the gold. The magnetic field is generated by five toroidal ferrite electromagnets fitted around half the channel circumference (Fig.2). The current is sent between the gold channel walls. A study of pumping characteristics of, and chromatography with the device is ongoing.

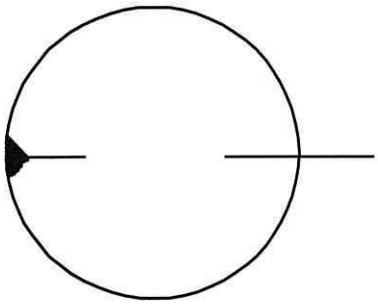

Figure 1. Channel layout of the circular micropump with straight injection channels

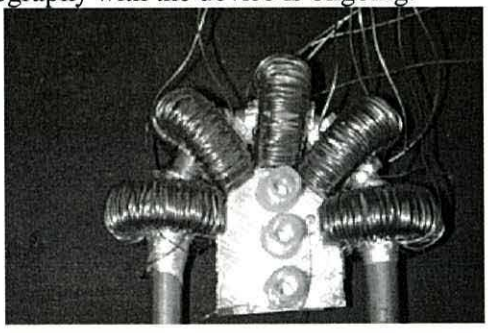

Figure 2. The micropump slotted in the toroidal electromagnets

J.M. Ramsey et al. (eds.), Micro Total Analysis Systems 2001, 541-542.

3. Wavelet transform detection

In a set-up where the separation channel is periodically illuminated, moving bands of fluorescent analyte generate a periodic emission signal (the Shah convolute of the detection signal) that can be transformed into frequency (and hence velocity) information by Fourier transformation [2]. This method increases detection sensitivity. For the last step, wavelet transformation offers a good alternative since it produces both frequency and time information. Two examples using data from electrophoretic separations in straight channels will demonstrate this. Fig.3a shows the Shah convolution detection signal generated for a separation of an analyte mixture, and Fig.3b its wavelet transform. Here the wavelet transformation enables not only frequency and hence component resolution of three analytes (y-axis), but it also shows how the fastest analyte leaves the channel first (x-axis). Fig.4 shows a conventional detection of the same sample. Fig.5 shows the detection signal and wavelet analysis obtained for a separation of two analytes [2]. A frequency drift is observed that went undetected in Fourier transform. In circular chromatography, an inhomogeneous coating of the stationary phase could easily cause periodical drifts, and their detection will be important to obtain maximal peak resolution in the frequency domain.

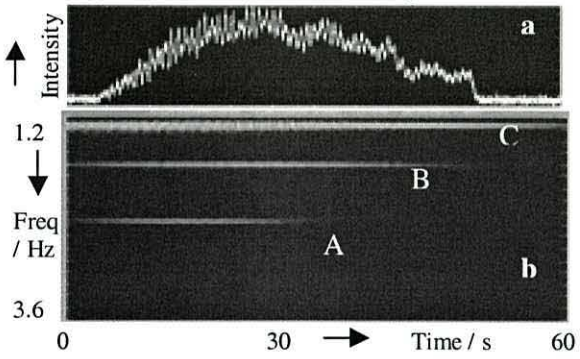

Figure 3. Demonstration of wavelet detection. (a) the convoluted detection signal; (b) the wavelet transform

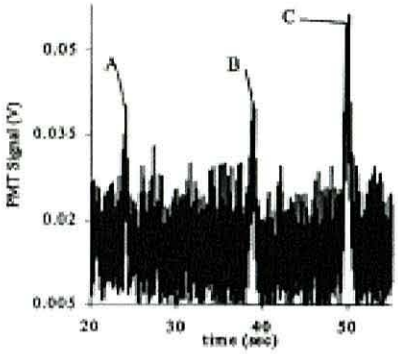

Figure 4. Electropherogram of the same sample containing analytes A, B and C

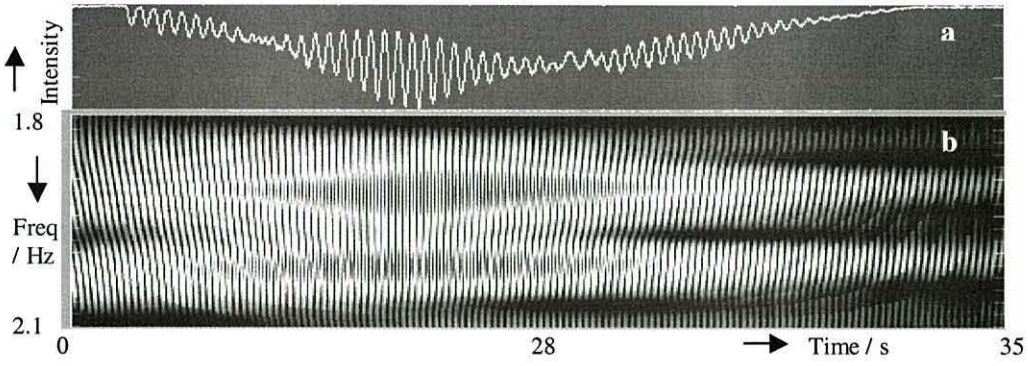

Figure 5. Demonstration of wavelet detection. (a) convoluted detection signal of an electrophoretic separation of two analytes; (b) the wavelet transform

Acknowledgement

The work presented here was partly sponsored by the EPSRC UK, the Department of Trade and Industry (DTI) and the Lab-on-a-Chip consortium (LOC).

References

1. A.V.Lemoff and A.P.Lee, Sensors and Actuators B 63 (2000), 178.
2. H.J.Crabtree, M.U.Kopp and A.Manz, Anal.Chem.71 (1999), 2130.

Inst. Phys. Conf. Ser. No 163
Paper presented at the 10th Int. Conf., Cambridge, 28–31 March 1999

Electric Field Interaction with Debris Generated by Laser Ablation of Polyimide Films

C J Hayden, R Pethig and J P H Burt

Institute of Molecular and Biomolecular Electronics
University of Wales, Bangor, Gwynedd LL57 1UT, U.K.

Abstract Laser ablation is a method of machining structures to micron resolution. This technique is being used to micro-machine Biofactory-on-a-chip devices for manipulating bio-particles. The laser ablation process removes material efficiently, but also generates debris that degrades the micro-structures produced. We have found that externally applied fields in the range 0.7 to 1 MVm^{-1} can be used to control debris deposition.

1. Introduction

Laser ablation is currently being used as a method of micro-machining biofactory-on-a-chip devices [1]. These devices utilise electric fields to generate dielectrophoresis forces for manipulating very small particles such as cells and bacteria. In order to do this the devices require electrode and fluidic channel features that are similar to the dimensions of cells, i.e. microns in size. Various materials are employed to form the required structures, including plastic insulator films, resists and conducting metal layers.

Constructing these devices is challenging and requires specialist equipment. The system used in our work consists of an Exitech Series 8000 microfabrication workstation with a Lambda Physik Compex 110 krypton-flouride excimer laser. The workstation allows the workpiece to be positioned both horizontally and vertically to an accuracy of 0.1 micron, under computer control. The laser generates 248nm light pulses that are guided to the workpiece via a beam profiling mask and projection lens that allow the incident laser beam to be shaped. The masks used are typically chrome on quartz, which are mounted in an X-Y motion stage that has a total movement of 300mm x 300mm. An attenuator provides for accurate control of the intensity of the laser and a homogenizer utilises a 6 x 6 lens array to average the total beam power. This provides a pulse energy variation of less than ±5% RMS in 86% of the total beam area. The maximum fluences that are attainable at the workpiece are around 3 to 10 J cm^{-2}, depending upon the magnification of the projection lens used.

This system allows various materials to be accurately machined using laser ablation. Typically, plastic films are used to either separate the electrical contacts (machined in gold films) or to allow channels to be formed for fluidic transport within the Biofactory devices. A common insulator used in such devices is polyimide, either in sheet form or spin coated onto underlying structures.

When polyimide is ablated, the incident photons of light cause the polymer to de-polymerise through photochemical bond breaking. This, combined with other destructive forces, such as induced shockwaves and localised heating, results in the production of predominately small (<4 atoms) products and the ejection of this debris at high (supersonic) velocities [2]. This debris (mainly elemental carbon) can degrade the quality of the micromachined structures. An example of this is shown in Fig 1.

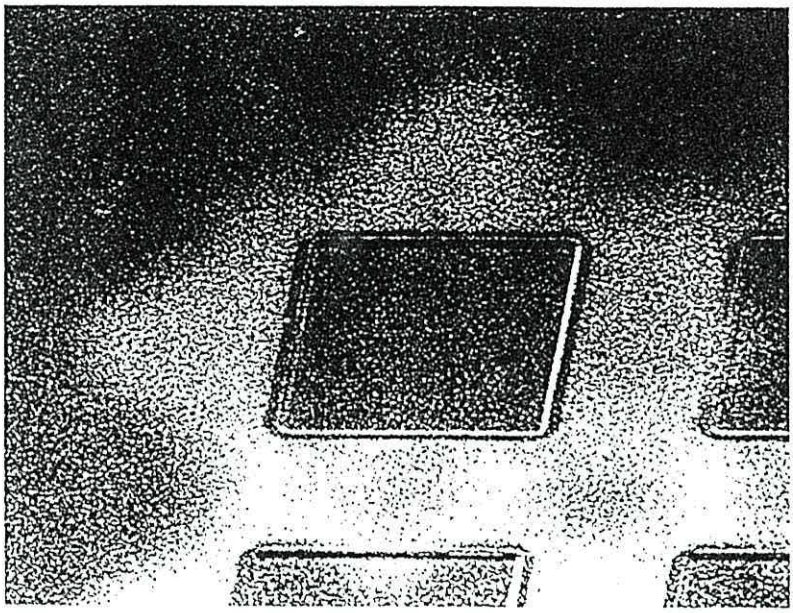

Fig 1. Scanning Electron Micrograph of a 50 micron square hole, ablated in a polyimide film. The debris can be seen to form a diamond pattern around the hole.

The debris generated can be seen as the pale, powder-like, material that surrounds or partially covers the ablated areas. In this report we describe how debris formation can be influenced by generating large, local, DC electric fields during the laser ablation process.

2. Experimental

Kapton HN® polyimide films, up to 100 micron thick, were mounted on glass substrates. Local electric fields were generated using 3.0mm ±0.01mm thick stainless steel electrodes (see Fig 2.) with a Fluke model 608B power supply capable of providing 6kV DC in 0.1V steps, with a maximum of 250mV ripple at full load.

To avoid electrical damage to the (earthed) laser workstation and associated systems, the electrodes were mounted in an insulated test area that in turn was mounted on a granite chuck. Glass apertures in the sides of the test area allowed use of the laser height measurement system and workpiece viewing cameras.

The same basic procedure was followed for all of the sample ablations. This consisted of a control test pattern being machined in the sample with no applied local electric field. The same test pattern was then machined in the polymer (at different sites) for different field strengths. The 'plumes' generated by the laser ablation process were photographed and estimated to extend about 1mm above the polyimide surface. The samples were then inspected using an optical microscope (OLYMPUS BX60). From this, images could be recorded directly to electronic format, using a video capture system. The samples were then gold-plated and examined using an ISI-40 scanning electron microscope.

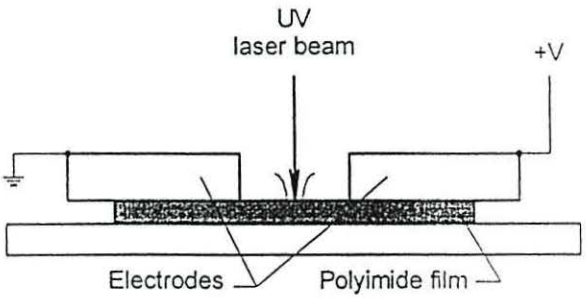

Fig. 2 Schematic of electrode setup used; inter-electrode spacing varied between 1 to 4 mm

3. Results

As shown in Fig. 3 the deposited debris pattern changed as the applied field was increased.

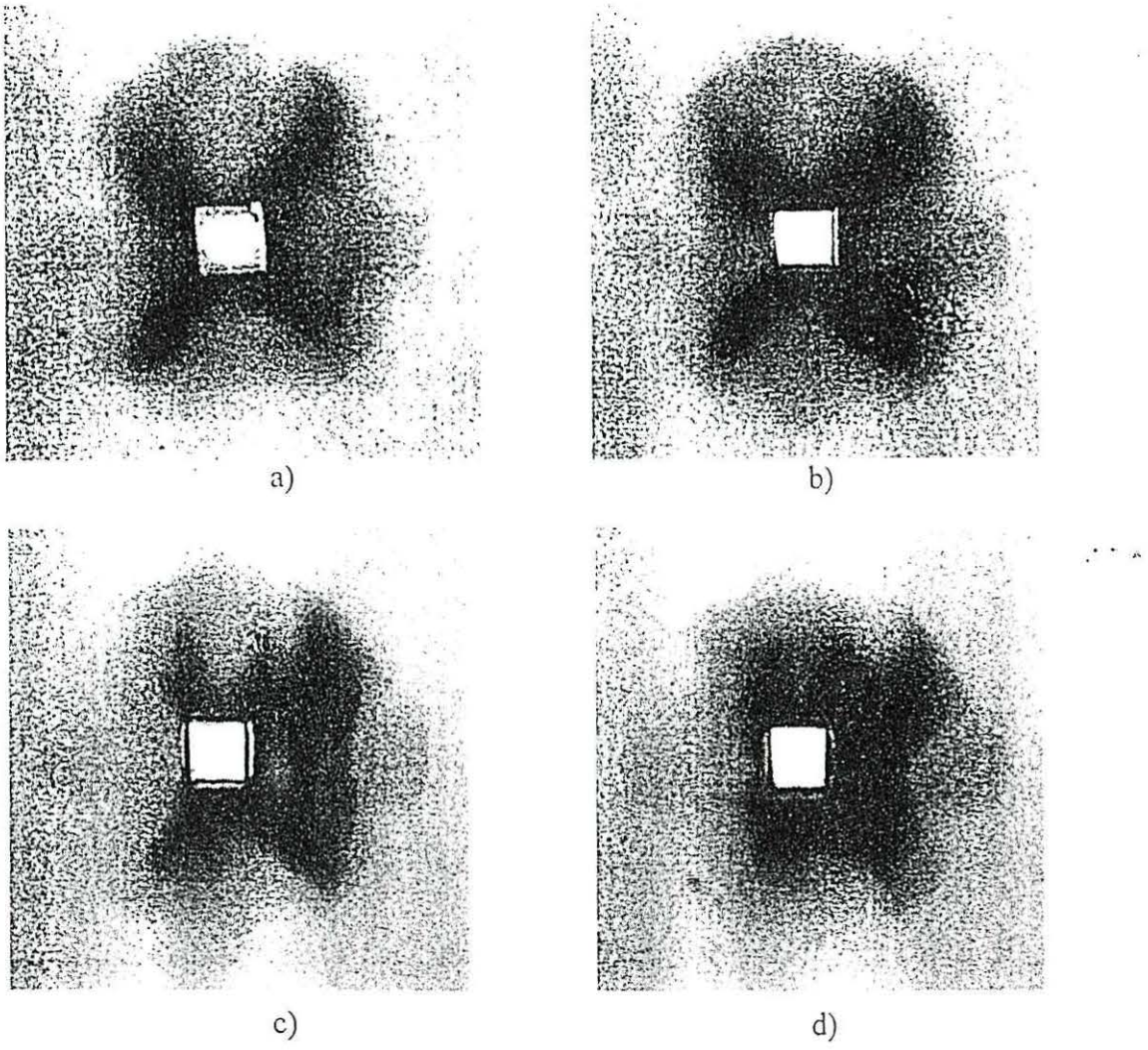

Fig. 3 Debris pattern formed around a 100 micron square, 30 micron deep, pit ablated in a polyimide film with a) zero b) 1kV c) 2kV d) 3kV applied to the electrodes shown in Fig. 2. See text for further details.

The debris can be seen to form 'petals' that surround the ablation area. With no applied field, the 'petals' are approximately symmetrical, and could result from the effect of shock waves thought to drive debris back onto the substrate [3]. As the applied field is increased

the debris 'petals' shift towards the right of the images until very little is deposited to the left of the ablated area. All images in Fig. 3 are oriented with the grounded electrode to the left and the positive electrode to the right of the ablated area. All of the sample ablations were in the middle of the inter-electrode gap (2.8mm), well away from the field fringing effects at the ends of the electrode strips. The electric field profiles were calculated using the Maxwell 2D field simulator (Ansoft, Pittsburgh). At mid-plume height (~0.5mm) the electric field at the centre of the ablated pit was found to be $0.35MVm^{-1}$, $0.68MVm^{-1}$ and $1.1MVm^{-1}$ for applied voltages of 1kV, 2kV and 3kV respectively.

4. Discussion

The results of Fig. 3 indicate that the trajectory of the ejected debris from the surface of the sample during ablation can be influenced by an external electric field. Because in all cases the debris particles are displaced towards the positive electrode, it can be deduced that either the particles themselves, or the associated plume of particles and gases carry a negative charge.

Although the particles of debris could be charged as a result of the ablation process producing free radicals (i.e. broken chemical bonds) another possible mechanism could be that of corona charging [4]. High voltage tests in normal atmospheric conditions on the electrode arrangement of Fig. 2 have shown that the threshold voltage for corona discharge occurs around 2kV (with complete electrical breakdown at around 3.5kV). Corona charging of the particles could therefore account for the non-linear relationship between the applied voltage and resulting debris deposition shown in Fig. 3.

5. Conclusion

The results of this investigation show that the debris generated by laser ablation can be affected by an applied DC electric field. Full control of this method will require a better understanding of the processes by which the debris particles are electrically charged. Corona charging appears to be a strong candidate for this process.

Acknowledgements

This work is funded by an EPSRC studentship (to C J Hayden) and a BBSRC grant (TO6337). We thank Prof. D M Taylor, A D Goater, M C Malpass, D Poirot, M S Talary and J A Tame for useful discussions and assistance.

References

[1] Pethig R, Burt J P H, Parton A, Rizvi N, Talary M S and Tame J A 1998 *J. Microtech. Microeng.* **8** 57-63

[2] Srinivasan R, Braren B and Dreyfus R W 1987 *J. Appl. Phys.* **61** 372-376

[3] Koren G and Oppenheim U P 1987 *Appl. Phys. B* **42** 41-44

[4] Taylor D M and Seeker P E 1994 *Industrial Electrostatics* Research Studies Press Ltd., Taunton. pp116-122.